

AIX-MARSEILLE UNIVERSITÉ
ECOLE DOCTORALE : Physique et Sciences de la Matière
(ED 352)

LABORATOIRE LASERS PLASMAS ET PROCÉDES
PHOTONIQUES

Thèse présentée pour obtenir le grade universitaire de docteur

Spécialité : Optique, Photonique et Traitement d'image

Margaux CHANAL

Space-time study of energy deposition with intense infrared laser
pulses for controlled modification inside silicon

Soutenue le 14/12/2017 devant le Jury composé de :

Pr. Hugues GIOVANINNI	Institut Fresnel, Marseille (France)	Président du Jury
Pr. Nadezhda BULGAKOVA	HiLASE (Czech Republic)	Rapporteur
Dr. Inka MANEK-HÖNNINGER	CELIA, Bordeaux (France)	Rapporteur
Pr. Stefan NOLTE	IAP, Jena (Germany)	Examineur
Pr. Andrei V. RODE	LPC, ANU, Canberra (Australia)	Examineur
Dr. Olivier UTEZA	LP3, Marseille (France)	Directeur de thèse
Dr. David GROJO	LP3, Marseille (France)	Co-Directeur de thèse

Numéro national de thèse/suffixe local : 2017AIXM0001/001ED62

À mon parrain, à ma Grande Mamie.

Résumé

Analyse spatio-temporelle du dépôt d'énergie par lasers infrarouge intenses pour la modification contrôlée du silicium

La modification du silicium dans son volume est possible aujourd'hui avec des lasers infrarouge nanosecondes. Néanmoins, le régime d'intérêt pour la modification contrôlée en volume des matériaux transparents correspond aux impulsions femtosecondes. Cependant, aujourd'hui aucune démonstration de modification permanente du volume du Si n'a été réalisée avec une impulsion ultra-brève (100 fs). Pour infirmer ce résultat, nous avons développé des méthodes de microscopie infrarouge ultra-rapides. Tout d'abord, nous étudions le microplasma confiné dans le volume, caractérisé par la génération de porteurs libres par ionisation nonlinéaire du silicium, suivie de la relaxation totale du matériau. Ces observations, couplées à la reconstruction de la propagation du faisceau dans le matériau, démontrent un dépôt d'énergie d'amplitude fortement limitée par des effets nonlinéaires d'absorption et de propagation. Cette analyse a été confirmée par un modèle numérique simulant la propagation nonlinéaire du faisceau femtoseconde. La compréhension de cette limitation a permis de développer de nouvelles configurations expérimentales grâce auxquelles l'endommagement local et permanent du volume du silicium a pu être initié en régime d'impulsions courtes.

Abstract

Space-time study of the energy deposition with intense infrared laser pulses for controlled modification inside silicon

The modification of bulk-silicon is realized today with infrared nanosecond lasers. However, the regime of interest for controlled modifications inside transparent materials is femtosecond pulses. Today, there is no demonstration of permanent modification in bulk-Si with ultra-short laser pulses (100 fs). To increase our knowledge on the interaction between femtosecond lasers and silicon, we have developed ultra-fast infrared microscopy experiments. First, we characterize the microplasma confined inside the bulk, being the generation of free-carriers under nonlinear ionization processes, followed by the complete relaxation of the material. These results, combined with the reconstruction of the beam propagation inside silicon, demonstrate that the energy deposition is strongly limited by nonlinear absorption and propagation effects. This analysis has been confirmed by a numerical model simulating the nonlinear propagation of the femtosecond pulse. The understanding of this clamping has allowed us to develop new experimental arrangements, leading to the modification of the bulk of Si with short pulses.

Remerciements

Cette thèse est le résultat de trois ans de recherches au sein du Laboratoire Lasers Plasmas et Procédés Photoniques (LP3) à Marseille. Je tiens à remercier en premier lieu Philippe Delaporte, directeur du LP3, de m'avoir accueilli et permis d'effectuer ces travaux de thèse.

Je souhaite remercier Pr. Nadezhda Bulgakova et Dr. Inka Manek-Hönninger qui ont accepté de rapporter cette thèse. Toutes leurs remarques, corrections et questions ont permis d'améliorer la qualité de ce manuscrit. J'adresse mes remerciements au Pr. Hugues Giovannini, Pr. Stefan Nolte, et au Pr. Andrei Rode pour avoir accepté de faire partie de ce jury. J'ai été honorée d'avoir ce jury composé d'experts venant de laboratoires de République Tchèque, d'Australie, d'Allemagne et de France pour ma soutenance de thèse.

J'ai été encadrée pendant ces trois années par deux chercheurs que j'admire beaucoup. Je tiens donc à remercier Dr. David Grojo, mon co-encadrant de thèse. David, je te remercie pour ta disponibilité, ton calme à toute épreuve, les réponses à toutes mes questions, ta confiance, et ton soutien. Être encadrée par un chercheur aussi brillant que toi a été une réelle chance pour moi. Je remercie également Dr. Olivier Utéza, mon encadrant de thèse. Olivier je te remercie d'avoir essayé d'augmenter mes connaissances scientifiques lors de nos réunions de thèse, ou encore mes connaissances en Histoire lors de notre voyage à Iéna. Ta culture (et pas seulement scientifique) m'a toujours impressionné, je me sens chanceuse d'avoir pu travailler à tes côtés. La façon dont tu te soucies humainement des autres est une qualité précieuse. Tous les deux vous formez un duo d'encadrants de choc !

Je tiens ensuite à remercier toutes les personnes qui ont contribué de près ou de loin au bon déroulement de cette thèse. Je m'excuse par avance si j'en oublie... Le laboratoire LP3 est un lieu de travail exceptionnel. J'ai rencontré dans ce laboratoire des personnes formidables, qui font de ces trois ans un souvenir inoubliable. Je pense à mon équipe de choc composé d'un blond et d'un bouclé, vous mes camarades de conf', de soirées, où on a refait le monde pendant des heures, merci pour tous ces bons moments à vos côtés. Merci à Lolo pour ta disponibilité générale, tes avis sur les expériences laser ou sur les trails au mont Puget. Nos débats et séances de dégustation autour du chocolat noir vont me manquer. Quand je pense au chocolat je pense à Marc et Philippe, mais ils me font aussi me rappeler que dans ce laboratoire, il y a des oreilles attentives à qui on peut toujours demander conseil. L'accueil du LP3 est tenu par Max, avec qui on peut discuter de beaucoup de choses, surtout de sport, de vin et de saucisson. Ton sourire tous les matins est le meilleur accueil qu'il soit. Je remercie également Jean-Luc, qui a passé des heures à confectionner mon support de sphère en silicium. J'ai été ravie du mélange de nationalités rencontré parmi les étudiants que j'ai côtoyé au sein du laboratoire : Isabel, Qingfeng, Shyama, Xin et tous les autres... Amélie, ma coéquipière bordelaise, continue de t'entraîner à la pétanque pour pouvoir un jour être la boss de ton bureau ! Merci à tous les chercheurs du LP3, Thierry, Pat, Gaëlle, Ahmed sans oublier J'örg, humoriste et

physicien brillant. Je souhaite bon courage à Thibault et Mathieu pour leur thèse. Profitez-en, c'est une période tellement enrichissante !

Cette thèse était pour moi plus qu'un simple projet professionnel, et je me suis impliquée totalement. Merci à mes amis et ma famille d'être venu à ma soutenance, ça a été un moment extraordinaire. Je pense surtout à ma Mamie Jacotte, ma marraine, mes parents, mon frère, toutes ces personnes qui m'ont toujours soutenu et qui ont grandement contribué à l'aboutissement de ce travail.

Cette thèse n'aurait pas été un si bon moment si ça n'avait pas été à Marseille. J'y ai rencontré des personnes incroyables, à vous tous MERCI !

Table of Contents

Synopsis	i
Introduction	i
1 Bulk silicon irradiated by an intense infrared laser flux: fundamental background	1
1.1 Introduction	2
1.2 Excitation processes	5
1.2.1 Photoionization inside a solid	6
1.2.1.1 Keldysh theory and ionization regime in Si	6
1.2.1.2 Multiphoton absorption	7
1.2.1.3 Tunneling ionization	8
1.2.2 Collisional ionization	9
1.2.3 Electron behavior described by the Drude model	10
1.2.4 Doped semiconductors: principle and applications	13
1.3 Relaxation mechanisms	14
1.3.1 Diffusion and recombination	14
1.3.1.1 Carrier diffusion	14
1.3.1.2 Carrier recombination	15
1.3.2 Free-carrier density rate equation	17
1.4 Nonlinear propagation inside Si	18
1.4.1 Nonlinear polarization	18
1.4.2 Kerr effect	18
1.4.2.1 Spatial domain: self-focusing	19
1.4.2.2 Spectral domain: self-phase modulation	20
1.5 Physics of bulk silicon nonlinear ionization: state of the art and remaining challenges	21
2 Description of the intense infrared laser sources used for investigations	25
2.1 ASUR platform	26
2.1.1 Titanium:Sapphire laser source	26
2.1.1.1 Generation of the femtosecond pulse	26
2.1.1.2 Time-frequency relationship	28
2.1.1.3 Dispersion of ultra-short pulses	29
2.1.2 Optical Parametric Amplification	31
2.1.2.1 General description	31

2.1.2.2	Description of the high-energy OPA	32
2.2	Characterization of the femtosecond pulses	34
2.2.1	Spatial features of the femtosecond pulse	34
2.2.1.1	Beam profile imaging	34
2.2.1.2	Propagation characteristics	35
2.2.2	Temporal and spectral measurements	36
2.2.2.1	Pulse duration	36
2.2.2.2	Spectrum	38
2.3	Presentation of the picosecond and nanosecond laser sources	39
2.3.1	Picosecond laser source	39
2.3.2	Nanosecond fiber laser	39
2.4	Conclusions	41
3	Experimental study of Si response to ultra-fast infrared pulses	43
3.1	Ultra-fast infrared imaging: amplitude measurements	44
3.1.1	Introduction	45
3.1.2	Experimental set-up	45
3.1.2.1	Characteristics of the pump and the probe illuminations	45
3.1.2.2	Imaging configuration inside the bulk	48
3.1.3	Results: micro-plasma confined in bulk-Si	49
3.1.3.1	Micro-plasma images	49
3.1.3.2	Estimate of the free-carrier density	49
3.1.3.3	Nonlinear propagation effects	50
3.1.3.4	Optical breakdown criteria and limitations of the interaction	52
3.1.4	Free-carrier recombination and diffusion	53
3.2	Ultra-fast interferometry: phase measurements	57
3.2.1	Extraction of the phase-shift induced by the micro-plasma	58
3.2.2	Experimental details	58
3.2.2.1	Interferometry set-up	58
3.2.2.2	Calibration of the measurements	60
3.2.2.3	Phase and amplitude stability	62
3.2.3	Experimental results	64
3.3	Conclusions	65
4	Ultra-fast energy deposition inside Si	67
4.1	3-D reconstruction of the beam propagation	69
4.1.1	Experimental context	69
4.1.1.1	Experimental set-up for ultra-fast beam imaging	69
4.1.1.2	Calibration in air and procedure to reconstruct the propagation of the beam	71
4.1.1.3	Propagation in air with increasing NAs	73
4.1.2	3-D reconstruction of the ultra-fast laser energy distributions inside Si	74
4.1.2.1	Procedure for the reconstruction	74
4.1.2.2	Results for NA=0.3	75

4.1.2.3	Influence of the NA on the beam propagation	78
4.1.2.4	Strict clamping of fluence delivered inside Si	79
4.1.3	Absorbed energy densities in bulk-Si	80
4.1.3.1	Laser flux absorbed in the region of the focal volume	81
4.1.3.2	Laser flux absorbed in a cone from the surface	83
4.1.3.3	Validity of the beam imaging experiment: integrated energy balance	84
4.2	Numerical model for nonlinear propagation inside Si	86
4.2.1	Description of the model	86
4.2.2	Identification of the factors limiting the fluence delivery to the focus	89
4.2.2.1	Physical mechanisms included in the model	89
4.2.2.2	Identification of the physical processes responsible for the clamping	90
4.2.2.3	Comparison between the experiments and the calculations	91
4.2.3	Comparison to the fluence threshold for surface modification	93
4.2.3.1	Methodology	93
4.2.3.2	Fluence threshold for surface damage of Si	94
4.3	Conclusions	94
5	Experimental solutions to bypass the limitations preventing ultra-fast modification in bulk silicon	97
5.1	Numerical study of new arrangements to improve the energy delivery inside Si	99
5.1.1	Three-photon absorption	99
5.1.2	Temporal optimizations	101
5.1.2.1	Simultaneous spatial and temporal focusing	101
5.1.2.2	Longer pulse duration	102
5.1.3	Spatial optimizations	104
5.1.3.1	Airy-ring beams	104
5.1.3.2	Extreme focusing with Gaussian beams	106
5.1.4	Conclusions on our choices	108
5.2	Laser induced modifications in bulk-Si with long pulse duration	108
5.2.1	Picosecond modification regime	108
5.2.1.1	Experimental set-up	109
5.2.1.2	Preliminary investigations on the picosecond regime	110
5.2.1.3	Conclusions on the picosecond irradiation regime	112
5.2.2	Nanosecond modification regime	113
5.2.2.1	Experimental set-up	113
5.2.2.2	Single-shot damage investigations inside the volume of Si	114
5.2.2.3	Energy balance and influence of the initial free-carrier concentration.	116
5.2.2.4	Conclusions on the nanosecond irradiation regime	118
5.3	Femtosecond laser modifications inside Si by hyper-NA focusing	119

5.3.1	Context	119
5.3.1.1	Existing solutions to exceed NA=1	119
5.3.1.2	Solid-immersion solution to reach NA up to 3.5	120
5.3.2	Experimental details	122
5.3.2.1	Femtosecond laser pulses focused inside Si spheres	122
5.3.2.2	Magnification of the imaging system	123
5.3.3	Demonstration of the first modification induced with a femtosecond pulse inside Si	124
5.3.3.1	Increase of the NA up to Si breakdown	124
5.3.4	Local change of the refractive index	127
5.3.4.1	Interferometry set-up	127
5.3.4.2	Estimation of the refractive index change	128
5.4	Conclusions	130
	Conclusion	133
	List of Figures	136
	Bibliography	145

Synopsis

Le silicium (Si) est un élément incontournable dans plusieurs domaines d'innovations technologiques comme la micro-électronique ou le photovoltaïque. La course à l'intégration de composants en Si et à leur rapidité de fabrication est au coeur des nouveaux défis technologiques. Un outil a considérablement fait évoluer notre façon de concevoir des objets micro/nanométriques : le laser, et plus particulièrement le laser femtoseconde. Dans des matériaux diélectriques comme la silice fondue, des structures guidant la lumière ont été développées et un éventail d'applications très variées s'est ouvert. Transposer ces technologies aux matériaux semi-conducteurs est un domaine de recherche d'autant plus intéressant qu'aucune démonstration technologique de la modification du volume de Si n'a été publiée jusqu'à aujourd'hui dans le régime ultra-court. Ce résumé présente les bases théoriques de notre étude, et décrit trois parties expérimentales accompagnées des résultats obtenus : la mesure pompe-sonde de l'excitation transitoire du matériau, la démonstration de la limitation optique à délivrer de l'énergie dans le Si, et finalement les solutions expérimentales permettant de contourner cette limitation.

Le silicium sous l'effet d'un champ laser intense

Dans un premier temps, nous nous concentrons sur l'étude d'un état transitoire imagé pour la première fois dans le volume du Si en 2014 [1] : l'ionisation du silicium en régime ultra-bref. La focalisation d'une impulsion laser intense dans un matériau transparent engendre une série de processus physiques entraînant l'excitation du matériau. Le silicium est un semi-conducteur possédant une structure cristalline identique à celle du diamant, où chaque atome est entouré de quatre atomes équidistants. Chaque atome possède un cortège électronique, dont leur énergie est décrite par la théorie des bandes. Dans le cas du Si, la bande de valence est remplie d'électrons pouvant être facilement excités vers la bande de conduction, initialement vide. Entre ces deux bandes, la bande interdite est égale à 1,12 eV pour le Si à 300 K. L'effet d'un champ électrique intense appliqué au matériau dépend des caractéristiques de ce champ, et contient une partie linéaire et une partie non-linéaire. Parmi les mécanismes d'excitation dans les solides, nous nous intéressons particulièrement à la photoionisation (ionisation multiphotonique et ionisation par effet tunnel) et l'ionisation collisionnelle (ionisation par impact suivie de l'avalanche électronique). L'ionisation multiphotonique est l'absorption simultanée de plusieurs photons par un électron. L'ionisation par effet tunnel correspond au franchissement par l'électron de la barrière de potentiel du fait de son abaissement par le champ laser appliqué. Enfin, l'ionisation par impact est la génération de nouveaux porteurs

par collisions quand la population d'électrons libres est suffisante et convenablement accélérée.

Le domaine de transparence du silicium commence à la longueur d'onde $\lambda=1,1 \mu\text{m}$ (correspondant à une énergie de photon de 1,03 eV). Afin de favoriser l'ionisation multiphotonique, nous réalisons nos expériences à la longueur d'onde $\lambda=1,3 \mu\text{m}$ (correspondant à une énergie de photon de 0,95 eV). Des études précédentes [2] ont révélé que dans des conditions d'irradiations identiques aux nôtres, l'ionisation multiphotonique prédomine sur l'ionisation tunnel. Aucune preuve expérimentale n'a démontré un rôle majeur de l'avalanche électronique. C'est pour cela que nous considérons dans notre étude que l'ionisation multiphotonique (ici d'ordre 2) est le mécanisme dominant concernant l'excitation du matériau.

L'ionisation non-linéaire du matériau se traduit par une élévation du nombre de porteurs libres que l'on appellera plasma dans la suite du manuscrit. Ce plasma est constitué d'électrons et de trous, avec une mobilité des électrons largement supérieure à celle des trous. Pour cette raison, la contribution des trous est négligée. Une fois l'impulsion laser propagée, le matériau revient progressivement à un état d'équilibre grâce à la recombinaison des porteurs. Tenant compte de l'excitation et de la relaxation du matériau, l'équation donnant l'évolution de la densité de porteurs N_e dans le matériau suit l'équation :

$$\frac{dN_e(t)}{dt} = \frac{\beta_2}{2\hbar\omega} I(t)^2 - \frac{N_e(t)}{\tau_{eff}} \quad (1)$$

où β_2 est le coefficient d'absorption à deux photons (en cm/GW), \hbar est la constante réduite de Planck, ω est la fréquence laser, $I(t)$ est l'intensité et τ_{eff} est le temps caractéristique de recombinaison des porteurs. Tout au long de ce manuscrit, nous développons des outils expérimentaux permettant d'estimer l'évolution de la densité de porteurs N_e du plasma ainsi formé dans Si. Sa valeur critique est calculée avec l'expression suivante : $N_{cr} = n_0 \epsilon_0 m_e \omega^2 / e^2 = 2,3 \times 10^{21} \text{ cm}^{-3}$ à $\lambda=1,3 \mu\text{m}$ dans le Si, est en particulier un critère pour atteindre le claquage optique du matériau. A cette densité critique, le plasma devient fortement absorbant au rayonnement laser, conduisant à l'endommagement du matériau. D'autres critères sont utilisés dans la littérature. Le changement d'état d'un solide peut s'associer au point de fusion du matériau. Ce dernier est atteint si la densité d'énergie déposée est suffisante : elle doit égaler la somme de l'énergie nécessaire pour chauffer le matériau à la température de fusion puis garder cette température constante, et de l'enthalpie de fusion [3], qui correspond à une densité d'énergie absorbée de $\Delta(E_{fus})=5 \text{ kJ}/\text{cm}^3$ [4]. Le dernier critère utilisé dans cette thèse porte sur la fluence (énergie par unité de surface) délivrée au plan focal dans le volume du Si. Contrairement au seuil de claquage dans le volume du Si, les seuils d'endommagement de sa surface sont publiés dans la littérature. Pour des raisons de confinement et de présence moins importante d'impuretés dans le volume, il est généralement admis que $F_{th}^{surface} < F_{th}^{volume}$. Cette fluence seuil est égale à $F_{th}^{surface} = 0,35 \text{ J}/\text{cm}^2$ pour du Si intrinsèque, déterminé avec une impulsion de 60 fs à $1,3 \mu\text{m}$ focalisée avec une ouverture numérique (NA) de 0,3.

Caractérisation de l'état transitoire dans le Si : plasma sous-dense

L'interaction entre un matériau transparent et une impulsion femtoseconde dépend de plusieurs paramètres matériau et également laser. Afin de caractériser de manière complète cette interaction, nous étudions la réponse du matériau pendant et après le dépôt d'énergie laser. Il existe plusieurs méthodes pour obtenir une résolution temporelle de la dynamique de l'excitation et de la relaxation du matériau. Nous avons choisi le montage d'imagerie pompe-sonde dans l'infrarouge.

L'étude de la dynamique de l'interaction laser-Si est réalisée sur la plateforme laser ASUR (Applications Sources Ultra-Rapides). Le système laser est basé sur la technique CPA (Chirped Pulse Amplification) et la technologie Titane :Saphir. Les impulsions délivrées sont centrées à 800 nm, domaine dans lequel le Si est opaque. En combinant ce système femtoseconde à un OPA (Optical Parametric Amplification), la longueur d'onde est convertie dans l'infrarouge. Les caractéristiques du faisceau utilisé dans la majeure partie de cette thèse sont présentées dans la table 1.

Le montage pompe-sonde est présenté sur la figure 1. Le faisceau sortant de l'OPA est séparé en deux pour générer une pompe (90% de l'énergie) et une sonde (10%). La pompe est focalisée à l'aide d'un objectif de microscope à fort NA (0,3 à 0,85) 1 mm sous la surface du cube de Si. La sonde se propage dans la direction transverse et le signal est collecté à l'aide d'un microscope IR et d'une caméra adaptée.

On obtient de ce montage pompe-sonde une photographie de l'interaction à un instant précis (figure 2) : la sonde présente une durée de 60 fs mais traverse 9 mm de silicium. Sa durée augmente du fait de la dispersion de vitesse de groupe dans le Si et atteint 280 fs dans la région de l'interaction. La résolution temporelle de notre expérience est donc d'environ 300 fs. Le délai entre la pompe et la sonde est fixé à 10 ps afin que tous les porteurs libres aient été générés sans avoir eu le temps de recombiner [1].

Cette expérience apporte de nombreuses informations qui nous aident à mieux comprendre notre échec à endommager le silicium. Tout d'abord, lorsque l'énergie de la pompe augmente, il existe un niveau d'excitation au-delà duquel l'absorption de la sonde cesse de croître : le dépôt d'énergie sature. En reportant l'absorption

Paramètre	Signal après OPA
λ	1160 nm to 2600 μm (Signal + Idler)
τ_{pulse}	60 fs
Taux de répétition	100 Hz
Energie maximale	2 mJ
Polarisation	linéaire
Stabilité (%RMS)	< 4

TABLE 1 – Paramètres laser en sortie d'OPA. La longueur d'onde de l'étude est choisie à 1,3 μm .

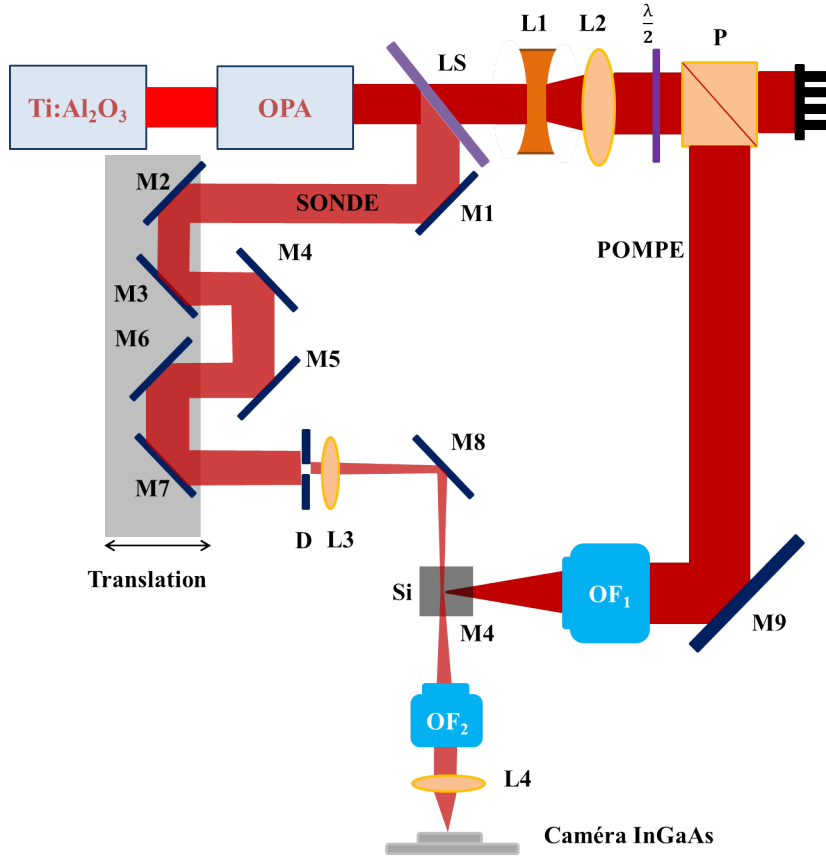


FIGURE 1 – Schéma du montage expérimental pour l'imagerie de plasma : un système laser titane saphir combiné à un OPA délivre des impulsions de 60 fs à $\lambda=1,3 \mu\text{m}$ avec une cadence égale à 100 Hz. Le faisceau polarisé linéairement est séparé en deux à l'aide d'une lame séparatrice (LS) : 10% de l'énergie est dédiée à la sonde, 90% constitue la pompe. La taille du faisceau est augmentée avec un système afocal composé d'une lentille divergente (L1) et une lentille convergente (L2) permettant un grandissement 1,5X. L'énergie de pompe est contrôlée grâce à une lame demi-onde et un polariseur ($\lambda/2 + P$) et focalisée avec un objectif de microscope (OF_1). Le délai entre la pompe et la sonde est ajusté avec une ligne à retard constituée de 4 miroirs or (M1 à M4). L'éclairement de la sonde est mis en forme à l'aide d'un diaphragme (D) et d'une lentille convergente (L3). Le plan focal de la pompe situé à 1 mm sous la surface du cube de Si est imagé à l'aide d'un microscope infrarouge constitué d'un objectif de microscope (OF_2), une lentille de tube (permettant un grandissement 20X ou 50X selon l'objectif) et une caméra infrarouge.

maximale de la sonde, nous calculons la densité maximale d'électrons libres créés en appliquant le modèle de Drude et la loi de Beer-Lambert :

$$T = \exp(-\alpha d_{\text{plasma}}) \quad (2)$$

avec α le coefficient d'absorption fonction de la densité électronique et calculé avec le modèle de Drude, et d_{plasma} le diamètre du plasma dans le volume du silicium. Cette densité électronique ne dépasse pas $3,0 \times 10^{19} \text{ cm}^{-3}$ dans ces expériences, ce qui est largement inférieure à la densité critique. De plus, en étudiant à énergie incidente

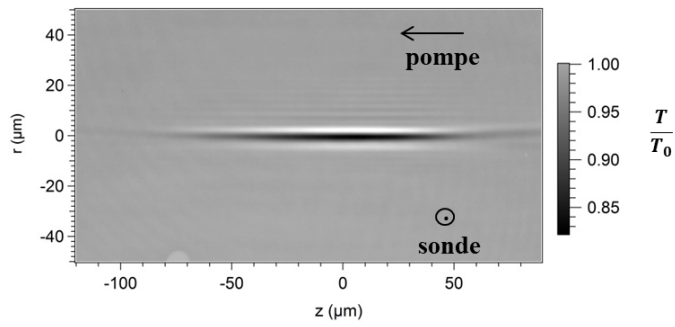


FIGURE 2 – Exemple d’image obtenue avec le montage pompe-sonde : le laser se propage de droite à gauche, un plasma d’électrons-trous est généré dans le volume. Les électrons libres absorbent les photons de la sonde par Bremsstrahlung inverse. Le délai entre la pompe et la sonde est de 10 ps, l’énergie de la pompe est de 10 nJ.

constante l’évolution de cette excitation en fonction du temps, il apparaît que la recombinaison et diffusion des porteurs s’effectue sur une durée caractéristique de 2,5 ns. Ces résultats indiquent qu’à l’échelle de l’impulsion laser (60 fs), l’interaction résulte en un plasma sous-dense n’atteignant pas la densité critique et qui relaxe avec une dynamique nanoseconde [5].

Energie délivrée dans le volume du silicium

Un premier résultat important obtenu de l’expérience pompe-sonde est que le niveau d’excitation du matériau mesuré est insuffisant pour pouvoir atteindre le claquage optique en régime femtoseconde. Afin d’expliquer cette limitation, nous avons choisi de nous concentrer sur la propagation du faisceau. Des études ont montré que dans le Si, des effets nonlinéaires liés au plasma et une forte absorption en région pré focale pouvaient empêcher de déposer efficacement l’énergie au foyer [6, 7, 8]. Une étude expérimentale permettant de reconstruire la propagation du faisceau dans le silicium pourrait nous apprendre quelles sont les pertes d’énergie lors de la propagation de l’impulsion.

Pour cela, un dispositif d’imagerie de faisceau est mis en place dans l’axe de propagation de la pompe. En imageant la face arrière d’un wafer de Si ayant une épaisseur d’1 mm, nous pouvons comparer ces résultats d’imagerie à la distribution du plasma détecté en pompe-sonde. Une calibration de l’expérience, réalisée dans l’air dans la gamme de réponse linéaire de la caméra IR utilisée, nous permet d’obtenir la distribution 3-D de la fluence délivrée dans le matériau.

Le faisceau pompe est focalisé sur la face arrière du wafer. L’image du faisceau directement dans le volume du silicium serait affectée par des effets de propagation nonlinéaires. Imager la face arrière d’un wafer de silicium garantit qu’il n’y ait que de l’air entre le plan imagé et le système d’imagerie. Afin de reconstruire la propagation du faisceau, un z-scan est réalisé par translation de l’objectif de focalisation. Le faisceau est imagé tous les 500 nm. Une coupe est réalisée pour chaque image,

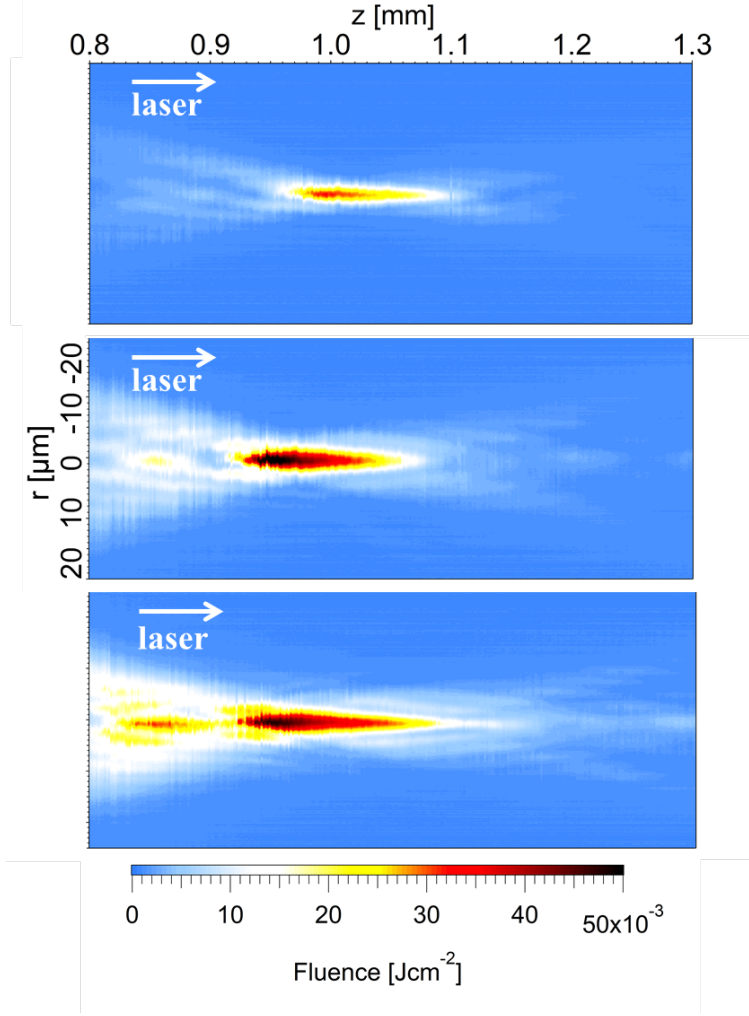


FIGURE 3 – Exemple de la reconstruction du faisceau focalisé avec $NA=0,3$ pour différentes énergies : 15 nJ (haut), 83 nJ (milieu) et 345 nJ (bas). Le point focal de la pompe est à la coordonnée $z=1$ mm.

et l'assemblage de tous les profils permet de reconstruire la distribution de l'énergie selon un plan contenant l'axe de propagation. Un exemple est présenté sur la figure 3. La distribution 3-D de la fluence délivrée dans le matériau est obtenue pour plusieurs énergies de pompe. La gamme d'énergie étudiée s'étend d'une dizaine de nJ (où l'excitation observée grâce au montage pompe-sonde est modérée), jusqu'à plusieurs centaines de nJ (où la saturation est atteinte). Les résultats obtenus avec cette expérience d'imagerie sont en accord avec ceux de l'expérience pompe-sonde : l'absorption de la sonde présente une saturation, et de manière similaire on observe une saturation de la fluence délivrée en fonction de l'énergie de la pompe. Pour $NA=0,3$, la fluence délivrée maximale atteint $F_{del}=0,05$ J/cm², très inférieure à la fluence seuil d'endommagement de la surface du Si ($F_{th}^{surface}=0,35$ J/cm²). Connaissant la fluence absolue, on peut alors résoudre l'équation 1 et ainsi évaluer la densité électronique maximale générée dans le matériau. Pour une énergie pompe de 50 nJ (énergie où l'excitation sature), on obtient une densité électronique maximale générée (sous l'hypothèse d'ionisation à deux photons) $N_e=2,0 \times 10^{19}$ cm⁻³, qui est

en bon accord avec l'estimation de la densité électronique par le modèle de Drude d'après les images pompe-sonde. Les cartographies 3-D de la propagation du faisceau dans le Si montrent une interaction en région pré focale qui s'intensifie avec l'énergie pompe. Cette absorption à deux photons avant le foyer peut être à l'origine de la difficulté rencontrée à alimenter l'interaction dans un volume suffisamment confiné pour induire le claquage optique du matériau.

Dans le but de limiter l'interaction en région pré focale, cette étude est réalisée pour différents NA : 0,3 (voir figure 3), 0,45 et 0,65. Des résultats similaires à NA=0,3 sont observés dans le cas de plus fortes NA : la fluence délivrée au plan focal dans le volume du Si sature sous le seuil d'endommagement de la surface (voir figure 4). Néanmoins, la reconstruction de la propagation du faisceau montre que l'interaction en région pré focale semble avoir été fortement limitée par les fortes ouvertures numériques, ce qui constitue un résultat encourageant. Cette expérience d'imagerie de faisceau est limitée par l'ouverture numérique du système d'imagerie (NA=0.7), mais les résultats montrent qu'augmenter l'ouverture numérique est prometteur.

Pour tous les valeurs de NA testées, nos résultats montrent une limitation systématique de la fluence délivrée dans le Si. Afin d'interpréter ces résultats et identifier les mécanismes impliqués dans cette limitation, un modèle numérique a été élaboré par l'IESL-FORTH (groupe de S. Tzortzakis) dans le cadre d'une collaboration bilatérale [9]. Simuler la propagation d'une impulsion laser focalisée avec de fortes ouvertures numériques (problème fortement non paraxial) avec un traitement vectoriel approprié nécessite des ressources informatiques très importantes et le plus souvent hors de portée. Afin de contourner cette limite, le modèle développé repose sur la transformation de la problématique de notre interaction fortement non paraxiale en

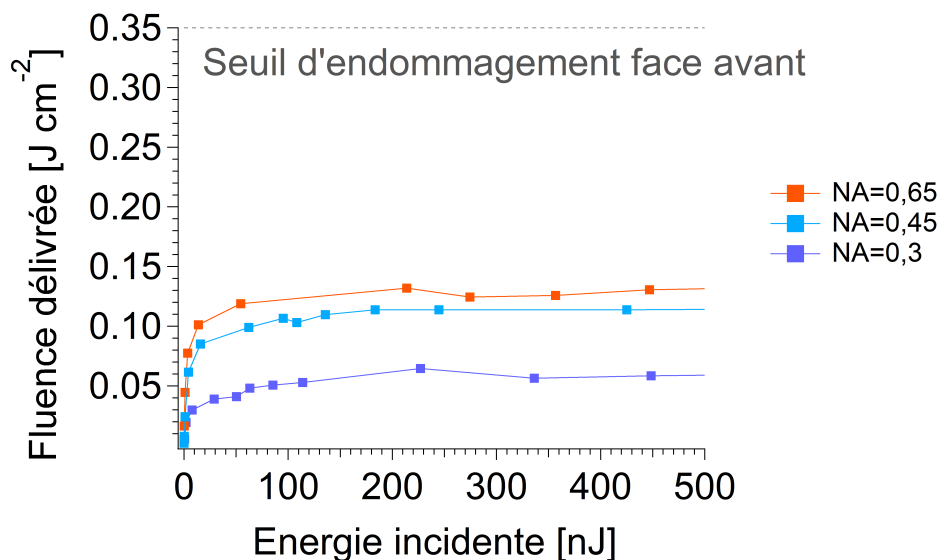


FIGURE 4 – Saturation de la fluence délivrée au plan focal en fonction de l'énergie incidente pour NA=0,3, NA=0,45 et NA=0,65. Le seuil d'endommagement de la surface est indiqué en pointillés.

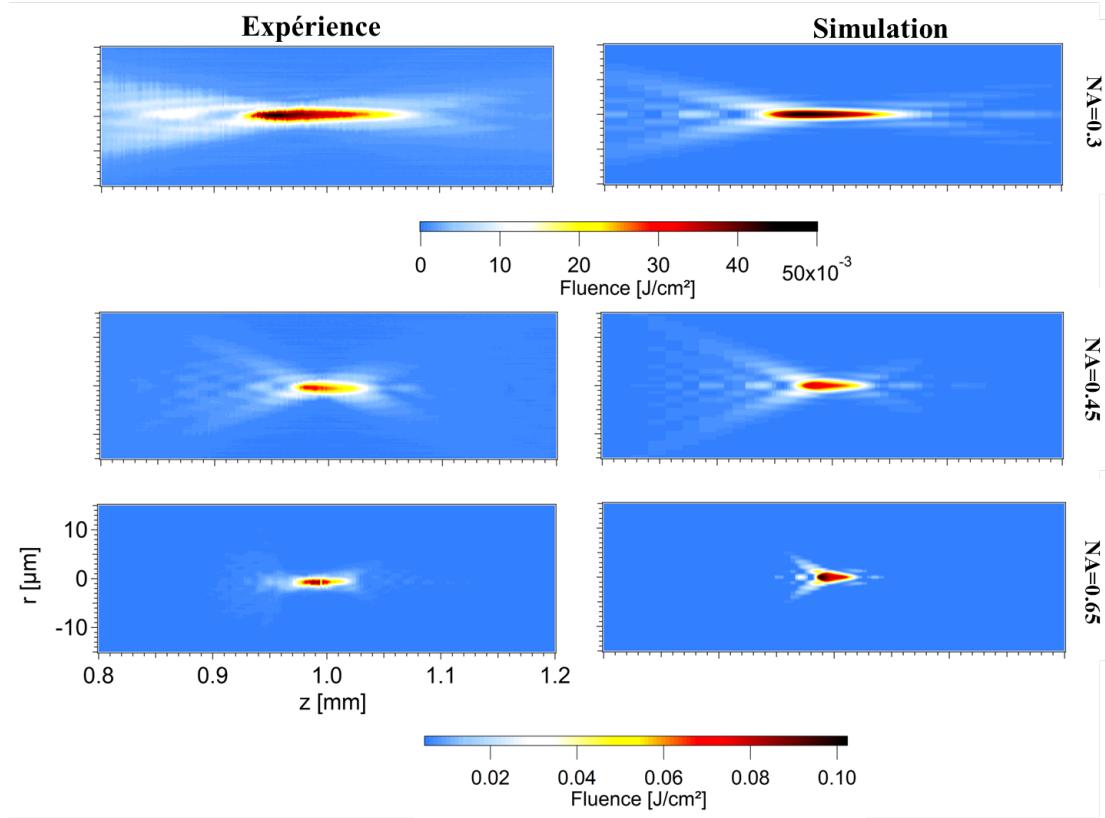


FIGURE 5 – Simulations et mesures expérimentales de la propagation de l’impulsion pour $NA=0,3$ ($E=50$ nJ), $NA=0,45$ ($E=12$ nJ) et $NA=0,65$ ($E=11$ nJ). La colonne de gauche présente les résultats expérimentaux et la colonne de droite les simulations correspondantes.

une interaction dans un milieu d’indice fortement supérieur. Cette transformation permet de simuler nos résultats expérimentaux avec des équations scalaires pour un temps de calcul raisonnable [9]. Les simulations obtenues sont en accord avec nos résultats expérimentaux (voir figure 5). Grâce à ce modèle, nous avons pu identifier certains mécanismes impliqués dans la limitation de l’énergie délivrée dans le Si : l’absorption à deux photons se développe en région pré focale et devient limitante à forte énergie. Cette absorption à deux photons induit de fortes pertes d’énergie dans un volume croissant avec l’énergie incidente. Aux alentours du foyer, où le plasma devient de plus en plus dense, l’absorption à un photon (Bremsstrahlung inverse) et la défocalisation par le plasma sont deux mécanismes physiques qui empêchent l’énergie laser d’être délivrée efficacement au foyer.

Contournement de la limitation du transport de l’énergie

L’accord entre ce modèle et nos résultats expérimentaux nous a permis de mieux comprendre la physique de l’interaction de notre impulsion laser dans le Si. Il nous a également servi d’outil pour contourner la limitation observée. Nous avons pu ainsi simuler numériquement des configurations expérimentales complexes qui per-

mettraient de limiter l'intensité en région pré focale, et améliorer le transport de l'énergie jusqu'au foyer. Plusieurs solutions ont été envisagées et simulées : augmenter l'ordre multiphotonique de l'ionisation, augmenter la durée d'impulsion, mettre en forme spatialement le faisceau (en utilisant un faisceau d'Airy par exemple), ou encore augmenter l'ouverture numérique à $NA=1,5$. Parmi toutes les configurations expérimentales testées numériquement, nous avons retenu deux solutions prometteuses. La première est d'augmenter la durée d'impulsion. L'utilisation d'impulsions plus longues (régime nanoseconde) pour l'endommagement du volume du Si n'est pas nouveau [10, 11, 12]. Cela présente des désavantages en termes de qualité (comme le manque d'homogénéité de la modification) et de contrôle (du fait des effets thermiques accrus en régime nanoseconde). De nouvelles études en régime nanoseconde sont présentées dans ce manuscrit, ainsi que des résultats préliminaires sur le régime picoseconde. Enfin, l'endommagement du Si avec des impulsions femtosecondes reste un défi expérimental limité par les mécanismes physiques non linéaires évoqués ci-dessus. Une deuxième solution pouvant cette fois être appliquée aux impulsions femtosecondes est d'augmenter le NA. L'indice élevé du Si ($n_{Si}=3,5$), induisant une forte réfraction à l'interface air-Si, est une difficulté supplémentaire à confiner le dépôt d'énergie. En supprimant la réfraction à la surface de l'échantillon de silicium, l'ouverture numérique peut être fortement augmentée. Nous présentons une nouvelle configuration expérimentale permettant pour la première fois d'observer la modification permanente du volume de Si avec une impulsion de 20 nJ et 60 fs.

En régime nanoseconde, nous réalisons une étude statistique de l'endommagement volumique du Si en mono-tir. Ensuite, afin de mieux comprendre la physique de l'ionisation en régime d'impulsions longues, nous étudions l'absorption laser dans le volume pour différentes concentrations de porteurs libres présents initialement dans le matériau (en changeant le dopage). Cette étude montre que pour des densités de porteurs libres initiales comprises entre $N_0=10^{11} \text{ cm}^{-3}$ et $N_0=10^{18} \text{ cm}^{-3}$, les valeurs de seuil d'endommagement mono-tir sont similaires, et aucune preuve expérimentale d'avalanche électronique n'est observée. Cette étude indique que l'ionisation à deux photons reste dominante pour initier le dépôt d'énergie jusqu'au seuil d'endommagement. En régime multi-tirs et en faisant varier le nombre de tirs, des effets d'incubation sont observés.

L'endommagement dans le volume du Si en régime picoseconde est encore peu exploré, comparé aux régimes femtoseconde et nanoseconde. Nous avons effectué des expériences au sein du groupe de S. Nolte à l'IAP (*Institute of Applied Physics*, Iéna, Allemagne), qui dispose d'un laser infrarouge délivrant des impulsions à $1.55 \mu\text{m}$ et dont la durée d'impulsion peut varier entre 800 fs et 10 ps. Cette étude offre des résultats préliminaires sur l'endommagement picoseconde, et met en évidence d'ores et déjà des difficultés (répétabilité des mesures, contrôle). Cependant, une première conclusion importante de cette étude est qu'au-delà d'une certaine énergie (quelques microJoules), la probabilité d'endommager le volume du silicium atteint 100 % pour des impulsions de 10 ps.

Dans les diélectriques (silice fondue ou saphir), les impulsions femtosecondes sont

incontestablement les impulsions les plus efficaces pour écrire de nouvelles structures dans le volume des matériaux de manière précise et contrôlée [13]. Dans le cas du Si, nous avons démontré expérimentalement et numériquement les limitations rencontrées empêchant de délivrer suffisamment d'énergie pour induire le claquage optique du matériau. Les simulations nous ont orienté vers la solution naturelle d'augmenter l'ouverture numérique pour la focalisation de l'impulsion pompe. Un aspect limitant fortement les angles de focalisation est l'indice élevé du Si, qui par réfraction à la surface conduit à une interaction quasi paraxiale à l'intérieur du matériau. Afin de contrecarrer cet effet de réfraction et ainsi atteindre des ouvertures numériques jusqu'à $NA=3$, l'échantillon cubique est remplacé par une sphère de Si de 2 mm de diamètre. La focalisation se faisant avec un objectif de microscope, l'onde plane incidente est convertie en onde sphérique par l'objectif de microscope, dont les rayons sont localement orthogonaux à la surface de la sphère. La réfraction à l'interface air-Si est ainsi supprimée, et l'ouverture numérique maximale atteinte avec l'objectif 100X ($NA=0,85$) et de $NA=0,85 \times n_{si} \approx 3$.

L'imagerie en lumière blanche au centre de la sphère (foyer géométrique de l'expérience) révèle dès le premier tir une modification permanente du matériau ($E=20$ nJ) (voir figure 6). L'expérience a été répétée 3 fois et présente des résultats identiques. La modification permanente du matériau peut être caractérisée de plusieurs façons : interférométrie (variation du changement d'indice), TEM ou encore diffraction à rayons X (structure cristalline). Nous avons choisi d'implémenter un montage d'interférométrie de phase afin de mesurer in-situ le changement d'indice au centre de la sphère une fois la modification engendrée. Le montage repose sur la séparation d'un faisceau sonde en deux bras : un bras de référence, et un bras objet (se propageant dans la modification). L'impulsion laser se propageant dans la modification subit un changement de phase, détectable quand elle interfère avec l'impulsion de référence. Après reconstruction de la figure d'interférence, le changement de phase induit par la modification (après 2000 tirs à 20 nJ) correspond à un changement d'indice $\Delta n = \Delta \Phi \lambda / (2\pi d) \approx -0,07$. Cette mesure de changement d'indice indique que ce nouveau résultat se rapproche de ceux obtenus dans les diélectriques, où un changement

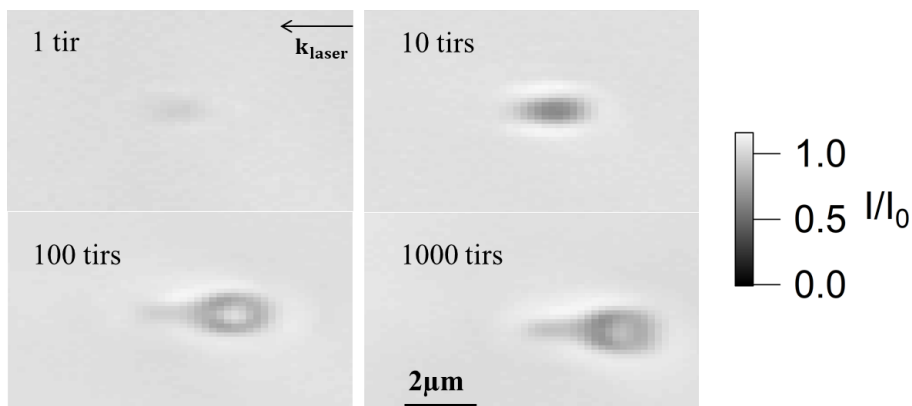


FIGURE 6 – Images du dommage au centre de la sphère de Si éclairée en lumière blanche. $E=20$ nJ, $NA=3$.

de la structure du matériau se produit entraînant des "nanodisruptions" associées à un changement d'indice négatif [14, 15]. Cette analyse reste préliminaire et nécessite d'autres méthodes plus précises et plus robustes pour affiner ces conclusions.

En conclusion, cette première démonstration technologique de modification du volume du Si par une impulsion femtoseconde arrive 20 ans après celle réalisée dans les matériaux diélectriques [16]. Grâce à des techniques de microscopie ultra-rapides et l'étude du dépôt d'énergie dans le matériau, la réponse du silicium à un champ laser intense a été caractérisée. La limitation de l'excitation due à des effets non-linéaires dans un matériau à très fort indice a été contournée et ouvre de nouvelles perspectives de recherche. D'un point de vue industriel, la mise en place d'un procédé d'usinage en volume du silicium nécessite des développements technologiques, notamment avec une demi-sphère jouant le rôle de lentille à immersion solide pour pouvoir travailler dans un wafer. D'un point de vue fondamental, l'ouverture numérique très forte procurée par la sphère est une opportunité d'induire des conditions de pressions les plus extrêmes dans les expériences de micro-explosion dans les solides [17].

Introduction

The invention of the laser has been unquestionably a turning point in scientific progresses concerning numerous scientific domains. At the beginning, the laser has been developed without definite applications, but it rapidly became an essential tool leading to major technological innovations. The laser has been first used for drilling inside diamond realized with a ruby laser in 1965. The progress of the laser technology has allowed from 1980 the development of lasers operating in the femtosecond range ($1 \text{ fs} = 10^{-15} \text{ s}$). The duration of these pulses is less than most of the characteristic times of energy transfers inside a material. Femtosecond lasers provide a temporal resolution convenient to study the dynamics of the excitation of a material under the effect of an intense electric field. The development of these ultra-fast lasers has yielded to major advances in the miniaturization of elements. Due to the ultra-short pulse duration, these lasers provide an interaction with optimally minimized thermal budget inside a reduced volume of matter, that has opened new perspectives to the 3-D laser writing inside materials. In practice, lasers with longer pulse durations (picosecond to nanosecond pulses) have been pioneers to modify the bulk of transparent materials [18]. However, femtosecond lasers have later brought control, precision and a diminution of the size of the modifications.

A research topic always in expansion from the year 2000, is the development of photonics with silicon. This field covers semi-conductor lasers, photonic crystals, light emitting diodes (LEDs), photonic circuit integration, or photodetectors. Some review publications provide a state of the art concerning the research on silicon for photonics [19, 20]. The fabrication of 3-D objects with silicon is done today by piling up 2-D layers. This process is time consuming and expensive, which motivates the development of new solutions. Femtosecond lasers can bring a major innovation in this domain : 3-D laser writing directly in the volume of silicon. However, any attempt to modify the crystalline structure of Si with ultra-fast laser pulses has failed so far [1, 6, 21, 22, 23]. This regime is strongly nonlinear and presents several complex phenomena in competition, limiting the level of excitation inside the material.

This PhD research is devoted to the fundamental study of silicon under the effect of an intense electric field. We aim to image for the first time the electronic cloud generated in the bulk of Si, with spatial and time resolved experiments. To gain knowledge and understanding of energy deposition in bulk Si with femtosecond pulses, we concentrate on the beam propagation study. A better understanding of the interaction which leads to the ionization of the solid will help us to control it in order to reach the optical breakdown of Si, and subsequent control of the laser-

induced modification inside Si.

In the first chapter, we introduce the theoretical aspects needed for our research. The physical mechanisms which are likely to occur during and after the propagation of an intense electric field inside a solid, and especially inside Si are described and discussed.

The second chapter presents the different laser sources used in this thesis. Most of our experimental work has been performed on a platform delivering femtosecond laser pulses which have been carefully characterized. Other laser sources (commercial laser sources) with longer pulse durations have been also used to compare different interaction regimes inside Si.

Chapter 3 constitutes the first experimental observation of a transient state (ionization) in bulk Si induced by the tight focusing of a pump ultra-short pump pulse. With a pump-probe experiment, we perform amplitude and phase measurements to fully retrieve the transient change of the complex refractive index inside Si.

Chapter 4 is dedicated to the reconstruction of the femtosecond laser beam propagation inside Si. This study demonstrates a strong limitation of the delivered energy which prevents the optical breakdown to be reached. In order to identify the physical mechanisms involved in this limitation, a numerical model retrieving our experimental results is presented.

In chapter 5, we use the model to simulate and find new solutions to improve the efficiency of the energy deposition inside bulk-Si. Among all the possibilities numerically tested, we propose and investigate two promising experimental arrangements.

The complete characterization of the laser beam propagation inside Si combined to the dynamic study of the plasma generated along this propagation provides a new study bringing essential information on the impossibility to modify bulk Si with femtosecond laser pulses. By bypassing the limitations of this interaction, the first modification of Si induced by a single 60 fs laser pulse has been observed for low energy (5 nJ). Primary results show a negative change of refractive index which open new perspectives to modify dramatically and locally the phase of semiconductors.

Chapter 1

Bulk silicon irradiated by an intense infrared laser flux: fundamental background

Contents

1.1	Introduction	2
1.2	Excitation processes	5
1.2.1	Photoionization inside a solid	6
1.2.1.1	Keldysh theory and ionization regime in Si	6
1.2.1.2	Multiphoton absorption	7
1.2.1.3	Tunneling ionization	8
1.2.2	Collisional ionization	9
1.2.3	Electron behavior described by the Drude model	10
1.2.4	Doped semiconductors: principle and applications	13
1.3	Relaxation mechanisms	14
1.3.1	Diffusion and recombination	14
1.3.1.1	Carrier diffusion	14
1.3.1.2	Carrier recombination	15
1.3.2	Free-carrier density rate equation	17
1.4	Nonlinear propagation inside Si	18
1.4.1	Nonlinear polarization	18
1.4.2	Kerr effect	18
1.4.2.1	Spatial domain: self-focusing	19
1.4.2.2	Spectral domain: self-phase modulation	20
1.5	Physics of bulk silicon nonlinear ionization: state of the art and remaining challenges	21

1.1 Introduction

Distribution of states and structures of solids are defined by the arrangement between atoms and their relative positions inside the solid. The periodic structure of a solid differentiates a crystal from an amorphous solid. In a crystal, atoms are organized according to a large-scale ordered lattice pattern. Silicon has a diamond-like structure [24], in which every atom is surrounded by four equidistant atoms. Every atom is surrounded by an electronic cortege, where one distinguishes the core electrons from the valence ones. The core electrons are strongly linked to the atom with a binding energy of ~ 100 eV [25], and are not concerned by the optical excitations generated in this thesis. Valence electrons are weakly bound to the ions, and are responsible for several thermal and electrical properties of solids.

The energies reached by the electrons are described by the band theory: this quantum theory provides the description of matter with band structures, by solving the stationary Schrödinger equation. The theory describes the behavior of electrons, whose displacements (energy and momentum) are submitted to the existence of this band structure (allowed states) inside the material. Among the band structures, the last band filled by bound electrons is called the valence band (VB). In this band, the electrons are more easily excited since they exhibit the lowest binding energy. The upper band allowed for electrons is the conduction band (CB). When electrons reach the CB, they are "free", meaning that they are not linked to ions anymore and can move inside the crystal.

The VB and the CB are separated by the forbidden band, in which there is no allowed states for the electrons. The difference between the maximum of the VB and the minimum of the CB corresponds to the energy of the so-called energy bandgap (or "gap") of a material. The gap of Si is $E_g=1.12$ eV at room temperature. Silicon has an indirect bandgap, as illustrated in figure 1.1, meaning that the maximum of the VB is not aligned with the minimum of the CB in \mathbf{k} -space. This indirect bandgap can induce significant consequences on the carrier motion, since all transfers across the bandgap follow the condition of moment \mathbf{k} conservation. In the case of the indirect bandgap of Si, this means that a phonon is implied in the transition of an electron from the VB to the CB. The involvement of a phonon in these transitions has direct consequences on the optical properties of the material. As an example, an indirect transition has a lower probability to happen than a direct transition, since it requires three particles to be involved. Despite the important role these aspects may have and because of the complexity of the nonlinear excitation processes described in section 1.2, we made the choice in this thesis to not account for the indirect bandgap structure of Si. For simplicity, we treat the problem in the same way we would have investigated a direct bandgap material. The band structures depicted on the different figures will be simplified schematics.

Solids can be divided into three parts: conductors, insulators and semiconductors. The distinction between insulators and semiconductors is still under debate, and different criteria differentiate these categories of solids. For example, Kittel dis-

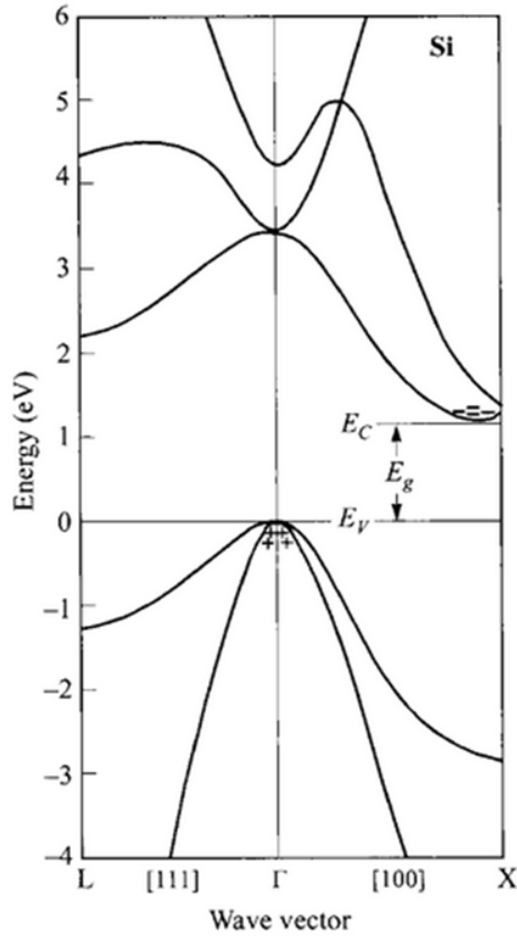


Figure 1.1 – Energy-band structure of Si from [26]. E_g is the energy bandgap. Positive signs indicate holes in the VB, and negative signs indicate electrons in the CB.

tinguishes solids by their electrical resistivity [24], whereas Ashcroft and Mermin use the value of the bandgap to classify conductors, insulators and semiconductors [27]. To resume, we can classify solids as follows:

- Metals: electrons are free in the CB. The CB is partially filled making easy the electron circulation in the material. The resistivity of metals is low ($\sim 10^{-6} \Omega \cdot \text{cm}$ [27]), with density of free electrons at $\sim 10^{22} \text{cm}^{-3}$, several orders of magnitude above the population in the CB of semiconductors.
- Insulators/Dielectrics: in an insulator, the VB is full and the CB is empty, and the energy width of the band-gap is sufficiently large that the electrons cannot move from a band to another, precluding their participation to the conductivity. In practice, insulators present a low probability for an electron in the VB to be promoted to the CB (through the ionization of impurities, the application of an electrical tension or application of ultra-short intense pulses through the processes detailed in section 1.2.). Typical resistivity of insulators ranges from $\sim 10^{14} \Omega \cdot \text{cm}$ to $\sim 10^{22} \Omega \cdot \text{cm}$ [27].
- Semiconductors: solids that are insulators at $T=0$, but with a band width

enough small to observe conductivity due to thermal excitation are called semiconductors [27]. The distinction between semiconductors and insulators is not obvious, but the bandgap is generally under 2 eV. A semiconductor can be conductor or insulator depending on the excitation. Semiconducting properties are generally initiated under thermal agitation, impurities or lattice defects [24], and electrons can move from the VB to the CB. When an electron is released in the CB, an empty space, called a hole, is left in the VB. Hole mobility is weak compared to electron mobility, and is sometimes neglected for excitation or relaxation mechanisms. The thermal and electrical properties of semiconductors strongly depend on its temperature. The resistivity depends on temperature and can vary from 10^{-2} to 10^9 Ω .cm [27].

Experimental results show that the value of the bandgap of most semiconductors decreases with increasing temperature [28]. The variations of bandgap with temperature can be expressed by:

$$E_g(T) = E_g(0) - \frac{aT^2}{T + b} \quad (1.1)$$

where $E_g(0)=1.169$ eV, $a=4.9 \times 10^{-4}$ eV/K and $b=655$ K for silicon [29, 26]. The temperature dependence of the bandgap is illustrated in figure 1.2, where one can retrieve the value of 1.1 eV for Si at room temperature. One can also deduce from the figure that to provide linear absorption (1-photon absorption at $\lambda=1.3$ μ m, corresponding to an energy of photon of 0.95 eV), the temperature needs to rise up to 800 K. This aspect will be discussed in this thesis concentrating on the effect of femtosecond pluses at this wavelength.

The resistivity of Si can vary by changing the level of impurities, called doping. The principle of doping in semi-conductors (particularly silicon) is described in section

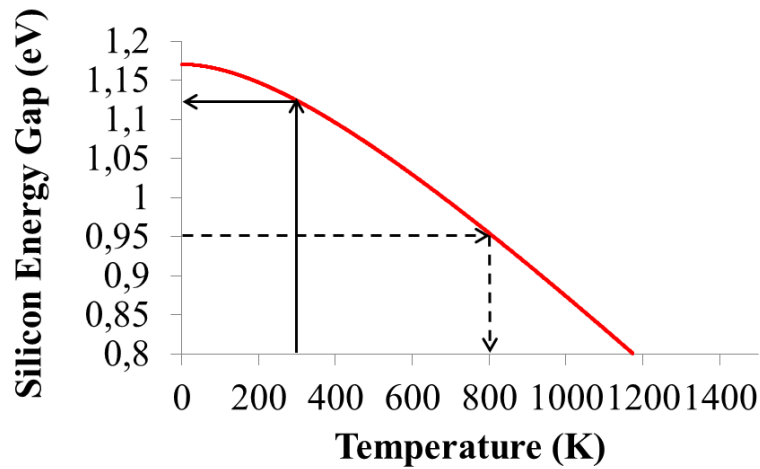


Figure 1.2 – Temperature-dependence of the bandgap energy of Si.

1.2.4. We first consider intrinsic silicon, without impurities added to the semiconductor. The number of electrons, occupying the conduction band levels, is described by the Fermi-Dirac distribution function:

$$F(E) = \frac{1}{1 + e^{[(E-E_F)/kT]}} \quad (1.2)$$

where E_F is the Fermi energy level, k is the Boltzmann constant and T is the temperature. The Fermi level is close to the middle of the bandgap. The concentration of carriers and holes are noted n and p , respectively. In the intrinsic case, $n = p = n_i$, where n_i is the intrinsic carrier density. Figure 1.3a shows the simplified band diagram of Si, b) is the Fermi-Dirac distribution $F(E)$, and c) is the carrier concentrations. In the intrinsic case, the carrier density follows:

$$n_i = N_C e^{-\frac{(E_C - E_F)}{kT}} \quad (1.3)$$

where N_C and E_C are the effective density of states in the CB and the corresponding energy level of the CB, respectively. After calculations, the intrinsic carrier density can be plotted as a function of the temperature. At room temperature, the commonly used value for the intrinsic carrier density is ([26]):

$$n_i = 1.45 \times 10^{10} \text{ cm}^{-3} \quad (1.4)$$

The second case, in opposition of the intrinsic case, is extrinsic Si. When a semiconductor is doped, impurities levels of energy are introduced. More details on doped silicon are provided in section 1.2.4.

1.2 Excitation processes

The interaction between a transparent solid and laser light radiation depends on the electromagnetic field, with linear and nonlinear parts in the excitation process.

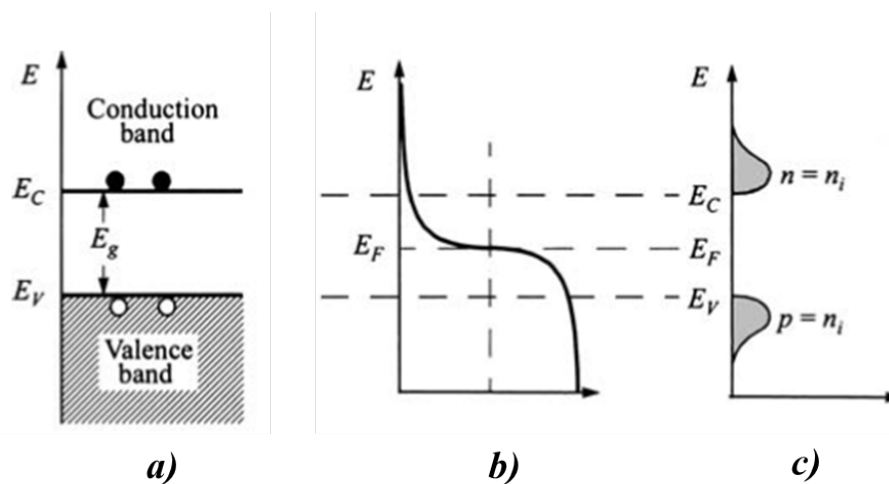


Figure 1.3 – a) Band diagram of Si; b) Fermi-Dirac distribution and c) carrier concentration for intrinsic silicon at thermal equilibrium. From [26].

Transitions of electrons from the VB to the CB can rely on the absorption of one photon. This linear absorption occurs when the energy of one electron, $\hbar\omega$ is superior to the bandgap (where \hbar is the reduced Planck constant, and ω is the angular frequency). For large bandgaps, the photons need to be at high energies, allowed by the use of short wavelengths (for example ultra-violet light delivered by excimer lasers: photon energies > 3 eV). However, there are other excitation processes which can occur for any type of radiation at high intensity, described by the nonlinear ionization processes, detailed in this section.

We distinguish two types of excitation mechanisms resulting in an increase of the electron density inside the solid :

- Photo-ionization processes: multiphoton ionization (MPI) and tunneling ionization (TI).
- Collisional excitation processes: impact ionization and electronic subsequent avalanche (also called avalanche ionization)

Bloembergen first proposed a rate of increase of the free electron density N_e [30]:

$$\frac{\partial N_e}{\partial t} = \eta(E)N_e + \left(\frac{\partial N_e}{\partial t}\right)_{PI} - \left(\frac{\partial N_e}{\partial t}\right)_{loss} \quad (1.5)$$

where the first term on the right side corresponds to avalanche ionization (see section 1.2.2.), with $\eta(E)$ the probability for one electron to be promoted from the VB to the CB under a collisional process. The second term corresponds to the photoionization term, and can be described by TI or MPI, depending on the laser frequency and the applied intensity, as we will see in section 1.2.1. The last term describes the decay of the number of electrons inside the solid resulting from recombination, local diffusion or trapping with exciton formation, described in section 1.3. After the presentation of the different types of laser excitation, we will point out the excitation processes that occur inside Si, according to previous studies published in the literature.

1.2.1 Photoionization inside a solid

In this section, we describe how electrons are promoted from the VB to the CB by photoionization that is the direct excitation of an electron by an intense laser field. The ionization barrier (the bandgap) can be overcome by electrons under two different regimes: multiphoton ionization and tunneling ionization. In the MPI case, electrons acquire enough energy by the simultaneous absorption of several photons, and the ionization barrier is crossed. In the TI case, the high intensity of the laser field allows to lower the potential barrier. These two photoionization processes and their domain of applicability are widely described by the Keldysh formalism.

1.2.1.1 Keldysh theory and ionization regime in Si

The Keldysh theory provides a general expression for the photoionization rate of atoms in a solid under the effect of an intense electromagnetic field [31]. With this formalism, the ionization potential J_i is compared with the ponderomotive energy

U_p , which corresponds to the maximum energy that the electron absorbs from the electric field in one optical cycle. This model introduces the Keldysh parameter, called adiabaticity parameter γ :

$$\gamma = \sqrt{\frac{J_i}{2U_p}} = \omega \frac{\sqrt{mE_g}}{eE} \quad (1.6)$$

where m and E are the reduced mass of the electron and the magnitude of the electric field, respectively. For $\gamma \gg 1$, MPI dominates. On the inverse, for $\gamma \ll 1$ the ionization rate given by this theory corresponds to the TI rate. The transition between the two regimes relies for $0.1 \leq \gamma \leq 10$, where both MPI and TI can occur. From equation 1.6, one can point out that the increase of the wavelength induces a decrease of γ , promoting ionization under tunnel mechanism. Another way to decrease the adiabaticity parameter (and then increase the dominance of TI), is to rise the intensity (shorter pulses for example).

An experimental study of ionization of dielectrics and semiconductors has been carried out to study the transition between MPI and TI by increasing the wavelength [2] in the near infrared (NIR). They measured the wavelength dependence of nonlinear ionization inside the bulk of various bandgap semiconductors and compare the results to the Keldysh theory. In an experimental context similar to this study (intensity around the absorption threshold (10^{10} W/cm²), $\tau_{pulse} < 110$ fs, high NA (0.3)), they found a strong wavelength dependence for Si, demonstrating in this way the predominance of MPI inside the bulk of Si. In this PhD research, we consider MPI as the main photoionization mechanism.

1.2.1.2 Multiphoton absorption

At $\lambda = 1.1 \mu\text{m}$, the energy of one photon is 1.12 eV, which is equal to the bandgap. The transparency domain of Si starts approximately at this wavelength and extends in the IR. To allow "pure" nonlinear ionization, we have chosen to concentrate our work with a wavelength of $\lambda = 1.3 \mu\text{m}$, corresponding to an energy of photon of 0.95 eV.

The number of photons N involved in the excitation of electrons from the VB to the CB is defined by:

$$N = \left\lfloor \frac{E_g}{\hbar\omega} \right\rfloor \quad (1.7)$$

This excitation results in the generation of free-carriers inside Si under two-photon absorption (TPA) process, as described in figure 1.4a) ($N=2$ in this thesis). The probability for one VB electron to absorb N photons is expressed as follows:

$$W(I) = \frac{\beta_N}{N\hbar\omega} I(t)^N \quad (1.8)$$

where β_N is the N -photon absorption coefficient. In this PhD research, intensities used in the experiments are low enough to neglect 3-photon absorption process, and

we will consider 2-photon absorption. The coefficient β_2 (N=2) inside Si was determined at $1.3 \mu\text{m}$ by Bristow and Dinu, [32, 33]. One robust and simple experiment to determine nonlinear coefficient such as the absorption coefficient for MPI or the nonlinear index of a material, is to perform a Z-scan measurement at low energy, using a closed and open aperture. The transmitted signal is collected after the sample, and the time-integrated signal for the open aperture is given by:

$$T_{open}(z) = 1 - \frac{1}{2\sqrt{(2)}} \frac{\beta_2 I_0}{1 + (z/z_0)^2} \quad (1.9)$$

where $z_0 = kw^2$ is the confocal parameter, with $k = 2\pi/\lambda$ the wave vector in the free space and w is the beam waist. Dinu reports a two-photon absorption coefficient of $\beta_2=0.79 \text{ cm/GW}$ at $1.27 \mu\text{m}$. This value will be used for our calculations in this manuscript.

1.2.1.3 Tunneling ionization

An electron is bound to its parent atom by the Coulomb potential. If the electric field is strong, the Coulomb potential can be suppressed and the electron can tunnel through the barrier and becomes free, as represented schematically in figure 1.4b. This nonlinear excitation process dominates for strong laser fields and low laser frequencies. The probability for an electron to be excited by tunnel ionization is expressed with [34]:

$$W(I) \approx \exp\left(\frac{-2E_g^{3/2}\sqrt{m}}{3e\hbar E}\right) \quad (1.10)$$

For long wavelengths (CO₂ lasers for example, where $\lambda=10 \mu\text{m}$ and the energy of the photons is about 0.12 eV), ionization of atoms is generally due to tunneling,

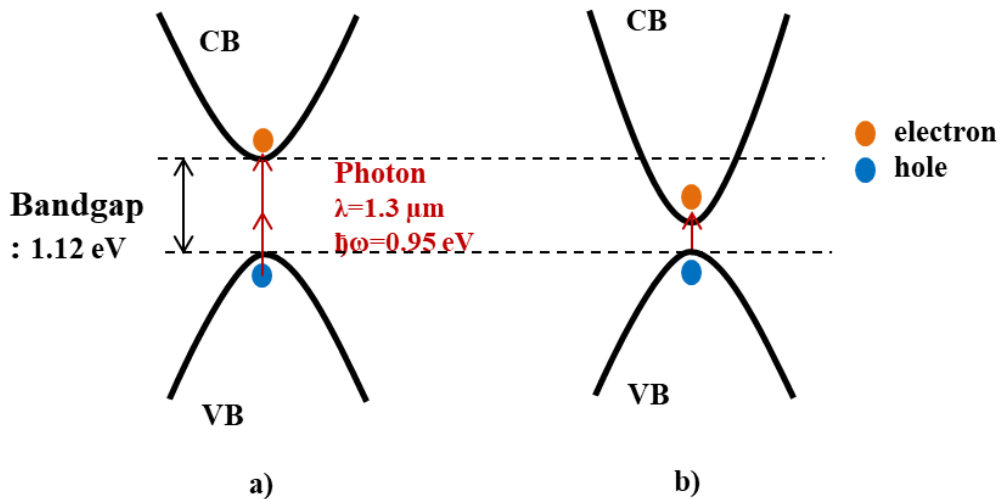


Figure 1.4 – Schematic view of the photoionization processes involved in Si at $1.3 \mu\text{m}$. a) Two-photon ionization, and b) Tunnel ionization. PI processes inside Si are depicted in the case of a direct bandgap.

because the order of the multiphoton absorption is high. In our range of energy of photons, we could not neglect TI in the excitation processes of large bandgap materials. Concerning Si, the gap is relatively low, and as already mentioned, we use the multiphoton ionization probability in the ionization rate for electronic density. Tunneling is interesting to increase the determinism of the interaction [2] but we will show that our irradiation conditions do not allow a significant proportion of TI.

1.2.2 Collisional ionization

Inside a solid, energy deposition, transport or transfer is governed by collisional mechanisms. During the propagation of the laser pulse, an electron situated in the CB can linearly absorb several photons under inverse Bremsstrahlung mechanism. When the electron acquires a kinetic energy up to the impact ionization threshold, it can collide with a valence electron, promoting this electron to the CB. These two electrons can reach an energy level superior to the impact ionization threshold, resulting in the generation of new electrons in the CB. Once this mechanism is initiated, electron multiplication follows, called avalanche. The electron density in the CB grows according to [35]:

$$\frac{dN_e}{dt} = W_{av}(I, N_e) \quad (1.11)$$

where η is the avalanche ionization rate. Stuart *et al* developed a model of avalanche ionization where the ionization rate takes the following general form [36]:

$$W_{av}(I, N_e) = \alpha N_e I \quad (1.12)$$

where α is the coefficient for avalanche ionization, which depends on the wavelength and the pulse duration.

The role of avalanche ionization process in the optical breakdown (generally resulting from the increase of the electron density up to the critical density, explained in section 1.2.3.) has been discussed for a long time in dielectrics [37, 38], and in surface Si interactions [39, 40]. In SiO₂, Du *et al.* compares the coefficients for avalanche ionization rate with experimental and theoretical data. In this publication, the theoretical α is calculated with a formula published by Thornber *et al.* [41] and is an expression for $\alpha(E)$ applicable for all electric field strengths. A good agreement is obtained and highlights the predominance of avalanche in the ionization process, for pulse duration widths from 150 fs to 7 ns.

In silicon, the impossibility to induce permanent modification inside the bulk of Si has motivated new studies of the nonlinear ionization physics. Recent studies revealed that the initial concentration of free-carriers, up to 10^{18} cm^{-3} had no influence on the ionization processes [42]. The experimental results highlight the predominance of multiphoton ionization process, responsible of the increase of the number of free-carriers at the absorption threshold. This study has been conducted with 100 fs pulses at low energy (up to 100 nJ). In 2015, Zavedeev developed a numerical model to investigate Si ionization under the effect of IR femtosecond pulses

[8]. In the equation describing the growth of the free-carrier plasma density, the impact ionization is neglected, justified by the value of the ionization impact coefficient that does not exceed $3.6 \times 10^{10} \text{ s}^{-1}$. They conclude that impact ionization is not significant before 10 ps, which is long compared to a femtosecond pulse duration.

Recent publications show with pump-probe that the free-carrier density induced inside Si with a few tens of nJ with femtosecond pulses is around 10^{19} cm^{-3} [1]. At this level of excitation, no demonstration has been published to show the evidence of impact and avalanche ionization inside Si. In this thesis, considering the strength of the laser field, we assume a value for avalanche ionization $\alpha=10^2 \text{ cm}^2/\text{J}$ in accordance with the literature [43].

1.2.3 Electron behavior described by the Drude model

After the ionization of the material, a population of free-electrons is accelerated under the effect of the intense laser field. This corresponds to single photon absorption through inverse Bremsstrahlung mechanism. To describe the electron behavior under the action of an external electromagnetic field, Drude provides a formalism for metals that we apply to semiconductors. This allows us to define the conductivity σ_e , the electronic susceptibility χ_e and the dielectric function ϵ of partially ionized silicon.

The system composed of free electrons is assimilated to a gas, whose behavior is described by the kinetic theory for gases. The Drude model is based on 4 major hypothesis:

- Between two collisions, electrons are free and interactions with other particles are neglected: the carriers with a positive charge are considered as immobile. The trajectory of electrons is rectilinear and uniform without the effect of an external field.
- Collisions are instantaneous: they brutally modify the speed of the electrons. When there is no external field, the average speed of the electrons is null, there is no current induced in the material.
- Between two collisions, the electron travels during a time called the relaxation time.
- Collisions are the only mechanism responsible for the local thermodynamic equilibrium.

The action of an intense electromagnetic field on a free electron is described with the Lorentz force:

$$\mathbf{F} = -e(\mathbf{E} + v_e \times \mathbf{B}) \quad (1.13)$$

where \mathbf{E} is the electric field, v_e is the speed vector of the electron, and \mathbf{B} is the magnetic component of the electromagnetic field. In this thesis, intensities are in a moderate regime (typically $10^{12} \text{ W/cm}^2 \leq I \leq 10^{15} \text{ W/cm}^2$), and the magnetic

part of the Lorentz force can be safely neglected. Then, the equation of motion of electrons takes the form:

$$m_e \frac{\partial^2 \mathbf{r}}{\partial t^2} = -e\mathbf{E} - \nu_c \frac{\partial \mathbf{r}}{\partial t} \quad (1.14)$$

where \mathbf{r} is the space coordinate, the first term in the right part of the equation is the Lorentz force, and the last term describes losses due to electron-ion collisions.

In the Fourier domain, \mathbf{r} and \mathbf{E} are time-dependent with a factor $e^{-i\omega t}$. The solution of the equation for motion is expressed as:

$$\mathbf{r}(\omega) = \frac{e}{m_e} \frac{\mathbf{E}(\omega)}{\omega^2 + i\omega\nu_c} \quad (1.15)$$

where $\nu_c=1/\tau_c$ is the collision rate and τ_c is the time between two collisions. In this thesis we consider the collision rate constant, that can be questionable for high level of injection. The current is transported by electrons in the CB, so we express the current density $\mathbf{J}=\sigma_e\mathbf{E}=-eN_e v_e$. Then, by identification and with $v_e = \frac{\partial r}{\partial t}$, the conductivity follows:

$$\sigma_e = \frac{e^2 N_e}{m_e(\nu_c - i\omega)} \quad (1.16)$$

Moreover, we can express the polarization P_e resulting from the electric field $P_e=\epsilon_0\chi_e\mathbf{E}$, and $P_e=-eN_e\mathbf{r}(\omega)$. We deduce the expression of the susceptibility χ_e , being the contribution of free-carriers to the dielectric function:

$$\epsilon_{free} = \chi_e(\omega) = -\frac{e^2 N_e}{m_e \epsilon_0} \frac{1}{\omega^2 + i\omega\nu_c} = -\frac{\omega_p^2}{\omega^2 + i\omega\nu_c} \quad (1.17)$$

where $\omega_p=\sqrt{N_e e^2/m_e \epsilon_0}$ is the plasma frequency. Because the density of free-carriers generated by TPA inside Si under our conditions of irradiation is "underdense", as we will see in Chapter 3, we use the reduced mass of electrons m^* for low density and relaxed plasma instead of m_e , corresponding to $m^* = 0.18m_e$ [44]. Considering a constant reduced mass of electrons is a strong hypothesis, but is applicable in this PhD research. Riffe has studied the variation of the reduced optical mass as a function of the temperature, and shows that this mass varies between 0.15 and $0.30 \times m_e$ ((at 300 and at 3000 K, respectively) [45], being consistent with the value published in Ref [44] ($m^* = 0.18m_e$)).

We introduce the critical density N_c , reached when $\omega = \omega_p$. In the free electron gas approximation, the critical density follows:

$$N_c = \frac{\epsilon_0 m_e \omega^2}{e^2} \quad (1.18)$$

Strictly speaking, the critical electron density N_c corresponds to achieving the so-called plasma resonance when the real part of the dielectric function is equal to 0. Its leads to take into account the linear refractive index of Si, resulting in a critical density value superior to the one calculated with equation 1.18. In this manuscript, N_c is calculated in the free electron gas approximation, and is $N_c=6.6 \times 10^{20} \text{cm}^{-3}$,

at $\lambda=1.3 \mu\text{m}$. This approximation has no incidence on the results presented in this thesis.

The critical density has a major role in the optical response of a plasma undergoing ionization processes. Electromagnetic waves cannot propagate into an "overdense region". Indeed, for $N_e/N_c < 1$, the imaginary part of the permittivity vanishes (Eq.1.18) showing that the plasma is transparent at the wavelength λ , whereas for $N_e/N_c > 1$, the laser cannot penetrate inside the plasma, and the incoming energy is absorbed or reflected (partially or totally), depending on the characteristics of the plasma (N_e , T_e the electron temperature, and τ_c the collision time). Finally, the dielectric function can be expressed as a function of the ratio N_e/N_c or ω_p/ω in the free electron gas approximation:

$$\epsilon_{free} = \frac{N_e}{N_c} \left(-\frac{1}{1 + \frac{\nu_c^2}{\omega^2}} + i \frac{1}{\left(1 + \frac{\nu_c^2}{\omega^2}\right)} \frac{\nu_c}{\omega} \right) \quad (1.19)$$

$$\epsilon_{free} = \frac{\omega_p^2}{\omega^2} \left(-\frac{1}{1 + \frac{\nu_c^2}{\omega^2}} + i \frac{1}{\left(1 + \frac{\nu_c^2}{\omega^2}\right)} \frac{\nu_c}{\omega} \right) \quad (1.20)$$

The dielectric function is a complex function, with a real and imaginary part that corresponds to the phase and amplitude of optical probe propagating through the plasma, respectively. These two components of the dielectric function will be studied in detail in Chapter 3 in order to characterize the response of Si to an external electric field. The refractive index of the material is directly related to the permittivity and takes the complex form:

$$\tilde{n} = \sqrt{\epsilon} = n' + in'' \quad (1.21)$$

where n' and n'' are the real and imaginary parts of the refractive index, respectively. Then the absorption coefficient follows:

$$\alpha = \frac{2\omega n''}{c} = \frac{\omega}{c} \frac{Im(\epsilon)}{Re(\sqrt{\epsilon})} \quad (1.22)$$

Then we note that the plasma formation, corresponding to a rise of N_e , leads to a decrease of the refractive index [46]: $n = n_0 - \frac{N_e(r,t)}{2N_c}$, then the medium is assimilated to a diverging lens. It also induces a rise of the linear absorption, described by inverse Bremsstrahlung absorption process. The Bremsstrahlung cross-section is expressed as:

$$\sigma_{IB} = \frac{e^2 k_0 \omega_0 \nu_c}{n_0^2 \omega_0^2 \epsilon_0 m^* (1 + \omega_0^2 / \nu_c^2)} \quad (1.23)$$

where n_0 is the refractive index of the material ($n_{0,Si}=3.5$ at $\lambda=1.3 \mu\text{m}$).

The collision rate in crystalline silicon is high, due to a strong electron-phonon coupling. Only theoretical collisions rates have been published. An averaged value that is used for this thesis is $\nu_c=0.3 \times 10^{15} \text{ s}^{-1}$.

1.2.4 Doped semiconductors: principle and applications

The injection of impurities inside a semi-conductor modifies the number of free-carriers initially present, and allows to control its conductivity. The excitation and recombination processes are governed by the carriers (electrons and holes), and the doping injection can induce electrons or holes in excess, as explained below. In practice, doping a semiconductor consists in substituting Si atoms in the lattice by another element, inducing carriers in excess. Doping can be realized by injecting electrons (N-doped) or holes (P-doped).

The two processes of doping are illustrated in figure 1.5, N-doped and P-doped, and are realized by adding for example Phosphorus atoms and Boron atoms, respectively. In negative doping, an atom with five electrons is added. A fifth electron is then free to move from the VB to the CB, carrying electric charge. In positive doping, an atom with three electrons is added. The missing electron induces a positive hole in the neighborhood of this atom.

In the literature on the study of laser interaction, the use of doped silicon has been strongly motivated by the questionable role of avalanche. So far, the role of avalanche is still under debate for femtosecond interaction inside Si. Leyder et al. has found no signature of avalanche with 100 fs pulses [42]. The advantage of semiconductors is the injection of impurities, or doping, allowing to study the excitation with different initial carrier density.

Semiconductors present a high mobility, and the injection of impurities presents a strong interest for example in microelectronics. For simplicity, this thesis has been conducted with intrinsic or very low doping silicon (to be close to the intrinsic case). For specific studies, we used also N-doped Si with phosphorus atoms, with initial free-carrier density varying between $N_e=10^{13} \text{ cm}^{-3}$ and $N_e=10^{18} \text{ cm}^{-3}$. The doped samples will be described in Chapter 5.

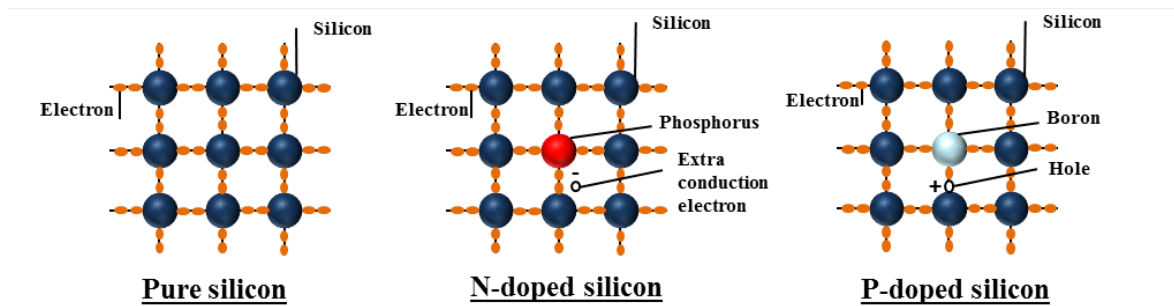


Figure 1.5 – Schematics of the atom arrangement in the case of pure Si, N-doped Si with phosphorus and P-doped Si with Boron.

1.3 Relaxation mechanisms

In the previous section, we studied the mechanisms responsible for the ionization of the material, leading to a rise of the free-carrier density during application of an intense laser pulse. Once the pulse has propagated through the material, the carrier population tends towards an equilibrium state, by carrier diffusion and electron-hole recombination. Relaxation mechanisms are strongly dependent on the mobility of carriers and holes. In this section, we consider the effect of an oscillating electric field (with an average value equal to zero). As a consequence, the conduction current is neglected and we assume that the conductivity results from the diffusion current.

1.3.1 Diffusion and recombination

1.3.1.1 Carrier diffusion

Electrons and holes are subject to the diffusion process, tending to establish a uniform distribution. The carrier movement is described by the Fick's law for diffusion, stating that the carrier flux is proportional to the gradient of concentration. The density of particles diffuses in the opposite direction to the gradient direction:

$$\mathbf{J} = eD\nabla\mathbf{n} \quad (1.24)$$

where D is the constant of diffusion. We note that \mathbf{J} is positive in case of electron diffusion and negative for hole diffusion. The electron mobility and the collision time are parameters important in diffusion. This process can be due to lattice or phonon vibrations, impurities and electron-electron or electron-hole collisions. The Einstein equations show the dependence between the mobility and the constant of diffusion:

$$\frac{\mu}{D} = \frac{e}{kT} \quad (1.25)$$

where μ is the mobility in $\text{cm}^2/\text{V.s}$. In Ref [47], one can find the following expression for electron mobility:

$$\mu = 1350\left(\frac{T_L}{300}\right)^{-2.4} \quad (1.26)$$

where T_L is the lattice temperature. As we will see in this thesis, the rise of the temperature due to the laser pulses in the femtosecond regime is negligible. The estimation of the electron mobility inside Si equal to: $\mu_n=1350 \text{ cm}^2/\text{V.s}$, 1000 times higher than in Al for example, due to the high population of free electrons in the CB. The hole mobility is $\mu_p=500 \text{ cm}^2/\text{V.s}$, justifying that hole participation is neglected in our work. To compare to the dielectric materials, the mobility of electrons in pure sapphire does not exceed $600 \text{ cm}^2/\text{V.s}$ [48].

Introduced for a conservative system, the second Fick's law allows to describe the temporal evolution of the diffusive carrier concentration :

$$\frac{\partial N_e}{\partial t} = \frac{\partial}{\partial x}\left(D\frac{\partial N_e}{\partial x}\right) \quad (1.27)$$

In Chapter 3, we develop an optical technique to study and characterize relaxation inside Si under diffusion and recombination processes. Based on experimental

measurements, we solve the rate equation for relaxation, including diffusion and recombination.

1.3.1.2 Carrier recombination

The free-carrier generation process is balanced by recombination processes. They happen in every solid under excitation, and lead to the decrease of the number of carriers, until equilibrium, called relaxation. After the excitation, the electrons and holes are redistributed in the CB and the VB under carrier-carrier or carrier-phonon processes.

A schematics of the main recombination processes is described in figure 1.6. Recombination is characterized by a recombination time, and the simplest evolution of the carriers under recombination follows:

$$\frac{dN_e}{dt} = -\frac{N_e}{\tau_{eff}} \quad (1.28)$$

where τ_{eff} is the recombination time. In reality, the recombination time depends on the free-carrier density (level of injection). In the rate equation for the carrier evolution, a term for recombination is added (see section 1.3.2.) We detail in the following sections the main recombination processes that must be taken into account for a study on semiconductors. Recombination can be described by :

- Radiative band-to-band recombination: the electron directly goes from the BC to the BV, and the exceeding energy is liberated as a photon.
- Indirect recombination: from the CB, the electron reaches an impurity level located in the forbidden gap, and then is emitted to the BV.

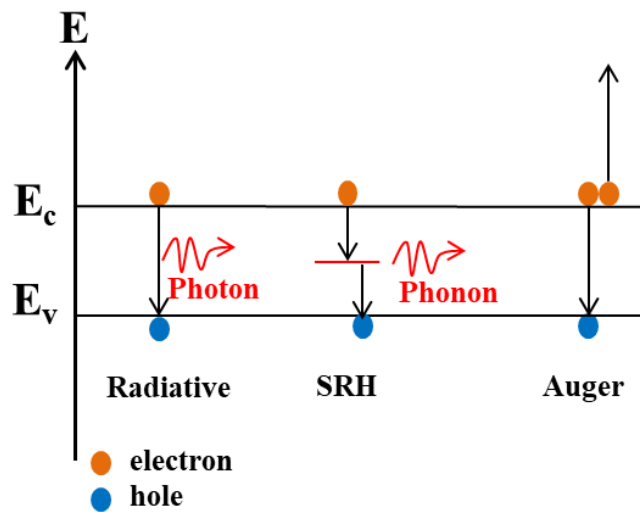


Figure 1.6 – Simplified schematics of the type of recombination processes considered in this study: radiative, Shockley-Read-Hall (SRH) and Auger recombination.

- Non radiative recombination: the exceeding energy is liberated as a phonon (lattice vibrations) or to another free electron (Auger recombination).

In semiconductors with an indirect bandgap, like Si, the radiative band-to-band recombination mechanism is characterized by the emission of a phonon, and presents a low probability [49, 50]. Even for high level of injection in the bulk of Si (10^{20} cm^{-3}), the recombination time for radiative band-to-band is of the order of microseconds. Then, band-to-band recombination is not playing a major role in our experiments.

Carrier lifetime in semiconductors has been measured with various methods, but only at the surface: photoconductive decay, conductivity modulation or surface photovoltage. In heavily doped silicon the order of magnitude of the lifetimes is 10^{-9} s, and these methods presented above are not suitable [49]. For high level of carrier injection, carrier lifetime can be measured by monitoring the decay of the luminescence after the laser pulse excitation [51, 52], photospectral response [53, 54] and Scanning-electron-microscope-electron-beam-induced-current (SEM-EBIC) [55]. Complementing the panel of available techniques, we study carrier recombination inside the bulk with an optical method (see Chapter 3) providing a direct observation of diffusion and recombination [5].

Shockley-Read-Hall recombination

This recombination process has been introduced in 1952 in a publication from Shockley and Read [56]. They first suppose that the crystal contains a certain number of traps, contributing to the recombination process. A neutral trap may capture an electron from the CB, and the energy liberated by this electron is converted into light (photon) or heat (phonon) (see figure 1.6). It can also capture an electron from the VB, and a hole is left in the VB.

Models for this process use equations for the density of electrons in the CB, holes in the VB and trapped electrons. A simplified model for SRH recombination is often used, with several assumptions: there is only one level of energy of trap in the bandgap, and the dynamics of the trapped electrons is quasi stationary, [57]. For a defect with a single energy level in the gap, the SRH recombination rate is available in various publications, such as [58]. The energy that is liberated during the recombination is transferred to the lattice via the emission of a phonon.

Auger recombination

Band-to-band Auger recombination in semiconductors has been introduced by Beattie and Landsberg [59]. Auger process is characterized by the participation of three particles, making this mechanism occurring at high level of carrier densities [60](see figure 1.6). In an indirect bandgap semiconductor, to fill the condition of energy and momentum conservation, this process needs the participation of a phonon. Auger recombination can occur between two electrons and one hole (eeh-process), requiring a small activation energy compared to electron-hole-hole process (ehh-process) [49].

The recombination rate for Auger is expressed as follows:

$$\tau_{Auger} = \frac{1}{C_a N_e^2} \quad (1.29)$$

where C_a is the Auger coefficient (in cm^6s^{-1}). The Auger coefficient has been experimentally and theoretically determined for heavily doped Si between 0.12×10^{-31} and $2.8 \times 10^{-31} \text{ cm}^6\text{s}^{-1}$ [60, 51]. For lower level of injection for carriers ($N_e \approx 10^{17} \text{ cm}^{-3}$), the Auger coefficient is $\approx 9 \times 10^{-31} \text{ cm}^6\text{s}^{-1}$ [61].

There are two existing processes for Auger recombination:

- Direct band-to-band Auger recombination: two electrons in the CB collide and the first electron loses energy while the second gains energy. Recombination is achieved because one electron and one hole both disappear. This is the mechanism for Auger recombination that does not include the assistance of phonon, thus being for direct bandgap semiconductors.
- Trap-assisted Auger recombination: in case of indirect bandgap, the theory for Auger recombination has been completed to fulfill the energy and conservation momentum. For heavily doped silicon ($N_e \approx 10^{18}\text{-}10^{19} \text{ cm}^{-3}$), direct band-to-band Auger recombination is not consistent with the experimental results [53, 62]. Trap-assisted Auger recombination is a second order process, that goes via intermediate state, and is phonon assisted. It has been demonstrated that for indirect bandgap semiconductors, phonon-assisted Auger Recombination was essential [63, 64].

1.3.2 Free-carrier density rate equation

According to the excitation and relaxation mechanisms described in this Chapter, we are able to solve the equation for the evolution of the number of carriers. In the absence of carrier diffusion, the general form is expressed as follows:

$$\frac{dN_e(t)}{dt} = W_{PI}(I) + W_{Coll}(I) - \frac{N_e(t)}{\tau_{eff}} \quad (1.30)$$

where $W_{PI}(I)$ denotes the photoionization contribution, $W_{Coll}(I)$ is the collisional ionization part, and the third is the recombination part including the processes described above. We can provide the evolution for our specific case, working in Si (1.12 eV for bandgap, and 0.95 eV for photon energy at 1.3 μm):

$$\frac{dN_e(t)}{dt} = \frac{\beta_2}{2\hbar\omega} I(t)^2 + \alpha N_e I(t) - \frac{N_e(t)}{\tau_{eff}} \quad (1.31)$$

One difficulty we face when solving this rate equation, is the estimation of the intensity $I(t)$ delivered to the interaction zone, being the intensity participating to the interaction inside the bulk. As we will discuss along the thesis, in the femtosecond regime, the real delivered intensity strongly depends on nonlinear propagation effects before the focus.

1.4 Nonlinear propagation inside Si

1.4.1 Nonlinear polarization

The previous questionable aspect on the intensity delivered inside the material emerges from nonlinear propagation of an ultra-short pulse inside a medium. This nonlinear propagation takes place when the electric field has an intensity so high that it modifies the medium response to this field.

In the case of linear optics, the induced polarization depends linearly upon the electric field, expressed with:

$$\tilde{P}(t) = \chi^{(1)} \tilde{E}(t) \quad (1.32)$$

with $\chi^{(1)}$ is known as the linear susceptibility. In nonlinear optics, the optical response of the material to an external electric field can be a generalization of equation 1.32 as a power series of the field strength $\tilde{E}(t)$ as:

$$\tilde{P}(t) = \chi^{(1)} \tilde{E}(t) + \chi^{(2)} \tilde{E}^2(t) + \chi^{(3)} \tilde{E}^3(t) + \dots = \tilde{P}^{(1)}(t) + \tilde{P}^{(2)}(t) + \tilde{P}^{(3)}(t) \dots \quad (1.33)$$

The quantities $\chi^{(2)}$, $\chi^{(3)}$ are the second and third-order nonlinear optical susceptibilities, respectively. Second order nonlinearities can be the origin of second harmonic generation, sum and difference frequency-generation and optical parametric oscillation [65]. Third-order nonlinearities result for example in Kerr effect (self-focusing), self-phase modulation or third harmonic generation.

Inside symmetric crystals, such as Si, second-order nonlinearities do not occur [65]. We will describe and discuss only the nonlinear processes described by $\chi^{(3)}$.

1.4.2 Kerr effect

The refractive index of a media is expressed as a function of the intensity I of the laser pulse:

$$n = n_0 + n_2 I \quad (1.34)$$

where n_0 is the linear refractive index and n_2 is the nonlinear refractive index of the media, defined by:

$$n_2 = \frac{12\pi^2}{n_0^2 c} \chi^{(3)} \quad (1.35)$$

At $\lambda=1.3 \mu\text{m}$, silicon has a linear index of $n_0 = 3.5$ and a nonlinear index $n_2 = 3.0 \times 10^{-14} \text{ cm}^2/\text{W}$ [33]. The consequence is that from intensities $I \approx 10^{12} \text{ W}/\text{cm}^2$, the nonlinear part of the refractive index of Si is no longer negligible. We distinguish two modulations of the refractive index: the Kerr effect that we just described, induced by the beam itself, and the plasma-induced refractive index change that are directly linked with the permittivity function given in section 1.2.3. The latter is the consequence of the generation of a density of free electrons that modulates the refractive index of the medium.

1.4.2.1 Spatial domain: self-focusing

Self-focusing happens when a laser beam with a nonuniform intensity profile (in our case: approximated Gaussian) propagates into a medium with a nonlinear index. The intensity-modulated index follows the shape of the pulse and generates an index gradient. This index gradient results in focusing the pulse as depicted in figure 1.7. In this figure, a Gaussian pulse propagating with a constant size (collimated) inside a medium with a nonlinear index, undergoes self-focusing: a transverse cross-section shows for a given axial position the modulation of this refractive index. This process can lead to the optical damage of the material if the focal spot of the self-focused beam has a size yielding high intensity. It can also lead to filamentation [66], which is a balance between self-focusing (Kerr effect) and the fact that the plasma resulting from ionization acts like a negative lens, called plasma defocusing (see Drude model in section 1.2.3.).

The process of self-focusing, initiated from a gradient of refractive index Δn , has to be strong enough to overcome diffraction [67], which leads to the criterion on the beam power for self-focusing [68]:

$$P > P_{cr} \equiv \frac{\pi(1.22\lambda)^2}{8n_0n_2} \quad (1.36)$$

The critical power at $\lambda=1.3 \mu\text{m}$ is $P_{cr}=24 \text{ kW}$. This value of power is relatively low compared to the case of fused silica, whose critical power is of the order of MW. One common effect of self-focusing when using Gaussian beams is the spatial shift of the focus towards the prefocal region [69, 70].

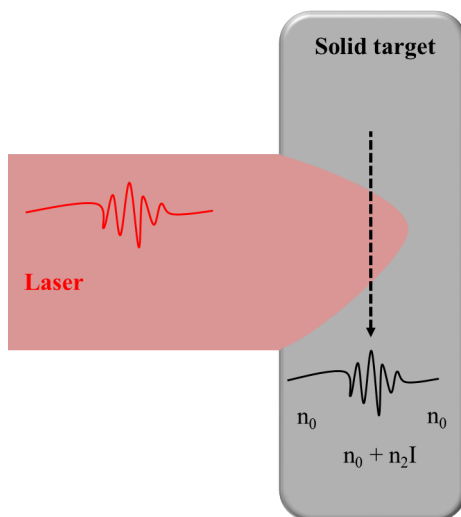


Figure 1.7 – Schematics of self-focusing process. The incoming laser beam with a Gaussian intensity profile propagates through a solid target whose refractive index becomes intensity-dependent. The refractive index increases and acts like a converging lens: the beam is focused.

Kerr effect induces a positive phase shift (being the real part of the dielectric function, as shown in section 1.2.3.), while plasma effects induce a negative phase shift. Inside Si, Kerr effect has been detected with interferometry measurements [6] by irradiating Si with pulses at a wavelength of 1200 nm and a pulse duration of 220 fs. Pulses were focused in the bulk of Si with energies up to 90 μJ , corresponding to a power largely above P_{cr} . Even at high energies, they show that the change of refractive index Δn induced by Kerr effect is almost one order of magnitude lower than the Δn induced by plasma effects. In Chapter 3 and 4 we will discuss the participation to Kerr effect in the ultra-fast beam propagation inside Si.

1.4.2.2 Spectral domain: self-phase modulation

When an intense laser pulse propagates through a medium, the nonlinear refractive index of this medium can induce phase shift. In the spectral domain, this is called self-phase modulation (SPM). The nonlinear phase shift for an ultra-short pulse with a center frequency ω_0 is written as

$$\phi_{NL}(t) = -\frac{\omega_0}{c}n_2I(t)z \quad (1.37)$$

Self-phase modulation is a result of third order non-linearities, and is the analog of self-focusing in the time domain, both based on the Kerr effect. It results in an enlargement and shift of the pulse frequency: the leading edge is shifted to the red and the trailing edge is blue-shifted. Figure 1.8 is a schematics of the propagation of an incoming Gaussian pulse through a medium whose refractive index has a nonlinear positive response. At the output of this medium, if the intensity is high enough, the spectral width of the pulse is broadened. This effect is largely used to broaden the spectrum of femtosecond pulses. One application of SPM is super continuum generation, used for example in an Optical Parametric Amplification (OPA) (this module is described in section 2). Another application of SPM is pulse compression [71], for example by propagation into a fiber.

In chapter 2, we characterize the temporal and spectral parameters of the femtosecond pulse used in most of the experiments presented in this thesis. We investigate if SPM is a nonlinear effect that can occur when focusing a femtosecond laser inside Si.

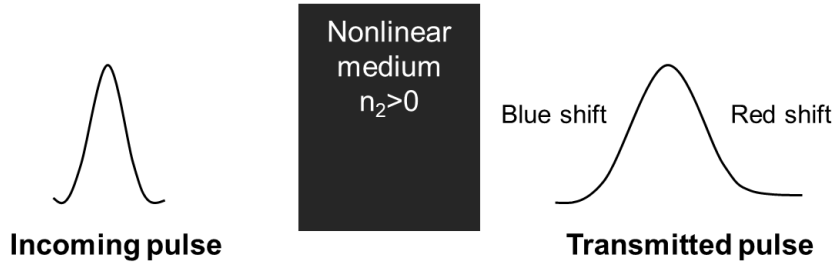


Figure 1.8 – Schematics of self-phase modulation and frequency shift in a medium irradiated with short optical pulse.

1.5 Physics of bulk silicon nonlinear ionization: state of the art and remaining challenges

The modification of silicon in its volume is a relatively recent field of interest, with fundamental and industrial goals. From a fundamental point of view, researches have been led to identify the ionization mechanisms induced by an infrared intense field in the femtosecond regime [6, 42, 2, 7, 72, 8].

Experimental and numerical results have induced new conclusions on this interaction regime and the main conclusions are summarized in the following tables. The experimental investigations presented in this PhD thesis have been performed on Si with lasers delivering femtosecond pulses combined with an OPA, described in Chapter 2. The range of pulse duration widths extends from 90 fs to 250 fs, but the intensity regimes differ from one group to another: the incoming energies of the beam are in the nJ scale in Ref [1, 5, 2, 42, 73], whereas in Ref [6, 7, 72, 8], the energy range is largely superior, up to a few tens of microJoules. Despite a high incoming energy, a clamping of the excitation is observed. One major goal of this thesis is the clear identification of the physical aspects behind this clamping. From an experimental point of view, the main challenge remains to induce for the first time a permanent modification in bulk-Si with a single femtosecond laser pulse.

Other regimes have been studied in order to induce permanent modifications inside Si. Longer pulses (nanosecond) seem to offer new possibilities to locally induce bulk-damage and is a promising field of applications. Ohmura *et al.* were the first to induce local modifications inside crystalline Si with 150 ns infrared pulses [10]. In 2014, Verburg *et al.* used a 3.5 ns infrared laser for wafer dicing [11], and have initiated the development of the writing of new structures [12]. This regime of interaction with infrared nanosecond laser pulses will be investigated in Chapter 5.

λ	τ_{pulse}	Ionization	Relaxation	Nonlinear propagation	Ref
1300 nm	90 fs	Two-photon absorption		Saturation of the excitation below the threshold of permanent modification inside Si (will be described and discussed in this thesis)	[1]
1300 nm	90 fs		Determination of a constant effective carrier lifetime, and a diffusion coefficient (will be described and discussed in this thesis)		[5]
1300 nm	100 fs	Photoionization in Si: domination of MPI and TI. Study of the wavelength dependance on photoionization under Keldysh theory			[2]
1300 nm	100 fs	Role of electronic avalanche: experimental demonstration of the minor role of avalanche during absorption			[42]
1300 nm	110 fs	Two-photon absorption		Saturation of the energy delivery with a Bessel beam below the threshold of permanent modification inside Si	[73]

Table 1.1 – Part 1: State of the art for femtosecond irradiation inside the bulk of crystalline Si. Spaces are left empty when no detail is given in the publication, or when the subject is not treated in the publication.

λ	τ_{pulse}	Ionization	Relaxation	Nonlinear propagation	Ref
1200 nm	250 fs			Strong light delocalization due to Kerr effect, plasma defocusing reflection from the plasma	[6]
1200 nm	250 fs	Two-photon absorption	Relaxation neglected	Numerical evidence of TPA in the prefocal region and plasma defocusing	[7]
1200 nm	250 fs	Two-photon absorption	Relaxation neglected	Generation of a filament at high energies (50 μ J), delocalization of the light by TPA, plasma defocusing and subsurface plasma, inducing the distortion of the wavefront	[72]
1200 to 5250 nm	250 fs	Two-photon absorption	Relaxation neglected	Strict clamping of the density generated. Investigations on 2 to 5 photon ionization efficiency to generate modifications inside c-Si: N_e and the energy delivered to the focus decrease with the wavelength.	[8]

Table 1.2 – Part 2: State of the art for femtosecond irradiation inside the bulk of crystalline Si. Spaces are left empty when no detail is given in the publication, or when the subject is not treated in the publication.

Chapter 2

Description of the intense infrared laser sources used for investigations

Contents

2.1 ASUR platform	26
2.1.1 Titanium:Sapphire laser source	26
2.1.1.1 Generation of the femtosecond pulse	26
2.1.1.2 Time-frequency relationship	28
2.1.1.3 Dispersion of ultra-short pulses	29
2.1.2 Optical Parametric Amplification	31
2.1.2.1 General description	31
2.1.2.2 Description of the high-energy OPA	32
2.2 Characterization of the femtosecond pulses	34
2.2.1 Spatial features of the femtosecond pulse	34
2.2.1.1 Beam profile imaging	34
2.2.1.2 Propagation characteristics	35
2.2.2 Temporal and spectral measurements	36
2.2.2.1 Pulse duration	36
2.2.2.2 Spectrum	38
2.3 Presentation of the picosecond and nanosecond laser sources	39
2.3.1 Picosecond laser source	39
2.3.2 Nanosecond fiber laser	39
2.4 Conclusions	41

In this manuscript, three regimes of interaction are investigated to induce permanent modifications inside Si: femtosecond, picosecond and nanosecond regime. Most part of this manuscript is dedicated to the femtosecond regime, that is why we give a detailed description of the ultra-fast laser facility. The beam has been carefully characterized with spatial, temporal and spectral measurements, essential to understand the propagation of the beam inside the material. For nanosecond and picosecond studies, compact laser sources have been used and are also briefly described in this section.

2.1 ASUR platform

2.1.1 Titanium:Sapphire laser source

2.1.1.1 Generation of the femtosecond pulse

The interaction between ultra-fast laser pulses and crystalline silicon has been investigated on ASUR facility (Applications laser Sources Ultra-Rapides, figure 2.1). This platform is a commercial laser system designed and manufactured by Amplitudes Technologies. It provides 4 beams devoted to different applications, with different characteristics (energy, repetition rate, pulse duration). Two Tera Watt (TW) beams are used to generate a secondary X-ray source from laser-produced plasmas at ultra-high intensity, one beam is devoted to our study on the interaction of infrared pulses inside Si. The last beam is used for damage and ablation experiments. It is also used for laser-dielectric interaction studies at the shortest pulse duration available on ASUR facility (30 fs and 10 fs).

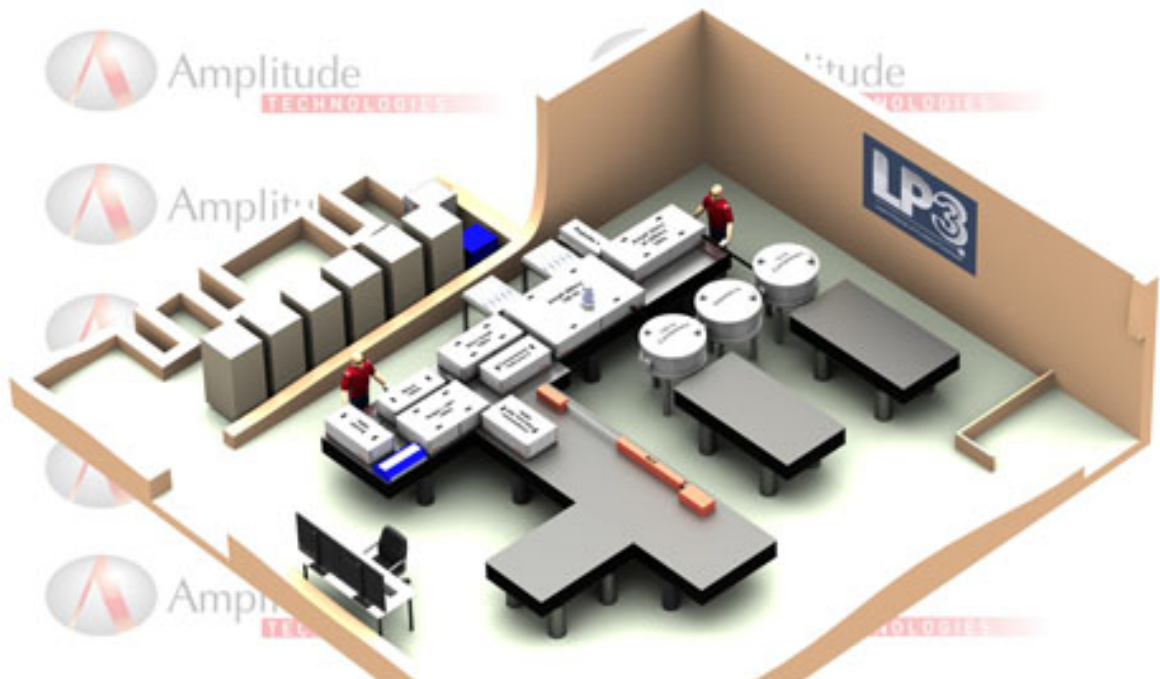


Figure 2.1 – Design of ASUR platform.

The technology of ASUR is based on Chirped Pulse Amplification (CPA) [74, 75] with the amplification in crystals of Titanium:Sapphire ($\text{Ti:Al}_2\text{O}_3$). The main advantage of this lasing medium is the large spectrum of emission, which allows the generation of pulses whose duration can be of few optical cycles, in the Near Infrared (NIR), centered at 800 nm. The common part for the four beams delivered by the facility, called "front-end", is composed of an oscillator, a booster, a stretcher, a regenerative amplifier and a multipass power amplifier. We describe briefly each of these stages. A schematics of the different stages is presented in figure 2.2, with the generation of the pulse with the oscillator, and the other elements (stretcher, amplifier, compressor) corresponding to the beam line with which we are developing our experiment.

- Oscillator: the commercial oscillator from Femtolasers generates ultra-short pulses (around 8 fs) at high repetition rate (80 MHz) with a wide spectrum extending from 650 to 900 nm. The energy of the pulses is about 3 nJ.
- Booster: the oscillator output signal is pre-amplified up to a few microjoules with this multipass amplifier module (14 pass amplifier with a gain of 10^4), pumped by a frequency doubled Nd:YAG laser at 100 Hz (4 mJ at 532 nm). The contrast ratio is improved by a saturable absorber (SA in figure 2.2) that removes Amplified Spontaneous Emission (ASE), and some pre-pulses (oscillator replicas). A Pockels cell is inserted to operate at 100 Hz repetition rate.
- Stretcher: the pulse is stretched from 10 fs to 600 ps. This stage is composed of two spherical concentric mirrors, constituting an Öffner-type stretcher [76].

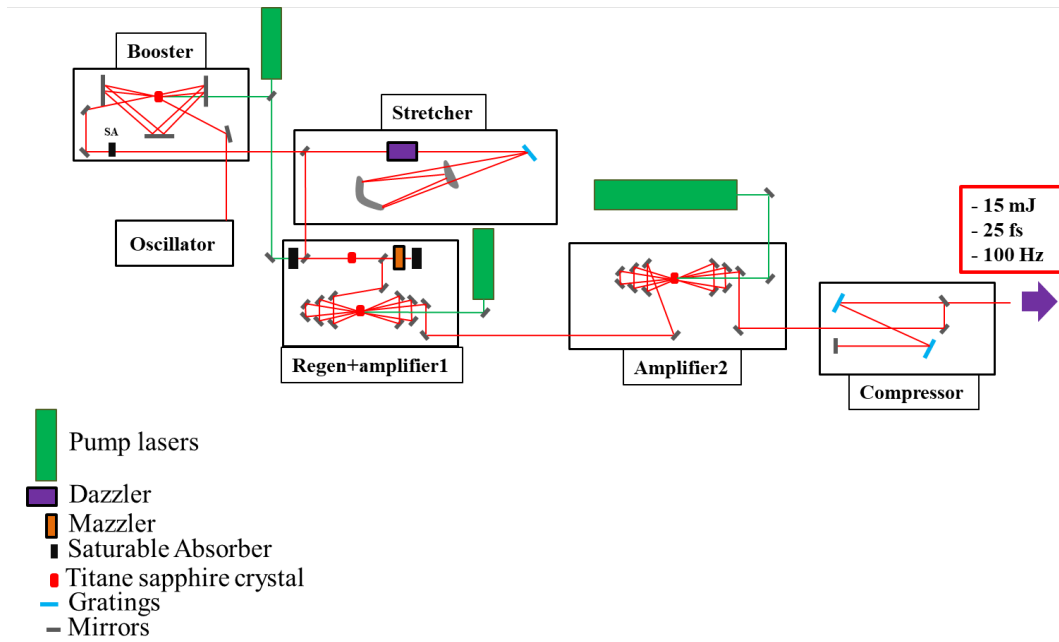


Figure 2.2 – Schematics of the stages of the laser system.

Stretching the pulse is the only solution to amplify the pulse energy above microJoules. A pulse whose pulse duration in the femtosecond range reaches intensities where nonlinear effects can occur during the beam propagation resulting in the deterioration of the beam. The spectral phase of the pulse is precisely controlled with a high resolution acousto-optic programmable dispersive filter (Dazzler from Fastlite).

- First amplifiers: once the pulse has been stretched, it can be amplified in a regenerative cavity combined to a multipass amplifier. Two frequency doubled Nd:YAG lasers (532 nm at 100 Hz) (Quantel) pump the crystals of Ti:Al₂O₃. A Mazzler (from Fastlite) is inserted in the regenerative cavity and allows to get a broad spectrum (770 nm to 840 nm) after amplification. The energy at the output of this stage is around 5 mJ.
- Final amplifier: The last stage of amplification is a 5-pass amplifier (with another Ti:Al₂O₃ crystal), with a pump laser from Innolas delivering pulses centered at 532 nm with a duration of 8 ns, and an energy of 100 mJ at 100 Hz. This last amplifier allows to rise the beam energy up to 23 mJ before compression.

The pulses are compressed down to ≈ 30 fs with a Treacy-type compression [77], using gold coated diffraction gratings. The total efficiency of the compressor is $\approx 65\%$. The relative distance between the gratings are controlled with motorized stages, in order to optimize the pulse duration. The energy available at the output of the compressor is 15 mJ, presenting a pulse to pulse energy stability inferior to 1% RMS (Root Mean Square).

2.1.1.2 Time-frequency relationship

At the output of the compressor, the characteristics of the beam are: $\lambda=800$ nm, $\tau_{pulse}=25$ fs, $f=100$ Hz, with a broad spectrum from 770 nm to 840 nm, as depicted

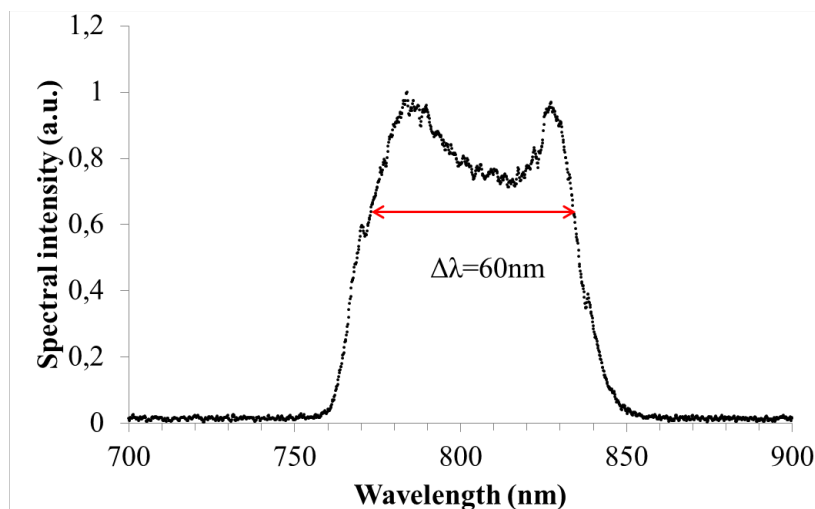


Figure 2.3 – Spectrum of the incoming pulse after compression.

in figure 2.3. One first observation of this spectrum is its non-Gaussian shape. We must note that it does not affect our experiment since after the compressor the pulse propagates through an Optical Parametric Amplification (OPA). Indeed, the OPA, because of the limited bandwidth of its optics, tends to transform the spectrum towards a Gaussian shape centered at a wavelength that can be adjusted. We will describe this module in section 1.1.2.

The spectral and time widths of ultra-fast pulses are related quantities, and can be expressed with the Fourier transform [78]:

$$E(t) = \frac{1}{2\pi} \int_{-\infty}^{+\infty} E(\omega) \exp(-i\omega t) d\omega, \quad E(\omega) = \int_{-\infty}^{+\infty} E(t) \exp(i\omega t) dt \quad (2.1)$$

where $E(\omega)$ and $E(t)$ are the frequency and time evolution of the electric field, respectively. The relationship between the duration and spectral width of the pulse can be expressed as [78]:

$$\Delta\nu\Delta t \geq K \quad (2.2)$$

where $\Delta\nu$ is the frequency bandwidth (at full-width at half-maximum (FWHM)), Δt is the duration width of the pulse at FWHM, and K is a number depending on the shape of the pulse. When the equality is reached in equation 2.2, one deals with a Fourier-transform-limited pulse. This equality is reached with a perfect flat phase. One can estimate the minimum time duration which can be achieved with a given spectrum:

$$\Delta t \geq K \frac{\lambda_0^2}{\Delta\lambda c} \quad (2.3)$$

where $K=0.441$ for a Gaussian pulse. Then, we calculate that with the spectrum presented in figure 2.3, the minimal pulse duration that could be obtained is $\tau_{pulse}=19$ fs. Experimentally, the shortest pulse duration measured was 23 fs (in our best conditions of operation), meaning that our incoming pulse is not a Fourier-transform pulse. However, for simplicity we use the Gaussian shape approximation for this PhD research.

2.1.1.3 Dispersion of ultra-short pulses

When an ultra-short laser pulse propagates through a dispersive medium (whose refractive index varies with the wavelength), the different wavelengths do not propagate at the same speed. Accordingly, the different spectral components of a pulse propagating into a dispersive medium acquire different spectral phases. This phase is therefore no longer flat, resulting in a stretching of the pulse. In a dispersive medium, two characteristic velocities exist: the phase velocity, corresponding to the displacement of the wavefront defined by $v_\phi = \frac{\omega}{k}$, and the group velocity, corresponding to the envelop displacement (the energy), defined by $v_g = \frac{\partial\omega}{\partial k}$. For a non-dispersive medium, such as air, $v_\phi = v_g$, whereas in a dispersive medium (solids), v_ϕ and v_g depend on k , the wave vector.

For a Gaussian Fourier-transform-limited pulse, the pulse duration after the propagation of a distance z in a dispersive medium is expressed as [79]:

$$\tau(z) = \tau_{pulse} \sqrt{1 + \left(\frac{z\beta_2}{\tau_0^2}\right)^2} \quad (2.4)$$

where β_2 is the Group Velocity Dispersion (GVD) expressed in fs^2/mm , and is a property of the material. For example, at $\lambda=1.3 \mu\text{m}$, $\text{GVD}(\text{SiO}_2)=-2.3 \text{ fs}^2/\text{mm}$, and $\text{GVD}(\text{Si})=1462 \text{ fs}^2/\text{mm}$. Positive GVD implies that longer wavelengths propagates faster than shorter wavelengths, and negative GVD is the inverse.

We compare in figure 2.4 the temporal dispersion due to the propagation inside silicon and fused silica. The high value of GVD for Si at $1.3 \mu\text{m}$ implies a strong broadening of the pulse duration. This will be taken into account in Chapter 3 for pump-probe experiments, with formula 2.4. We must emphasize here that the hypothesis of a Fourier-transform-limited pulse is highly questionable for our case. We use formula 2.4 only for estimate the change of the pulse duration due to dispersion. For example, when our IR pulse propagates inside Si between 1 and 10 mm, the pulse duration increases from 64 to 250 fs, whereas the same distance of propagation inside fused silica does not change the pulse duration. Considering this low dispersion in most glasses, we do not consider the temporal dispersion resulting from the propagation of the pulse inside transmission optics.

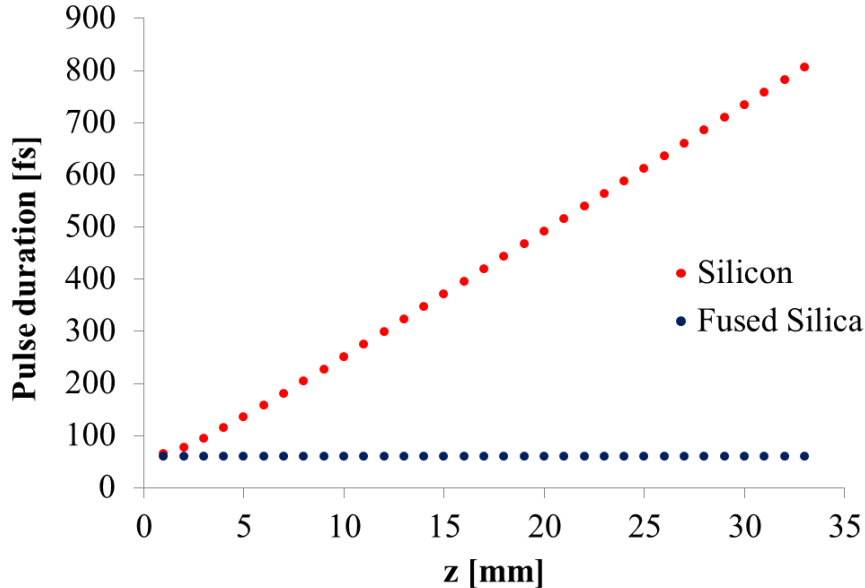


Figure 2.4 – Evolution of the pulse duration when propagating through Si (red) or SiO_2 (blue) at $\lambda=1.3 \mu\text{m}$. The GVD for fused silica is equal to $-2.3 \text{ fs}^2/\text{mm}$, whereas for Si the GVD is $1462 \text{ fs}^2/\text{mm}$.

2.1.2 Optical Parametric Amplification

2.1.2.1 General description

Because silicon is opaque below $1.1 \mu\text{m}$, we need to turn to infrared wavelengths within the transparency spectral domain. Different technological solutions exist to generate ultra-fast infrared pulses, such as Erbium or Ytterbium doped fiber lasers, or Optical Parametric Oscillators (OPO). In this thesis, the technique employed to convert our 800 nm pulse into a 1300 nm pulse is Optical Parametric Amplification (OPA). A commercial module (TOPAS-HE, Light Conversion) is inserted after the compressor, and has been designed to work with high input energies ($\approx 10 \text{ mJ}$), with a stability of the output energy of $\approx 3 - 4\%$ RMS.

Optical parametric amplification results from the second-order susceptibility, and allows the generation of new frequencies. Figure 2.5.a illustrates the principle of amplification by difference frequency generation: the pump (ω_p) is attenuated, the signal is amplified (ω_s), and a third wave is generated: the idler (ω_i). Three photons are involved in this process, which follows the energy conservation (figure 2.5.b) as well as momentum conservation. The first wave mixing experiment has been performed in 1965, by Wang and Racette [80]. We saw in Chapter 1 that nonlinear interaction of light is characterized by the induced nonlinear polarization. This polarization is expressed as a function of the susceptibility, and the second order susceptibility is responsible for sum and difference frequency generation.

This technique provides a large wavelength tunability, realized by focusing a high energy pulse inside a transparent material, such as sapphire, to generate the seed signal. Above 10^{13} W/cm^2 , self-focusing and self-phase modulation take place [78]. A filament with white spectrum is generated. An OPA is based on the use of nonlinear crystals with a large $\chi^{(2)}$. In such crystals, amplification by difference frequency generation can occur:

$$\omega_1 = \omega_3 - \omega_2 \quad (2.5)$$

where ω_1 and ω_2 are the frequencies of the interacting laser fields. Wave 3 is the

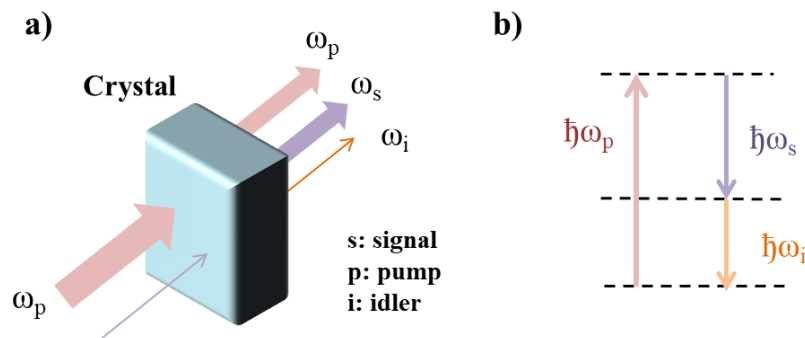


Figure 2.5 – a) Schematics of the amplification by frequency difference and b) Conservation of the energy.

pump, and wave 1 and 2 are called signal and idler, respectively. For an efficient transfer of energy between the waves, the k vectors follow

$$\vec{k}_3 = \vec{k}_1 + \vec{k}_2 \quad (2.6)$$

This frequency conversion system relies on two physical processes: energy and momentum conservation through phase matching, by adjusting the crystal angles. For our studies, the signal is at 1.3 μm and the idler is at 2.0 μm . We only perform experiments with the 1.3 μm signal beam because of the better quality of the signal, in comparison to idler. Our system is a three-stage amplifier of white-light continuum.

2.1.2.2 Description of the high-energy OPA

The OPA used in this thesis is a system made by the company *Light Conversion* under the model named HE-TOPAS. The term HE, meaning High Energy, is related to the input energy of the beam. It is usually hundreds of microjoules, but this OPA is designed for a pump energy of up to 10 mJ. This energy is chosen to be below the generation of white light inside the first amplification crystal. This threshold needs to be verified from time to time since it is dependent on the divergence of the beam, that can change during the alignment procedure of the laser chain. The characteristics of the pump beam entering the OPA are described in Table 2.1.

Figure 2.6 describes the different stages of amplification inside the OPA. A white light continuum is generated to provide a large spectrum. For that, a fraction of the beam is focused in a sapphire plate resulting in self-phase modulation and white light continuum generation (stages 1 and 2 in figure 2.6). This white light continuum and a fraction of the pump beam are then focused in a crystal where the parametric amplification takes place. The amplified signal is then expanded, collimated and transported to the second stage of amplification (stage 3 in figure 2.6). The pump and the seed are overlapped collinearly in a third nonlinear crystal to finally provide a Signal and an Idler (stage 4 in figure 2.6).

The amplification stages can be realized only under the condition of synchronized pump and seed, spatially and temporally inside the nonlinear crystal. For that, several systems of lenses allow to control the size of the beams along the propagation

Parameter	Value before the OPA
λ	800 nm
τ_{pulse}	25 fs
Rep rate	100 Hz
Input energy	10 mJ
Polarization	linear
Stability (%RMS)	<1

Table 2.1 – Laser parameters before optical parametric amplification.

Parameter	Signal after the OPA
λ	1160 nm to 2600 μm (Signal + Idler)
τ_{pulse}	60 fs
Rep rate	100 Hz
Maximum energy	2 mJ
Polarization	linear
Stability (%RMS)	< 4

Table 2.2 – Laser parameters after propagating through the OPA. The measurement of the pulse duration is shown in section 2.2.2.1 with a single-shot autocorrelator.

inside the OPA. A motorized delay line (see figure 2.6) controls the temporal synchronization. The crystals are installed on motorized stages to tune the wavelength by changing the phase-matching angles of the crystals with a computer. The parameters of the beam at the output of the OPA are listed in table 2.2. In this thesis, the wavelength used with the OPA is 1.3 μm . We provide in the following section a characterization of the beam with the wavelength centered at 1.3 μm .

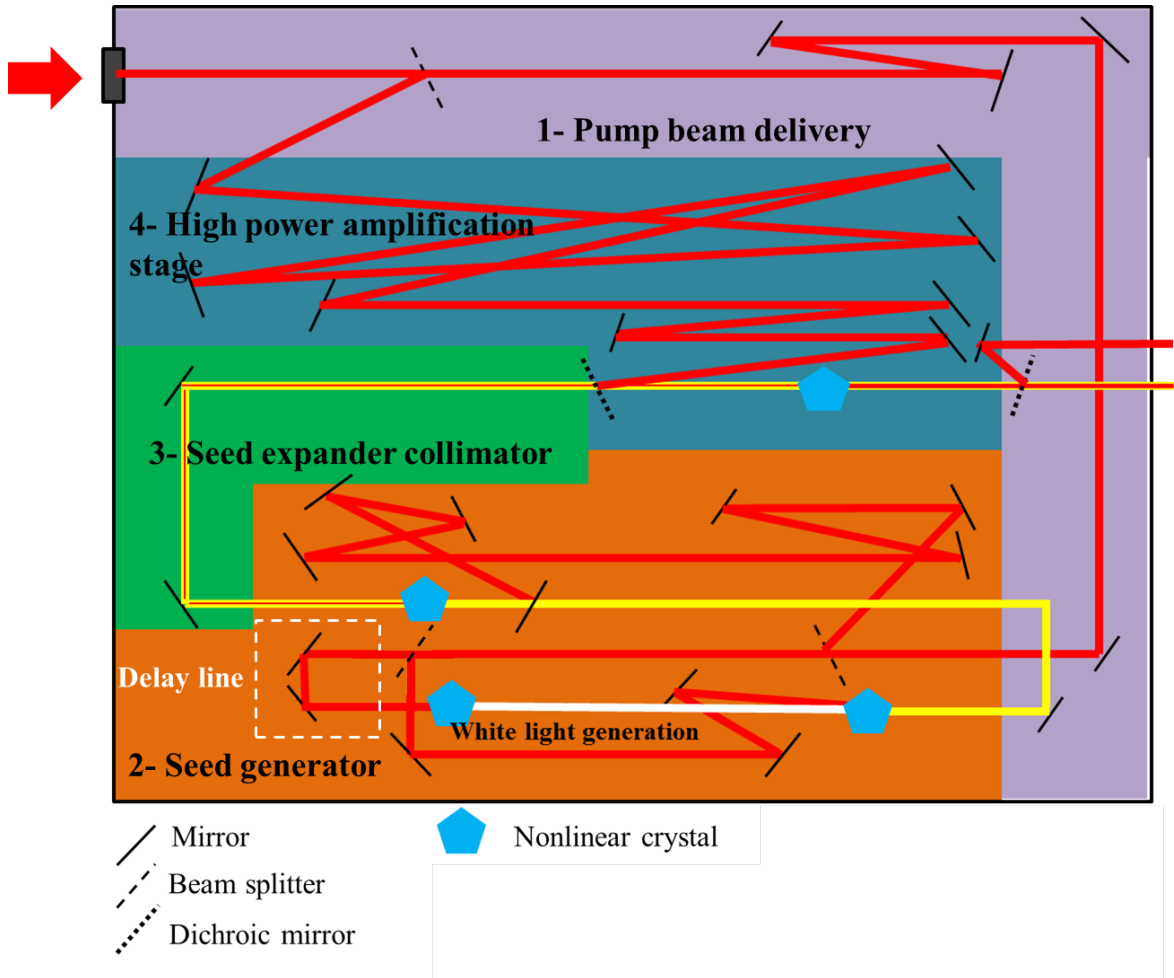


Figure 2.6 – Schematics of the different stages inside an OPA.

2.2 Characterization of the femtosecond pulses

2.2.1 Spatial features of the femtosecond pulse

2.2.1.1 Beam profile imaging

The generation of our laser pulse in the infrared has required numerous stages of amplification and frequency conversion by nonlinear interactions. These stages and associated nonlinear propagation effects can reduce the spatial quality of the beam. We use a CMOS camera (DCC1545M, Thorlabs), with a silicon detector providing a nonlinear response at $1.3 \mu\text{m}$. At this wavelength, because of the two-photon absorption response, the signal of the camera is proportional to the square of the intensity (checked by a calibration not shown here). By taking the square root of the camera signal, we obtain images of the beam (fluence distribution).

The size of the sensor is smaller than the beam diameter, and therefore the size of the beam has to be reduced. The technique employed is depicted in figure 2.7. By simply focusing the beam with a converging lens ($f'=200 \text{ mm}$), the beam is imaged with the CMOS camera placed after the focus. The energy of the beam has to be low in order to avoid nonlinear propagation at the focus which would affect the profile of the beam that we image. This set-up allows us to image the beam with 0.4X magnification, by adjusting the distance between the lens and the camera.

The beam is presented in figure 2.8. The camera provides images with a size of pixels of $5.2 \mu\text{m}$ with a total field size of $6.66 \times 5.32 \text{ mm}$. With the 0.4X magnification, we finally observe the beam at the output of the OPA with a size matching the camera sensor. We also image the beam after 1 meter of propagation to quantify the divergence of the laser.

The size, the ellipticity and the divergence of the beam have been quantified and are reported in table 2.3. The profile in figure 2.8 can be considered as approximately Gaussian. The beam at the output of the OPA is not homogenous, but does not present hot spots. Another important point is the influence of the energy of the pump coming in the OPA. We have seen that the optimal input energy was $\approx 10 \text{ mJ}$,

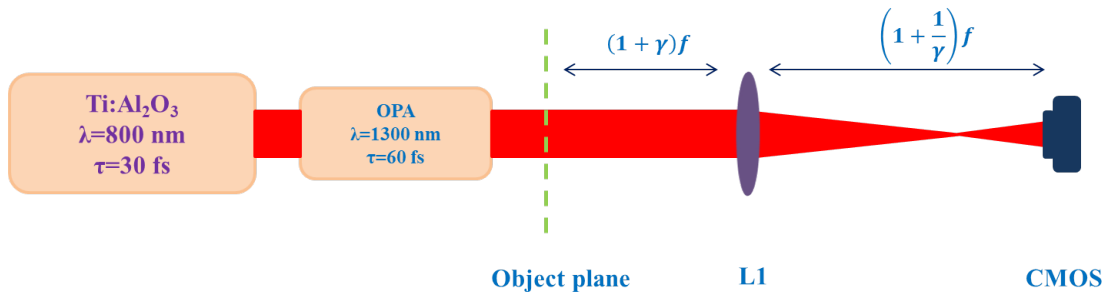


Figure 2.7 – Experimental set-up for the beam imaging: the beam that we image is at the output of the OPA. We use a lens ($f'=200 \text{ mm}$) to image the beam onto a CMOS camera with a magnification of $\gamma=0.4$.

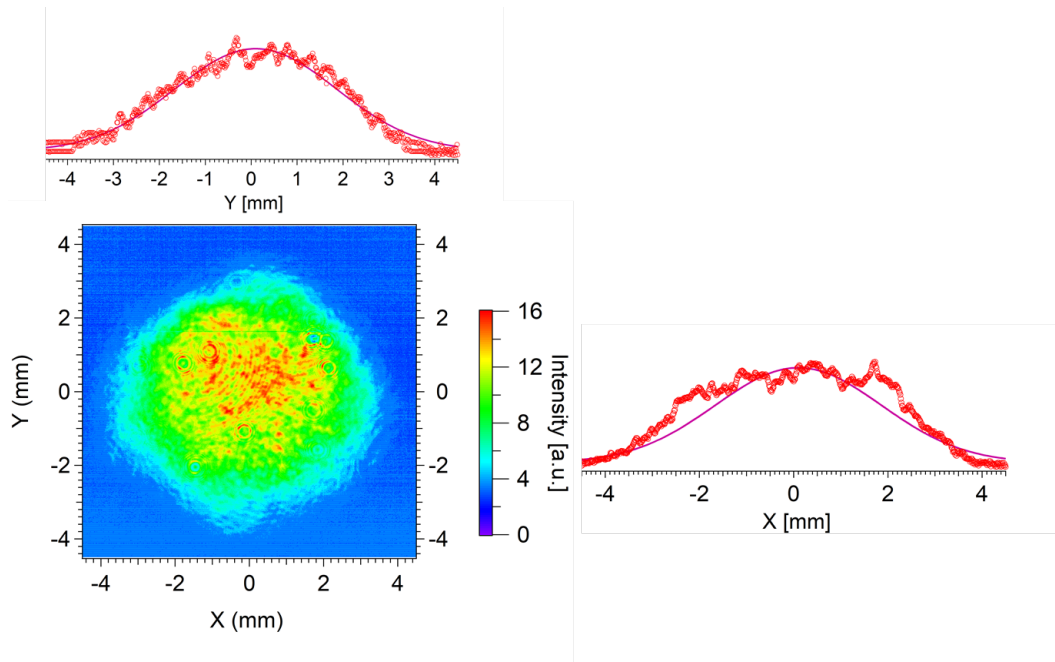


Figure 2.8 – Image of the beam taken with a CMOS camera. The fluence image is proportional to the square root of the camera image, due to nonlinear response of the camera at $1.3 \mu\text{m}$. The graphs are cross-sections (dots) of the beam profile, with a Gaussian fit (curves).

but we have verified that the spatial quality of the beam is not affected by a low input energy. From 8 mJ to 10 mJ, the profile of the beam does not change, but the stability tends to decrease when the input energy decreases. One important aspect for this study will be how the beam characteristics are transformed with focusing optics. A complete study of the propagation of the beam focused in air and inside Si is detailed in Chapter 4.

2.2.1.2 Propagation characteristics

The quality of a Gaussian beam is usually expressed with the M^2 factor, called quality factor. It represents the degree of variation of a laser beam from an ideal gaussian propagation. The quality factor is the link between the beam divergence and the minimal spot size that can be obtained. This factor is helpful for example

	Diameter ($1/e^2$)		Ellipticity	Divergence
OPA output	Horizontal	8.15 mm	0.86	8.6×10^{-2} mrad
	Vertical	7.1 mm		
2 m away	Horizontal	9.5 mm	0.82	
	Vertical	7.9 mm		

Table 2.3 – Spatial parameters of the laser pulse.

to estimate the size of the focus (the waist). The waist is defined as follows:

$$w_0 = \frac{\lambda M^2}{\pi NA} \quad (2.7)$$

where NA is the numerical aperture. The value of M^2 for an ideal gaussian beam (TEM00) is 1. A beam presenting $M^2 > 1$ diverges more rapidly than an ideal gaussian beam. The measurement of the caustic allows to determine the quality factor of the beam by reporting the size of the beam along the propagation axis. By inserting a converging lens with a camera placed on a translation stage around the Rayleigh zone, the evolution of the size of the beam follows:

$$W(z) = w_0 \sqrt{1 + \left(M^2 \frac{z}{z_R}\right)^2} \quad (2.8)$$

with z the distance from the focus and z_R is the Rayleigh zone. The modest quality of the beam at the output of the OPA does not allow us to determine a M^2 near 1. To guarantee a $M^2 < 1.3$, the OPA requires an input beam with $M^2 < 1.2$ (specified by the OPA manufacturer). The quality of our pump beam does not fill this requirement. The beam can hardly be considered as Gaussian away from the focal point. In Chapter 4 we use a camera adapted to the infrared wavelengths to image the focused beam along the propagation axis. This study provides the size and the shape of the beam plane after plane in the context of our experiments.

2.2.2 Temporal and spectral measurements

2.2.2.1 Pulse duration

Measuring the temporal extent of the laser pulse is crucial to precisely estimate the intensity. Photoelectric response times are not adapted to ultra-fast temporal profile measurements. Photodiodes are convenient for sub-nanosecond pulses, and streak cameras are convenient for several hundreds of femtosecond pulses. For a few tens of femtoseconds, we use an optical method based on autocorrelation.

The principle of autocorrelation measurements relies on comparing the beam to itself by generating interferences between two replicas of the beam. The incoming pulse is split into two beams which interfere inside a crystal with a high second-order susceptibility. By collecting the second harmonic after the crystal and varying the delay between the two replicas, the pulse length of the fundamental is reconstructed under assumptions on the temporal pulse shape. In this configuration, the signal collected is the spatial spread of the 2ω signal, thus encoding the temporal delay at different spatial locations. As a result, no delay stage is needed.

Figure 2.9 depicts how the autocorrelation trace is obtained: the beam is separated into two beams with a 50:50 beam splitter. These two beams are supposed to be uniform, with $I_1(t) = I_2(t)$, their respective intensity. By nonlinear propagation effects, the second harmonic is generated at a frequency equal to 2ω , whose signal is

proportional to $I_1(t-\tau)I_2(t+\tau)$, where τ is the delay between the two beams, given by:

$$\tau = \frac{nx_0 \sin(\phi/2)}{c} \quad (2.9)$$

where x_0 is the distance from the center of the crystal, and ϕ is the angle between the two arms inside the crystal. The spatial profile $S(x)$ of the second harmonic generation is proportional to the second order autocorrelation function $G_2(2\tau)$:

$$S(x) \propto \int I_1(t - \tau)I_2(t + \tau)dt = G_2(2\tau) \quad (2.10)$$

We present in figure 2.10 the results of the temporal profile measurement of the femtosecond pulse. The autocorrelator (TiPA , Light Conversion) is positioned at

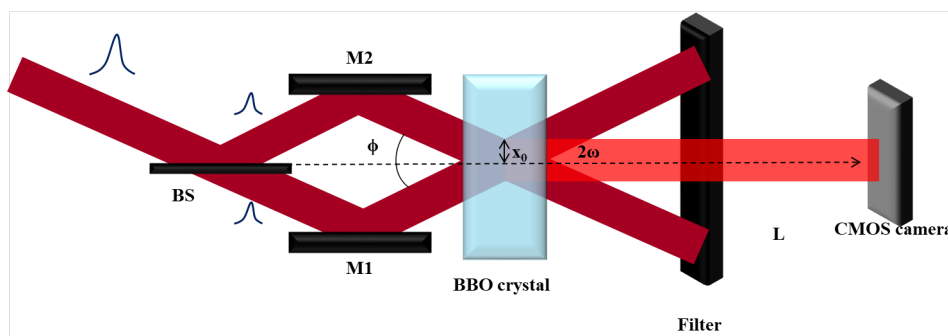


Figure 2.9 – Schematics of measurement of the pulse duration with single-shot autocorrelation: the incoming beam is split with a beam splitter (BS) and propagates through a BBO crystal. The spatial and temporal overlap allows second harmonic (2ω) generation, and the autocorrelation trace is imaged on a CMOS camera. x_0 is the distance from the center of the crystal, and ϕ is the angle between the two arms inside the crystal.

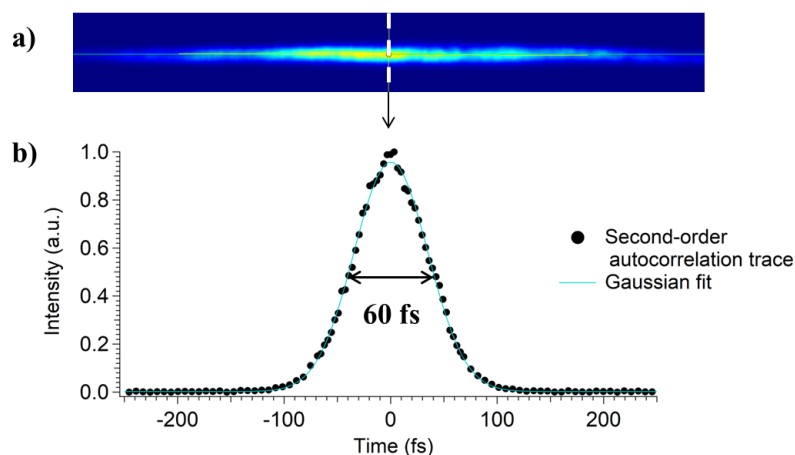


Figure 2.10 – Analysis of the signal $S(x)$: a) image captured by the single-shot autocorrelator and b) autocorrelation trace corresponding to a vertical profile. The profile is fitted by a Gaussian envelope corresponding to a pulse width of ≈ 60 fs (under the Gaussian pulse shape hypothesis).

the output of the OPA, and the measurement is realized in air. The BBO crystal supports a spectral range between 750 and 2000 nm, and the filter is chosen to transmit the second harmonic (650 nm) and block the signal at 1300 nm. The deconvolution of the $S(x)$ function with a Gaussian shape hypothesis is shown in figure 2.10.b. It provides a pulse duration in air of $\tau_{pulse} \approx 60$ fs (FWHM).

2.2.2.2 Spectrum

The spectral characterization of the pulse is realized after the OPA. Since the experiments have been performed only at $\lambda=1.3 \mu\text{m}$, we give only the spectrum for this wavelength. The measurement of the spectrum profile is realized with an infrared spectrometer (NIRQuest 512-2.5, Ocean Optics). The sensitivity of the device relies on the response of an extended InGaAs array sensor from 0.9 to 2.5 μm which is adapted for our IR beam. The fiber collects the light after the OPA and the spectrum is depicted in figure 2.11.a. The spectrum is centered at 1.32 μm with a FWHM width $\Delta \approx 90$ nm, which is two times larger than the width of Fourier-transform pulses at 60 fs (≈ 41 nm). The measurement of the spectrum after the OPA has been realized on different areas of the beam. The goal was to study the homogeneity of the spectral characteristics of the beam. The spectrum appears to be homogeneous and centered at 1.32 μm and we do not observe any significant spatial transverse chirp.

To detect self-phase modulation, due to high intensities inside Si, we perform a spectrum measurement once the beam has propagated inside Si. For that, we collect the signal after a test sample. The range of energies in most studies in this manuscript do not exceed 100 nJ. To have enough sensitivity, we recollect with a lens the transmitted beam and we focus this signal on the fiber (see figure 2.11.b). The spectrum obtained after focusing inside Si is similar to the one obtained in air: we do not observe any spectral shift or broadening that could directly highlight self-phase modulation in the range of energy under investigation in this Thesis.

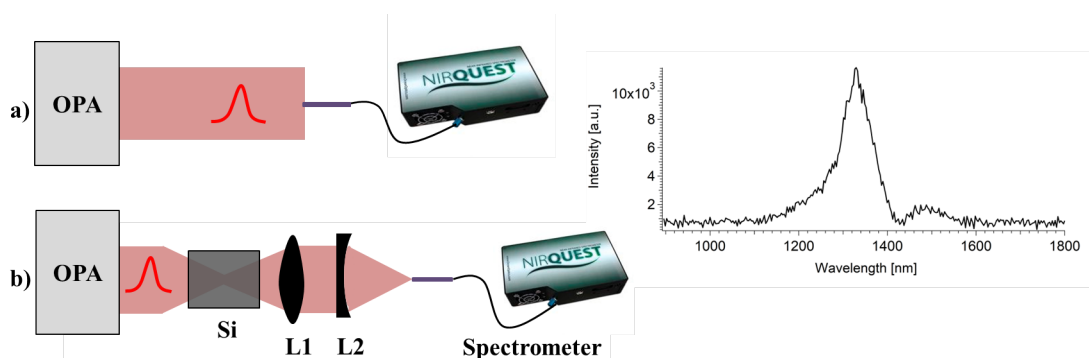


Figure 2.11 – Analysis of the spectrometer signal. The signal is centered at 1325 nm and the width at FWHM is $\Delta\lambda \approx 90$ nm.

2.3 Presentation of the picosecond and nanosecond laser sources

2.3.1 Picosecond laser source

This manuscript is first dedicated to the experimental investigation of bulk-modifications induced inside Si. The major part of the study concentrates on the femtosecond regime, but other regimes can be interesting to investigate. In dielectrics, picosecond laser pulses are also employed to induce localized modifications inside fused silica [81]. A central theme of this thesis is to adapt the classical experiments realized in dielectrics to semiconductors. A collaboration has been established with the *Institute of Applied Physics* in Jena, since an infrared laser with a tunability on the pulse duration in the picosecond regime is available in this laboratory. This complements ideally the LP3 facilities for this work.

This laser source is provided by Rofin (Raydiance), and delivers pulses centered at $\lambda=1.55 \mu\text{m}$, with a pulse duration that can vary from 800 fs to 10 ps. The laser can operate at different repetition rates and different energies, summarized in the following table:

Wavelength	1552 nm
Pulse duration	800 fs to 10 ps
Repetition rate	30 kHz to 400 kHz
Maximum energy	30 to 80 μJ

Table 2.4 – Laser parameters given by the manufacturer of the picosecond laser source used for this study.

The source is equipped with a pulse picker controlled by a program allowing single shot experiments. This source has been used for only one week for preliminary investigations on this regime and all characteristics given here are those specified by the manufacturer (but not effectively measured during the experiments).

2.3.2 Nanosecond fiber laser

A third laser source was used in this thesis: a commercial laser delivering nanosecond pulses. The use of this laser has been motivated by recent studies demonstrating the possibility to induce permanent modifications inside Si [11, 12]. Recent developments with infrared fiber lasers have allowed new studies on semiconductors. Sub-surface modifications have been initiated in Si by focusing nanosecond pulses under the surface of a wafer. To improve the understanding of this regime, we have chosen to study single-shot modifications induced by a nanosecond laser source, presented below.

The laser is a commercial source provided by *MWTechnologies*, operating at 100 Hz. The pulses are centered at $1.55 \mu\text{m}$ with a pulse duration of 3.5 ns (FWHM). The system is based on a Master Oscillator Power Amplifier (MOPA) [82] designed

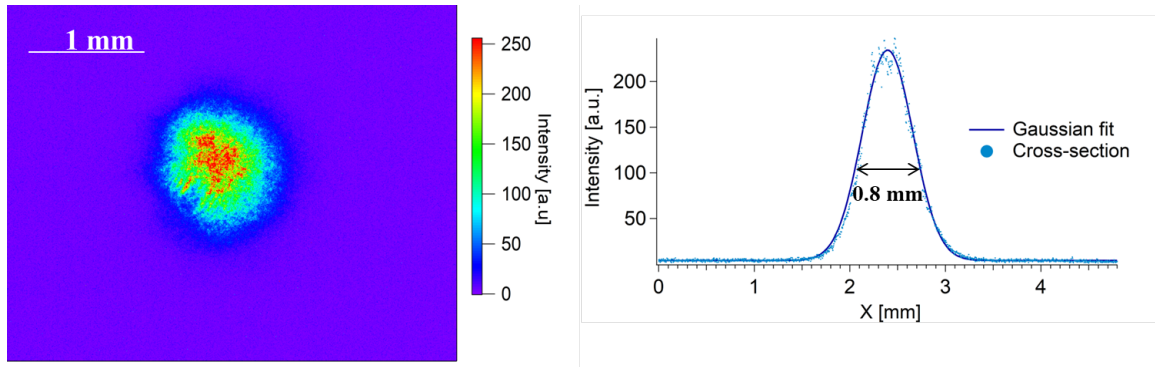


Figure 2.12 – Spatial profile taken with a CCD camera at the output of the fiber.

with an Erbium doped silica fiber as amplification medium. Amplification fibers doped with Erbium allow the amplification of a signal from $1.53 \mu\text{m}$ to $1.56 \mu\text{m}$, corresponding to minimal losses in silica. In this system, the master oscillator generating a low-energy pulse is a semiconductor laser (a Distributed Feedback Laser (DFB)).

This technology provides laser pulses with a high beam quality and can produce pulses with energy of a few tens of microjoules. The spatial profile of the nanosecond beam in figure 2.12 is taken with a NIR camera (Edmunds Optics) with a response within a spectral range from 1500 nm to 1600 nm . The sensor is a silicon array with Phosphorus coating for fluorescence generation at visible wavelength. The size of the pixel is $3.75 \mu\text{m}$. The image is taken at the output of the fiber, equipped with a collimator. The beam is nearly circular with a Gaussian distribution and a diameter at $1/e^2$ of 1.2 mm (see figure 2.12). The temporal profile in figure 2.13.a is measured at the output of the collimator attached to the fiber, with a photodiode (Thorlabs, DET01CFC/M) and analyzed with a fast oscilloscope (Tektronix, DPO7354). The

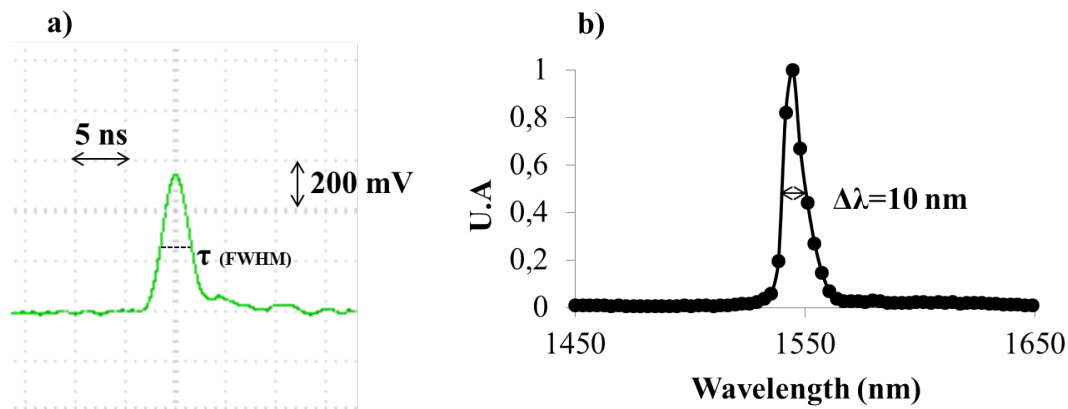


Figure 2.13 – Pulse duration and spectrum measurement taken at the output of the fiber. The pulse duration is measured by collecting the temporal profile with an ultra-fast photodiode and a 33-GHz oscilloscope. The spectrum is measured with the spectrometer presented on section 1.2.2.2.

bandwidth of the photodiode and the oscilloscope are 1.2 and 3.3 GHz, allowing enough temporal resolution for the measurement of our nanosecond pulse.

The signal in figure 2.13.a is a screen shot from the oscilloscope, with an horizontal division of 5 ns. The pulse width is then 3.5 ns (FWHM). Finally, the spectral measurement of the nanosecond pulse is depicted in figure 2.13.b. The signal is measured with the spectrometer presented in section 1.2.2.2. The spectrum is centered at 1.55 μm with a bandwidth of ≈ 10 nm. The pulse coming out of the fiber is not linearly polarized and exhibits a maximal energy of 20 μJ .

2.4 Conclusions

This Chapter was dedicated to the presentation of the different laser sources available in the context of this PhD research. Three different lasers have been described presenting different characteristics, summarized in the following table:

	ASUR facility	Picosecond laser source	Nanosecond laser source
Wavelength	1300 nm	1552 nm	1550 nm
Pulse duration (FWHM)	60 fs (measured)	800 fs - 10 ps (specified)	3.5 ns (measured)
Repetition rate	100 Hz	30 - 400 kHz	0 - 100 Hz
Energy	1.5 mJ	up to 80 μJ	20 μJ

Table 2.5 – Laser sources and their parameters.

Chapter 3 and 4 are dedicated to the experimental investigations on Si realized on ASUR facility. The large level of energy available with this facility allows to perform experiments in which the beam can be split, such as pump-probe or interferometry measurements with an ultra-fast temporal resolution (60 fs in air). The last Chapter explores different pulse duration regimes where modifications inside the bulk of Si can be achieved. The motivation is to compare the difficulty and the level of control that can be achieved inside Si depending on the temporal regime.

Chapter 3

Experimental study of Si response to ultra-fast infrared pulses

Contents

3.1	Ultra-fast infrared imaging: amplitude measurements	44
3.1.1	Introduction	45
3.1.2	Experimental set-up	45
3.1.2.1	Characteristics of the pump and the probe illuminations	45
3.1.2.2	Imaging configuration inside the bulk	48
3.1.3	Results: micro-plasma confined in bulk-Si	49
3.1.3.1	Micro-plasma images	49
3.1.3.2	Estimate of the free-carrier density	49
3.1.3.3	Nonlinear propagation effects	50
3.1.3.4	Optical breakdown criteria and limitations of the interaction	52
3.1.4	Free-carrier recombination and diffusion	53
3.2	Ultra-fast interferometry: phase measurements	57
3.2.1	Extraction of the phase-shift induced by the micro-plasma	58
3.2.2	Experimental details	58
3.2.2.1	Interferometry set-up	58
3.2.2.2	Calibration of the measurements	60
3.2.2.3	Phase and amplitude stability	62
3.2.3	Experimental results	64
3.3	Conclusions	65

Inducing femtosecond laser modifications inside transparent materials has been investigated for decades. Ultra-fast lasers are today the basis for high quality and precision 3-D micro-machining [83, 84], nano-processing of biological cells [85] or surgery applications [86, 87]. A goal of this study is to adapt what is performed inside dielectrics to narrow-gap solids irradiated with an infrared wavelength. As we will see, focusing ultra-fast infrared light tightly inside the material can induce strong energy concentration enough to turn the transparent solid into an absorbing one, but permanent modification is hardly achieved.

Previous attempts to achieve laser induced breakdown in the bulk of Si with femtosecond infrared pulses have failed [6, 21, 22, 23]. However recent investigations have shown that the laser flux can be almost totally absorbed inside Si by nonlinear excitation processes [2] (mainly due to MPI, which is described in Chapter 1). So far, a small number of publications reports on the response of bulk-Si in this regime [6], highlighting a strong delocalization of the IR light. The electronic density (induced by nonlinear ionization) in [6] is estimated with an interferometry set-up ($N_e=1.5 \times 10^{20} \text{ cm}^{-3}$ at 90 μJ energy). In this work, they irradiate Si with high energy femtosecond pulses standing in a strongly nonlinear regime, where it can be complicated to separate the effects of the physical mechanisms involved in the interaction. This PhD research focuses on a lower range of energy for the incoming pulse: up to 100 nJ. This range of energy will be detailed and justified in this Chapter.

Recent studies have shown that above a certain amount of energy, nonlinear effects induce losses leading to an excitation limitation [1]. In this section we present an optical method to image the generation of free-carriers induced by the laser, in the energy range of 1-100 nJ. We detect electrons generated by nonlinear ionization, and illuminated by a probe pulse. Time-resolved pump-probe experiments allow us to study the dynamics of the plasma, and to bring crucial information such as the electronic density, physical constants of diffusion, and characteristic times for recombination and collision.

3.1 Ultra-fast infrared imaging: amplitude measurements

In wide bandgap dielectrics, the response of the material to ultra-fast intense laser pulses is known to be complex, including electronic excitation, energy transfer to the lattice, recombination...(see Chapter 1). In this thesis, we transpose the experiments usually achieved to study dielectrics in the infrared domain so that bulk silicon can be investigated. To study the carrier excitation induced by a femtosecond pulse, three methods are generally used : ultra-fast imaging [88], interferometry measurements [89], and time-resolved absorption [90]. This Chapter is dedicated to ultra-fast imaging to study the changes of the imaginary part of the refractive index \tilde{n} , and then an interferometry set-up is used to study the real part of \tilde{n} . Combining these two measurements provides a complete characterization of the complex dielectric function through the Drude model, as explained in Chapter 1.

3.1.1 Introduction

Femtosecond lasers have allowed significant progresses in understanding and identifying the ionization processes, responsible for the generation of electron-hole plasmas, followed by the relaxation of the material or its permanent modification. Understanding the phenomena involved in these processes can improve our control of 3-D micro-fabrication, or in our case it helps to explain why we do not induce any permanent damage inside Si. Pulses at short time scales allow to probe the interaction to study its physics. Pump-probe experiments provide one beam used to trigger the physical processes of ionization, and a second beam used to probe the interaction. This combination leads us to study plasmas insides the material, characterized by their lifetimes and levels of excitation (free-carrier density). For bulk experiments, two types of pump-probe schemes are possible, collinear or orthogonal propagation. One difficulty with collinear pump and probe geometry is due to the high index of refractive index of Si ($n_0=3.5$), leading to a long interaction zone inside the bulk in the direction of the beam propagation. The absorption and refractive index variations are integrated along the propagation axis. For that reason, we chose to use an orthogonal experimental geometry. In this Chapter we perform time-resolved observations by optical transmission microscopy with a spatial resolution limited by our customized optical microscope system, which is presented in the following section.

3.1.2 Experimental set-up

3.1.2.1 Characteristics of the pump and the probe illuminations

We present the experimental set-up employing the pump-probe technique to perform time-resolved studies of the interaction inside Si [1]. The pump-probe set-up is implemented on ASUR platform. The sample used in this section is a cubic target sample of Si (from Crystal GmbH) with all $10 \times 10 \text{ mm}^2$ sides polished. The crystal orientation is 100, the sample is n-doped Si with a low level of doping (near the intrinsic case) with high resistivity ($935\text{-}1500 \text{ }\Omega\cdot\text{cm}$) corresponding to an initial concentration of free-carriers of about 10^{11} cm^{-3} . As it was described in section 1.2.2., we can access the density of excitation induced by a pump pulse in a transparent solid by measuring the local change of the refractive index. In practice, a pump pulse modifies the optical properties of the materials, and a probe photographs the interaction by monitoring the absorption through the pump depletion.

Figure 3.1 describes the experimental set-up. The OPA described in the previous Chapter converts the initial 800 nm-pulses into 1300 nm-pulses. The beam is linearly polarized, with a pulse duration $\tau = 60 \text{ fs}$ measured with a single pulse autocorrelator. The maximum energy available after the OPA is $\approx 1.5 \text{ mJ}$, giving access to intensities in vacuum (being the intensity which would be reached if the beam was focused in vacuum) up to 10^{17} W/cm^2 for a micrometer spot size. This maximum intensity is largely above the ionization threshold for air (10^{14} W/cm^2 [91]) or Si (10^{10} W/cm^2 [2]). The beam is separated into one pump (90% of the incoming beam) and one probe (10%) with a beam splitter (BS).

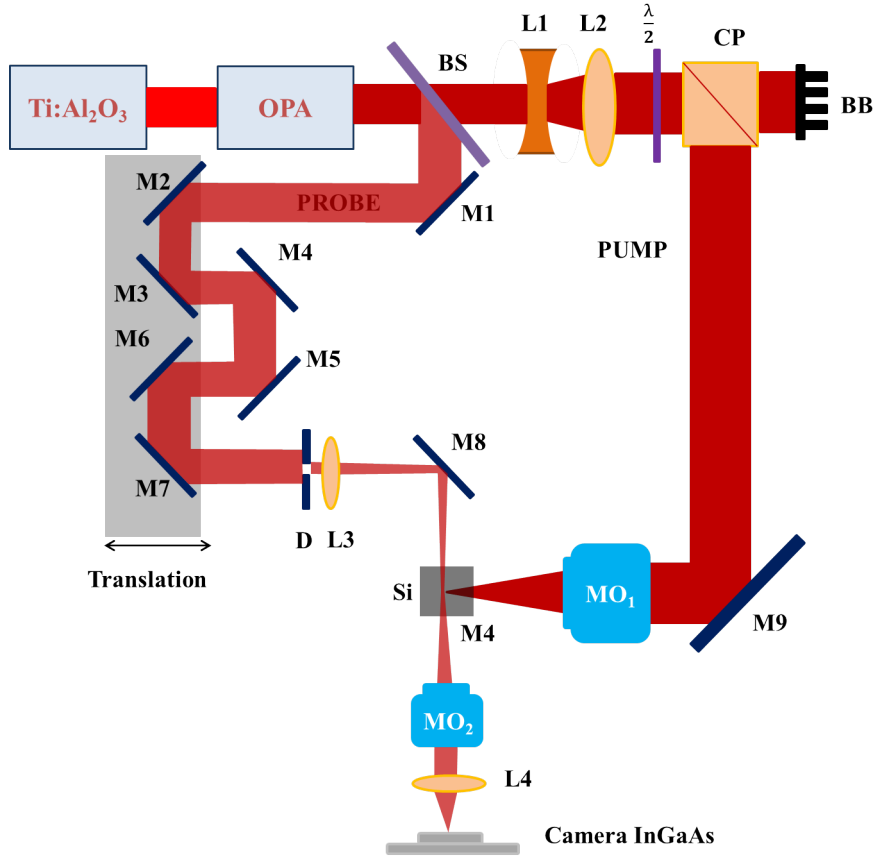


Figure 3.1 – Description of the pump-and-probe experiment on ASUR. A Titanium:Sapphire laser source delivers 800 nm pulses at 30 fs, and an OPA converts the wavelength to 1300 nm to work in the transparency domain of Si. A 90:10 beam splitter (BS) separates the pump and the probe beams; an afocal system composed of a divergent lens (L1) and a convergent lens (L2) changes the size of the beam with a magnification 1.5; an half-wave plate (HWP) and a polarizing beam splitter (PBS) control the energy; the energy in excess is blocked on a beam dump (BD), and we use a microscope objective (MO) to focus the laser. For the probe, mirrors (M1 to M7) constitute the manual delay line; the homogeneity is controlled with a diaphragm (D) and a lens (LS).

Description of the pump

The pump beam, containing most part of the incoming energy, is used for the excitation of Si. To reach a sufficient intensity to generate a high density of electrons and holes, the pump is focused with a microscope objective (MO₁) working in the IR range (LMPLN-IR/LCPLN-IR, Olympus). The size of the pump beam is expanded with an afocal system (L1: LB1437-C and L2:LD1120-C from Thorlabs) to fill the entrance pupil (12 mm) of the objective. The energy is first controlled by a half-wave plate ($\lambda/2$) and a polarizing beam splitter cube (PBS104, Thorlabs). The horizontal polarization is rejected on a beam dump, and then we attenuate the beam with neutral IR densities (not represented in the figure). The objectives are corrected for spherical aberrations for depth of focusing in Si up to 1.2 mm. We must note that

the dispersion of an IR pulse due to its propagation through transparent optics like glasses is negligible (as calculated in Chapter 2). Several NAs have been tested for confined excitation inside Si: 0.1, 0.3, 0.45, 0.65 and 0.85.

The waist of the Gaussian beam follows:

$$w_0 = \frac{\lambda M^2}{\pi NA} \quad (3.1)$$

The confocal parameter b is related to the Rayleigh zone in air z_R :

$$b = 2 \times z_r = 2 \times \frac{\pi w_0^2}{\lambda} \quad (3.2)$$

These different microscope objectives provide very small spot sizes for an extreme confinement, summarized in Table 3.1. The experiment can run in single-shot regime, controlled by a mechanical shutter (SH05, Thorlabs). The energy is measured before the microscope objective with a Joulemeter (Solo2, Gentec). The energy measurements given in this thesis are average values on a few hundreds of shots.

Description of the probe

The probe beam is a fraction (10%) of the incoming beam. Observing the dynamic of the interaction implies that the pump and the probe must be temporally synchronized and spatially overlapped. The temporal synchronization between the pulses is first approximately obtained by adjusting the beam paths in order to make them equal. Then, a delay line composed of four gold mirrors that can be translated together (M2, M3, M5, M7) allows to synchronize the probe on the pump. The particularity of our set-up is that long delays can be reached: up to 4 ns between the pump and the probe. To synchronize the pump and the probe beams, we adjust the delay between the two beams to image a plasma presenting the highest absorption as a function of the delay. As it is placed on a manual line, the error on the measurements can be higher than if the delay line was on a motorized stage. The approximated error is evaluated at 6 ps, assuming that an error of 0.5 mm is possible on the measurement of the distance of propagation. This error seems relatively high compared to the pulse duration (60 fs), so we have performed measurements with a motorized stage in a range of delay of 0-200 ps. This motorized stage can provide relative movements with an error of 4 μm , corresponding to 13 fs. By reporting the

Reference	NA	Theoretical waist w_0	Theoretical confocal parameter b
LMPLN5XIR	0.1	6.4 μm	238 μm
LMPLN10XIR	0.3	2.36 μm	25.9 μm
LCPLN20XIR	0.45	1.44 μm	11 μm
LCPLN50XIR	0.65	1 μm	4.6 μm
LCPLN100XIR	0.85	0.73 μm	2.0 μm

Table 3.1 – Characteristics of the objectives and the corresponding sizes expected for the focal regions. The diameter of the incoming beam is 15 mm at 1.3 μm wavelength.

transmission of the probe after the propagation through the plasma, it appears that during the first 200 ps the plasma density is stable [1], meaning that the recombination time exceeds largely 200 ps. For delays $\gg 6$ ps, the resolution of our manual delay line is enough for our experiments.

Since the quality of the collimated probe is not sufficient to provide an homogeneous illumination, we have chosen to focus the probe where the pump generates an excited area. A pinhole (P) and a lens (L3) are installed before the sample: the pinhole generates a smooth Airy diffraction pattern inside Si, and by closing it we control the size of the region which is illuminated with the central part of the diffraction-limited spot. The energy of the probe is attenuated with optical densities to avoid TPA induced by the probe.

3.1.2.2 Imaging configuration inside the bulk

The area excited by the pump is imaged transversely with the probe. The pulse duration of the probe at the focal plane inside Si is about 300 fs because of group velocity dispersion giving a theoretical spatial and temporal resolution of our pump-and-probe set-up of about $1.3 \mu\text{m}$ (limited by the wavelength of the probe) and about 300 fs (limited by the pulse duration of the probe), respectively. The size of the probe at the focus is largely higher than the waist of the pump pulse, ensuring that the probe fully retrieves the plasma information.

The schematics of the transverse illumination of the plasma by the probe is il-

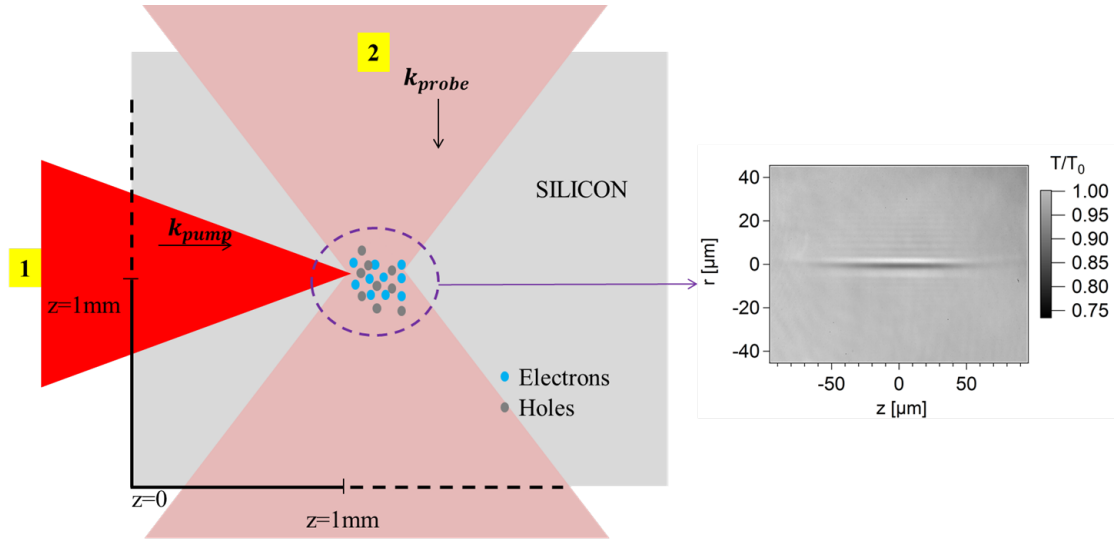


Figure 3.2 – Transverse illumination of the interaction by the probe. The probe propagates through 9 mm of Si before imaging the free-carrier generation, which leads to pulse broadening by dispersion. The detection of the excitation is shown on the image (right), the dark area is the pump excitation coming from the right. The energy of the pump is 6 nJ and the delay between the pump and the probe is fixed at 10 ps.

lustrated in figure 3.2. The probe propagates through an IR homemade microscope composed of a microscope objective (MO₂), a tube lens (L4) that images the plasma on an InGaAs array (Xenics Xeva). This imaging system provides a 20 or 50X magnification, depending on the microscope objective which is used (NA=0.45 gives 20X and NA=0.65 gives 50X magnification). The IR camera has a linear response from 900 nm to 1700 nm with an image composed of 640x512 pixels, with a pixel size of 20 μm .

3.1.3 Results: micro-plasma confined in bulk-Si

3.1.3.1 Micro-plasma images

Here, we describe the images obtained with our ultra-fast infrared imaging set-up and how we calculate the free-carrier density N_e from the images. Infrared ultra-fast imaging inside the bulk of Si relies on the probe absorption measured with the IR camera. We have first verified that there is no nonlinear absorption of probe. For that we focus the pump inside Si and we generate a plasma, illuminated by the probe. We report the transmission of the probe for different probe energies. The transmission of the probe should not vary with the energy. We did not observe a signature of nonlinear effects in the range of energies for the probe (a few hundreds of nJ), meaning that the intensity of the probe is below the nonlinear ionization threshold of Si ($\approx 10^{10}$ W/cm² [2]). A cleaning procedure is systemically applied to the measurement, consisting in taking one image with and one image without the plasma. The ratio of these two images gives the normalized transmission of the probe.

A typical image of a plasma observed in bulk-Si is presented in figure 3.2, on the right side. The laser is coming from the right with an energy of 6 nJ. The delay between the pump and the probe is fixed a 10 ps, delay at which the plasma is fully established and has not started to recombine [1]. The image is the average acquisition of several laser shots. It is important to remind at this stage of the manuscript that from previous studies, we know that the density of free-carriers generated does not lead to permanent modifications inside Si [1]. If the pump is turned off, the material comes back to its initial state at rest. The length of the plasma is remarkable since the Rayleigh zone in air does not exceed 60 μm with NA=0.3, whereas the plasma is much longer on the image. This is due to the refractive index of Si, $n_0 = 3.5$ at $\lambda=1.3$ μm . We also observe white edges corresponding to the diffraction induced by the plasma edges.

3.1.3.2 Estimate of the free-carrier density

In Chapter 1, we expressed the dielectric function of a plasma, and the corresponding change of refractive index : $\tilde{n} = \sqrt{\epsilon} = n' + in''$. Here, n'' is the nonlinear part of the refractive index, related to the absorption α by $\alpha = 2\omega n''/c = 4\pi n''/\lambda$. The images obtained with the microscope system denotes the transmission T of the electronic plasma inside the bulk of the material: $T = I/I_0$. The absorption α is

obtained with the Beer-Lambert law assuming a homogeneous plasma:

$$\alpha = -\frac{1}{d_{plasma}} \ln \frac{I}{I_0} \quad (3.3)$$

where d_{plasma} is the measured plasma diameter. Finally, under these assumptions, the signal on the camera is directly linked to the imaginary part of the refractive index change of the plasma by:

$$\frac{I}{I_0} = T = e^{-\frac{4\pi n''}{\lambda} d_{plasma}} \quad (3.4)$$

We report the transmission of the probe for different pump energies in figure 3.3. First, we can easily observe the diminution of the normalized probe transmission reaching a saturation level, suggesting that the number of free electrons generated by the pump is no more increasing. The 0.77 minimum of transmission corresponds to a free-carrier density of $N_e=3 \times 10^{19} \text{ cm}^{-3}$. The Drude model has been employed to calculate N_e generated by the propagation of an ultra-fast laser pulse assuming a constant collision time of $\tau=3 \text{ fs}$ [92]. In section 3.2, we present an interferometry set-up allowing to map the phase shift of the probe induced by its propagation through the plasma. Combining the amplitude and phase measurements yields to an experimental estimation of τ_c used to calculate the free-carrier density N_e . This method to calculate the free-carrier density implies strong hypothesis such as an uniform energy deposition, or a cylindrical symmetry of the plasma. The calculation on the free-carrier density would be more rigorous with the Abel transformation, but it is not investigated in this thesis.

3.1.3.3 Nonlinear propagation effects

Nonlinear effects may be responsible for that limitation, such as in dielectrics when filamentation is observed, described by a competition between the Kerr effect and plasma defocusing [70]. Such nonlinear effects can be significant when the

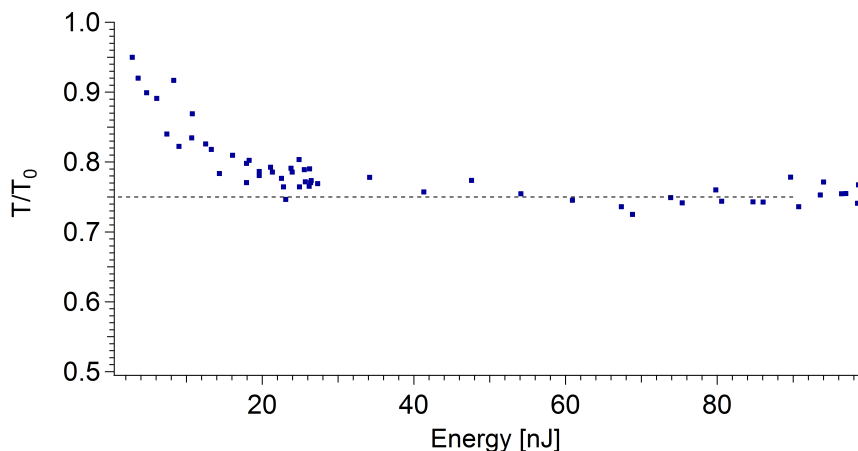


Figure 3.3 – Evolution of the probe transmission as a function of the incoming pulse energy. The dash-line is an eye guide for the saturation.

power is above the critical power. The nonlinear refractive index of Si ($n_{NL} = 3 \times 10^{-14} \text{ cm}^2/\text{W}$ [32]) is relatively high (100 times higher than in fused silica [93]), inducing a low critical power (equation 1.36). In our study, we calculate a critical power $P_{cr} = 24 \text{ kW}$ at $1.3 \text{ }\mu\text{m}$, and it corresponds for our laser beam to an energy of 1 nJ. The sample being irradiated with high energies compared to 1 nJ, we try to identify potential self-focusing or nonlinear distortions that could occur in the interaction.

We report the position of the geometrical focus for different pump energies in figure 3.4. We observe a modest spatial shift towards the prefocal region, which is a signature of nonlinear effects during the pulse propagation. To be more precise, we can attribute this shift to self-focusing (Kerr effect) in the prefocal region. However, when increasing the intensity, one expects also a development of the interaction in the prefocal region resulting from TPA. Also, TPA occurs on a large volume before the focus [7], depleting the pulse reaching the focus and lowering in this way the apparent power in this region. For these reasons, we suspect that self-focusing and TPA are concurrent effects which explains the very modest shift of the focus observed in figure 3.4.

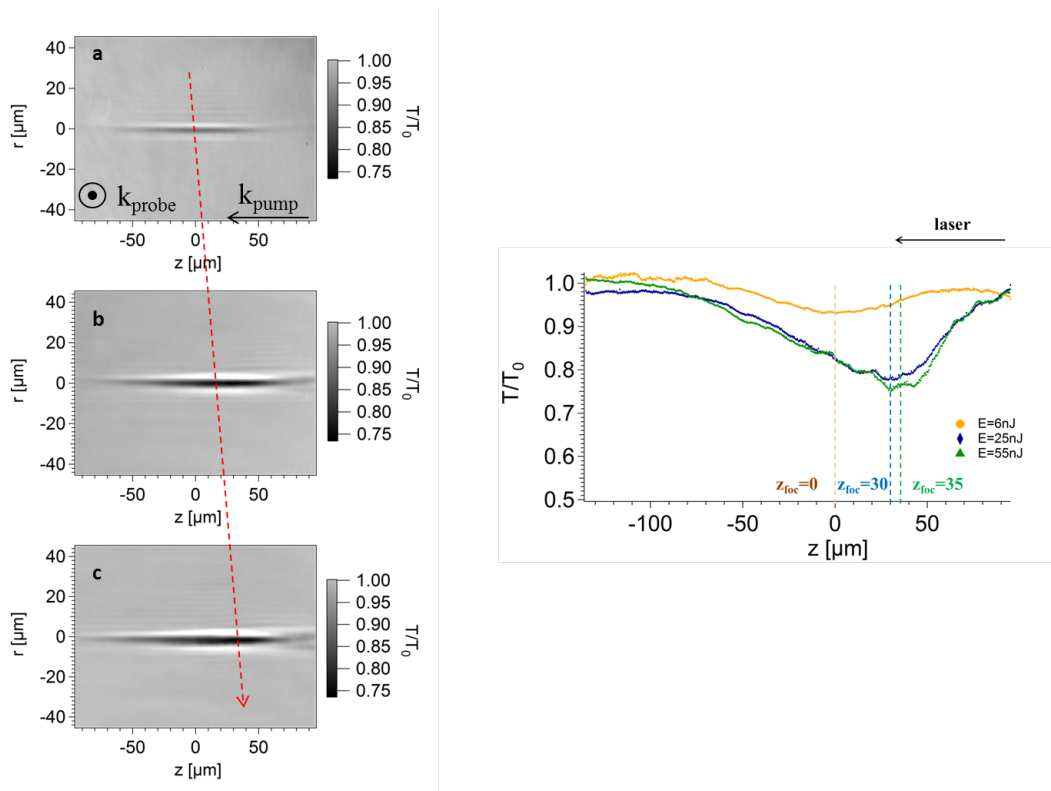


Figure 3.4 – Probe transmission as a function of the pump pulse energy and the depth inside Si. Pump-probe delay is fixed at 10 ps. Dashed arrow follows the shift of the absorption front. a) 6 nJ, b) 25 nJ and c) 55 nJ.

3.1.3.4 Optical breakdown criteria and limitations of the interaction

In dielectrics, the optical breakdown is generally associated with the critical density [37, 36, 38] because it is the level of excitation transforming the initially transparent material in a strongly absorbing one. The critical density has been introduced with the Drude model in section 1.2.2, we remind its expression below in the free electron gas approximation:

$$N_c = \frac{\epsilon_0 m_e \omega^2}{e^2} \quad (3.5)$$

The critical density at 1.3 μm inside Si is $N_c = 6.6 \times 10^{20} \text{ cm}^{-3}$. In our focusing conditions, irradiating the sample with more than 30 nJ does not increase the number of free-carriers generated above $N_e = 3.0 \times 10^{19} \text{ cm}^{-3}$, which is one order of magnitude below the critical density. The micro-plasma generated inside the volume of Si is therefore at an under-dense level.

To compare the observed excitation to a requirement for material modification, one can also rely on energy considerations. If we consider that the consumption of two photons generates one electron, the absorbed energy density is directly given by:

$$U = 2\bar{h}\omega N_e \quad (3.6)$$

The number of electrons generated inside Si ($N_e = 3.0 \times 10^{19} \text{ cm}^{-3}$) corresponds to a maximum energy density of $\Delta(E_{exp})=9 \text{ J/cm}^3$. We can compare this result to the density of energy that has to be absorbed to reach the melting point of Si. This calculation is made taking into account only thermal effects, considering that a permanent modification can be due to a change of phase inside the material. For Si, $\Delta E_{fus}=5 \text{ kJ/cm}^3$ [4].

One can wonder if thermal contribution to the observed absorption can be demonstrated. It leads to study the potential bandgap closure due to energy transfer to the lattice. With thermodynamics considerations, the local heating induced by the pump pulse can be estimated as [1]:

$$\Delta T(^{\circ}\text{C}) = \frac{E}{V\rho C} \quad (3.7)$$

where E is the pump energy, V is the interaction volume (assumed as a cylinder with 100 μm length and 3 μm diameter, see the plasma in the right side in figure 3.2), ρ is the Si density (2.33 g/cm^3) and C is the thermal capacity (0.712 $\text{J}/(\text{g}\cdot\text{C})$). We finally obtain a potential local heating $\leq 1 \text{ K}$ for our experiments (with $E \leq 100 \text{ nJ}$), allowing us to exclude any thermal contribution to the probe absorption.

All these considerations are consistent with the experimental observations that Si does not undergo any permanent modification in its volume: the pump excitation seems to be not efficient enough, mainly because of a huge loss of the incoming energy before reaching the focus.

3.1.4 Free-carrier recombination and diffusion

In this section we present an optical method to study the free-carrier recombination and diffusion inside the bulk of Si. Limitations exist in optical methods to study the dynamics of the carriers, the sensitivity of the measurement being the main one. To measure bulk responses, one needs to inject carriers inside Si. Here, we directly inject free-carriers by two-photon absorption, and observe the material response with the infrared camera combined with the microscope system. Generally, recombination experiments are performed at the surface of the sample whereas we can monitor here free-carrier recombination in bulk-Si. This experiment is realized in the same silicon sample as the one used in the probe transmission measurements. The free-carriers are confined 1 mm under the surface, and we concentrate on high levels of injection. At high density of free-carriers, recombination is supposed to be dominated by Auger mechanism [94, 95], leading to relatively simple calculations of the recombination time. This study is strongly motivated by the previous experimental demonstration of the saturation of the excitation inside Si with femtosecond infrared pulses. One reason could be a fast carrier diffusion leading to the increase of the volume during thermalization, resulting in a lower energy density transferred to the lattice.

The experimental set-up is the same as in the previous section: we use the pump and probe microscopy set-up to study the dynamics of the micro-plasma generated inside the bulk of Si by TPA. The optical path can be adjusted up to 4 ns between the pump and the probe. The experiment is computer-controlled and the cleaning procedure of the images (previously described) is systemically done to attenuate the non-uniformity in the probe illumination.

Figure 3.5 is a map of the normalized transmission T/T_0 inside Si for different pump-probe delays (0 to 2 ns). The propagation direction of the pump and the probe are orthogonal, as depicted in figure 3.1. The first qualitative observation is the drop of the normalized transmission of the probe. For long delays (>10 ns), we have verified that the transmission returns to 1, meaning that we are dealing only with transient changes and the material returns to its original state after each laser shot. Using a X50 magnification allows us to precisely measure from the images the width of the micro-plasma. For long delays, the plasma spreads in the radial direction, as one can see in figure 3.5. This is taken as a direct evidence of the free-carrier diffusion. We assume the cylindrical symmetry of the plasma in the propagation axis.

To analyze the results, we use a model based on the resolution of the rate equation for free-carriers. According to the description of section 1.3, the radial and time dependent free-carrier density N_e can be modeled by:

$$\frac{\partial N_e(r, t)}{\partial t} = D_a \left(\frac{\partial^2 N_e(r, t)}{\partial r^2} + \frac{1}{r} \frac{\partial N_e(r, t)}{\partial r} \right) - \frac{N_e(r, t)}{\tau_{eff}} \quad (3.8)$$

with D_a the ambipolar diffusion coefficient and τ_{eff} the effective carrier lifetime. In this equation we chose to express the global effective lifetime of carriers as follows [96]:

$$\frac{1}{\tau_{eff}} = \frac{1}{\tau_{Auger}} + \frac{1}{\tau_{rad}} + \frac{1}{\tau_{SHR}} + \frac{1}{\tau_{others}} \quad (3.9)$$

where τ_{Auger} is the Auger recombination time, τ_{rad} is the radiative recombination time, τ_{SHR} is the Shockley-Read-Hall (SRH) recombination time and τ_{others} (like traps) the other possible contributions. The different mechanisms for recombination have been described in Chapter 1. The radiative lifetime follows the expression [96]:

$$\tau_{rad}^{HLI} = \frac{1}{BN_e} \quad (3.10)$$

with $B_{Si}=2 \times 10^{-15} \text{ cm}^3/\text{s}$ [97]. Taking the electronic density as evaluated in the previous section at $N_e=3.0 \times 10^{19} \text{ cm}^{-3}$, we estimate a radiative lifetime of $20 \mu\text{s}$ for our level of injection. The expression of Auger recombination coefficient is the following [96]:

$$\tau_{Auger} = \frac{1}{C_a N_e^2} \quad (3.11)$$

with C_a the ambipolar coefficient for Auger recombination. According to the literature [61], this coefficient varies from $C_{a,min} = 4.0 \times 10^{-31} \text{ cm}^6/\text{s}$ to $C_{a,max} = 9.0 \times 10^{-31} \text{ cm}^6/\text{s}$ for low injected electron density, leading to decay times between $\tau_{Auger} = 1.2 \times 10^{-9}\text{s}$ and $\tau_{Auger} = 2.8 \times 10^{-9}\text{s}$. Auger recombination is considered as the mechanism having the main contribution in free-carrier recombination inside Si for high-injection levels and it will be discussed later.

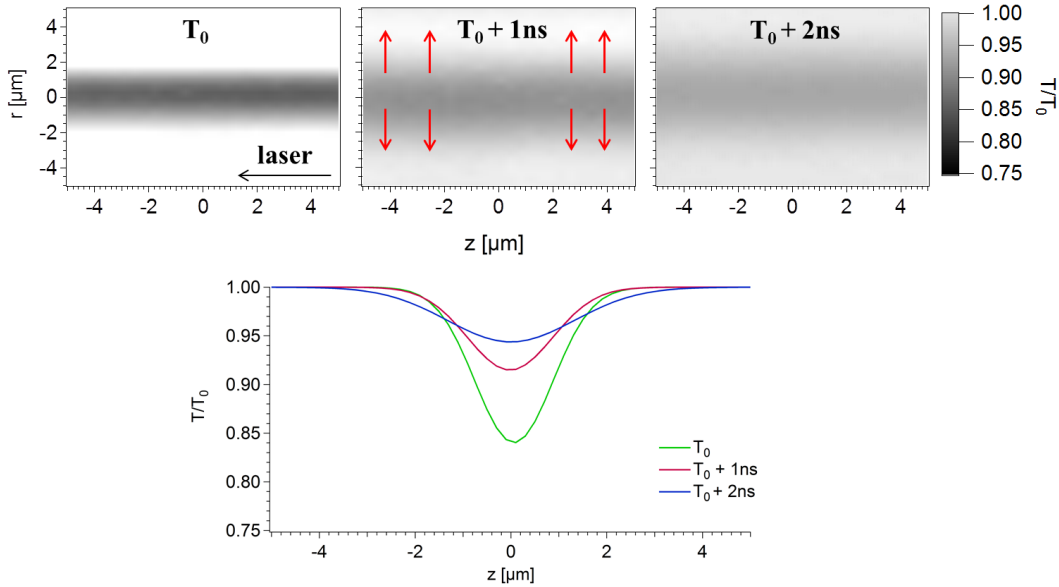


Figure 3.5 – Pump-probe observation of free-carrier diffusion inside Si. Images are taken with the InGaAs camera for different delays between pump and probe to observe the spatial spread of the plasma. Cross-sections are fitted by a Gaussian curve (bottom). The energy of the pump is 20 nJ focused with NA=0.3.

To estimate the different contributions of the different processes to free-carrier recombination, we can first ensure that at the end of the delay line, being a delay between the pump and the probe beam of 4 ns, the plasma has fully disappeared at the nanosecond timescale. It means that the radiative recombination contribution which occurs on a microsecond timescale can be neglected in our model. Then, we simplify equation 3.9 with only two contributions: one from Auger and one called HLI for all contributions independent on N_e (such SRH). The effective lifetime is then :

$$\frac{1}{\tau_{eff}} = \frac{1}{\tau_{Auger}} + \frac{1}{\tau_{HLI}} \quad (3.12)$$

The model described above helps us to calculate the distribution of $N_e(Y)$ corresponding to the initial distribution of $T(Y)$ (as plotted in figure 3.5), meaning for short delays between the pump and the probe. The electronic density is calculated with the Drude model, and the example depicted in figure 3.5 presents an initial free-carrier density $N_{e,max}=3 \times 10^{19} \text{ cm}^{-3}$ with a $2.5 \mu\text{m}$ FWHM. We apply the equation 3.9 to determine the evolution of the distribution with time. The calculations are compared to the experimental data (the transmission profiles). The goal is to extract the diffusion coefficient D_a and τ_{eff} , independently (possible taking a constant τ_{eff}).

First, we assume a constant effective lifetime for the free-carriers. By reporting FWHM calculated data and the one extracted from the experiments FWHM as a function of the delay and for different pump energies, we can determine the coefficient of diffusion. Results are presented in figure 3.6, where we compare the experimental data (dots) and the calculations (lines). When the best agreement is obtained, we finally determine $D_a=2.5 \text{ cm}^2/\text{s}$. This coefficient depends on the electron and hole mobility. This value is low compared to those reported in the literature

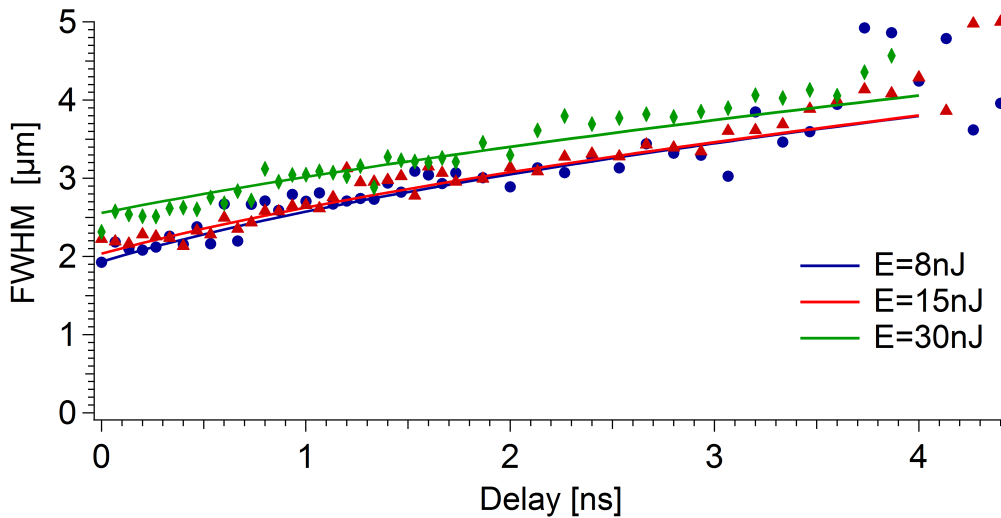


Figure 3.6 – Evolution of the width of the plasma as a function of the delay in ns, for three different pump pulse energies. Markers are experimental data and lines are calculations.

($D_a=18 \text{ cm}^2/\text{s}$ in [98]). It can be explained by the high excitation level of our experiment where the carrier mobility is lower due to scattering [99]. An intermediate value of the diffusion coefficient has been published ($D_a=7 \text{ cm}^2/\text{s}$ in [100]) for an injection level of 10^{18} cm^{-3} , somehow consistent with our conclusion. We use a constant value for D_a to simplify the model. We are aware that this simplification can be questionable since this coefficient usually depends on the temperature.

Once the value of D_a is determined, we study the carrier effective lifetime. The estimation of the characteristic time of our micro-plasma is realized by reporting the minimal transmission of the plasma for different delays. The value of $T(Y)$ is always taken at the same coordinate. The results are displayed in figure 3.7. The increase of the transmission for long delays is the signature of recombination and diffusion in the nanosecond timescale. The best agreement between the model and the experiments is for a constant recombination time $\tau_{eff}=2.5 \text{ ns}$.

Other calculations taking into account density dependent recombination rates have been performed but failed to fit correctly the experimental data. Figure 3.8 illustrates the comparison between experiments and calculation when considering Auger as the main recombination mechanism. It does not allow to reproduce the results and it largely underestimates the probe transmission. Taking a constant free-carrier lifetime retrieves in a better way the experimental data. It is consistent with a Shockley-Read-Hall mechanism process of recombination, by trapping in the presence of defects. Since semiconductors always contain impurities, this mechanism is always active. In our case, a conclusion could be that SRH appears to be dominant. However, not taking into account Auger recombination remains questionable since estimations give a range of values for recombination considering Auger mechanism between 1.6 ns to $4.4 \mu\text{s}$ [5]. With these investigations, we can safely conclude that the recombination of the free-carrier population is a very slow mechanism compared

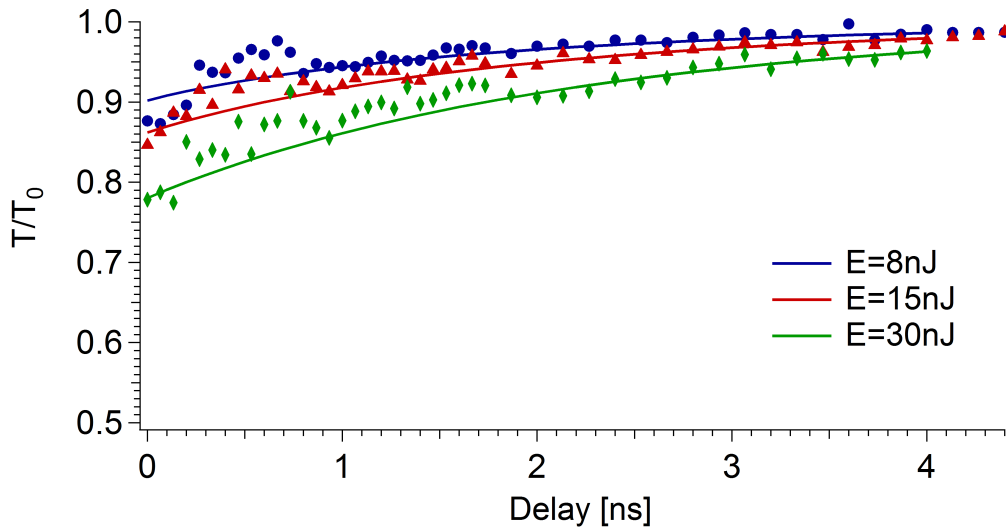


Figure 3.7 – Evolution of the probe transmission as a function of the delay in ns, for three different energies. Markers are experimental data and lines are calculations

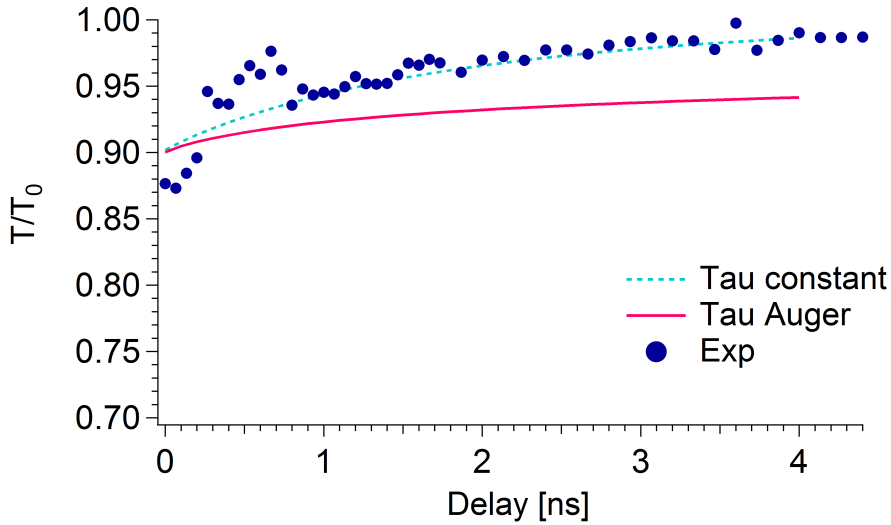


Figure 3.8 – Evolution of the probe transmission as a function of the delay in ns for 8-nJ pulses, taking a constant carrier lifetime (blue line) or recombination by Auger (red line). Experimental data are the blue circles.

to the pulse duration. As an important conclusion, this means that incoming energy losses are not due to fast energy dissipation in the material.

3.2 Ultra-fast interferometry: phase measurements

In the previous section we have estimated through absorption the free-carrier density generated inside Si assuming $\tau_c=3$ fs. The full optical response of a transparent solid to an intense laser pulse is contained in the complex dielectric function. The real part can be retrieved by phase measurements, and the imaginary part is deduced from amplitude measurements. This section is dedicated to phase measurements with an interferometry technique. Among the techniques for interferometry measurements, we distinguish spatial, temporal and spectral interferometry. Spatial interferometry can be realized with double slits and a screen on which we detect fringes. Temporal interferometry uses amplitude split (e.g. Michelson), inducing two beams interfering, one containing information on the excited medium, and the other being unperturbed. Spectral interferometry relies on mixing two waves with a different frequency.

In this section, we use the temporal interferometry technique. We develop a pump-probe experiment similar to the one described in section 3.1., but we split the probe into two arms, one reference beam and one object beam that contains the information on the ionization of Si. This set-up provides an amplitude measurement (without the reference beam) and a phase measurement, both on the same plasma. We have then access to the full dielectric function of Si and under the Drude model approximations we can determine the electron-phonon collision rate as the unknown parameter. For now, only experimental data have been published in fused silica and sapphire on this rate [101][102]. In the literature, theoretical data for Si vary from

$\nu_c=0.18 \text{ fs}^{-1}$ and $\nu_c=0.5 \text{ fs}^{-1}$ [103][104][92], depending on the injected free-carrier density. The same interferometry set-up will be also used in Chapter 5 to evaluate the change of refractive index in case of permanent damage inside Si.

3.2.1 Extraction of the phase-shift induced by the micro-plasma

The pump pulse locally modifies the refractive index of Si because of the generation of a density of free-carrier population generated inside the material. The goal of interferometry is to measure the real part of the refractive index. The free-carrier contribution to the local change of the complex refractive index takes the form [102]:

$$\Delta\tilde{n} \approx \frac{-e^2 N_e}{2n_0 \epsilon_0 \omega^2 (0.18 m_e)} \frac{1}{1 + \frac{i}{\omega \tau_c}} \quad (3.13)$$

The phase shift is directly related to the real part of the refractive index and the amplitude is related to the imaginary part of the refractive index. Assuming a uniform distribution of free-carriers on a cylinder with a diameter d_{plasma} , the phase shift and the amplitude can be expressed as:

$$\Delta\phi = \frac{2\pi d_{plasma}}{\lambda_{probe}} Re(\Delta\tilde{n}) \quad (3.14)$$

$$T = e^{-\frac{4\pi}{\lambda} d_{plasma} Im(\Delta\tilde{n})} \quad (3.15)$$

By injecting the real part and the imaginary part of $\Delta\tilde{n}$ in equation 3.14 and 3.15, respectively, we obtain two equations with two unknown parameters (N_e and τ_c):

$$\Delta\Phi = \frac{2\pi d_{plasma}}{\lambda} \frac{-e^2 N_e \tau_c^2}{2n_0 \epsilon_0 (0.18 m_e) (1 + \omega^2 \tau_c^2)} \quad (3.16)$$

$$T = exp\left(-\frac{4\pi d_{plasma}}{\lambda} \frac{e^2 N_e \tau_c}{2n_0 \epsilon_0 \omega (0.18 m_e) (1 + \omega^2 \tau_c^2)}\right) \quad (3.17)$$

Finally, analytical expressions of N_e and τ_c are obtained and can be calculated independently with experimental values for $\Delta\phi$ and T:

$$\tau_c = \frac{2\Delta\phi}{\omega \ln(T)} \quad (3.18)$$

$$N_e = -\frac{\Delta\Phi \lambda n_0 \epsilon_0 (0.18 m_e) \left(1 + \left(\frac{2\Delta\Phi}{\ln(T)}\right)^2\right)}{\pi d_{plasma} e^2 \left(\frac{2\Delta\Phi}{\omega \ln(T)}\right)^2} \quad (3.19)$$

3.2.2 Experimental details

3.2.2.1 Interferometry set-up

We adapt the previous experiment to combine infrared ultra-fast plasma imaging and an interferometry set-up relying on a Mach-Zehnder configuration [105]. In this

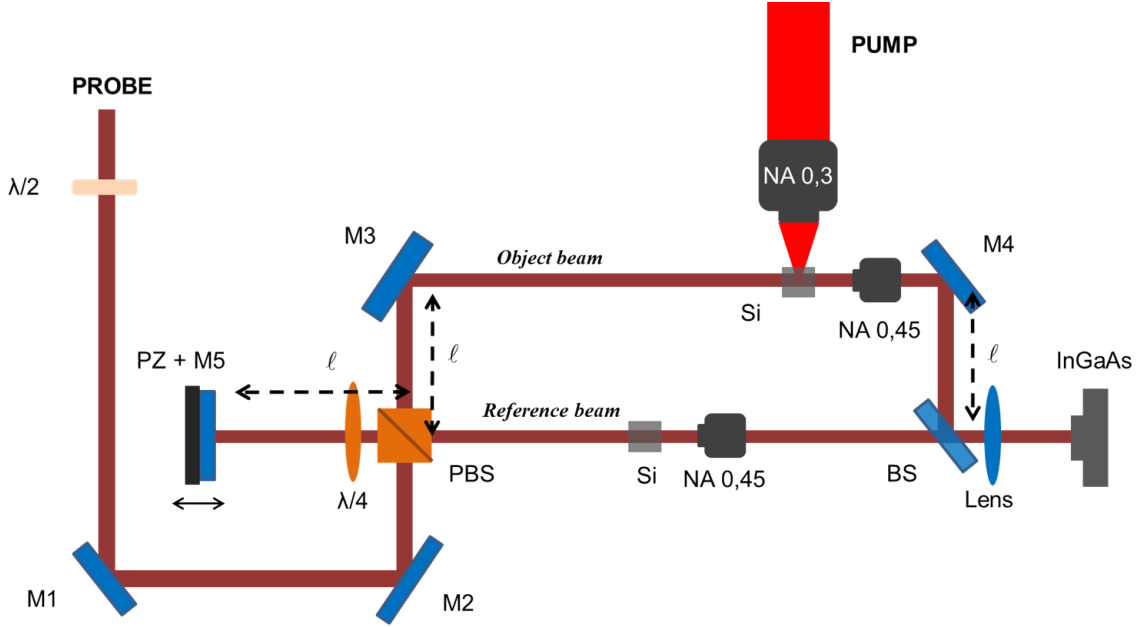


Figure 3.9 – Description of the ultra-fast-imaging microscope combined with Mach-Zehnder interferometer.

section we use crystalline Si, the same as in section 3.1.1. The optical arrangement is represented in figure 3.9. The probe is separated into two beams with orthogonal directions by a polarizing beam splitter (PBS). The object beam that images the plasma inside Si is the classical probe presented in section 3.1.1 with a microscope imaging system composed of a microscope objective (Olympus LCPLN20XIR), an associated tube lens giving a $20\times$ magnification, and an InGaAs array (Raptor, OWL SWIR 640 with $15\ \mu\text{m}$ pixel size). The reference beam propagates through a quarter-wave plate ($\lambda/4$) and illuminates a gold mirror mounted on a piezoelectric stage ($M5 + PZ$, Physik Instrumente). The piezoelectric stage provides a very precise motion ($5\ \text{nm}$ precision). The quarter-wave plate is essential to have the same polarization direction for the object and reference beam. The reference beam is imaged with the same microscope objective and has a common tube lens with the object beam to avoid large differences of the wave front curvature of the two beams. A sample of Si is placed on the reference beam to compensate for the optical path difference induced by Si on the object beam.

Then, the phase measurement relies on a four-step procedure [106][107]. Between the acquisitions, the PZ mirror makes precise moves of $\lambda/8 = 162.5\ \text{nm}$, inducing a phase delay of $\pi/2$ between two images. For a two-beam interferometry system, the general expression for the intensity on our camera can be written:

$$I_k(x, y) = A_0^2(x, y)A_r^2(x, y) + 2A_0(x, y)A_r(x, y) \cos(\Delta\phi(x, y)) \quad (3.20)$$

where $I(x, y)$ is the interference pattern intensity distribution, $A_0(x, y)$ and $A_r(x, y)$ are the object and reference beam amplitude distributions, respectively. $\Delta\phi(x, y)$ is the phase shift between the two beams. The acquired four interference intensity

distributions can then be expressed as:

$$I_k(x, y) = A_0^2(x, y)A_r^2(x, y) + 2A_0(x, y)A_r(x, y) \cos(\Delta\phi(x, y) + \frac{(k-1)\pi}{2}) \quad (3.21)$$

with k varying from 1 to 4, the number of the image. Then the phase image simply follows:

$$\Delta\phi(x, y) = \arctan\left(\frac{I_4 - I_2}{I_1 - I_3}\right) \quad (3.22)$$

The last step to obtain the final phase-shift map is an unwrapping procedure to avoid jumps of phase from π to $-\pi$ or from $-\pi$ to π as displayed in figure 3.10 (see blue to red transitions for example). When a phase jump is detected, we add a phase value of π or $-\pi$ to obtain the final phase image. Then a flattening procedure consisting in fitting the rings by a polynomial function is applied to the final image, as shown in figure 3.10. Those rings are due to a non-perfectly equal wave front curvature between the reference and the object beam. By subtracting the phase data and the polynomial fit, we obtain a flat background phase image revealing the phase shift induced by the plasma.

3.2.2.2 Calibration of the measurements

A calibration of our interferometer is essential to provide reliable results. A thin film of 25 nm of silicon has been deposited with an evaporator on a microscope slide and observed with AFM measurements. Then we selectively ablate the Si layer without damaging the glass. Silicon and glass present two distinct laser induced damage thresholds: 0.3 J/cm² and 1.5 J/cm², respectively. These thresholds have been experimentally determined with the same laser set-up, with the same focusing conditions. We detail only the silicon damage threshold in section 4.2.3. We just have to adjust the fluence between these two thresholds to ablate only the thin film of Si. To confirm the selective ablation of Si, verifications with an optical microscope and the Atomic Force Microscope (AFM) are performed.

Figure 3.11 illustrates the step measured by AFM at the edge of the ablated region. The theoretical phase-shift induced by the Si film is given by the following

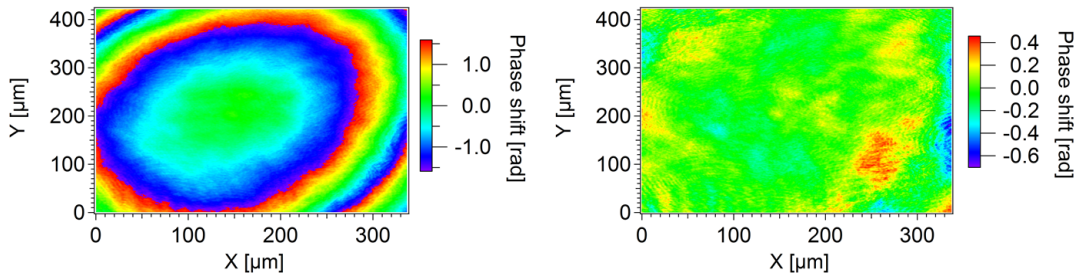


Figure 3.10 – Phase map without (left) and with (right) the image processing procedure.

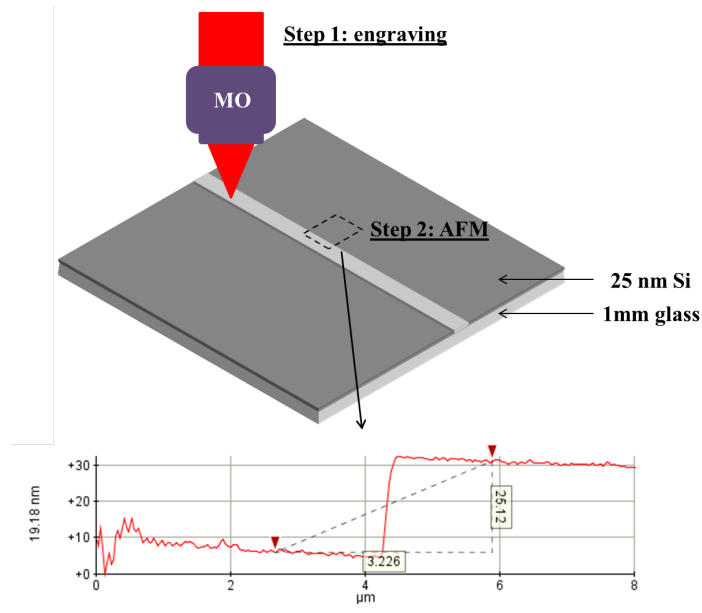


Figure 3.11 – Description of the preparation of the calibrated sample. Step 1 is the ablation of the thin film of Si, and step 2 is the AFM scan to measure the optical path difference.

formula:

$$\Delta\phi = \frac{2\pi\Delta nh}{\lambda} \quad (3.23)$$

where Δnh is the optical path difference induced by the presence of the film of a thickness $h=25$ nm, and $\Delta n = n_{Si} - n_{air}$. This leads to the theoretical value of $\Delta\phi = 0.3$ taking the refractive index of crystalline silicon.

Figure 3.12 depicts the four-step measurement without the cleaning and un-

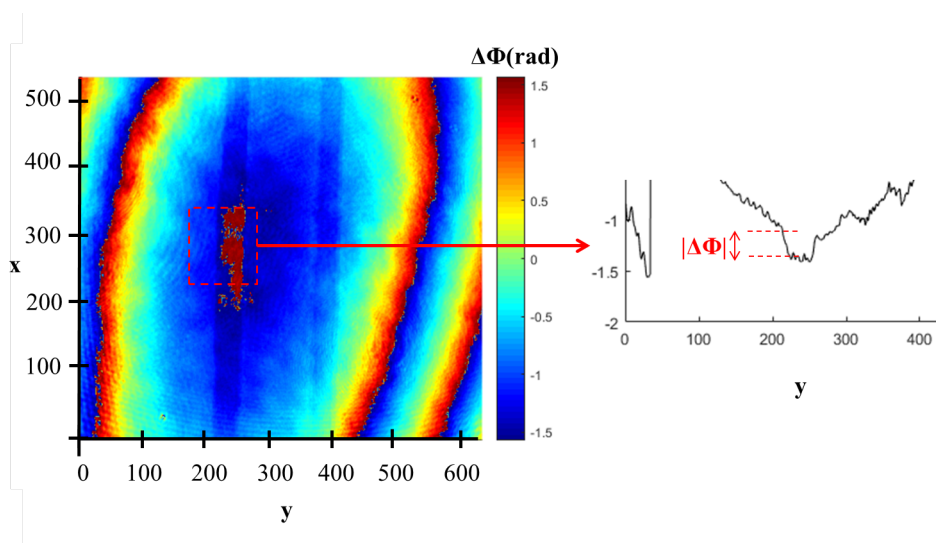


Figure 3.12 – Interferometry measurement without the unwrapping and flattening procedure. The engraving line is in the red square.

wrapping procedure which has not been applied on this measurement. Without this procedure, we can observe the curvature on the phase map. Taking this curvature into consideration, we obtain a phase-shift $\Delta\phi \approx 0.3$ that corresponds to our expectations. We can safely conclude that on that range of phase-shift measurement, our method is reliable for estimating the sign and amplitude of phase shifts.

3.2.2.3 Phase and amplitude stability

Stability issues and precision estimations have been performed to discuss the limitations of this measurement. To obtain the collision rate, we need amplitude and phase measurements, so we have also performed investigation on the stability of these two measurements. First, we present a study on the stability of the phase measurement.

First, we apply a procedure to reduce the background intensity on the interference pattern. For that, we can suppress the noise (not due to laser fluctuations but due to dusts on the optics and on the sample surfaces which induce diffraction patterns). We map the phase with and without the plasma and then we subtract those two phase images, as described in figure 3.13. Moreover, we take four images for every piezoelectric position to average the signal and then avoid the laser fluctuations. Every image relies on 4 ms camera exposure, which corresponds to four laser shots with the 100-Hz repetition rate of our laser. The final phase map that we

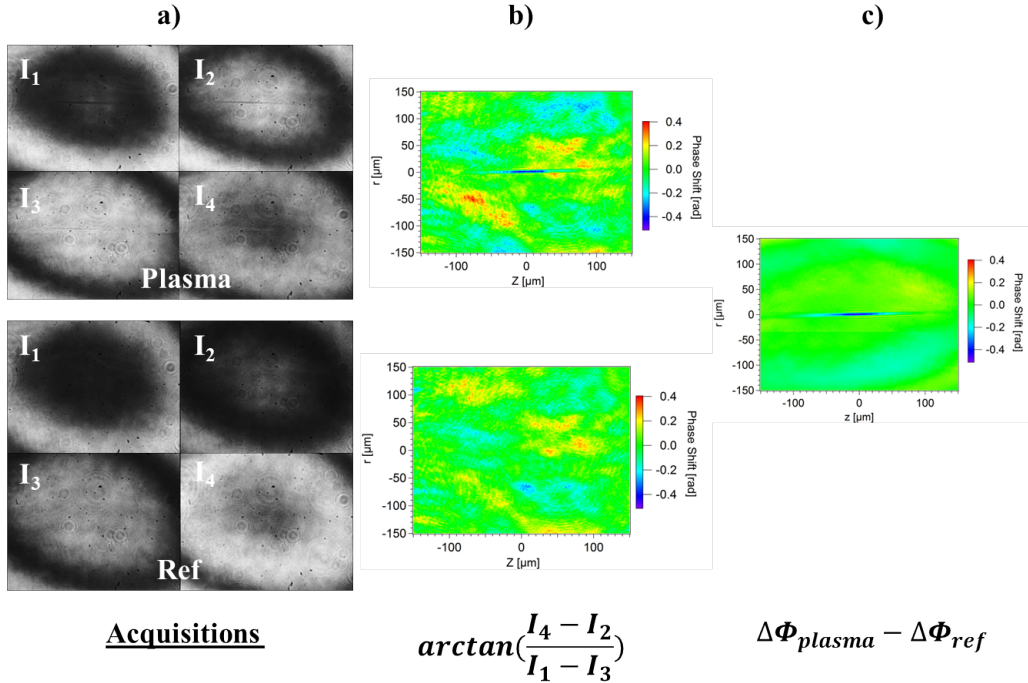


Figure 3.13 – Cleaning procedure for the phase-shift measurement. (a) Four-step procedure is applied with and without the pump beam, (b) the phase maps are reconstructed with equation 3.22 and (c) the subtraction of the maps with and without the plasma to get the phase shift.

obtain is shown in figure 3.13. First we perform the four-step procedure two times: one for the reference and one with the plasma. Then we apply equation 3.22 and the unwrapping procedure illustrated with figure 3.10. We see the same noise composed of dust and some diffraction patterns on the two maps. The final phase-shift map is the subtraction of the reference map to the map with the plasma. The phase image presents a better quality with a reduced noise.

The phase reproducibility has been estimated by performing 96 times the same phase-shift measurement with the same conditions (same energy, same depth, same delay between the pump and the probe) and automated procedures.

We report in figure 3.14 the phase profile for the same coordinates. We note a phase-shift measurement of $\Delta\phi_{average}=0.29$ rad with a standard deviation estimated at $\sigma=0.02$ rad on 96 acquisitions. The phase-shift measurement that we report are given within stability error (measurement fluctuations) of 7%. Measurements on the stability of the plasma have also been performed. In these experiments, we simply focus the pump inside Si and one thousand acquisitions are made on the same plasma. For that, the interferometry setup is used but the reference beam is blocked. Similarly to the phase measurement, we systematically subtract the plasma images by the reference determined before each measurement. As it is illustrated in figure 3.15, a cross-section is extracted at the same coordinate and we study the

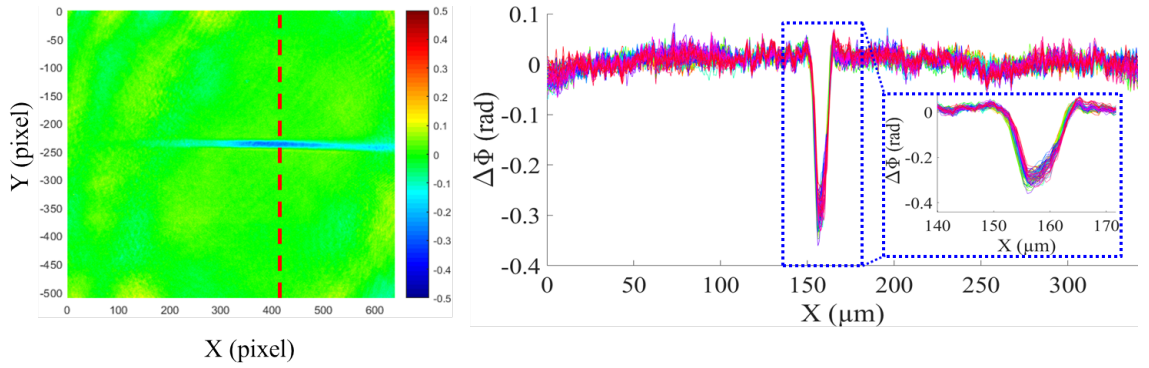


Figure 3.14 – Phase-shift measurement stability of the plasma for 96 acquisitions. The energy of the pump is constant and fixed at 15 nJ.

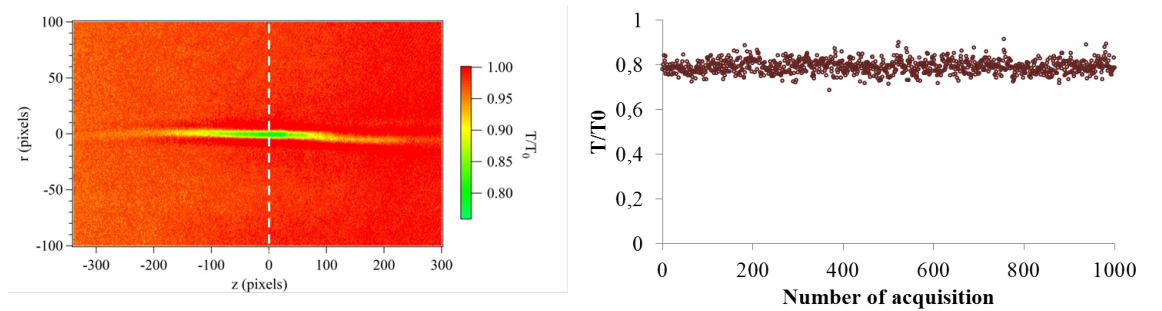


Figure 3.15 – Amplitude stability of the minimal transmission of the plasma for 1000 acquisitions. The energy of the pump is constant and fixed at 15 nJ.

stability of the minimum value of transmission. We obtain 3% of error on the value T_{min} . Finally, taking into account all our reproducibility measurements, we assume a typical 10% of potential error due to stability in all estimations obtained with our interferometry system.

3.2.3 Experimental results

The goal of adapting an interferometer on the pump-probe experiment is to study the excitation dynamics inside Si, induced by an intense pump. With this experimental method, we aim to determine the collision rate between electrons and phonons. In Si, only theoretical estimations of τ_c are published and are situated in the range 2.0-5.5 fs [103][104][92]. Since every numerical study of laser-Si interaction needs this collision time, it is a major issue to be able to compare an experimental evaluation of a physical parameter to the theory.

Figure 3.16 presents the amplitude and the phase for a 60 nJ-pulse focused inside the volume of Si. According to equations 3.18 and 3.19, we find at the geometrical focus: $\left\{ \begin{array}{l} T_{min} \approx 0.79 \\ \Delta\phi_{min} \approx -0.35 \end{array} \right\}$ giving $\left\{ \begin{array}{l} \tau_c \approx 2.05 \times 10^{-15} \text{ s} \\ N_e \approx 2.2 \times 10^{19} \text{ cm}^{-3} \end{array} \right\}$.

There is only one publication in which the phase change of the probe propagating through a plasma inside Si is studied [6]. They evaluate the change of refractive index due to the plasma and they find $\Delta n \approx -0.015$ for energies around 100 nJ. The phase shift that we determine in this section corresponds to $\Delta n \approx -0.02$ ($\Delta n = \Delta\Phi\lambda/2\pi d_{plasma}$, and taking $d_{plasma} = 3 \mu\text{m}$), meaning that our results are consistent with their findings.

Our interferometry set-up presents some limitations, and we can hardly report on the accuracy error on the collision time. This experiment gives a collision time inside Si of : $\tau_c \approx 2.0 \times 10^{-15} \text{ s}$. We are aware that the collision time can depend on the free-carrier density. This experiment has been performed with a level of excitation of $N_e \approx 10^{19} \text{ cm}^{-3}$ and we cannot vary significantly the electron density because of the sensitivity of the measurement. Below a few nJ, the plasma is not detected with the IR camera, meaning that we cannot study the evolution of this collision time depending on the free-carrier concentration. However, one must note that this study comforts us in the value taken for the collision time in section 3.1.2.

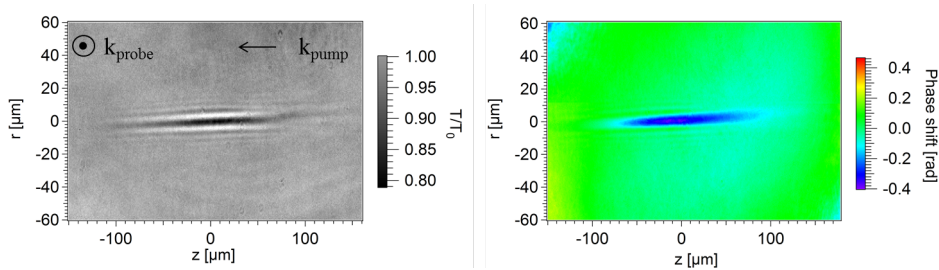


Figure 3.16 – Amplitude (left) and phase (right) measurements for Si. The laser is coming from the right with 60 nJ energy pulses. $z=0$ is the geometrical focus.

to calculate the free-carrier density with the Drude model. This electron collision frequency estimation is not accounting for its dependency on the electron density and electron energy which can be varying both in time and in space across the plasma string, being a limit to this investigation.

3.3 Conclusions

Regardless the amount of energy Si is irradiated with, no permanent modification is observed in the volume of Si even with high NA. Pump-probe infrared experiments have been performed in order to characterize the plasma inside crystalline and low-doped Si. We image a transient state assimilated to a plasma composed of free electrons generated by two-photon absorption by focusing very tightly the pump beam. We can fully describe its characteristics with a simple Drude model.

Studying the probe transmission has given more details on the interaction: the number of free-electrons generated by the pump excitation does not exceed $3 \times 10^{19} \text{ cm}^{-3}$, which is one order of magnitude below the critical density. We have first investigated a first hypothesis that may be responsible for this limitation: energy dissipation. The recombination time for free-carriers has been evaluated at $\tau_{eff}=2.5 \text{ ns}$ and the diffusion coefficient at $D_a=2.5 \text{ cm}^2/\text{s}$. The pump-probe experiment has permitted to exclude energy dissipation for the possible mechanisms explaining the saturation.

In order to have a full experimental overview on the plasma characteristics, we have combined an interferometry set-up to the plasma ultra-fast IR imaging arrangement. This experiment has given access to the coupling between the energy and the lattice, with a collision time $\tau_c \approx 2 \text{ fs}$, compared to a theoretical value of $\tau_c \approx 3 \text{ fs}$. This estimation of the collision time is the first attempt of experimental measurement for Si.

Since energy dissipation at the timescale of the pulse is not a limiting factor to the excitation, we must continue our investigations to understand why the optical breakdown is not reached in our experiments. A critical point can be a strong optical limitation of the energy transport inside Si. Knowing exactly the amount of energy that is delivered at the focus in these experiments would be helpful to understand better this limitation concerning the excitation.

Chapter 4

Ultra-fast energy deposition inside Si

Contents

4.1	3-D reconstruction of the beam propagation	69
4.1.1	Experimental context	69
4.1.1.1	Experimental set-up for ultra-fast beam imaging	69
4.1.1.2	Calibration in air and procedure to reconstruct the propagation of the beam	71
4.1.1.3	Propagation in air with increasing NAs	73
4.1.2	3-D reconstruction of the ultra-fast laser energy distributions inside Si	74
4.1.2.1	Procedure for the reconstruction	74
4.1.2.2	Results for NA=0.3	75
4.1.2.3	Influence of the NA on the beam propagation . .	78
4.1.2.4	Strict clamping of fluence delivered inside Si . .	79
4.1.3	Absorbed energy densities in bulk-Si	80
4.1.3.1	Laser flux absorbed in the region of the focal volume	81
4.1.3.2	Laser flux absorbed in a cone from the surface .	83
4.1.3.3	Validity of the beam imaging experiment: integrated energy balance	84
4.2	Numerical model for nonlinear propagation inside Si . .	86
4.2.1	Description of the model	86
4.2.2	Identification of the factors limiting the fluence delivery to the focus	89
4.2.2.1	Physical mechanisms included in the model . . .	89
4.2.2.2	Identification of the physical processes responsible for the clamping	90

4.2.2.3	Comparison between the experiments and the calculations	91
4.2.3	Comparison to the fluence threshold for surface modification	93
4.2.3.1	Methodology	93
4.2.3.2	Fluence threshold for surface damage of Si . . .	94
4.3	Conclusions	94

The impossibility to achieve permanent modifications inside the volume of Si in the ultra-fast regime has motivated a complete study of the beam propagation. So far, experiments have been performed in order to deliver the energy with a longer pulse duration [11], longer wavelengths [8] or with non-diffractive beams [73]. However, a limitation is systematically observed, especially concerning the free-carrier density generated in the bulk, being largely under the critical density of Si at 1.3 μm (as shown in the previous Chapter). The solutions to bypass this clamping seem experimentally complex, such as changes of the spatio-temporal characteristics of the beam, without any guarantee to induce successfully modifications in bulk-Si. Before thinking about a new strategy to modify the volume of Si, we need to understand the interaction in Si with ultra-short pulses.

In this Chapter, we concentrate on the beam propagation inside the material. We investigate how the micro-plasma revealed by the pump-probe imaging is generated. In order to understand why no permanent modification is observed, even at high energies, we image the beam propagation along the propagation axis to fully reconstruct the interaction inside Si [73, 108]. After a calibration in air, we determine the absolute peak fluence delivered inside the volume of Si. We also quantify the losses during the energy delivery to the focus. Then we try to optimize the energy delivery by increasing the NA to achieve the highest possible confinement of the interaction.

Besides, a collaboration with a Greek laboratory, IESL-FORTH (Institute of Electronic Structure and Laser, Foundation for Research and Technology) has been established to develop a model to simulate our experiments [9]. By adjusting the model parameters to fit the experimental data, we try to identify the physical processes involved in Si ionization. This complete study explains how an under-dense micro-plasma is formed by the beam and retro-acts on it. As this model retrieves the experimental data with a good agreement, it is a convenient tool to imagine new arrangements for our bulk-modification experiments.

4.1 3-D reconstruction of the beam propagation

4.1.1 Experimental context

We have experimentally demonstrated in the previous Chapter that the free-carrier density generated by TPA does not exceed $3.0 \times 10^{19} \text{ cm}^{-3}$, and seems limited by strong nonlinear effects in the prefocal region. To quantify the amount of energy which is delivered at the focus, we develop a set-up to image the beam profile in the Rayleigh zone, allowing to reconstruct in 3-D the fluence delivery along the propagation axis.

4.1.1.1 Experimental set-up for ultra-fast beam imaging

We develop an experimental set-up on ASUR facility, allowing us to image the propagation of the beam tightly focused (in air and in Si). One can directly image the propagation of the pulse inside the material, but nonlinear propagation effects induce

losses and distortions that need to be quantified. Without a precise calibration, the results can only be expressed with relative fluences or energies. For these reasons, we first perform this experiment in air and realize the calibration of our measurements. This calibration, presented in the next paragraph, allows us to quantify the absolute fluence which is delivered inside Si.

The experimental set-up is shown in figure 4.1. The pump (1300 nm at $\tau_{air} = 60$ fs) is focused with a microscope objective (MO) (LMPLN-IR/LCPLN-IR, Olympus). The MO is placed on a motorized stage providing a translation in the direction of the propagation axis, with a 4 μm -precision. The beam is imaged with a long-working distance objective in the IR-range (100X Mitutoyo Plan Apo NIR) with NA=0.7. Then a tube lens ($f'=200$ mm) refocuses the image on an IR camera (OWL SWIR 640, Raptor). This homemade microscope gives a 105X magnification (measured with a calibrated target). A long-pass filter (1200 nm cut-off) is placed at the exit of the imaging objective in order to avoid any parasitic signal. The time of exposure of the camera is set at 40 ms, corresponding to a measurement averaged over 4 laser shots. It contributes to reduce the effects of the peak-to-peak pulse energy fluctuations on the quality of the reconstructions. We note that we have verified that the beam pointing stability was good enough to allow a measurement averaged on 4 shots. We chose to move the focusing microscope objective of the pump beam, so that the plane imaged by the camera remains the same all along

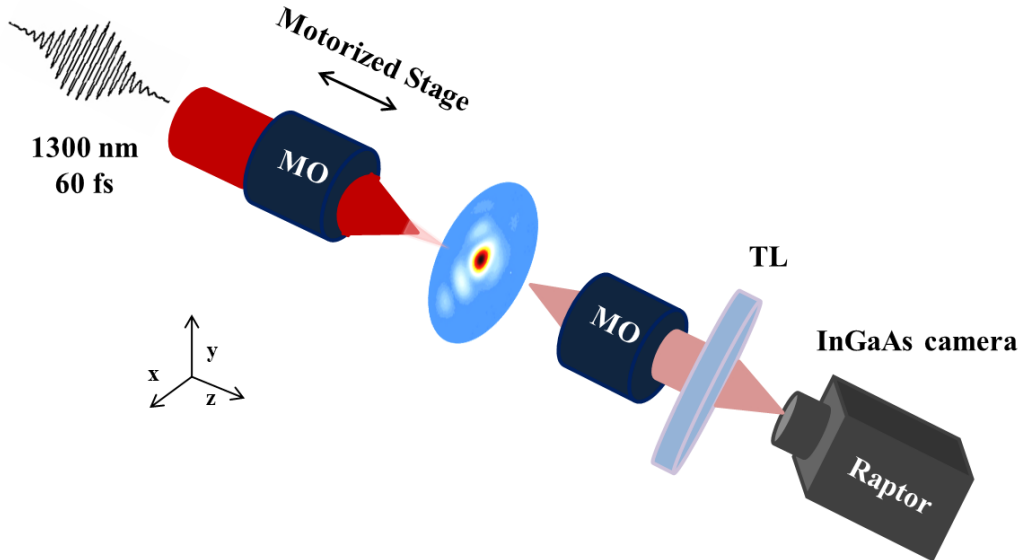


Figure 4.1 – Description of the beam imaging set-up. The pump (1300 nm-wavelength with a duration of 60 fs (FWHM)) is focused with a microscope objective (MO) in air, and is imaged by an IR microscope composed of a MO, an associated tube lens (TL) allowing 105X magnification on the IR camera.

the experiment. Another solution would have been to keep the microscope objective to focus the pump fixed, and to do the translation of the sample together with the imaging microscope. The experimental requirement is that the imaging microscope always images the same plane, and there must be only air between the object plane and the microscope. The beam profile is acquired every 500 nm.

4.1.1.2 Calibration in air and procedure to reconstruct the propagation of the beam

First, we should note that the calibration is valid due to several requirements:

- There is no aberration introduced by the imaging microscope system (IR-range optics).
- The response of the InGaAs camera is linear at 1.3 μm (which has been verified, not shown here).
- There is only air between the plane which is imaged and the microscope objective used for the imaging microscope (for real space images).
- For high pump energies, IR optical densities are installed after the microscope objective of the imaging microscope to avoid the saturation of the camera.
- The intensity is maintained below ionization or nonlinear propagation effects in air.

The experiment is realized in air at low laser flux ($E \approx 23$ pJ). This energy has been chosen to be well under the air ionization threshold, which is 10^{14} W/cm² [91]. Indeed, in the regime of intensities above the nonlinear ionization threshold of air, we expect energy losses during the propagation due to non-linear ionization. We need to avoid any losses during the propagation to assume that $E_{incoming} = E_{focus}$. In our case, the laser intensity does not exceed 10^9 W/cm², meaning that the fluence at the focus is the theoretical one without any losses.

A cross-section is taken at the center of the beam for every image. Then, we reconstruct the beam propagation by assembling all the line profiles, as described in figure 4.2. The scale of the reconstruction is first in pixel intensity, and the goal is to convert the scale into absolute delivered fluence (in J/cm²). For that, the experiment in air provides a calibration and the maximum value of pixel is attributed to the maximum fluence which is locally delivered.

Assuming the linear response of the camera at 1.3 μm and a low energy propagation, the incoming energy of the laser (measured with a Joulemeter), is proportional to the sum of the pixel amplitude, as illustrated in figure 4.3:

$$E_i \propto \sum_{i,j} P_{i,j} \quad (4.1)$$

We introduce the coefficient C , defined by:

$$C = \frac{E_i}{\sum_{i,j} P_{i,j}} \quad (4.2)$$

To obtain a fluence unit (J/cm^2), we must divide by the ratio between the maximum value of the pixel and the surface of the pixels:

$$F_{max,air} = \frac{C \times P_{max}}{S_{Pixel}} \quad (4.3)$$

where P_{max} is the maximal amplitude value of the pixels, and S_{Pixel} is the surface of one pixel. Accounting for the magnification of our measurement set-up, the surface of one pixel is $S_{pix} = (15 \times 10^{-4}/105)^2 \text{ cm}^2$. For the example shown in figure 4.3, the highest value of the pixels is 217. The input energy for this calibration is $E_i=26 \text{ pJ}$ so the peak fluence at the focus (corresponding to the maximum value of pixel) is

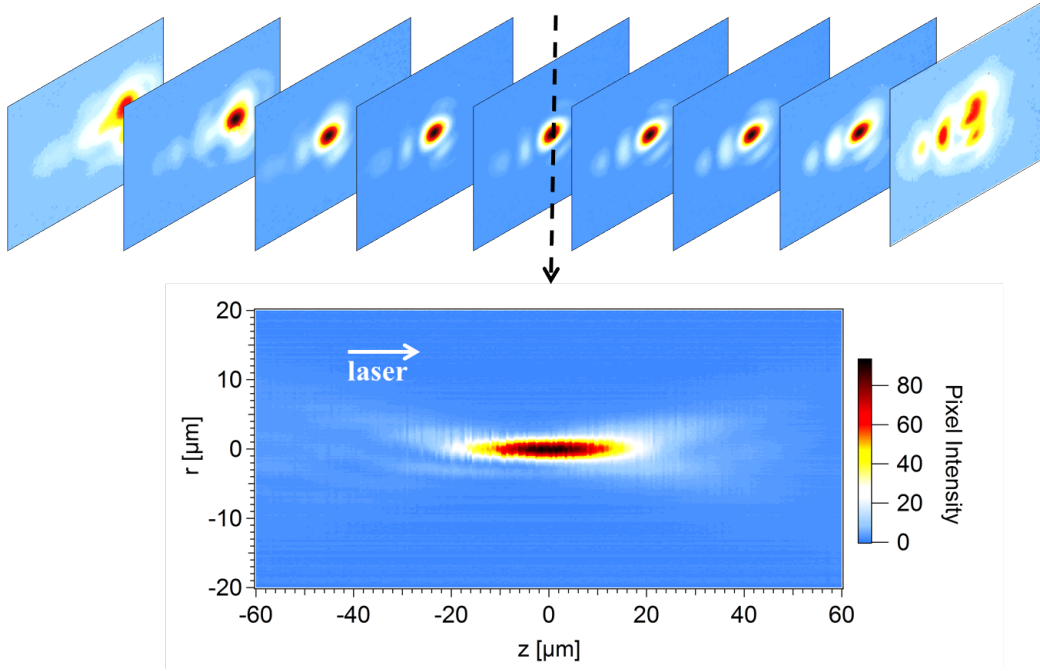


Figure 4.2 – Beam profiles acquired in air at low energy (26 pJ) for $\text{NA}=0.3$ (top). The reconstruction of the propagation (bottom) is all the cross-sections side by side.

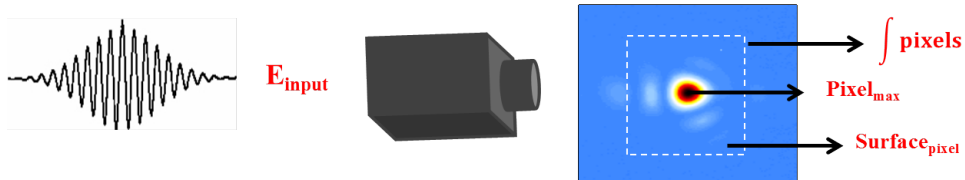


Figure 4.3 – Image of the beam taken at the focus of the propagation in air for $\text{NA}=0.3$. We extract from the image the sum of the pixels constituting the beam signal, the maximal value of the pixels, and the surface of the pixels.

$F_{max,air} = 5.4 \times 10^{-4} \text{ J/cm}^2$. We can finally convert the signal of each pixel to a local fluence with a simple rule of proportionality (equation 4.3), attributing a pixel value to a corresponding energy density.

4.1.1.3 Propagation in air with increasing NAs

The same experiment in air has been repeated for different NAs: 0.3, 0.45 and 0.65. A microscope objective with NA=0.85 is available but our beam imaging system provides NA=0.7, implying that we are unable to collect the pump signal focused with NA>0.7. We repeat exactly the same procedure: the energy is first measured with a Joulemeter, and is adjusted with calibrated optical densities to perform our reconstruction of the propagation of the beam without attenuation on the imaging microscope.

The maps of the 3-D reconstructions in absolute fluence are reported in figure 4.4 for NA=0.3 (top), NA=0.45 (middle) and NA=0.65 (bottom), and the curves on the right are the corresponding fluence profiles at the focus. The color scales in figure 4.4 are different because the three numerical apertures have not been tested at the same maximum fluence: the energy has been adjusted to be under the ionization threshold of air. The size of the collimated beam before the focusing objective is the same whereas the diameter of the entrance of the objective changes from one objective

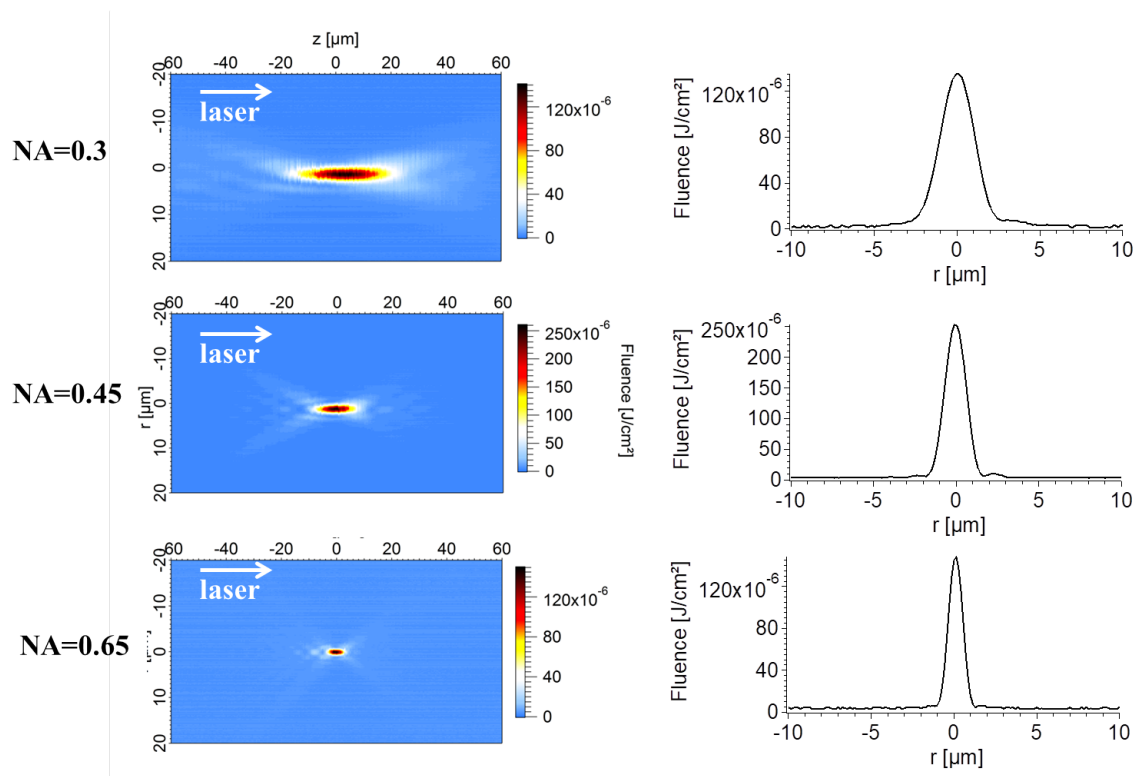


Figure 4.4 – Reconstruction of the beam propagation in air for NA=0.3 (top), NA=0.45 (middle) and NA=0.65 (bottom). At $z=0$, a line profile is taken to retrieve the beam diameter (right images).

Objective	NA	T(%)	E_{foc} (pJ)	Measured spot FWHM (μm)	Calculated spot FWHM (μm)
10X	0.3	63.4	26	2.4	2.36
20X	0.45	34.6	11.3	1.4	1.44
50X	0.65	7.7	2	1	1

Table 4.1 – Transmission of the different objectives and beam diameter at $1/e^2$ deduced from the beam profiles for NA=0.3, 0.45 and 0.65.

to another. That is why the transmission of the objectives has been experimentally determined at 1300 nm for our specific beam.

We deduce from the beam profile in figure 4.4 the beam diameter (at $1/e^2$) in table 4.1. We observe asymmetry along the propagation axis with NA=0.3. We characterized the beam of ASUR facility in Chapter 2 and we remind that the profile of the beam did not allow to determine a M^2 . We see with figure 4.4 that despite the difficulty we had to estimate the quality factor, the cross-sections at the focus present a Gaussian profile. The diffraction pattern before the focus for NA=0.45 and NA=0.65 is due to the oversized beam compared to the entrance diameter of the objectives. We have chosen to work with that diffraction pattern and not to adjust the beam for each objective since it does not represent any inconvenience to our study. To convert the maps in fluence unit (J/cm^2), the calibration procedure is systematically applied.

4.1.2 3-D reconstruction of the ultra-fast laser energy distributions inside Si

4.1.2.1 Procedure for the reconstruction

We repeat the experiment with Si, by focusing the pump at the rear face of a wafer (see figure 4.5). We choose a wafer of 1mm-thickness to compare the beam propagation imaging to our pump-probe experiments realized at 1 mm depth inside the Si samples. Imaging a plane inside Si would be affected by nonlinear propagation of the beam after it. By imaging the beam focused at the rear face of the wafer, we ensure that there is only air between the imaging microscope and the imaged plane. To ensure that we image the rear face, the wafer is illuminated with a white light source (Tungsten, THORLABS) and we image dusts at the two surfaces separated by $1\text{mm}/n_0=0.285$ mm with $n_0=3.5$ at 1.3 μm . We note that the Rayleigh zone in air is 40, 20 and 10 μm for NA=0.3, 0.45 and 0.65, respectively. This length is multiplied by the index of Si ($n_0=3.5$) for experiments at the rear face of the wafer. We no longer talk about the Rayleigh zone but we name it the interaction zone in the following sections. The length of scanning is 160 μm in air corresponding to 560 μm in Si. This scan area is smaller than the sample thickness, a requirement for proper reconstructions of the beam as it would be if it would have been focused in the bulk of Si (no influence of the front surface). We apply the same

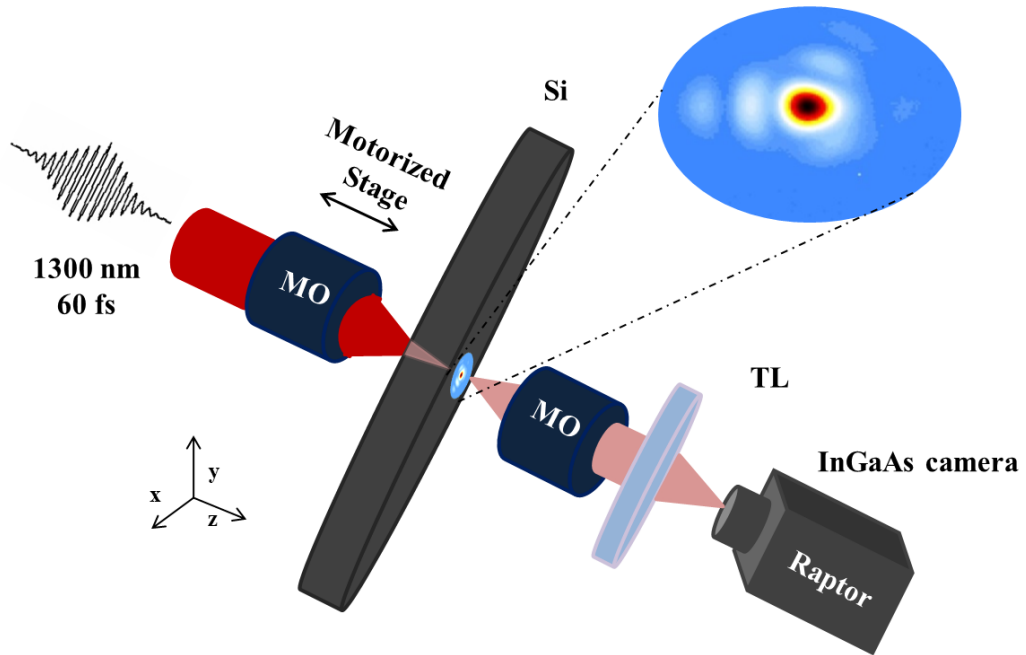


Figure 4.5 – Description of the beam imaging set-up. The pump is focused with a microscope objective (MO) at the rear face of a Si-wafer, and is imaged by an IR microscope composed of a MO, an associated tube lens (TL) allowing 105X magnification and an IR camera.

procedure as in air: we collect the images and we take a cross-section for every image.

In this study, the goal is to see if nonlinear propagation effects occur, and could explain the saturation of our under-dense plasma. For that, Si is irradiated with intensities starting from 10^{11} W/cm², which is above the threshold for two-photon ionization inside Si at $1.3 \mu\text{m}$ (2.0×10^{10} W/cm² [2]). As we have seen before, because of spectral dispersion of ultra-short pulses, the pulse duration is increased from 60 fs to 90 fs after 1 mm of propagation inside Si.

4.1.2.2 Results for NA=0.3

Figure 4.6 shows examples of the reconstruction of the beam propagation inside the wafer for NA=0.3. The fluence delivered at the focus increases for incoming energies varying from 15 nJ to 83 nJ, but saturates for 345 nJ (figure 4.6). Intermediate energies have been studied to compare with more details the difference between the energy delivered and the incoming one (see Section 4.1.3.). We also observe that the geometrical focus moves towards the prefocal region. Similar observations have been noticed for the pump-probe plasma in section 3.1.1., confirming nonlinear propagation inside Si. It is not surprising to observe a shift of the focus, since the laser power ($P_{las} \geq 100$ kW) largely exceeds the critical power for self-focusing ($P_{cr}=24$ kW).

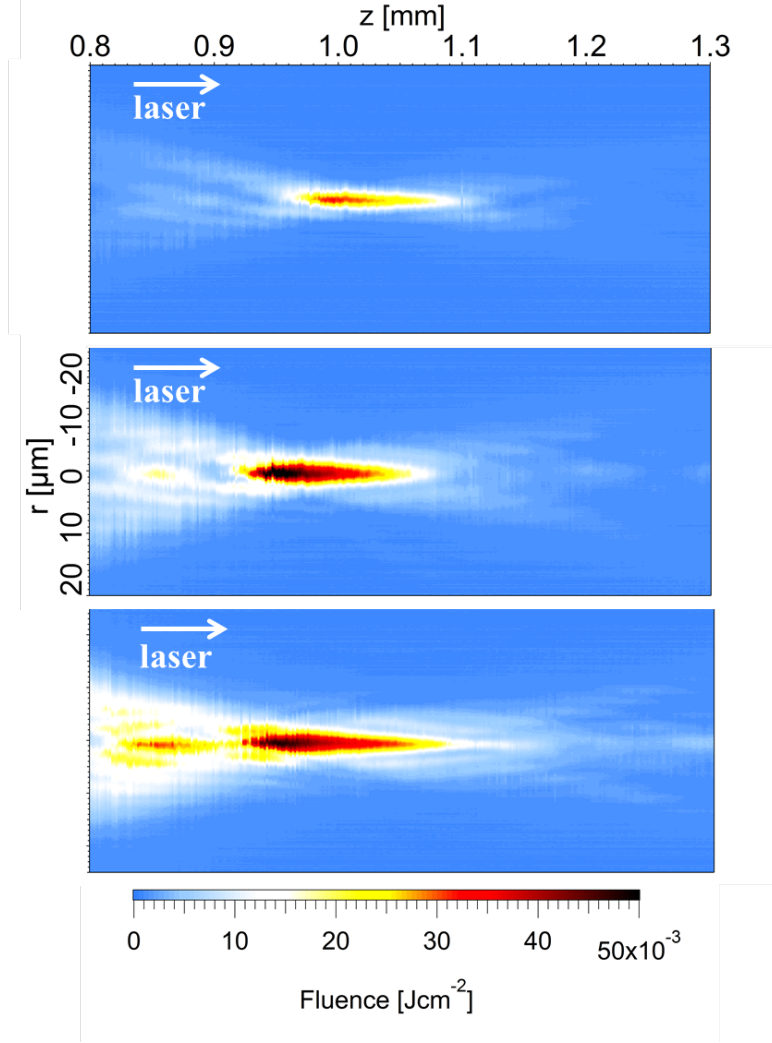


Figure 4.6 – Reconstruction of the beam propagation in Si for NA=0.3 at 15 nJ (top), 83 nJ (middle) and 345 nJ (bottom). The geometrical focus is located at $z=1$ mm.

We estimated the free-carrier density generated inside the material with the pump-probe experiment, implying some hypothesis such as a cylindrical and a homogenous plasma. With this beam imaging experiment, we know the fluence that is delivered at the focus, and we can evaluate theoretically the free-carrier density generated by our Gaussian pulse.

Assuming that one electron is generated by the absorption of two photons because of the predominance of TPA on the electronic avalanche on our range of excitation [42], the evolution of the number of electrons with time follows the equation:

$$\frac{dN_e}{dt} = \frac{\beta_2}{2\hbar\omega} I^2(t) - \frac{N_e}{\tau_{eff}} \quad (4.4)$$

The right part of this equation describes the evolution of the number of electrons by two photon ionization using the two-photon absorption coefficient $\beta_2 \approx 0.8 \times 10^{-11}$ m/W

[109], $\hbar = 1.05 \times 10^{-34}$ J.s, and $\omega = 2c\pi/\lambda$. Electron-hole recombination is expressed with the last term. Taking a constant time $\tau_{eff}=2.5$ ns as determined in section 3, this recombination can be neglected to estimate the maximum free-carrier density at the end of the pulse because $\tau_{eff} \gg \tau_{pulse}$.

$$N_e(t) = \frac{\beta_2}{2\hbar\omega} \int (I^2(t)dt) \quad (4.5)$$

$I(t)$, characterized by I_0 (figure 4.7), has a Gaussian shape:

$$I(t) = I_0 e^{-4 \ln(2) \frac{(t-t_{max})^2}{FWHM^2}} \quad (4.6)$$

Then,

$$F(t) = \int (I(t)dt) \quad (4.7)$$

$$F(t) = I_0 \int (e^{-4 \ln(2) \frac{(t-t_{max})^2}{FWHM^2}} dt) \quad (4.8)$$

$$I_0 = \frac{F(t)}{\int (e^{-4 \ln(2) \frac{(t-t_{max})^2}{FWHM^2}} dt)} \quad (4.9)$$

Finally we can resolve the electronic density equation (4.5):

$$N_e(t) = \frac{\beta_2}{2\hbar\omega} \int \left(\frac{F(t)}{\int (e^{-4 \ln(2) \frac{(t-t_{max})^2}{FWHM^2}} dt)} e^{-4 \ln(2) \frac{(t-t_{max})^2}{FWHM^2}} \right)^2 dt \quad (4.10)$$

With our beam propagation study, we know the exact integrated fluence at the focus and therefore we can evaluate the electronic density N_e . Considering a 50 nJ pulse focused with NA=0.3, we find: $N_{emax} = 2.0 \times 10^{19}$ cm⁻³. In our pump-probe experiment, the free-carrier density has been estimated with the Drude model and the Beer-Lambert law, giving a maximal electronic density $N_{emax,Drude} =$

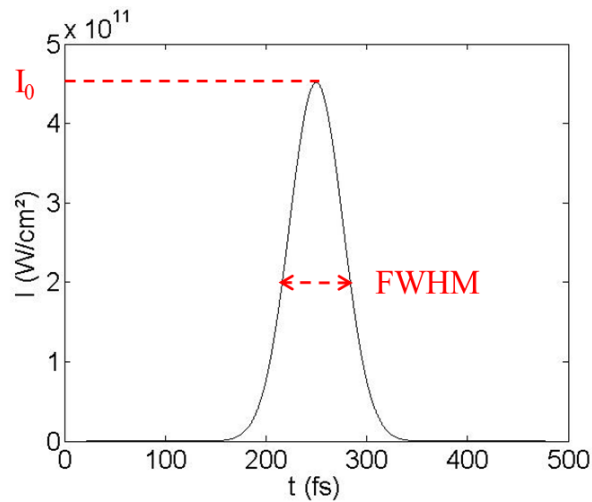


Figure 4.7 – Gaussian pulse defined by its maximal intensity I_0 and FWHM.

$3.0 \times 10^{19} \text{ cm}^{-3}$. The good agreement between these two different measurements confirms the level of saturation of the electronic density generated and the accuracy of our measurements.

The saturation of the generation of free-carriers observed with the pump-probe experiment at NA=0.3 is reached after a few tens of nJ. In our reconstruction of the beam propagation, a large range of incoming energies have been studied from a low excitation level, 15 nJ, corresponding to:

$$\begin{cases} F_{focus} = 0.032 \text{ J/cm}^2 \text{ (figure 4.6)} \\ N_e = 1.0 \times 10^{19} \text{ cm}^{-3} \text{ (equation 4.10)} \end{cases}$$

to a level where the saturation is fully established (≥ 30 nJ), corresponding to:

$$\begin{cases} F_{focus} = 0.05 \text{ J/cm}^2 \text{ (figure 4.6)} \\ N_e = 2.0 \times 10^{19} \text{ cm}^{-3} \text{ (equation 4.10)} \end{cases}$$

We compare the fluence delivered to the focus to the theoretical average fluence (without any losses): $F_{theory} = E_i / \pi w_0^2$. For an incoming energy $E_i = 15$ nJ, we find a theoretical fluence $F_{theory} = 0.24 \text{ J/cm}^2$, which is more than 13 times higher than the experimental results. Then, for $E_i = 30$ nJ, the theoretical delivered fluence is $F_{theory} = 0.48 \text{ J/cm}^2$, being 10 times higher than the experimental one.

The beam propagation reconstruction in figure 4.6 confirms that a strict optical limitation related to the fluence delivery at the focus is happening when our ultra-fast laser beam propagates inside the material. We also note that strong prefocal interaction is taking place at high energies, that can reasonably be attributed to two-photon absorption.

4.1.2.3 Influence of the NA on the beam propagation

In order to limit the influence of nonlinear effects and then to improve the efficiency of the energy transport, a solution is to reduce the length on which they develop. Consequently, we increase the NA of the focusing optics.

The reconstructions of the beam propagation for NA=0.45 and NA=0.65 are presented in figure 4.8. Images a) b) and c) are the reconstructions of the beam propagation with NA=0.45, and d), e) and f) describe NA=0.65. The range of incoming energy studied is similar to figure 4.6. The results concerning the saturation of the fluence delivered to the focus are also similar: this fluence does not increase with the energy after a few tens of nJ. However, this level of clamping seems to be higher compared to NA=0.3. Moreover, we observe that the interaction in the prefocal zone has decreased, reducing the losses before the focus. The shift of the focus prior to the prefocal region is minimized at high NAs, which is consistent with the decrease of the nonlinear effects with high NAs. For NA=0.45 at high energies, the intense zone in the prefocal region is attributed to the diffraction pattern before the focus (figure 4.8). The incoming energy was not high enough to observe the same consequence for NA=0.65. We observe a slight improvement of the confinement of

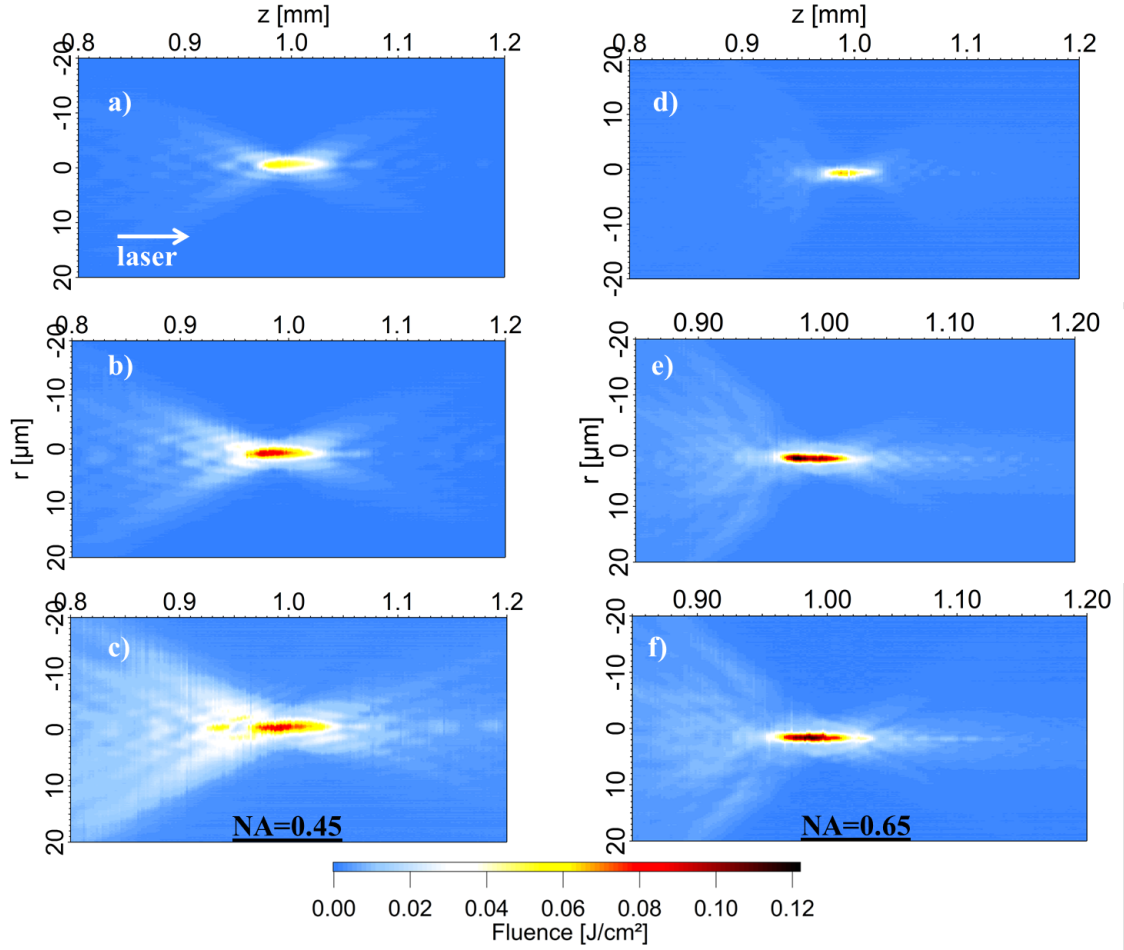


Figure 4.8 – Reconstruction of the beam propagation in air for NA=0.45 at a)12 nJ, b)35 nJ and c)260 nJ; NA=0.65 at d)11 nJ, e)80 nJ and f)240 nJ The geometrical focus is $z=1$ mm.

the interaction from NA=0.45 to NA=0.65. According to the propagation results (figure 4.8), increasing the NA clearly improves the efficiency of the energy delivery to the focus.

4.1.2.4 Strict clamping of fluence delivered inside Si

We report in figure 4.9 the peak fluence as a function of the incoming energy for the three different NAs studied. The fluence delivered at the focus increases with the NA, confirming that the critical point in our study is the transport of the beam energy up to the focus. For NA=0.3, 0.45 and 0.65 the peak fluences that can be delivered to the focus are 0.05, 0.10 and 0.12 J/cm², respectively. Resolving the free electron equation (equation 4.10) with the highest fluence ($F_{max}=0.12$ J/cm²), the highest density of electrons is $N_{e,max} = 2.0 \times 10^{20}$ cm⁻³ which is below the critical density ($N_c = 6.6 \times 10^{20}$ cm⁻³).

This is consistent with the absence of breakdown induced inside the material for all these cases. To summarize the different limitations observed with increasing NAs,

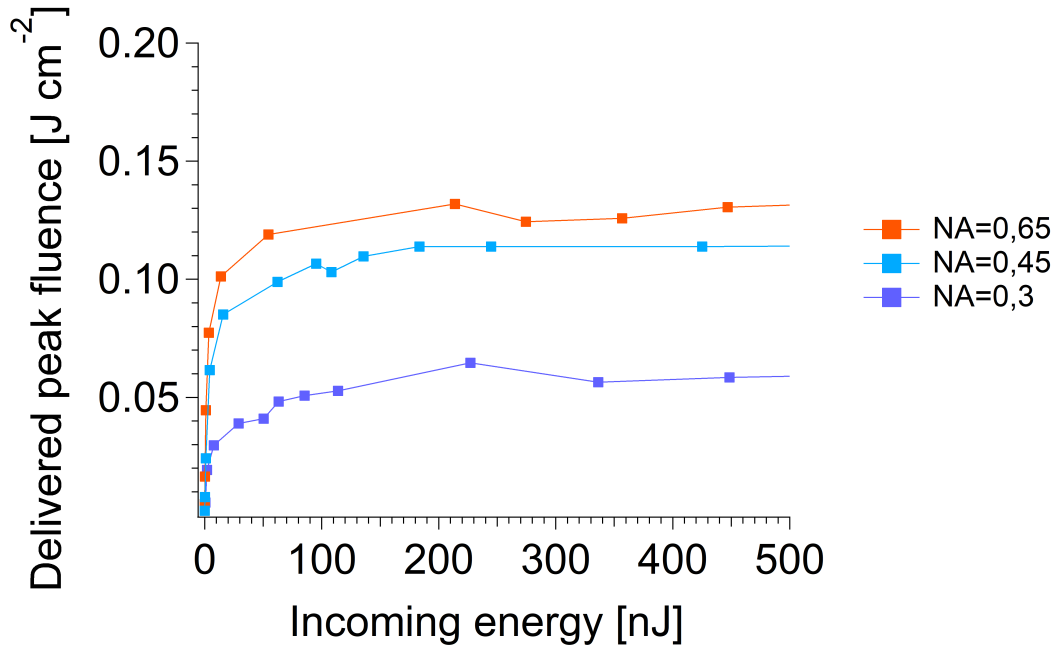


Figure 4.9 – Saturation of the peak fluence as a function of the incoming energy for NA=0.3, NA=0.45 and NA=0.65.

Table 4.2 reports the different results as a function of the numerical aperture. When the pump energy is in the range where the interaction saturates, the free-carrier density reaches a level approaching the critical density (Table 4.2).

4.1.3 Absorbed energy densities in bulk-Si

In order to estimate how far we are from inducing permanent changes in our experiment, we use two criteria generally taken into account for dielectrics. Both criteria have been introduced in Chapter 1. One is based on the electron and hole density: $N_e \geq N_c$ [36]. The second one relates to the absorbed energy density: $E_{abs} \geq E_{fus}$. In the literature, to reach the melting point inside the material, the absorbed energy density has to be the sum of the energy needed to reach $T_{melting}$ and the enthalpy of fusion [3]. The temperature of the material increases from T (at room Temperature) to $T_{melting}$ (1400° for Si). In this paragraph, we focus on the energy density for fusion inside Si, $\Delta(E_{fus})=5 \text{ kJ/cm}^3$ [110]. The energy absorbed inside the material can be determined with several methods. Here we compare the energy absorbed deduced from the beam propagation imaging set-up with the energy deduced from an inte-

Objective	NA	F_{max} in J/cm ²	N_{emax} in cm ⁻³
10X	0.3	0.05	2.0×10^{19}
20X	0.45	0.10	1.1×10^{20}
50X	0.65	0.12	2.0×10^{20}

Table 4.2 – Maximal electronic density generated at the focus for different NAs.

grated energy balance. In this section, we focus the investigations on NA=0.3. The goal is also to estimate the absorption volume to calculate precisely the density of absorbed energy. However, this is an unknown parameter of our experiment. We try in this section to give only a range of values for this volume of absorption, and also to think about the possible geometry of this volume.

4.1.3.1 Laser flux absorbed in the region of the focal volume

First, we can imagine that the zone of interaction (where the beam imaging reveals a density of free-carriers) is the zone where the laser energy is absorbed. It leads to consider a cylinder as the absorption volume, where the length of this cylinder is deduced from figure 4.6. This is the lower case of the volume for the estimation of the absorbed energy density.

From the ultra-fast beam imaging results (still figure 4.6), we can calculate an absorbed energy density by determining the energy delivered to the focus, plane after plane. For a given beam profile (at every coordinate), the energy of the pulse is defined by:

$$E_{pulse} = C \times P_{av} \times \sum_{i,j} P_{i,j} \quad (4.11)$$

where C is the coefficient introduced in equation 4.2, P_{av} is the average value of the pixels summed up on $\sum_{i,j} P_{i,j}$.

The losses in the prefocal zone are calculated with equation 4.11. The nonlinear effects during the propagation of a laser beam obviously increase with the intensity.

Nonlinear propagation effects induce losses that can be directly shown with figure 4.10 reporting the pulse energy as a function of propagation distance. For example, a pulse with $E_i = 15$ nJ leads only to $E_{foc} = 9$ nJ at the focus, undergoing 40% of losses, whereas a 952 nJ-pulse presents 96% of losses. We can deduce from figure 4.10 the energy density absorbed, and compare it to the enthalpy of fusion for the

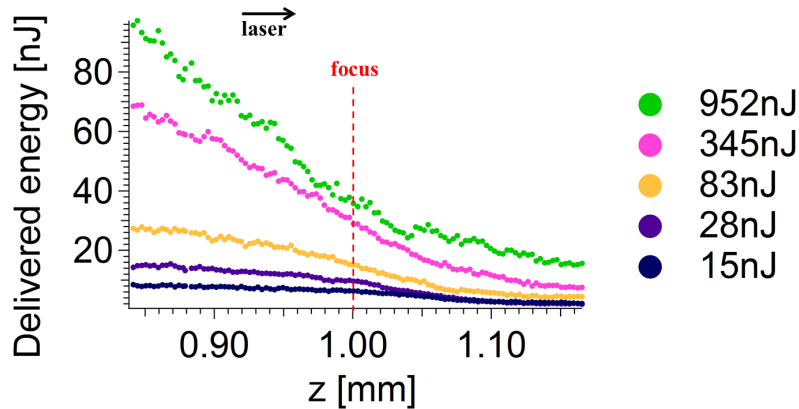


Figure 4.10 – Energy delivered on each plane which has been imaged along the z-axis for different incoming energies at NA=0.3. The geometrical focus is at z=1 mm.

different incoming energies. The density of energy absorbed inside the material is the difference between the incoming energy and the transmitted one, divided by the interaction volume. We consider that 100 μm after the focus (see figure 4.6), the volume of absorption ends. As a consequence, at the coordinate $z=1\text{ mm}$, we deduce $E_{delivered}$ and we calculate $E_{abs} = E_i - E_{delivered}$. One can note that E_i takes into account the reflected signal ($E_i=0.7 \times E_{laser}$). We verify this assumption in section 4.1.4. To convert the energy at $z=1.1\text{ mm}$ extracted from figure 4.10 in J to an energy density in J/mol we simply calculate (considering a uniform energy deposition):

$$\Delta(E_{exp}) = \frac{E_{del} \times M_{Si}}{V \times \rho_{Si}} \quad (4.12)$$

with $M_{Si}=28.01\text{ g/mol}$ the molar mass of Si, V the volume of the interaction in cm^3 , and $\rho_{Si}=2.33\text{ g/cm}^3$ the density of Si. To calculate this energy density which is absorbed inside the material, the critical parameter is then the volume of absorption.

We first make the hypothesis that the energy is absorbed only along the interaction zone approximated with a cylinder, being easily determined with figure 4.6. We expect that this volume of absorption is under-estimated: indeed, the graph of the delivered energy along the z coordinate (see figure 4.6) shows losses before reaching the focus which indicates that a huge absorption may begin far away from the geometrical focus. However, we calculate first the absorbed energy density corresponding the volume revealed by the 3-D reconstruction of the propagation of the beam. The volume is calculated under the cylindrical symmetry with $V = \pi w_0^2 L$ where w_0 is the beam waist and L is the length of the cylinder.

Table 4.3 shows the different energy densities calculated with equation 4.12, according to figure 4.10. The density of energy that contributes to the generation of the electronic density is less than 3% of the enthalpy of fusion of Si, as reported in Table 4.3. These calculations have been made taking into account the energy in the interaction zone, where the interaction takes place. As expected, these calculations may over-estimate the density of absorbed energy because the volume considered is smaller than the real volume of absorption.

In reality, the energy is absorbed in a huge volume. The critical point is to

E_i (nJ)	E_{abs} (nJ)	L (cm)	V (cm^3)	$\Delta(E_{exp})$ (J/cm^3)	$\frac{\Delta(E_{exp})}{\Delta(E_{fus})}$
15	13	$150 \cdot 10^{-4}$	$3.7 \cdot 10^{-9}$	3.5	0.8×10^{-3}
28	26	$150 \cdot 10^{-4}$	$3.7 \cdot 10^{-9}$	7	1.6×10^{-3}
83	78	$190 \cdot 10^{-4}$	$4.7 \cdot 10^{-9}$	16	4.0×10^{-3}
345	334	$250 \cdot 10^{-4}$	$6.2 \cdot 10^{-9}$	53	0.012
952	932	$350 \cdot 10^{-4}$	$8.6 \cdot 10^{-9}$	108	0.025

Table 4.3 – Estimations of the density of energy $\Delta(E_{exp})$ absorbed in a volume V for different incoming energies E_i at $\text{NA}=0.3$.

estimate from which z-coordinate the absorption begins. Pump-probe experiments in Chapter 3 have revealed an electronic density yielding to a density of absorbed energy of 9 J/cm^3 . With the calculations in Table 4.3, we obtain for the highest incoming energy an absorbed energy of 108 J/cm^3 , which is 12 times higher than for the pump-probe results, meaning that we may under-estimate the volume of absorption during the interaction, in reality not restricted to the high intensity zone. One can note that even for the highest incoming energy leading to a density of absorbed energy equal to 108 J/cm^3 , it is still below the melting threshold ($\Delta E_{fus}=5 \text{ kJ/cm}^3$ [4]).

4.1.3.2 Laser flux absorbed in a cone from the surface

In the previous paragraph, we have taken into account a small volume of absorption described by a cylinder whose length was the equivalent of the high intensity zone found inside Si. This hypothesis appears to be not relevant since it leads to high energy density absorbed found in comparison to the pump-probe results in Chapter 3. The only possibility to better estimate the absorbed energy density is to take into account a volume of absorption more important. Let us take the upper case: a volume with the geometry of a cone, starting from the surface, as shown in figure 4.11.

We calculate the cone of absorption from the surface to the focus (see figure 4.11), taking into account the $\text{NA}=0.3$ focusing the beam with an angle θ defined by: $\text{NA}=n_{\text{Si}} \sin(\theta)$. In our case, the half-angle defining the cone of focusing is only $\theta=4.5^\circ$. The radius of the beam entering Si 1 mm before the focus is then $r=\tan(\theta) = 80 \mu\text{m}$. Under the assumption of an uniform energy deposition in this cone, the volume where the absorption takes place is defined by:

$$V_{abs} = \frac{1}{3}\pi r^2 z \quad (4.13)$$

We obtain a significant volume of absorption compared to the volume calculated taking the interaction zone as shown in table 4.3. With our new considerations,

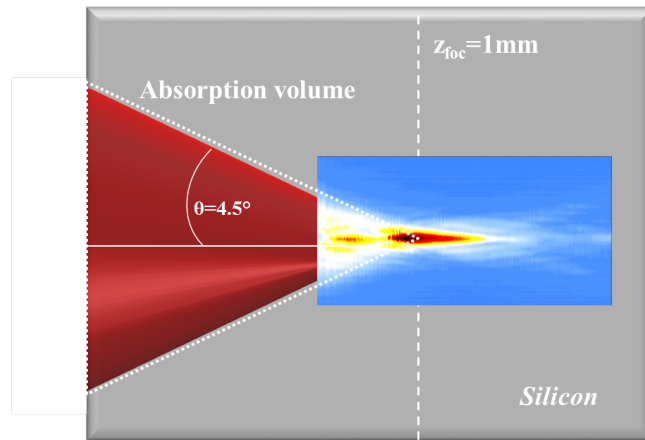


Figure 4.11 – Volume of energy absorbed from the surface for $\text{NA}=0.3$. The front face is at $z=0$, and the focus is at $z=1 \text{ mm}$.

$V=6.4\times 10^{-6}$ cm³. The density of energy absorbed from the surface (calculated under the hypothesis of an uniform energy deposition inside the cone) is $\Delta(E_{exp}) = 1.8$ J/mol = 0.14 J/cm³ (equation 4.12). This value of the absorbed energy is low compared to the one found by pump-probe imaging (9 J/cm³). We have first considered the energy delivery along the interaction zone in figure 4.6, which leads to overestimate the absorbed energy. Then we assume that the volume of absorption is a cone starting from the surface of Si, which leads to underestimate the absorbed energy density.

4.1.3.3 Validity of the beam imaging experiment: integrated energy balance

To verify the validity of our beam imaging experiment and the way we calculated the energy absorbed inside Si, we have also performed integrated energy balance measurements as illustrated in figure 4.12. It relies on the beam energy measurement before and after the sample. The energy balance is described by the following formula:

$$E_{abs} = E_i \times (1 - R - T) \quad (4.14)$$

where R and T are the reflection and transmission of the sample, respectively. At low intensity, when there is no absorption of the laser energy, the losses induced by the reflections at the interfaces of Si are calculated with the reflectivity of Si [42]:

$$T_0 = (1 - R)^2 + R^2 \times (1 - R)^2 + R^4 \times (1 - R)^2 \dots \quad (4.15)$$

where R is the reflection coefficient that is $R=0.30$ at 1.3 μm . Taking into account losses at the interfaces, the initial transmission is $T_0=0.53$.

The set-up is presented in figure 4.12. We use an integrating sphere (IS) to monitor the reflection from the incoming beam (reference signal) on a microscope slide. The sphere operates in the range of wavelength 0.7-2.5 μm . We record the incident signal with a calibrated photodiode (Pd₁), and the transmitted signal is collected with (Pd₂). The transmitted signal is low (in the nJ range), we cannot use an integrating sphere behind the sample. We collect and refocus the transmitted beam to have enough signal on the photodiode (InGaAs detector, DET10C).

The transmitted signal is reported in figure 4.13, for an incident energy from 1 to 600 nJ. At low energy, the transmission is equal to 0.53, which corresponds to the losses induced by silicon-air interfaces, as described by equation 4.15. At higher energies, nonlinear ionization takes place and induces losses of the incoming beam energy. The curve saturates at $T=0.9$, meaning that almost all the incoming energy is absorbed.

We report the absorbed energy from the two methods we employed: the energy balance, and the beam imaging. We compare the two methods to determine E_{abs} in figure 4.14. The values calculated with equation 4.14 (blue triangles) are compared to the value from the beam imaging study (green circles). The superposition of our

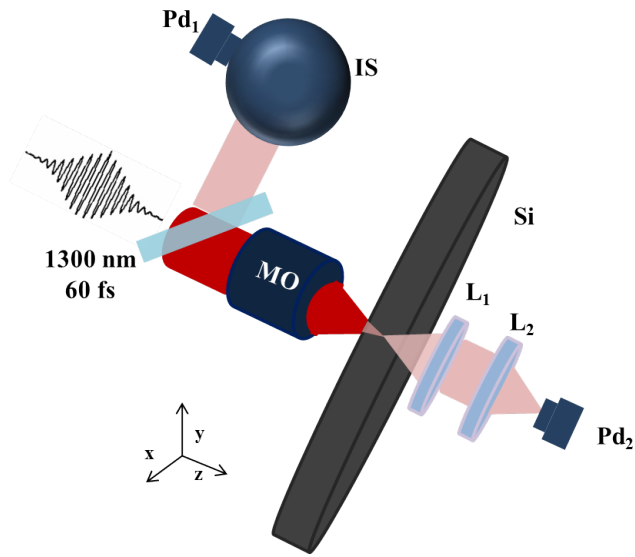


Figure 4.12 – Experimental set-up for energy balance inside Si with $NA=0.3$. The incoming energy is measured with a photodiode (Pd_1) combined with an integrating sphere (IS) and the transmitted beam is collected and refocused with L_1 and L_2 on a second photodiode (Pd_2).

two measurements shows identical results obtained with two different methods. The results also demonstrate how important is the absorption inside Si: almost all the incoming energy is absorbed inside the material, without inducing any damage.

The simple estimations of the volume of absorption show that the energy is delivered on a significant volume not restricted to the equivalent Rayleigh zone in Si. We may wonder about the uniformity of the laser energy deposition because of hot spots generated by diffraction, or aberrations. Such considerations help us to understand that the confinement of the interaction is one of the key parameters to succeed in inducing permanent modifications inside Si. The beam imaging study contains more information than the energy balance (since the energy balance is an

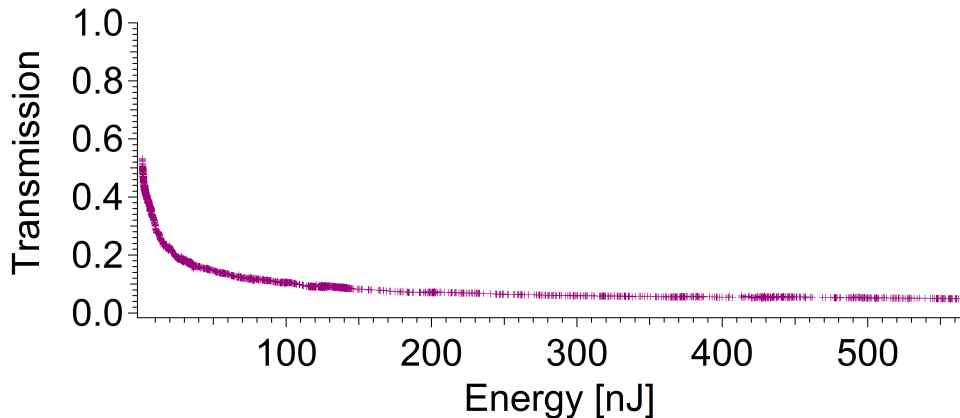


Figure 4.13 – Transmitted signal collected after the wafer of Si.

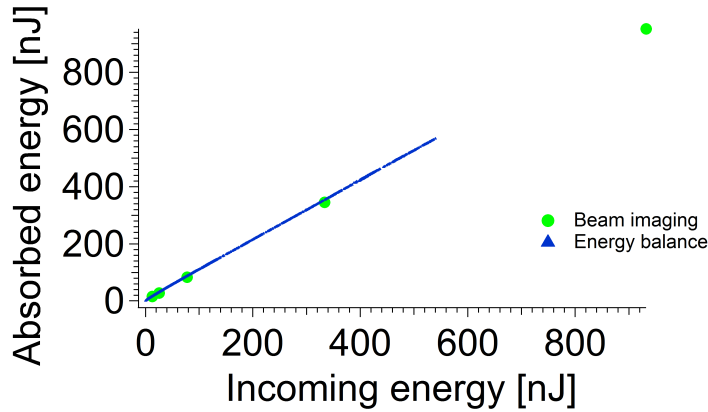


Figure 4.14 – Energy absorbed (in nJ) determined with two methods: the imaging set-up (green) and the energy balance with the photodiodes (blue).

integrated measurement) but the imaging method requires more verifications. As the two results of the absorbed energy are similar, it confirms the validity of the results presented for the beam imaging study.

4.2 Numerical model for nonlinear propagation inside Si

The experimental study of the beam propagation inside Si highlights the difficulty to confine the pulse energy, mainly because of strong nonlinear effects such as TPA before the focus (see Chapter 1). We turn to a nonlinear propagation model to identify the mechanisms involved in the clamping, and to investigate solutions that are experimentally complex. Because of the high refractive index of Si and the use of high NAs, only a numerical model valid for non-paraxial interaction can highlight the physical mechanisms involved in the clamping of the fluence delivery. A small number of publications has investigated vectorial and non-paraxial simulations, but they are extremely complex and computational time consuming [111, 112, 113, 114, 115]. In this section we introduce a model using scalar equations. These calculations have been developed by IESL-FORTH in the framework of a bilateral collaboration. This modeling allows us to highlight the peculiarities of the beam propagation in Si and to help in interpreting our experimental results. This numerical tool is also an efficient way to imagine new experimental arrangements that would lead to the optical breakdown of Si.

4.2.1 Description of the model

The main idea of this model is to transform the non-paraxial problem into an equivalent problem in a solid with a higher refractive index. The parabolic phase of the initial field is located in a plane perpendicular to the propagation direction. The field of a tightly focused beam is distributed on a curved plane, and needs to be flatter for our calculations. In focusing conditions with high NA and in ionized

transparent media, the nonparaxial nature of the problem needs vectorial equations, being the use of Maxwell solvers [116]. However, a medium with high refractive index makes the propagation paraxial (due to refraction inside the material) and the use of scalar equations is possible. In practice, the method assumes an equivalent medium with a rescaled refractive index n_s :

$$n_s = sn \quad (4.16)$$

with s the scaling factor.

We show in figure 4.15 that the wavefront curvature of the incoming beam can be reduced. Above a certain scaling factor s the phase is flattened enough to apply the scalar wave equations. We can calculate the distance z_a , being the distance between the edge of the spherical surface and the plane $z=0$. According to the schematics of figure 4.15, $z_a = f(1 - \cos(\theta))$. Since NA is defined by $NA = n \sin(\theta) = n \frac{a}{f}$, by combining to equation 4.16 we obtain:

$$z_a = a \frac{sn}{NA} \left(1 - \sqrt{1 - \frac{NA^2}{(sn)^2}}\right) \quad (4.17)$$

The use of scalar wave equation becomes inexact when z_a exceeds the confocal parameter [115], which would limit the use of scalar equations in the simulations to $NA \approx 0.2$. However, we consider stronger conditions: $z_a \approx \lambda$. We obtain:

$$s = \frac{NA}{n} \frac{a^2 + \lambda^2}{2a\lambda} \quad (4.18)$$

For $NA=1$, $a=1$ mm and $\lambda=800$ nm, we calculate the scaling factor $s=625$. To be above this limit we use $s=1000$. The validity of the method has been verified in the case of the linear propagation of a pulse with $NA=0.3$ (not shown here). The simulations show that by taking $s=1000$, the intensity distribution fits with a perfect agreement the vectorial theory, compared to $s=1$ (without the calculation trick) where the beam is strongly distorted. For $NA=1$ (not shown here), less than one wavelength differentiates the theoretical and simulated intensity distributions.

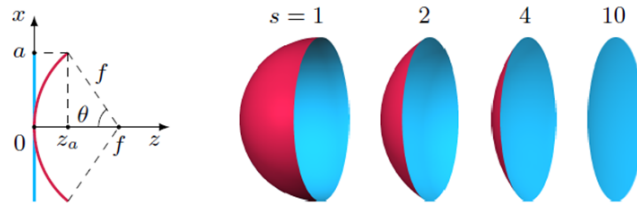


Figure 4.15 – Schematics of the transformation principle: the initial strong curved wavefront becomes flatter and the nonparaxial propagation becomes close to a paraxial by increasing the factor s . f is the focal distance, a is the radius of the focusing objective's aperture, and θ is the half-angle of the maximum cone of light. Figure from [9].

Now we turn to nonlinear propagation in silicon. The results obtained with the model will be compared to the experiments performed in the previous section. One can note that there is no theoretical comparison available on the literature. We use the Unidirectional Pulse Propagation Equation (UPPE) [117] (Non linear Schrödinger equation) taking the following form:

$$\frac{\delta \hat{E}}{\delta z} = ik_z \hat{E} + i \frac{\mu_0 \mu \omega^2}{2k_z} \hat{N} \quad (4.19)$$

where $\hat{E} = \hat{E}(\omega, k_x, k_y, z)$ the spatio-temporal spectrum of the laser pulse, $k_z = [k^2(\omega) - k_x^2 - k_y^2]^{1/2}$ is the propagation constant, k_x, k_y and ω are the spatial and angular frequencies, μ and μ_0 are the permeability of the medium and of the vacuum, respectively. The right term of equation 4.19 \hat{N} includes the third order nonlinear polarization P_{nl} , the current for free electrons J_f and the current that is responsible for multiphoton absorption J_a in the spatio-temporal spectrum. The UPPE becomes:

$$\frac{\delta \hat{E}}{\delta z} = ik_z \hat{E} + i \frac{\mu_0 \mu \omega^2}{2k_z} [\hat{P}_{nl} + \frac{i}{\omega} (\hat{J}_f + \hat{J}_a)] \quad (4.20)$$

where

$$\hat{P}_{nl} = \frac{3}{4} \epsilon_0 \chi^3 |\hat{E}|^2 \hat{E} \quad (4.21)$$

$$\hat{J}_f = \frac{q_e^2}{m_e} \frac{(\nu_c + i\omega)}{(\nu_c^2 + \omega^2)} N_e \hat{E} \quad (4.22)$$

$$\hat{J}_a = K \bar{h} \omega_0 \frac{\delta N_e}{\delta t} \frac{1}{\hat{E}} \quad (4.23)$$

where ϵ_0 is the vacuum permittivity, $\chi^3 = 4n_2^2 \epsilon_0 c_0 n_2 / 3$ is the cubic susceptibility with n_2 being the nonlinear index, K the order of multiphoton ionization. The real part of J_f describes the absorption by inverse Bremsstrahlung and the imaginary part describes the plasma defocusing. By solving the UPPE combined to the plasma equation:

$$\frac{\delta N_e}{\delta t} = \sigma_N I^N (N_{nt} - N_e) + \sigma(\omega_0) \frac{I}{E_g} N_e \quad (4.24)$$

where $I = n_0 \epsilon_0 c_0 |E|^2 / 2$ is the pulse intensity, $N_{nt} = 5 \times 10^{22} \text{ cm}^{-3}$ is the number of electrons in the valence band, σ_N is the cross-section of multiphoton ionization ($\beta_N = N \bar{h} \omega_0 \sigma_N N_{nt}$ is the coefficient of the multiphoton absorption introduced in Chapter 1), E_g the bandgap and $\sigma(\omega_0)$ the inverse Bremsstrahlung cross-section at the pulse frequency ω_0 given by:

$$\sigma(\omega_0) = \frac{2q_e^2}{m_e n_0 \epsilon_0 c_0} \frac{\nu_c}{(\nu_c^2 + \omega_0^2)} \quad (4.25)$$

The initial condition of the calculation is a flat-top beam with a Gaussian temporal profile, which is close to the experimental conditions. For ultra-short pulses (large

spectrum), the dispersion of the refractive index has to be taken into account and it corresponds to the following transformation:

$$n_s(\omega) = \frac{n(\omega) - n(\omega_0)}{s} + sn(\omega_0) \quad (4.26)$$

We apply the same scaling factor as in the linear propagation case: $s=1000$, and we compare the contribution of different physical process during the propagation of the ultra-short pulse. The material parameters used in the simulations are presented in table 4.4.

4.2.2 Identification of the factors limiting the fluence delivery to the focus

4.2.2.1 Physical mechanisms included in the model

The use of scalar equations allows reasonable times of calculations. It is thus possible to perform a parametric study to identify the mechanisms responsible for the intensity clamping. In that model, several physical mechanisms have been included:

- The diffraction induced by the small entrance pupil of the microscope objectives with respect to the beam size.
- The dispersion due to ultra-short pulses (as described on section 2.1.1.3).
- Kerr effect (section 1.4.2).
- Plasma defocusing (section 1.2.3).
- Plasma absorption by inverse Bremsstrahlung (section 1.2.3).
- Two-photon absorption (section 1.2.1.2).
- Avalanche corresponding multiplication of the electrons in the laser field by impact ionization (section 1.2.2).

	Parameter	Value	Units	Ref
Refractive index	$n(\lambda)$			
Linear refractive index	n_0	3.51		[118]
Nonlinear refractive index	n_2	1.5×10^{-18}	m^2/W	[119]
Electron collision rate	ν_c	0.3×10^{-15}	s^{-1}	[1]
Bandgap	E_g	1.12	eV	
Multiphoton order	N	2		
Multiphoton absorption coefficient	β_2	0.8×10^{-11}	m/W	[120]
Atomic density	N_{nt}	5×10^{28}	m^{-3}	

Table 4.4 – Material parameters for silicon at 1300-nm wavelength used in the simulations.

In this manuscript, we consider only the case $NA=0.45$. For the different contribution investigated, we compare two pump energies: 10 nJ and 500 nJ, which are respectively near and far above the level of energy where the clamping occurs (see figure 4.9). We study and compare the peak plasma density and the peak fluence which is delivered along the propagation axis. We also have compared the pulse energy along the z-axis (not shown here).

4.2.2.2 Identification of the physical processes responsible for the clamping

Kerr nonlinearities

To interpret the experiments, the model has been running with and without some physical mechanisms enunciated before. The critical power inside Si at $1.3 \mu\text{m}$ corresponds to pulses of only 1 nJ energy in our conditions of irradiation, and we have first investigated the impact of Kerr nonlinearities on the propagation. The results are displayed in figure 4.16. For $NA=0.45$ with 10 nJ pulses (where $P/P_{cr}=2.7 \times 10^3$), the peak fluence delivered to the focus is $F_{focus} \approx 0.075 \text{ J/cm}^2$ with and without Kerr contribution. At low energy, there are very modest differences in the peak fluence and the plasma density. We also do not observe significant shift of the focus along the propagation axis. For high energies, the plasma density calculated when Kerr nonlinearities are included in the model is twice less than the case where Kerr is switched off. Figure 4.16 shows that Kerr effect is not a limiting factor for the energy delivery to the focus at low incident energy. At 500 nJ (where $P/P_{cr}=1.3 \times 10^5$), the effect of Kerr nonlinearities is more important but does not play a significant role in the intensity clamping.

Plasma defocusing and absorption

One can expect that plasma effects play an important role in the intensity clamping observed before. Some publications have shown that plasma defocusing was the

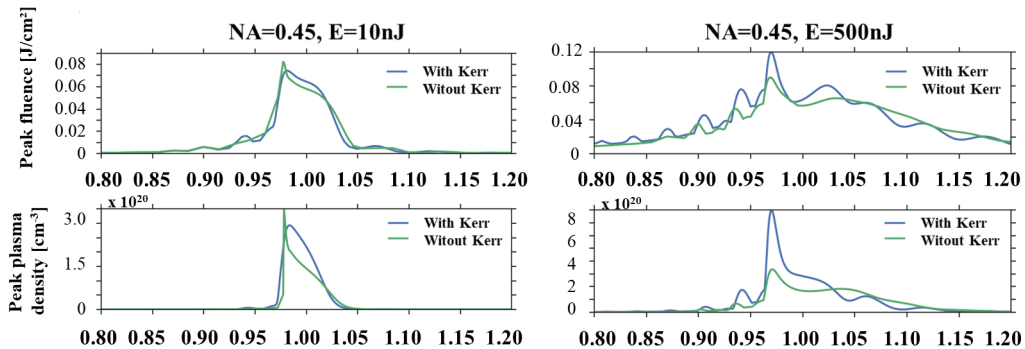


Figure 4.16 – Simulations of the peak fluence distribution for two incoming energies with and without the term including Kerr effect for $NA=0.45$. The geometrical focus is $z=1 \text{ mm}$.

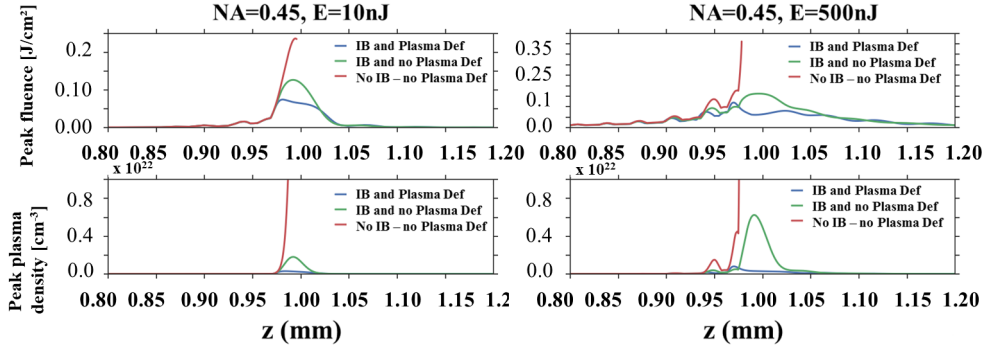


Figure 4.17 – Simulations of the peak electronic density for 10 nJ (left) and 500 nJ (right) with and without plasma effects for NA=0.45. IB is Inverse Bremsstrahlung and Plasma Def is plasma defocusing. The geometrical focus is $z=1$ mm.

main limiting factor to the energy delivery [7, 8]. We investigate also plasma absorption by inverse Bremsstrahlung. In the model, plasma effects are included by the complex free-current term. Its real part corresponds to the losses induced by the plasma absorption and its imaginary part corresponds to losses by IB.

We compare in figure 4.17 the delivered fluence and the peak plasma density along the z -axis for low and high energy when plasma effects are switched on and off. Indeed, without any plasma effects (red line on the graph), the electronic density inside Si would largely exceed the critical density ($N_c = 6.6 \times 10^{20} \text{cm}^{-3}$). It is interesting to note that taking into account only plasma absorption without defocusing does not limit the electronic density enough to be consistent with our experiment results on the free-carriers generated in bulk-Si. We have also verified that considering defocusing without absorption by IB is not correct either. To conclude, plasma defocusing and plasma absorption play an important role in our infrared propagation experiments.

4.2.2.3 Comparison between the experiments and the calculations

Once all the major contributions have been identified, we compare the reconstructions of the beam propagation between experiments and calculations for the three NA tested. This model has been verified for NA=0.3, 0.45 and 0.65, as illustrated in figure 4.18. Only one energy per NA is shown here but other cases have been performed. The shape and also the fluence values of the simulations correspond with the experiments. We are able to retrieve the fluence delivered to the focus for every NA and for any incoming energies.

There is a good agreement between the experiments and the model for the absolute values of the fluence delivered to the focus in figure 4.19. It is not shown here but the same experiments and calculations have been performed for NA=0.1. Such a low NA provides a quasi paraxial interaction inside Si. So we did not apply any scaling factor to the model. Considering the good agreement between calculations and ex-

perimental results, we conclude that the optical transformation done to account for high NA and scalar equations in the modeling is valid. The different contributions

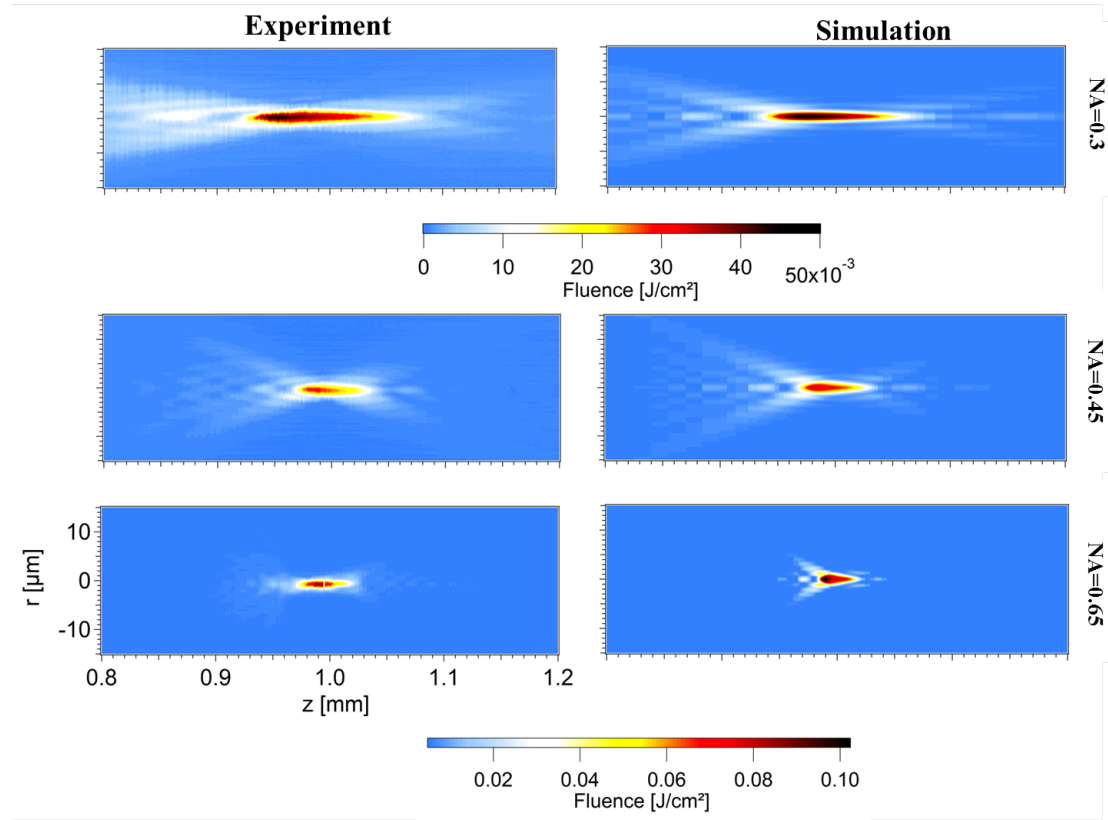


Figure 4.18 – Simulations of the beam propagation for NA=0.3 ($E=50\text{nJ}$), NA=0.45 ($E=12\text{ nJ}$) and NA=0.65 ($E=11\text{ nJ}$). The left column is the experiments and the right column is the corresponding simulations.

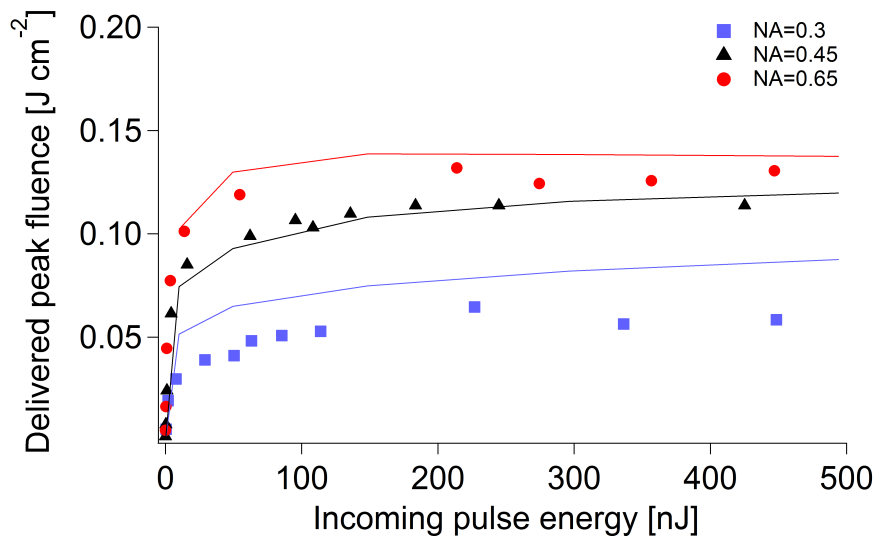


Figure 4.19 – Comparison between experiments (symbols) and calculations (lines) for NA=0.3, 0.45 and 0.65.

of the physical processes involved in the intensity clamping are identified: we report two-photon absorption in the prefocal region leading to important energy losses. Other simulations have shown that only TPA does not explain the clamping: indeed the free-carrier density continues to increase, without undergoing a strict limitation. We have identified plasma effects as the limiting factor in the energy transport. The good agreement of the reconstruction of the beam propagation between experiments and calculations allows us to take advantage of a predictable model for future new solutions to bypass this clamping.

4.2.3 Comparison to the fluence threshold for surface modification

Before thinking about how we could improve the energy transport inside Si, we concentrate on how much energy we have to deliver to the focus to induce damage in bulk Si. Any attempt to reach the optical breakdown inside Si with ultra-short pulses has failed before [21, 6, 1, 23], meaning that no threshold in the bulk has been published yet. We consider in first approximation that the threshold is at least equal to the surface damage threshold. Indeed, one can suppose that defects at the surface like cracks, scratches or chemical contamination can easily induce damage and reduce the threshold, whereas high purity of Si and strong nonlinear effects deteriorate the spatial confinement, and increase the apparent threshold for bulk-damage [121].

4.2.3.1 Methodology

Several techniques are employed to determine if the material has been damaged or not: Atomic Force Microscopy (AFM) [122], optical microscopy [123], or spectroscopy [124]. Here we use an optical microscope (Zeiss, Axiotech-R), to detect *post – mortem* if there is a modification. In this study, we consider damage as a visible permanent alteration of the surface [36].

Experimental data have been published in the literature with other wavelengths (620 and 800 nm) in the ultra-short regime [125, 126, 127] and show an ablation threshold between 0.2 J/cm² and 0.3 J/cm². The LIDT (Laser Induced Damage Threshold) has been measured at the surface of a Si-wafer, the same as in the imaging experiments. We use the same laser source delivering 60 fs pulses at 1.3 μ m, focused with a microscope objective (NA=0.3) at the front face of a Si wafer. We perform a short single-shot damage study by irradiating the sample with gradually increasing pulse energies. The energy is measured with a Joulemeter (GENTEC QE25-LP-H-MB-D0). To optimize the surface positioning of the wafer, a z-scan procedure is applied by changing the position of the focus along the propagation axis. The relative move of the focusing objective is realized with a motorized stage providing 10 μ m increments. We find the right position of the sample by analyzing the sample with bright field reflection microscope (ZEISS Axiotec): the best focus is deduced from the modifications with the lowest energy threshold.

We use the beam propagation characterization realized previously in air to have

the beam profile at the focal plane. We report a nearly Gaussian energy distribution (see figure 4.4) and a beam waist $w_0=2 \mu\text{m}$ (with a FWHM= $2.4 \mu\text{m}$ from table 4.1). We calculate the fluence with $F=E/\pi w_0^2$ where E is the pulse energy. The energy of the laser pulse can undergo fluctuation inducing an uncertainty of 4%. Moreover, the motorized positioning of the sample is realized with an error of $\pm 5 \mu\text{m}$, leading to an error of $\pm 5\%$. Finally, our study presents a global error of 9%.

4.2.3.2 Fluence threshold for surface damage of Si

According to the experiment, we report in figure 4.20 that the fluence damage threshold at the surface of Si is $F_{th} \cong 0.35 \pm 0.03 \text{ J/cm}^2$ for 60 fs laser pulses at $1.3 \mu\text{m}$. This fluence is consistent with the ablation threshold announced in [125, 127]. This measurement can be improved with a statistical study (higher number of irradiated sites). We only consider here that this fluence is the minimal fluence which must be delivered to the focus in order to induce permanent modification inside the volume of Si. We remind that the highest NA tested (0.65) have allowed a delivered fluence at $F_{del} = 0.12 \text{ J/cm}^2$, meaning that less than half of the fluence needed to induce damage at the surface of Si in that regime is delivered.

4.3 Conclusions

This complete study on the beam propagation inside Si has highlighted several points allowing us to understand the unsuccessful attempts to damage Si with fs lasers. First, an experimental study of the beam propagation has provided a full characterization of the interaction inside the material. We confirm the free-carrier density generated inside the bulk by TPA, being more than one order of magnitude under the critical density ($N_e = 2.0 - 3.0 \times 10^{19} \text{ cm}^{-3}$ and $N_c = 6.6 \times 10^{20} \text{ cm}^{-3}$). The absorbed energy density, calculated with $E_{abs} = 2\hbar\omega N_e$ gives 9 J/cm^3 . This energy

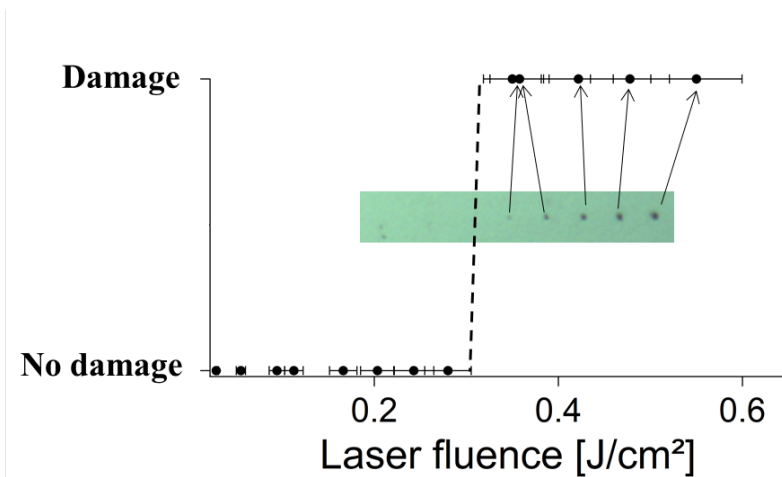


Figure 4.20 – Determination of the fluence threshold for silicon surface modification with 60-fs laser pulses at 1300 nm. The threshold is defined as the fluence above which a modification of the surface is systematically detected with an optical microscope.

calculated with the energy balance considering that the energy is absorbed from the surface gives 0.14 J/cm^3 . These simple calculations highlight the large volume of absorption, not starting from the surface but not restricted to the interaction zone detected with our cameras. A strict limitation on the fluence delivered at the focus has been highlighted with strong losses by nonlinear effects in the prefocal region. Two-photon absorption is the main mechanism responsible for energy losses in the prefocal region, but does not explain this clamping by itself. To identify the other mechanisms responsible for this optical limitation, we turned to nonlinear propagation modeling.

Calculations have been performed and reproduce convincingly the experimental beam reconstruction for different NAs. We conclude that plasma effects, such as strong absorption by IB, and plasma defocusing due to the local change of the refractive index, induces the delocalization of the light. Increasing NA rises the level of clamping, but it seems not to be sufficient to reach the LIDT measured at the front face of Si. As we dispose of a numerical model that retrieves our experiments correctly, we can simulate new arrangements that could minimize the interaction in the prefocal region. These experimental solutions can be complex to realize, especially for long wavelengths. To reach the optical breakdown of Si, we have fixed two criteria: one is $N_e \geq N_c = 6.6 \times 10^{20} \text{ cm}^{-3}$, and/or $F_{del} \geq F_{th} = 0.35 \text{ J/cm}^2$.

Chapter 5

Experimental solutions to bypass the limitations preventing ultra-fast modification in bulk silicon

Contents

5.1	Numerical study of new arrangements to improve the energy delivery inside Si	99
5.1.1	Three-photon absorption	99
5.1.2	Temporal optimizations	101
5.1.2.1	Simultaneous spatial and temporal focusing . . .	101
5.1.2.2	Longer pulse duration	102
5.1.3	Spatial optimizations	104
5.1.3.1	Airy-ring beams	104
5.1.3.2	Extreme focusing with Gaussian beams	106
5.1.4	Conclusions on our choices	108
5.2	Laser induced modifications in bulk-Si with long pulse duration	108
5.2.1	Picosecond modification regime	108
5.2.1.1	Experimental set-up	109
5.2.1.2	Preliminary investigations on the picosecond regime	110
5.2.1.3	Conclusions on the picosecond irradiation regime	112
5.2.2	Nanosecond modification regime	113
5.2.2.1	Experimental set-up	113
5.2.2.2	Single-shot damage investigations inside the volume of Si	114
5.2.2.3	Energy balance and influence of the initial free-carrier concentration.	116

5.2.2.4	Conclusions on the nanosecond irradiation regime	118
5.3	Femtosecond laser modifications inside Si by hyper-NA focusing	119
5.3.1	Context	119
5.3.1.1	Existing solutions to exceed NA=1	119
5.3.1.2	Solid-immersion solution to reach NA up to 3.5	120
5.3.2	Experimental details	122
5.3.2.1	Femtosecond laser pulses focused inside Si spheres	122
5.3.2.2	Magnification of the imaging system	123
5.3.3	Demonstration of the first modification induced with a femtosecond pulse inside Si	124
5.3.3.1	Increase of the NA up to Si breakdown	124
5.3.4	Local change of the refractive index	127
5.3.4.1	Interferometry set-up	127
5.3.4.2	Estimation of the refractive index change	128
5.4	Conclusions	130

It has been previously demonstrated that nonlinear effects prevent the energy to be efficiently delivered to the focus inside silicon. We observed a strict clamping of the delivered fluence below the threshold for permanent modifications. A numerical model has allowed to identify the physical mechanisms involved in this limitation. The main conclusion is that we ideally need to strongly decrease the intensity in the prefocal region. We present in this section simulations of the beam propagation for different experimental arrangements: longer wavelength, temporal focusing, temporal stretching, and spatial beam shaping. We study the feasibility of the different experiments. For that, we take into account the complexity for a rapid implementation in the IR domain, and the results of the calculations. Some appear insufficient to reach one of the two criteria fixed in the previous Chapter (on the fluence delivered and the free-carrier density generated) to expect the material modification.

In this Chapter, we present and discuss simulated cases. We show that some experimental solutions seem to be promising to induce permanent modifications inside the bulk of Si. We chose to investigate the potential of two of them, which are also detailed in this Chapter. A first solution relies on the use of longer pulses, that has been already demonstrated by Verburg *et al.* [11] and Chambonneau *et al.* [12]. The goal of our investigations is to improve the physical understanding of the laser induced damage in bulk-Si with such pulses. Finally we describe and demonstrate a second experimental solution in the femtosecond regime. The technique, that we will call "hyper-NA" ($NA > 1.5$), based on extreme focusing, minimizes the nonlinear propagation effects detailed in Chapter 4.

5.1 Numerical study of new arrangements to improve the energy delivery inside Si

The model, presented in section 4.2, allows us to solve the problem of nonparaxial interaction. The transformation approach for the calculation has provided a tool able to simulate the propagation of our IR beam tightly focused inside the bulk of c-Si. Before to envision any complex experimental implementation, we have tried numerically tentative arrangements to increase the energy delivery to the focus. These are detailed in the following section.

5.1.1 Three-photon absorption

With femtosecond pulses, the optical breakdown in transparent solids is generally considered to occur when the density of free-carriers generated at the focal point reaches the critical density. These free-carriers are generated by nonlinear excitation processes, with an initial predominance of multiphoton ionization in our case as described in Chapter 1. We remind that the probability for an electron to be promoted from the valence band to the conduction band by multiphoton absorption is described by the following formula:

$$W(I) = \frac{\beta_N}{N\hbar\omega} I^N \quad (5.1)$$

where W is the probability for multiphoton ionization, β_N is the N -photon absorption coefficient, and I is the pulse intensity. In this thesis, the wavelength is $1.3 \mu\text{m}$, so this order of MPI is 2 in the experiments. In Si, we consider two-photon absorption coefficient $\beta_2 \approx 0.8 \times 10^{-11} \text{ m/W}$ [32, 33]. One solution to increase the confinement of interaction at the focus is to increase the nonlinearity that is the order of the multiphoton ionization process. This requires the use of higher wavelengths.

All the experiments presented before have been performed at $\lambda=1.3 \mu\text{m}$, corresponding to a photon energy below the band-gap of Si, allowing the two-photon absorption process (energy of one photon: 0.95 eV and bandgap: 1.12 eV). Three-photon absorption requires $\lambda \geq 2.2 \mu\text{m}$. Technically, the OPA allows to reach wavelengths up to $10 \mu\text{m}$, but the main difficulty is the availability of experimental tools (lenses, camera, or polarizing optics) which are not always appropriate to work with long wavelengths. In the literature, there are two different values for three-photon ionization rate, $\beta_3^{(1)}=2.9 \times 10^{-26} \text{ m}^3/\text{W}^2$, and $\beta_3^{(2)}=\beta_3^{(1)}/15$ [8]. One disadvantage of working with a long wavelength is the size of the waist, given by :

$$w_0 = \frac{\lambda M^2}{\pi NA} \quad (5.2)$$

where M^2 is the quality factor of the beam. The direct consequence of using a wavelength at $\lambda=2.2 \mu\text{m}$ is that, for a constant energy, the intensity at the focus is lower.

We turn to numerical simulations with the model presented in section 4.2 for a pulse focused with $NA=0.3$ at 500-nJ energy, a level of energy for which the saturation is fully established.

Figure 5.1 shows the results for the fluence delivered, the peak plasma density and the pulse energy along the z -axis. We observe that the peak delivered fluence and the peak plasma density are lower for 3-photon absorption than for 2-photon absorption. A large focal spot, higher plasma defocusing (that increases with the wavelength) and small ionization rates (even if it scales with I^3) can be explanations to this low excitation regime. The results on the pulse depletion along the propagation for 3-photon absorption show that as expected, the energy losses before the focus decrease with the wavelength, due to a better localization of the laser light at the focus.

This study is consistent with the literature, where the excitation of Si under two, three, four and five photon absorption is theoretically studied [8]. Calculations reveal that increasing the wavelength does not lead to increase the free-carrier density in the focal volume inside the bulk. The decrease in the free-carrier density is mainly due to plasma defocusing, whose strength increases with the wavelength. To conclude, increasing the wavelength of the experiment is not a promising solution to induce bulk-Si damage in the ultra-fast regime.

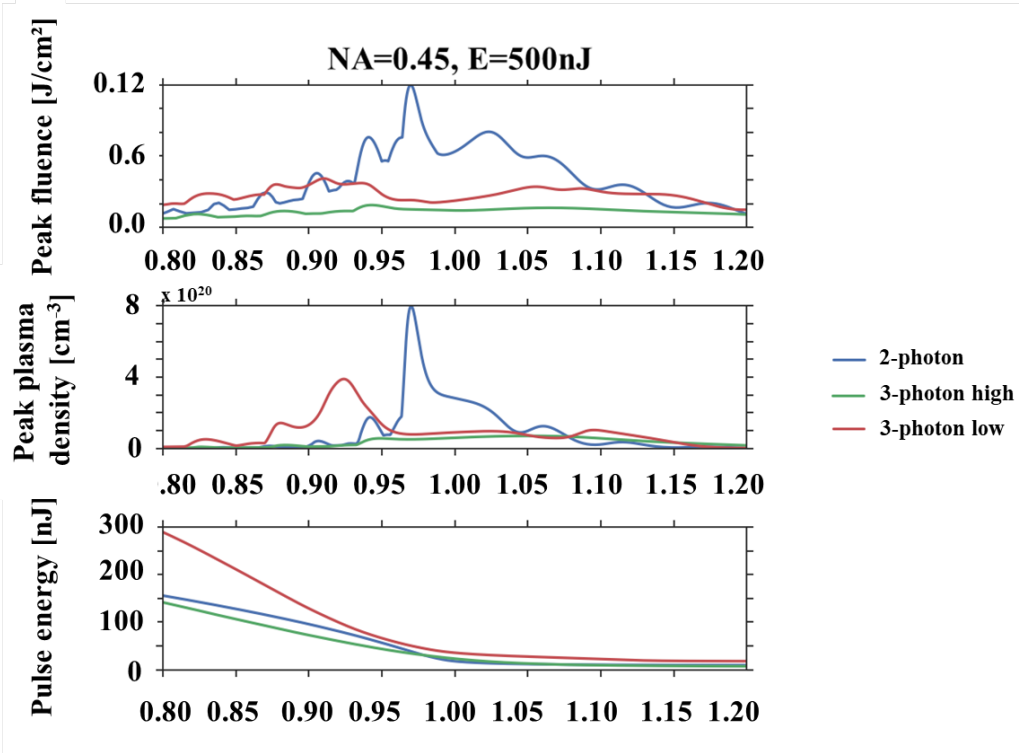


Figure 5.1 – Numerical simulation of the delivered peak fluence (top), peak plasma density (middle) and pulse energy (bottom) along the propagation axis. Calculations for two-photon absorption with $\lambda=1.3 \mu\text{m}$ (green line) are compared to the numerical case where $\lambda=2.2 \mu\text{m}$, allowing 3 photon ionization, shown for two different values of the ionization rate (blue and red). The incoming energy is 500 nJ with $\text{NA}=0.45$.

5.1.2 Temporal optimizations

5.1.2.1 Simultaneous spatial and temporal focusing

In order to decrease the losses before the focus, a natural solution is to decrease the intensity in the prefocal region. A possible solution is to reduce the intensity only before the focus, and increases it at the focus. For that the idea is to have a long pulse duration before the focus, providing low intensities, and a short pulse duration at the focus, providing high intensities. This is possible with simultaneous spatial and temporal focusing (SSTF). This technique consists in increasing the intensity along the optical axis by space-spectrum manipulation of the pulse.

As illustrated in figure 5.2, the pre-chirped laser pulse is firstly dispersed with two gratings (G1 and G2). The spectral components of the pulse are then spatially separated. These separated spectral components start to overlap once propagated through focusing optics (focusing lens L). In the focal volume, the entire bandwidth is recovered, and the initial pulse duration is reconstructed. Before the focus, a longer pulse duration induces a lower intensity of the beam. As a consequence, nonlinear effects are more strongly confined inside the focal volume [129].

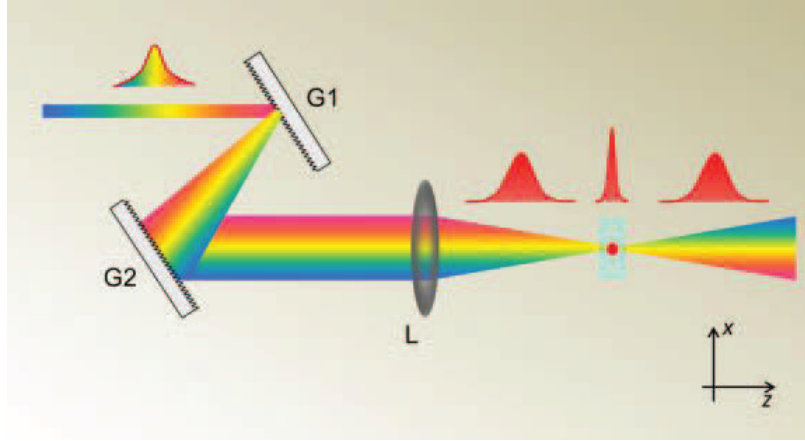


Figure 5.2 – Schematics of the temporal and spatial focusing from [128]. The wavelengths of the initial spectrum are separated and recombined at the geometrical focus.

In the field of femtosecond laser micro-machining, Kammel *et al.* have demonstrated the enhancement of the precision in laser-material processing with SSTF [129]. The initial pulse duration of the beam was 50 fs. After space-time focusing, the pulse duration on the collimated beam before the focus was ≈ 300 fs, and 55 fs at the focus. They show a significant improvement of the intensity confinement in the propagation direction with reduced nonlinear side effects, which yielded to confined modifications inside the volume of the material.

This focusing can be realized in two directions [130], by the use of concentric gratings. This method lowers the intensity before the focus, but are complex to implement, especially for long wavelengths. The perfect spatial overlapping that has to be realized at the focus is an additional difficulty. This solution is experimentally complex to adapt in the IR domain, and will not be experimentally investigated despite promising new results on simultaneous spatial and temporal focusing for femtosecond laser modification of dielectrics at conventional wavelengths [130].

5.1.2.2 Longer pulse duration

To limit the strong nonlinear propagation effects of an ultra-short pulse inside Si, we can reduce the whole intensity of the pulse (without decreasing the energy), since it will reduce the contribution of the nonlinear part of the refractive index. This can be realized by irradiating the sample with longer pulse durations limiting in this way the nonlinear effects and helping for avalanche or thermal buildup to achieve energy deposition. In order to succeed in modifying permanently the local properties of Si, other research groups have investigated longer pulse duration, such as nanosecond pulses, experimentally [11, 12] and numerically [131]. Working with nanosecond pulses appears to be the simplest way to induce modifications inside Si. However, one can anticipate two main disadvantages about the nanosecond regime: a fluence threshold for surface modifications which is more statistical than in femtosecond regime (due to the increased importance of defects for material excitation), and a

modification threshold in terms of fluence which is normally higher for long pulse durations [132]. We have demonstrated that 60 fs pulses are not efficient to induce any modification in the volume of Si, and primary studies show 3-D writing with nanosecond infrared lasers. We think that it is interesting to explore the interaction inside Si with laser pulse durations between these two regimes and in particular the sub-picosecond regime.

Numerical simulations of the propagation of our beam (centered at $1.3 \mu\text{m}$) are represented in 5.3, with varying pulse durations. The laser pulse durations investigated in this section are 60 fs, 120 fs and 600 fs, while keeping all material and other laser parameters the same as for the previous simulations. All the simulations in figure 5.3 have been performed at 500 nJ, since it is far above the energy needed to reach the saturation of the delivered energy. Between 60 fs and 120 fs, no significant difference is observed when plotting the peak fluence delivered along the propagation axis. The peak fluence delivered at the focus is calculated at $F=0.11 \text{ J/cm}^2$. For 600 fs, this fluence increases up to $F=0.18 \text{ J/cm}^2$ which is promising and consistent

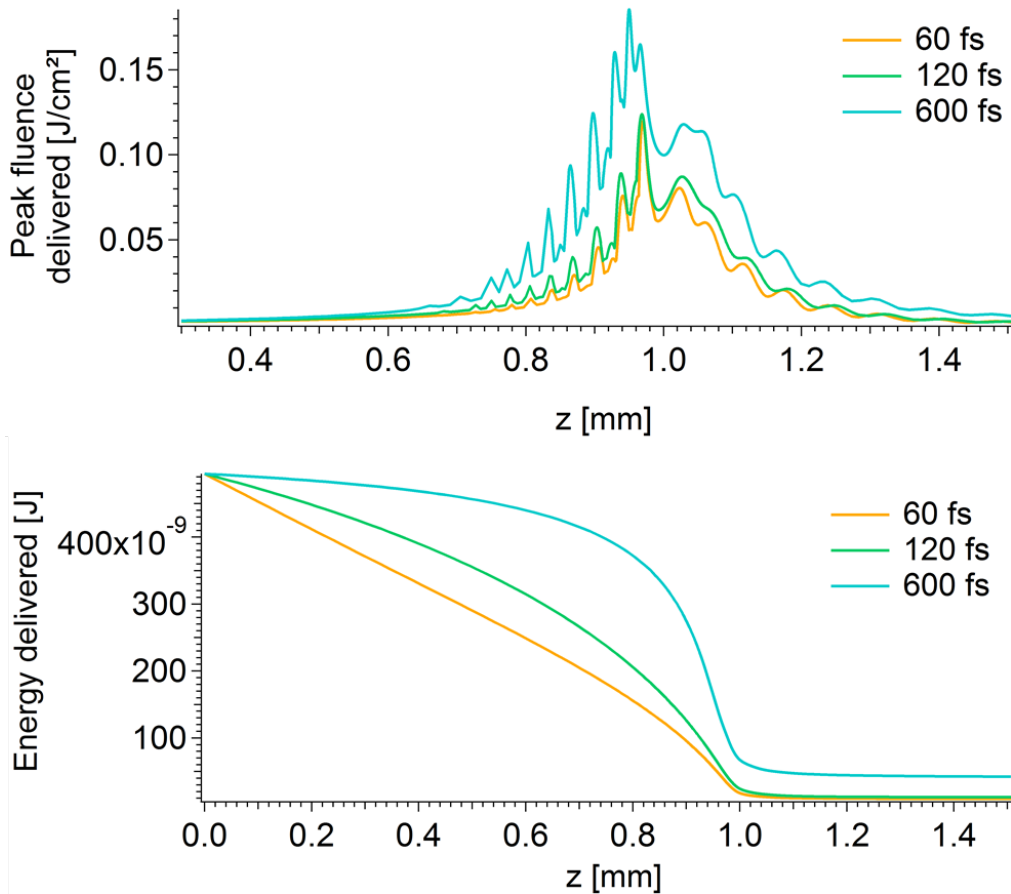


Figure 5.3 – Numerical simulation of the peak fluence delivered (top) and the energy delivered along the propagation axis (bottom). Calculations are performed for 3 pulse durations: 60 fs (orange), 120 fs (green) and 600 fs (blue). The incoming energy is 500 nJ with $\text{NA}=0.45$.

with the literature. According to figure 5.3 (bottom), we confirm that increasing the pulse duration reduces the losses before the focus: the evolution of the delivered energy along the propagation axis shows the reduced losses, with a delivered energy at the focus of 20 nJ and 70 nJ for 60 fs and 600 fs, respectively. In dielectrics, it has been demonstrated that longer pulses favor the development of the electronic avalanche, often leading to damage [37].

These calculations highlight one first promising and simple solution to reach Si breakdown in its volume: stretching the pulse in time to more than 600 fs. Nanosecond modification regime is still a new experimental domain for 3-D Si manufacturing, since it has been originally developed in 2008 by Izawa *et al.* [133] and further investigated in 2014 by Verburg *et al.* [11]. To our knowledge, the picosecond regime has not been investigated so far inside crystalline Si. For this reason, we have performed a preliminary study in the context of this thesis (section 5.2.1.) to confirm the potential of the picosecond regime.

5.1.3 Spatial optimizations

We have mentioned several possibilities to optimize the interaction in the focal region. Among them, changing the wavelength or shaping the beam temporally are possibilities but are not always efficient. In our case, it constitutes complex experiments without any guarantee of success. We investigate now the spatial beam shaping. This method consists in a general way to transform the initial Gaussian beam into a beam with a different intensity distribution. For example, a Gaussian beam can be transformed in a top-hat, Bessel, Airy or vortex beam. A large range of spatial beam shaping is achievable with a Spatial Light Modulator (SLM).

One example of beam shaping which presents interesting propagation characteristics for micro-machining experiments is Bessel beams. The propagation of a Bessel beam inside a transparent medium, free from aberrations, is interesting especially for silicon whose refractive index is high. Secondly, Bessel beams are non-diffractive beams and the intensity becomes high in the core region, concentrating at the center the nonlinear effects such as beam distortion and nonlinear absorption [73]. Experimental studies have been performed with Bessel beams and high aspect ratios (exceeding 100) have been obtained by focusing tightly a Bessel beam inside glass [134]. The problem is that when transposing the technique inside Si, the same optical limitation to the energy delivery than with Gaussian beam has been observed [73]. The peak fluence delivered inside the material saturates at a level below the threshold for bulk-modification.

5.1.3.1 Airy-ring beams

A beam shaping that can be interesting to bypass this clamping is Airy beam [135]. Finite-energy Airy beams has been recently investigated as non-diffractive beams exhibiting a parabolic energy flux [136, 137], and especially with a cylindrical symmetry (called ring-Airy beams). It has been experimentally demonstrated that Airy-ring beams were able to deliver high energy at the rear face of a sample, without

damaging the surface [138]. In our model we introduce the propagation of an Airy beam, where the radial distribution is described by:

$$u_0(r, 0) = Ai\left(\frac{r_0 - r}{\omega}\right) \exp\left(\alpha \frac{r_0 - r}{\omega}\right) \quad (5.3)$$

where Ai describes the Airy function, r is the radius, r_0 is the radius of the primary ring, ω is a scaling factor and α is an exponential decay factor.

We numerically reconstruct the focal region of an Airy-ring beam inside Si for a 10 nJ pulse. Delivering too much intensity in the prefocal region is one of the main limiting factors to the energy delivery to the focus. We clearly see that Airy-ring beams are efficient to reduce this prefocal intensity and concentrate the interaction at the focus. However, the interaction remains relatively paraxial in this case (despite we simulated an abruptly focusing case) because of the parabolic trajectory of the laser energy, and the fluence delivered is not high enough to generate a dense plasma. We must add that we have verified that similar conclusions are obtained with an incoming energy of 500 nJ.

Figure 5.4 (on the top) illustrates the reconstruction of the beam propagation, and the bottom of the figure shows the peak plasma density generated along the z-axis. We compare this plasma density for a Gaussian beam focused with NA=0.3, and for the simulated abruptly focusing Airy-ring beam. Accordingly, the interaction generated with the Airy-ring beam is likely not a solution. Airy-ring beams present a high intensity contrast between the prefocal region and the focus, but the low

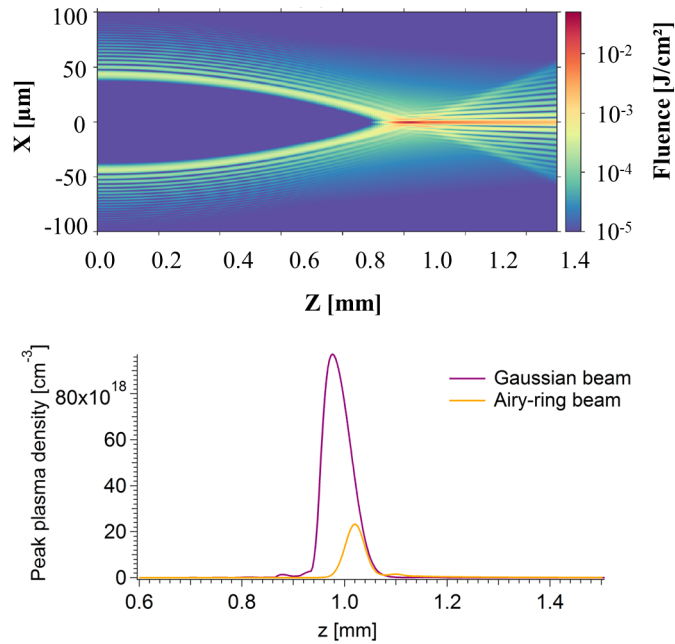


Figure 5.4 – Numerical simulation of the fluence distribution for an Airy-ring beam focused inside Si, with a 10 nJ pulse.

plasma density found in these simulations indicates that this beam shaping strategy will hardly solve the limitation to breakdown in Si.

5.1.3.2 Extreme focusing with Gaussian beams

Focusing an intense Gaussian beam inside the bulk of transparent material presents many advantages such as the precision and the controllability of the modification induced. However, inside Si, some limitations can occur preventing the laser energy to reach the focus. We defined two strategies to develop in order to envision the optical breakdown of Si with our femtosecond pulse: deliver $F \geq 0.35 \text{ J/cm}^2$, and/or generate a peak plasma density around $N_e = N_c = 6.6 \times 10^{20} \text{ cm}^{-3}$. For that, the last potential solution that has been simulated is to push the focusing conditions to the extreme, with NA values up to 1. With tight focusing, we expect that the intensity of the laser pulse before the focus will be low enough to minimize the losses due to nonlinear interaction. The energy deposition is expected to be more efficient, and extremely confined. It can have direct consequences on the bulk damage energy threshold. In fused silica, high-NA configurations for micro-machining experiments have demonstrated a decrease of the energy damage threshold for bulk modifications, which is $\approx 70 \text{ nJ}$ with NA=0.3 compared to $\approx 5 \text{ nJ}$ with NA=1.4 [35]. This low energy threshold is interesting for micro-machining applications, where high repetition rates (MHz) can be easily provided for reasonable costs, with low energies

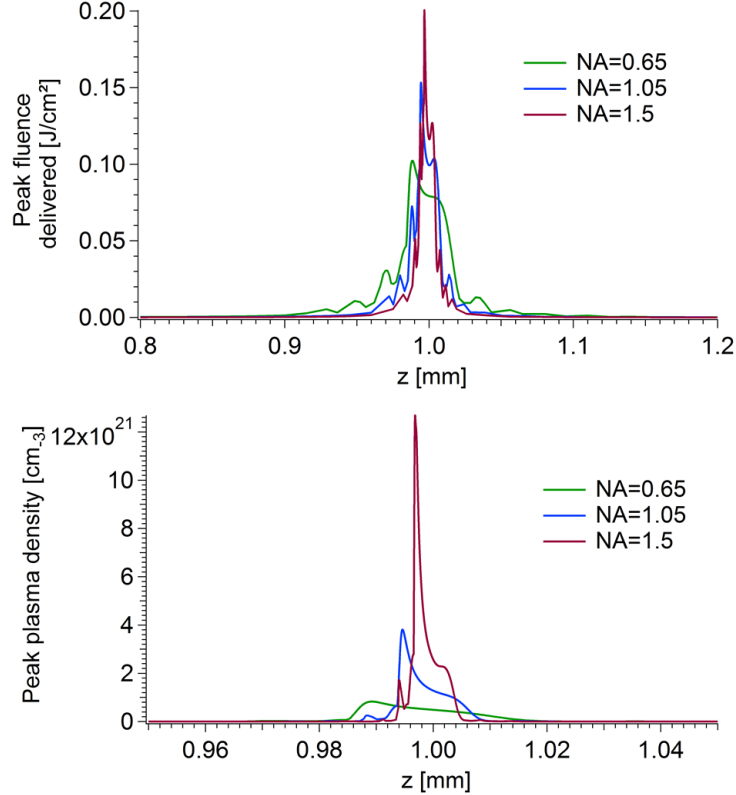


Figure 5.5 – Simulated focusing conditions for NA=0.65, 1.05 and 1.5 inside Si with 10 nJ pulses.

available ($\leq 50\text{nJ}$), in the "oscillator regime".

The use of lasers with increased focusing conditions inside Si has been simulated with the model presented in the previous Chapter. We present in figure 5.5 the peak fluence and the peak plasma density along the axis of propagation, for different NA values at 10 nJ (in this case, the range of interest for the incoming energy is more 10 nJ than 500 nJ, but we have confirmed that for high energies the results are similar). We clearly see the increase of the peak fluence delivered to the focus, reaching $F=0.20\text{ J/cm}^2$ for $\text{NA}=1.5$, whereas the minimal target for the fluence is $F=0.35\text{ J/cm}^2$ (see surface modification study in section 4.2.3). Our calculations predict that $\text{NA}=1.5$, corresponding to the use of oil-immersion objective, is not high enough to reach the targeted fluence for Si modification.

We observe in figure 5.6 that the maximum fluence that can be delivered increases with NA. A linear extrapolation (blue dashed line) of the experimental (dark triangles) and simulated data (red circles) shows that to exceed the target fluence of 0.35 J/cm^2 , values up to $\text{NA}=3$ are required. Concerning the plasma density, the critical density would be exceeded for $\text{NA}=1.5$. This density could be over-estimated since these calculations are the ideal case of a complex system providing $\text{NA}=1.5$, without introducing aberrations. Therefore, we can safely conclude that rising the NA is an interesting direction of research. The extrapolation in figure 5.6 is a simple estimation without any physical justification but it indicates that classical configurations with high NA do not suffice to reach the fluence threshold. We have to imagine a new experimental arrangement that can provide extreme NA focusing (up to $\text{NA}\approx 3$).

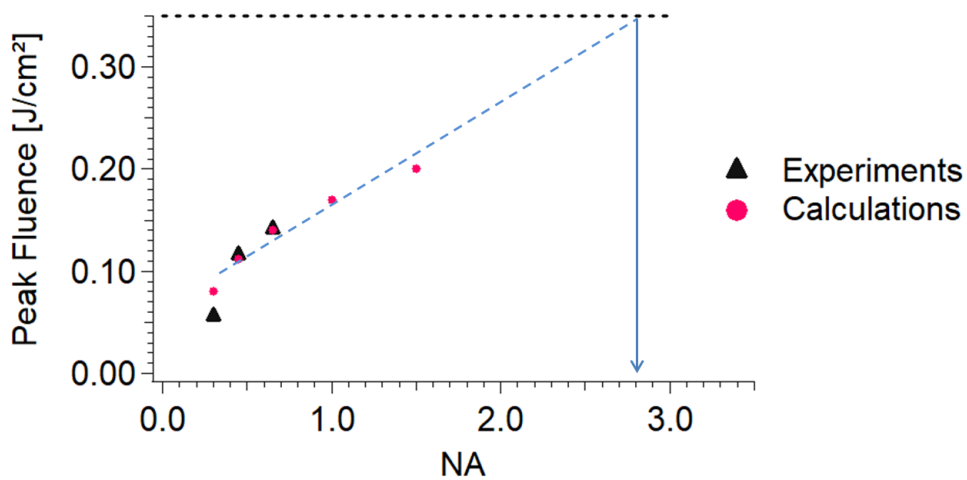


Figure 5.6 – Maximum peak fluence as a function of NA, in comparison with the surface damage threshold at 0.35 J/cm^2 . The dashed line in blue is a guide for the eye.

5.1.4 Conclusions on our choices

We have numerically or theoretically investigated solutions to bypass the optical limitation to the energy deposition inside Si: 500 fs pulses, Airy beams, 3-photon absorption, temporal focusing or $NA \geq 1.5$. Longer pulses (sub-picosecond) and higher NAs seem promising. Ring-Airy beams, 3-photon absorption and temporal focusing present interesting aspects but we chose not to investigate these options, often experimentally complex. In most of our simulations, the peak fluence and peak plasma density, on which are the two criteria fixed to reach bulk-modifications, are for most of the cases far from being sufficient. We have retained two experimental strategies that are the most promising configurations. We have shown that longer pulses were a potential solution to induce modifications inside Si, but it presents some disadvantages. The reproducibility and controllability are two qualities typically obtained in micro-machining of transparent solids with femtosecond laser pulses [139, 140]. The other configuration that is relevant for our study is to increase the NA up to 3. Focusing tighter allows us to decrease the energy threshold for bulk damage, but also allows us to reduce the volume of the interaction, implying hard detection of the modifications for single-shot experiments. The main difficulty here is to find a method to reach $NA=3$ for focusing the pump inside a transparent media, that has never been demonstrated so far. Both configurations (longer pulses and extreme focusing) are investigated and discussed in the following sections.

5.2 Laser induced modifications in bulk-Si with long pulse duration

5.2.1 Picosecond modification regime

This study on laser induced modifications inside the volume with picosecond pulses has been motivated by several points. First, a natural solution to reduce the intensity is to increase the pulse duration. Femtosecond laser irradiation can induce localized and confined 3-D structures in dielectrics, but strongly depends on the linear and non-linear effects during the pulse propagation. The significant volume of absorption before the focal spot may induce the growth of the modified area towards the prefocal region. Because the intensity is reduced before the focus, some results in dielectrics show a better confinement of the interaction in the picosecond regime [81]. Moreover, one of the most interesting advantages of longer pulses (compared to femtosecond pulses) is the role of avalanche. The electronic avalanche usually follows MPI and increases rapidly the number of free-carriers, eventually up to the critical density. Another important characteristic of the material is the electron-phonon relaxation time, related to heat transfer to the lattice. Inside Si, this electron-phonon coupling time is less than 10^{-12} s [141], making heat transfer possible in long pulse duration regimes. Besides, a rise of temperature inside the material during the pulse propagation can induce bandgap closure, and then increased absorption leading to breakdown [142].

In the framework of a collaboration with the *Institute of Applied Physics* of

Jena (Germany), we have investigated picosecond laser irradiation in the bulk of Si. We have performed damage experiments with an infrared erbium-doped laser, with a pulse duration from 800 fs to 10 ps, delivering pulses centered at $1.55 \mu\text{m}$, presented in Chapter 2.

5.2.1.1 Experimental set-up

The study on picosecond laser induced damage inside Si has been performed with a commercial source (Rofin, Raydiance) introduced in section 2.3.1. The experimental set-up is shown in figure 5.7. The laser source delivers $1.55 \mu\text{m}$ pulses, with different pulse durations and different repetition rates. The pulse duration is adjusted by changing the distances between the gratings inside the compressor. The pump propagates through an afocal system composed by one divergent lens and then one convergent lens, providing 3X magnification. The energy is controlled with an half-wave plate combined with a polarizer. The pump is focused with a microscope objective (LCPLN20XIR, Olympus), providing a theoretical beam waist

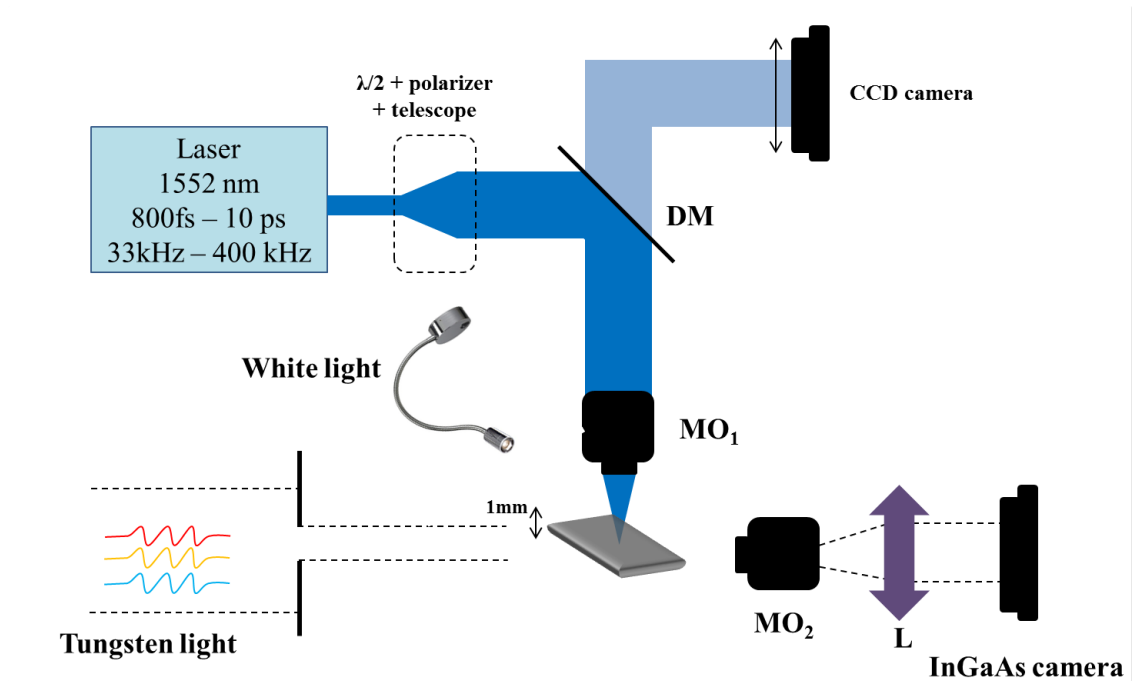


Figure 5.7 – Experimental set-up for bulk modifications in Si with transverse illumination and imaging with an infrared camera. The laser delivers $1.55 \mu\text{m}$ -wavelength pulses with pulse durations between 800 fs and 10 ps. A half wave-plate ($\lambda/2$) combined with a polarizer controls the energy; a telescope with one diverging and one converging lens provides the adapted size of the beam; a dichroic mirror reflects the pump and transmits the visible white light (DM); and microscope objectives are used to focus the pump (MO_1) and collect the light (Tungsten) for the imaging system composed of a microscope objective (MO_2) and a tube lens (L). The image is obtained on a camera working in the NIR.

$w_0=1.3 \mu\text{m}$ with $\text{NA}=0.45$. A dichroic mirror (DMLP1180, Thorlabs) reflects the pump at $1.55 \mu\text{m}$ and is transparent for wavelengths below $1.1 \mu\text{m}$. This system allows to image the sample and to focus the beam with the same microscope objective, mainly used in the alignment procedure. A white light source illuminates the surface of the wafer, providing a first alignment of the sample: the beam is focused at the surface to create a plasma and locate the focal plane. We image the surface of the wafer with a CCD camera (DCC1545M, Thorlabs). Transversely, a tungsten light (QTH10, Thorlabs) illuminates the wafer and a microscope imaging system is implemented: a microscope objective (10X Plan APO NIR, Mitutoyo) and a converging lens image the bulk of Si on an infrared camera (WiDy SWIR 320 U). The laser source provides several pulse durations between 800 fs and 10 ps. We investigate laser induced damage threshold inside Si for 800 fs, 5 ps, 8 ps and 10 ps. One can note that the pulse durations are those specified by the laser manufacturer and have not been experimentally measured. The energy is measured with a power-meter after the afocal system, and the transmission objective is determined by collecting the signal before and after the objective. According to our measurements, $T_{obj} = 40 \%$.

The sample is a Si wafer of 1 mm-thick with all sides polished, allowing to image the bulk by the side of the sample. Since the imaging system has a depth of field allowing to see both faces of the wafer, we can induce damage at the front surface, at the back surface, and then position the focal point in the bulk.

5.2.1.2 Preliminary investigations on the picosecond regime

The goal of this experimental campaign is to demonstrate localized permanent modification confined in the bulk of silicon induced by ps laser pulses and further to determine the laser induced damage threshold inside the bulk of silicon for different ps pulse durations. To our knowledge, there is no study on damaging the bulk of silicon in the picosecond regime that has been published so far. In the femtosecond regime, focusing an infrared laser beam inside the volume of a Si wafer does not induce any permanent modification. In the nanosecond regime, waveguides have been written, with 5-ns pulses of a few μJ at $1.55 \mu\text{m}$. The problem is the lack of controllability on the modification uniformity. Finally we want to determine if the picosecond regime can be an efficient intermediate regime to induce controlled modifications inside the bulk of crystalline Si.

First, we concentrate our attention on the determination of a regime where permanent modifications would be systematically detected inside the volume, without damaging the front and rear faces. The parameters that can vary in this experiment are the energy, the pulse duration, the repetition rate and the number of shots. We perform a first damage study consisting in the irradiation of bulk-Si at a fixed laser pulse duration and increasing energy. We repeat the experiment for every pulse duration available on the laser: 800 fs, 5 ps, 8 ps and 10 ps. All experiments in this section have been performed with $\text{NA}=0.45$.

Investigations on bulk modifications for $\tau_{pulse}=800$ fs

The pulse duration of the laser is fixed at 800 fs (the shortest pulse duration available with the laser), and we first study the possibility of damaging the bulk of Si. The experiment is performed at a repetition rate of 30 kHz with an exposure time of 0.5 s, corresponding to 15 000 shots. The focal point is located at the middle of the sample, and we irradiate the sample on ten sites separated by 100 μm . The energy of the pulse is $E=23.7$ μJ , corresponding to an energy on target $E=6.6$ μJ (considering the transmission of the focusing objective and the reflection at the surface of silicon). The probability of damage is $P=40$ %. We present in figure 5.8a) the images of bulk Si illuminated with continuous white light. We observe vertical areas (modifications) confined inside the bulk which are relatively reproducible but not systematically initiated. The energy has not been increased above 6.6 μJ to avoid damage on the optics, especially inside the focusing objective. As a conclusion, we did not observe 100% of damage probability for $\tau_{pulse}=800$ fs.

Investigations on bulk modifications for $\tau_{pulse}=5$ ps

The pulse duration of the laser is now fixed at 5 ps. At the highest energy tested (5.6 μJ on target), the damage probability has reached 60% , for a repetition rate fixed at 200 kHz with 0.5 s of exposure time, corresponding to 100 000 shots. The same damage study has been realized at 33 kHz and similar results have been observed (60% damage probability for an energy of 5.6 μJ). One can note according to figure 5.8b) that damage has been initiated independently from the two surfaces, similarly to the 800 fs case. However, we did not obtain 100% of damage probability for $\tau_{pulse}=5$ ps.

Investigations on bulk modifications for $\tau_{pulse}=8$ ps

We also investigated the laser induced damage inside Si for a pulse duration fixed at $\tau_{pulse}=8$ ps. The results lead to the same conclusions as for the 5 ps study. We obtain for the maximum energy tested ($E=6.6$ μJ on target) a damage probability of 60%.

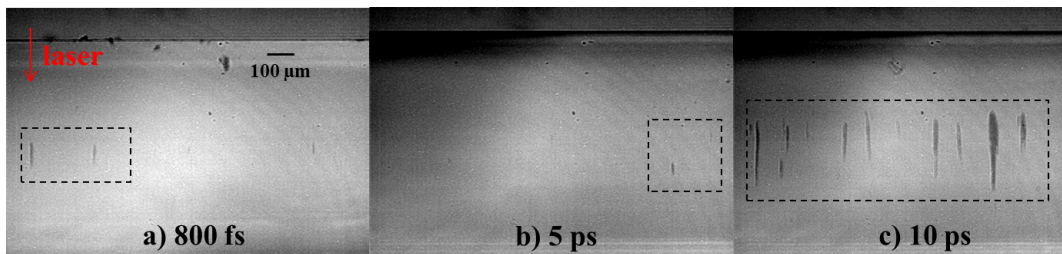


Figure 5.8 – Image of the bulk of Si: laser is coming from the top, and dark areas are permanent modifications induced by pulses at: a) 6.6 μJ at 800 fs; b) 5.6 μJ at 5 ps and c) 6.6 μJ at 10 ps.

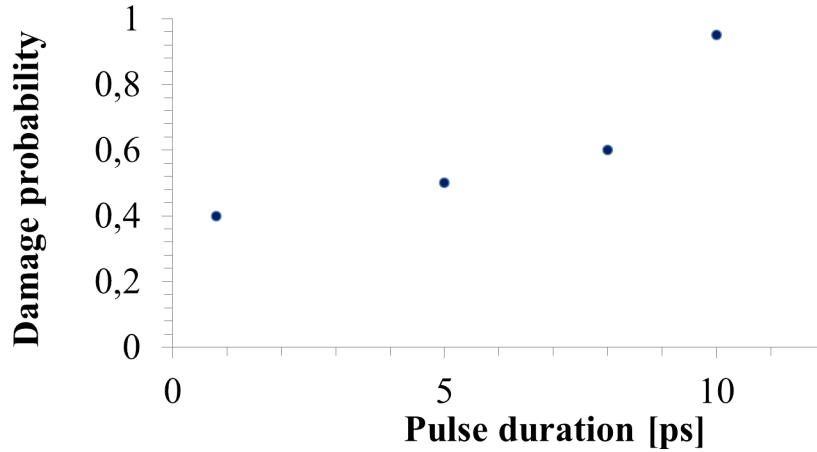


Figure 5.9 – Evolution of the damage probability in bulk-Si as a function of the pulse duration. The energy is $E=6.6 \mu\text{J}$, and the number of shots is 15 000 (0.5 s of exposure at 30 kHz).

Investigations on bulk modifications for $\tau_{pulse}=10 \text{ ps}$

The last pulse duration investigated is 10 ps, with a repetition rate fixed at 200 kHz. With this pulse duration, a systematic permanent modification is detected with the lateral microscope. At $5.6 \mu\text{J}$, the laser induced damage probability of bulk silicon reaches 100%, for different exposure times: 0.5 and 0.1 s, corresponding to 100 000 shots and 20 000 shots, respectively. However, we observe in figure 5.8c) that the control and the precision of the laser induced modifications are relatively low (concerning the length, the width and the uniformity). This study has also been conducted in single-shot regime, but it could not lead to reliable results. The detection of single-shot damage in our experimental configuration is limited by the resolution of our microscope, and/or exhibits a higher energy threshold, which has not been reached.

The probability to induce bulk modification for a constant energy is reported in figure 5.9 for the different pulse durations. We compare the damage probability of bulk silicon irradiated in the same conditions: $E=6.6 \mu\text{J}$, 15 000 shots (0.5 s of exposure at 30 kHz). One first important conclusion is that the clamping of the delivered energy observed in the femtosecond regime is bypassed with longer pulses since permanent damage is observed. We finally obtain systematic damage of bulk-Si with $\tau_{pulse}=10 \text{ ps}$ and $E=6.6 \mu\text{J}$ on target, independently of the two surfaces.

5.2.1.3 Conclusions on the picosecond irradiation regime

These first results on picosecond modification regime show the possibility to modify locally the bulk of Si with a few microJoules. Between 800 fs and 10 ps, the different results on the energy damage threshold and the morphology are obtained. For sub-picosecond pulses (800 fs), the modifications are not systematically initiated. For a pulse duration of 10 ps, we reach 100% of damage probability confined inside the bulk. However, the quality of these modifications is not acceptable yet

for controlled laser-processing applications. These preliminary results constitute the first permanent modifications induced inside Si with picosecond laser pulses. Further investigations on this regime are needed to explore the potential of picosecond laser writing inside Si.

5.2.2 Nanosecond modification regime

Picosecond laser pulses have shown an interesting modification regime. While the interaction physics is only very partially understood at that time, we found that it presents a strong deficiency of reproducibility and controllability requiring further work before to envision laser processing applications. Recent technological advances in the development of infrared laser sources have allowed to develop new powerful and high quality infrared nanosecond lasers. New experiments for investigations of Si modification in its volume have been performed. The first applications of generating subsurface modifications in the nanosecond regime was wafer dicing [11], and waveguide writing [12]. These new guiding structures were written in crystalline Si with several energies and several speeds of writing, allowing to investigate the best conditions to write waveguides in a Si wafer. Despite non-uniformities, a characterization of the modified area has revealed an apparent positive change of the refractive index of $\Delta n \approx 10^{-3}$, which is a first promising result for the manufacturing of new micro-electronic devices. In this section, we investigate the laser induced damage threshold inside the volume. We also investigate the effect of the doping concentration on the damage initiation to detect if the initial level of free-carriers plays a role in the modification regime.

5.2.2.1 Experimental set-up

We present in figure 5.10 the experimental set-up used in two different studies. The first experiment is the detection of single-shot damage with an infrared imaging system. Then we determine the threshold for bulk modification, and the evolution of the damage probability with the increase of the energy. This investigation is performed on a cube of crystalline Si, similar to the one used in Chapter 3 for pump-probe experiments. The second experiment is an energy balance study providing the evolution of the absorption of the laser energy inside a Si wafer. The wafers used in this integrated energy measurement are described after.

The optical path of the beam is the same for both experiments from the laser source to the sample (figure 5.10): only the diagnostic changes. The commercial laser source (MWTechnologies) has been introduced in section 2.3.2 where we detailed the characterization of the pulses (spatial, temporal and spectral profile). An erbium doped fiber laser source delivers 1550 nm pulses with a pulse duration of 3.5 ns at a repetition rate of 100 Hz. At the output of the fiber, the Gaussian beam has a diameter of 3.8 mm, and is not polarized. An afocal system composed of one diverging lens ($f'=-50$ mm) and a converging lens ($f=150$ mm) provides a 3X magnification. The energy is adjusted with a half-wave plate (Thorlabs, PBSW-1550) and a polarizing beam splitter (Thorlabs, PBS104). The pump, is focused with a

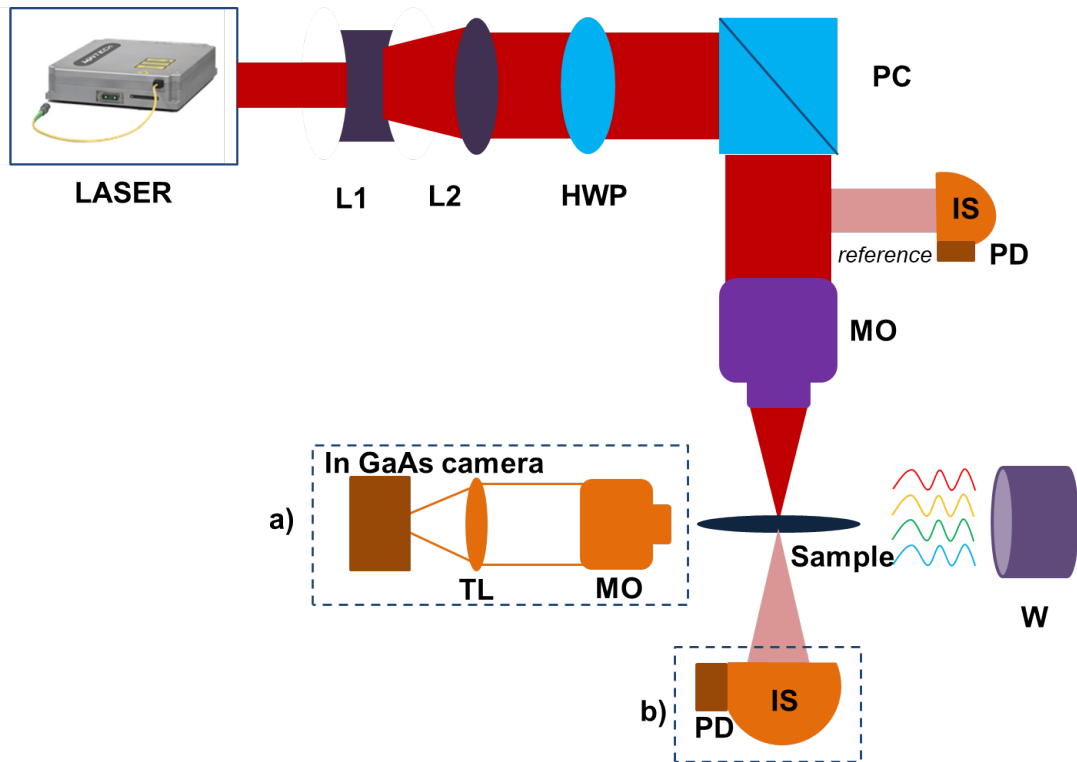


Figure 5.10 – Experimental set-up for the study of nanosecond modifications in the volume of Si. The detection of damage is realized with an infrared microscope for imaging (a), and the energy balance measurement set-up is composed of (L1) diverging lens; (L2) converging lens; (HWP) half waveplate; (CP) polarizing beam splitter; (IS) integrating sphere; (PD) photodiode; (MO) microscope objective; (TL) tube lens; (W); white light (b).

microscope objective with $NA=0.3$ (Olympus, LMPLN10XIR), 1 mm under the surface of the cube. A white light source (Thorlabs, QTH10) illuminates the sample orthogonally to the pump direction. A microscope imaging system composed of a microscope objective (Olympus, LMPLN20XIR and LMPLN50XIR) and a tube lens provides an image of the bulk of Si on an InGaAs array (XenicsXeva). A mechanical shutter (Thorlabs, SH05) is installed before the afocal system to achieve single pulse experiments. The energy balance presented in this section relies on the same principle as the one presented in Chapter 4. A reference signal is collected before the sample with an integrating sphere (819-C-OPT, Newport) and a Germanium photodiode (Thorlabs, PDA50B-EC), and the transmission signal is collected after the sample with a second integrating sphere (819-D-OPT, Newport) and a photodiode. The acquisition of these two electronic signals is automated with a Boxcar Averager (Stanford Systems, SR280) and an acquisition card connected to a computer.

5.2.2.2 Single-shot damage investigations inside the volume of Si

Nanosecond modification regime is a complex succession of physical processes. With nanosecond pulses, thermal effects play a significant role during the interaction. In particular, one can expect bandgap collapse. In this case, the band structure of the

material is modified and the absorption of the laser flux reaches a higher probability. As shown in Chapter 1, when the temperature reaches 800 K, linear absorption can take place. The combination of multiphoton ionization, electronic avalanche, thermal effects and bandgap collapse can occur at the time scale of pulse duration, making the understanding of the damage initiation challenging. This study was realized by detecting single-shot damage sites, making the comprehension of the phenomena involved in the modification generation easier than in multiple shots regime.

To rapidly locate the focal plane, we first accumulate laser shots with high energy ($\geq 6 \mu\text{J}$) to generate damage, as shown in figure 5.11. Once we have located the geometrical focus, we perform single-shot experiments while keeping the focus at the same depth. With a mechanical shutter, we can select only one pulse and then move the sample perpendicularly to the optical axis to irradiate a fresh material region. Here, we would like to remind that the laser is operating at 100 Hz at all times of this experiment which explains the use of the mechanical shutter.

We report in figure 5.12 the damage probability as a function of the energy. Every irradiation condition (at fixed energy) has been repeated 10 times for statistical measurements. The probability rapidly increases from 0 to 1, with an energy threshold for single-pulse measurements at $E_{th} \approx 2.8 \mu\text{J}$. In our focusing conditions, it corresponds to an average fluence threshold of $F_{th} = 27.4 \text{ J/cm}^2$ (if the beam were focused in vacuum). In [11], they report the first modification at the intensity $I_{th} = 5.1 \times 10^9 \text{ W/cm}^2$, and we find in our experiments $I_{th} = 4.4 \times 10^9 \text{ W/cm}^2$, which is very consistent by comparison. By increasing the number of shots, we observe a

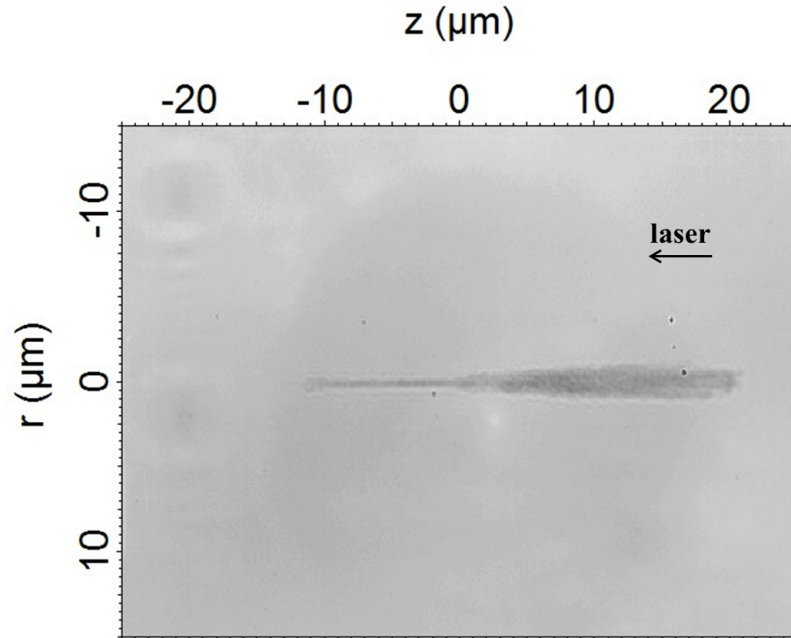


Figure 5.11 – Infrared image of the focal region after 500 laser shots in bulk-Si: laser is coming from the right, and the dark area is the permanent modification induced by 3.5 ns laser pulses at $E = 13 \mu\text{J}$.

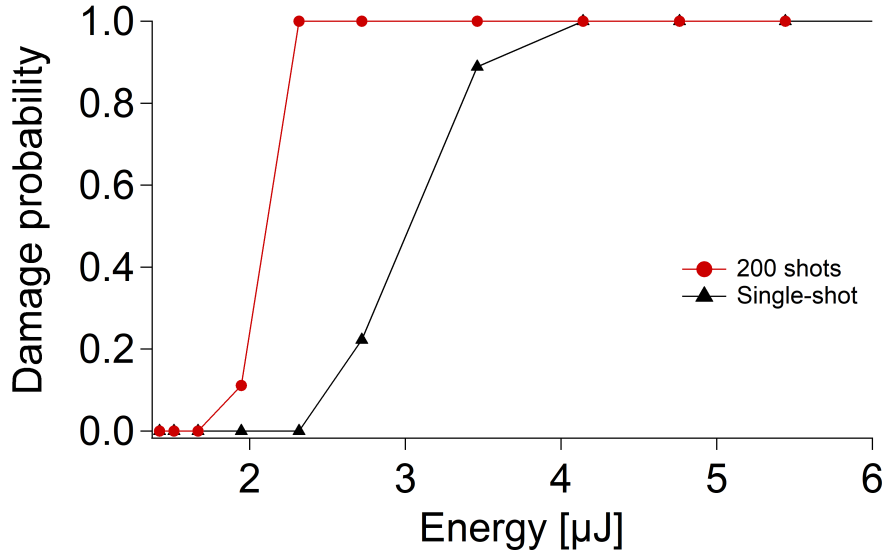


Figure 5.12 – Probability for bulk modifications in Si, in single-shot regime (black triangles) and multiple-shots regime (red circles). We deduce the energy threshold in our case: $E_{th} \approx 2.3 \mu\text{J}$ for single-shot measurement, and $E_{th} \approx 1.7 \mu\text{J}$ for 200 shots.

diminution of the energy threshold. We can hardly compare this result to the picosecond regime where the threshold is not significantly different, since we did not perform single shot investigations in the picosecond regime. The difference observed in the energy thresholds between single and multiple shot regime is not surprising. This result highlights the fact that accumulation effects take place in this case.

5.2.2.3 Energy balance and influence of the initial free-carrier concentration.

The investigation on the influence of the doping concentration on Si response to nanosecond pulses can bring precious information on the absorption processes. This study has been strongly motivated by the one led in the femtosecond regime [42]. Measurements of the transmitted beam after focusing in the bulk of a Si wafer have been performed for several levels of carrier injection. This energy balance gives direct information on the laser flux absorption inside the material. The superposition of the transmitted signal after the sample between the different doping concentrations revealed that the absorption appears to be independent on the free-carrier concentration. This highlights the minor role of the electronic avalanche with ultra-short pulses. As in the nanosecond regime avalanche is expected to play a significant role in the damage initiation, we perform similar measurements with the infrared nanosecond laser. For different initial carrier concentrations, we focus the pump inside the wafer and we collect the transmitted signal. The additional difficulty is that contrary to the femtosecond study, permanent modifications are induced with nanosecond pulses. In order to stay in a single-shot modification regime, every laser shot irradiates a fresh zone of the sample.

Table 5.1 presents the different resistivity and corresponding free-carrier concen-

trations characterizing our samples. They are provided by the same manufacturer (Siltronix), and have a thickness of 1 mm. The same procedure has been applied for the different wafers. We localize the bulk of the wafer with a z-scan method, consisting in collecting with a photodiode the response of Si to a low laser flux. Losses at the interfaces allow to locate the two surfaces. Then we position the focus inside the bulk, 500 μm from the two surfaces. For every transmitted beam which are measured, a reference signal is also collected before the focusing objective.

Figure 5.13 presents the evolution of the transmitted signal when the energy of the pump is increasing. For doping concentrations up to 10^{13} cm^{-3} , the signal starts at 0.53, being the transmission through the sample taking into account the losses at the interfaces of Si (as calculated in section 4.1.4.). The signal is then decreasing, showing the nonlinear absorption of the laser energy inside Si. One first trend is the low slope compared to the one reported in the femtosecond regime, where the signal decreases down to 0.1 (presented in section 4.1.3.3. in figure 4.13). This can be a signature from a low absorption, mainly due to the reduced intensity with a

Resistivity (Ωcm)	Initial free electron concentration (cm^{-3})
50-100	$5 \pm 2 \cdot 10^{13}$
10-14	$3.7 \pm 0.7 \cdot 10^{14}$
2-6	$1 \pm 3 \cdot 10^{15}$
0.5-0.8	$1 \pm 1 \cdot 10^{16}$
0.02	$1.1 \pm 0.1 \cdot 10^{18}$

Table 5.1 – Properties of the different N-doped samples used for the experiments.

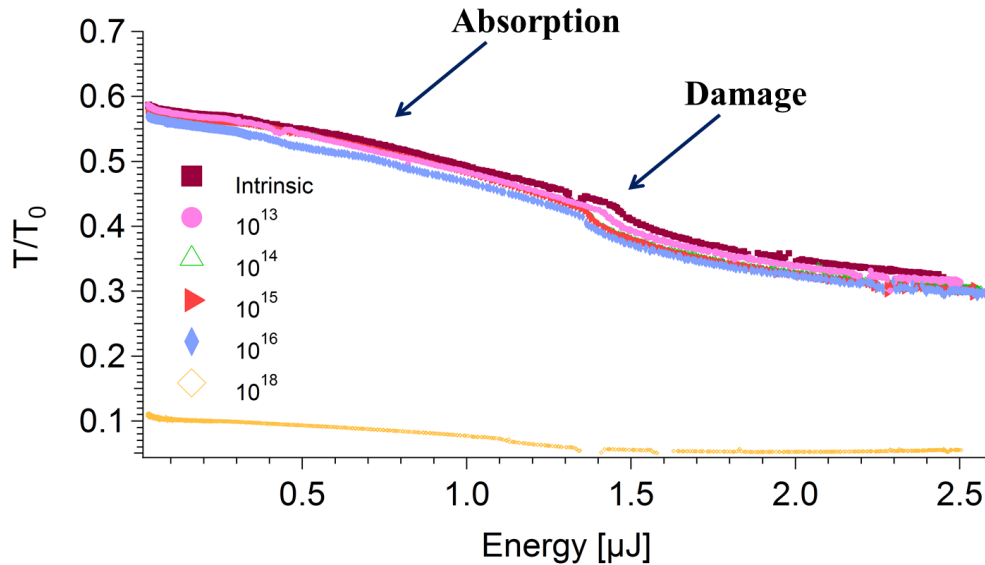


Figure 5.13 – Integrated measurement of nanosecond laser pulses transmitted through the sample for different doping concentrations.

longer pulse duration. The small change of slope before $1.35 \mu\text{J}$ is attributed to the single-shot modification detection. It is consistent with the occurrence of damage which is accompanied by significant changes of absorption and scattering properties of the excited material. We have compared the energy corresponding to the change of slope to the bulk energy damage threshold determined in figure 5.12, and we confirm that we can attribute this small drop of signal to the damage of the material. We observe that the energy threshold slowly evolves with the doping concentration. We could expect that, due to avalanche, the doping concentration would strongly affect the energy threshold for permanent modification. On the contrary, it remains almost negligible, like in the femtosecond regime [42]. Even if electronic avalanche is known to play a significant role in damage initiation, integrated measurements do not detect any significant change in the absorption for the different initial doping. As mentioned above, we have verified that the two threshold values for single-shot modification (by imaging with an infrared microscope and the energy balance measurements) are close when the experiments are performed in the same configuration (beam size, alignment etc). However, we found that the single-shot detection by imaging the bulk with the infrared camera remains a less sensitive measurement.

In the context of a collaboration, the group of S.Lei in Kansas State University (USA) has performed multiple-shot modifications inside the same samples as those that we used [143]. After the laser irradiation, they have achieved polishing and chemical etching steps to reveal the modifications. Applying this procedure, they have measured the length and the width of the modifications for different energies, and with different doping concentrations. Their conclusions on the influence of the doping concentration on the modifications induced by nanosecond pulses are similar to ours: when the initial free-carrier concentration increases, they do not observe any significant change in the morphology of the damage.

5.2.2.4 Conclusions on the nanosecond irradiation regime

Nanosecond infrared laser pulses appear to be an efficient way to bypass the optical limitations to Si modification. However, few drawbacks remain limiting: several μJ are needed to induce permanent damage, the change of refractive index induced by nanosecond regime modification can be inhomogeneous [12], with positive and negative changes on the same modification, showing the complexity of the interaction. Nevertheless, adapting the energy and the writing velocity have shown promising new structures that can be useful for modest precision applications such as marking, dicing, etc.... In microelectronics, Si is generally used with various doping concentrations. The relatively low influence of the doping concentration constitutes an important information for any future applications.

5.3 Femtosecond laser modifications inside Si by hyper-NA focusing

5.3.1 Context

5.3.1.1 Existing solutions to exceed NA=1

The capacity of long infrared laser pulses to induce modifications inside Si is now admitted. However, inducing damage inside crystalline Si with femtosecond pulses remains challenging. The numerical simulations of 60 fs pulses focused with NA=1.5 have shown promising results, with an improvement of the energy delivery to the focus. Experimentally, reaching NA>1 is achievable with liquid immersion lenses, where a liquid with a high index of refraction replaces the air between the output of the objective and the sample.

By definition, the numerical aperture is expressed by :

$$NA = n \sin(\theta) \quad (5.4)$$

with n the refractive index of the medium and θ the half-angle of the focusing cone, as illustrated in figure 5.14 (top). When the light propagates from a medium 1 to a medium 2 with a different refractive index, there is refraction at the interface of the two media:

$$NA = n_1 \sin(\theta_1) = n_2 \sin(\theta_2) \quad (5.5)$$

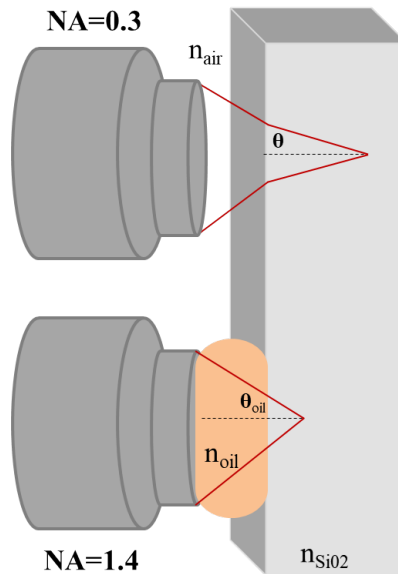


Figure 5.14 – Comparison between classical focusing in glass with microscope objective (top) and oil-immersion lens focusing (bottom). With air, ($n_{air}=1$), focusing inside fused silica (SiO_2) with NA=1.45 at 800 nm, refraction at the interface lowers the half-angle. With an oil-immersion objective, there is no refraction at the interface of the sample since oil and glass have the same refractive index. θ is the half angle of the focusing cone. It provides a tighter focusing condition.

In a classical configuration, medium 1 is air and medium 2 can be a solid (fused silica for example in figure 5.14 (top)). As at 800 nm $n_{SiO_2}=1.45 > n_{air}=1$, the refraction law induced $\theta_{SiO_2} < \theta_{air}$. To bypass this angle reduction, one can replace air by a liquid whose refractive index is higher than air. For example, oil replaces air in figure 5.14 (bottom), and since $n_{oil}=1.45 \approx n_{SiO_2}$, then the refraction is suppressed. For our experiments, the refractive index of Si is 3.5 at $\lambda=1.3 \mu\text{m}$, one would need a liquid with an equivalent refractive index, which does not exist.

5.3.1.2 Solid-immersion solution to reach NA up to 3.5

A second technique mainly used in microscopy to enhance the resolution of the system is to replace the oil by a solid. This technique is called solid-immersion lens (SIL) and has been developed by Mansfield *et al.*, [144] with a solid lens with a refractive index $n=2$ (glass). The solid immersion lens is a perfect hemisphere and is employed for microscopy for the characterization of nanophotonic devices [145, 146, 147, 148]. Two types of SIL exist: the standard hemispherical solid immersion lens (h-SIL) and the super-solid immersion lens (s-SIL) [149]. Both of these techniques rely on a theory described by Born and Wolf [150]. According to this theory, the light can be focused in a high index sphere (such as Si) without any aberrations, as shown in figure 5.15. In practice, there are two different points, called "aplanatic points" that are aberration-free focal points in a sphere. We directly treat the case for a Si-sphere. Aplanatism is a property of optical systems capable of forming an image perpendicular to the optical axis for an extended object perpendicular to the optical axis.

The first aplanatic point is the center of the sphere. The incoming angular components of focused laser pulse arrive all at normal incidence to the surface of the sphere. According to the Fresnel's law, these rays are not refracted at the surface of the sphere. Then, the spherical wave formed by the objective for focusing inside Si can totally match with the spherical interface air-Si. Figure 5.15 is a schematics

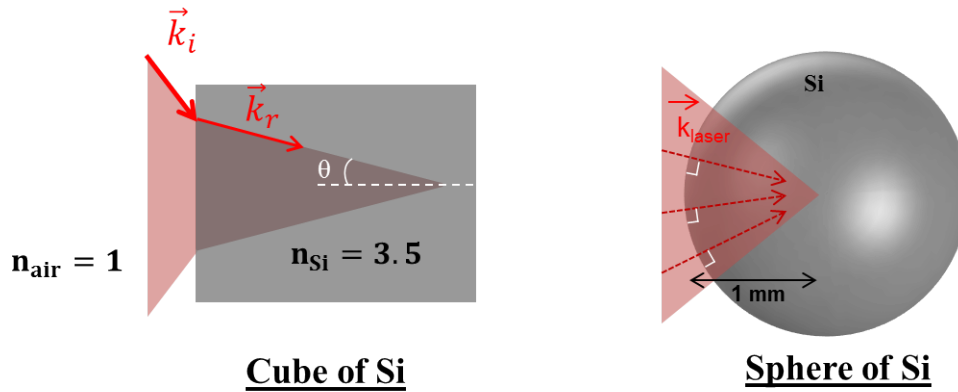


Figure 5.15 – Refraction at air-Si interface in case of the cube of Si where k_i and k_r are incoming and refracted rays, respectively. We do not show the reflected one in the opposite direction. The right part shows the suppression of the refraction when the beam is focused at the center of a sphere of Si.

illustrating the suppression of the refraction at the surface of the sphere compared to the cube, by focusing at the first aplanatic point of the sphere. In this thesis we concentrate on this first geometrical focus, but we briefly detail the second one.

The second aplanatic point inside a high-index sphere is located at a distance $z_0 = (1/n_{Si})R$ where R is the radius of the sphere. When the focus of the microscope objective is at z_0 , the incident refracted beam has a focus at $z_1 = n_{Si}R$, as described in figure 5.16.

We decide to investigate the possibility of laser writing at the center of the sphere, being the first aplanatic point described above. The spatial resolution provided by such an experiment is about $\lambda/2NA$ [151]. In this section, we demonstrate that $NA \approx 3$ can be reached, providing a spatial resolution at $\lambda = 1.3 \mu\text{m}$ of 230 nm. The following section is the description of the experiments realized at the center of a 1mm-radius Si sphere. Therefore, we can directly compare this experiment to the previous one, where the interaction takes place, 1 mm inside silicon.

We compare in table 5.2 the two focusing arrangements obtained with our differ-

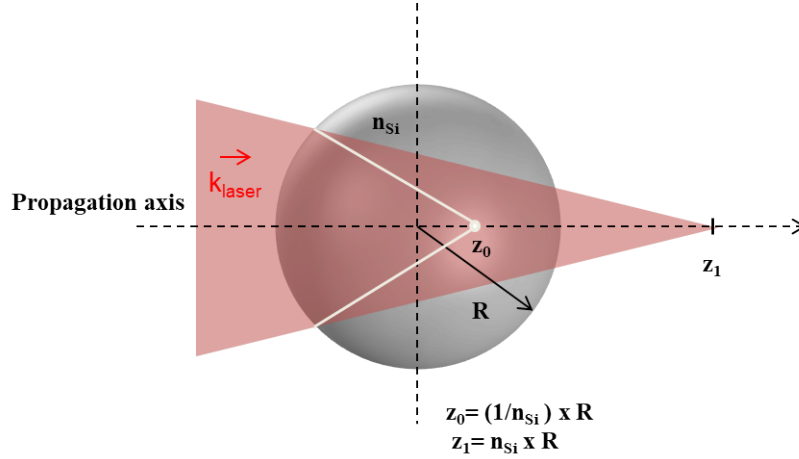


Figure 5.16 – Schematics of the second aplanatic point inside a high-index sphere. R is the radius of the sphere.

NA	θ in a cube of Si	$NA_{eq,sphere}$	θ in a sphere of Si ($=\theta_{air}$)
0.3	5.05	1.05	17.9
0.45	7.60	1.57	27.5
0.65	11	2.27	41.6
0.85	14.4	2.97	59.8

Table 5.2 – Comparison of the focusing parameters (NA and half-angle of focusing) in a cube of Si (left part of the table) and at the center of a Si sphere (right part of the table). The NA equivalent in the sphere is the multiplication between the NA in air and n_{Si} .

ent microscope objectives. We compare the maximum angle obtained in air, and in silicon. We clearly see the effect of the high index of Si, preventing the interaction to be locally confined in the bulk of the Si cube. Even for strong focusing conditions (up to $NA=0.45$), the interaction remains relatively paraxial (maximum angles less than 28 degrees).

The spheres are from Tydex (HRFZ-Si), with a very high resistivity: ≥ 10 k Ω .cm. The silicon is crystalline with very low impurity level as evidenced with the high resistivity value. It is generally used in THz experiments to collect signals. According to the new geometry of the set-up, we can reach numerical apertures close to 3 (table 5.2). Considering figure 5.6 as an estimation of the NA needed to induce breakdown in bulk-Si, focusing inside the sphere with the objective of $NA=0.85$ is expected to be a successful experiment to induce permanent modifications at the center of the sphere. If we succeed in inducing modifications inside Si, it should be located only at the center, meaning that such an experiment requires a new sphere for every new damage test.

5.3.2 Experimental details

5.3.2.1 Femtosecond laser pulses focused inside Si spheres

The experimental set-up is adapted to the new spherical sample as described in figure 5.17. We apply a systematic procedure for the alignment of the experiment. First, we generate a plasma in air by focusing the pump with a microscope objective. Block 1 in figure 5.17 shows the imaging system of the experiment to obtain a clean image of the focus in the direction of Y and Z axis, with a 20X magnification. Then,

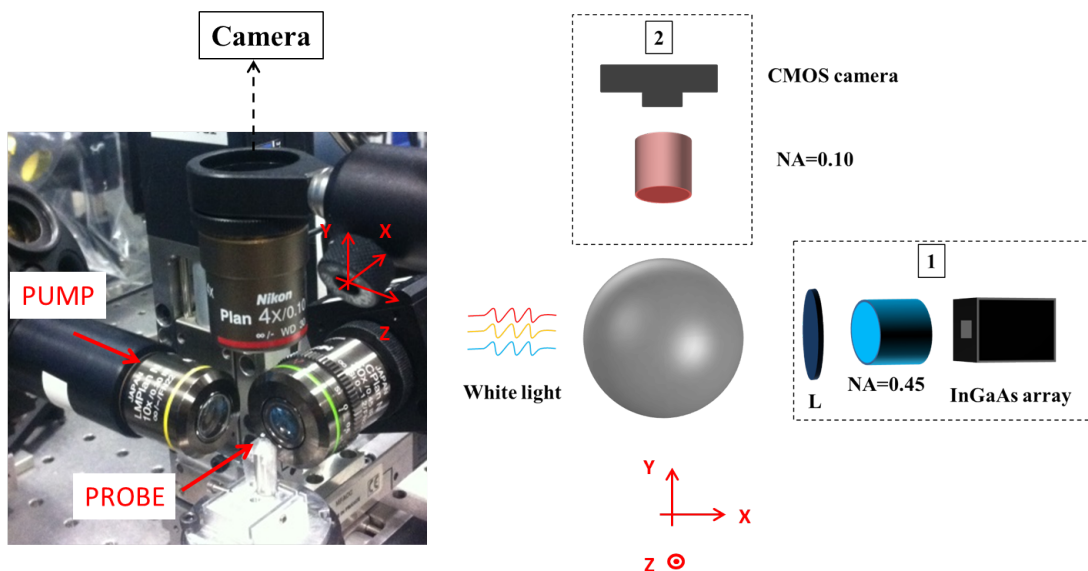


Figure 5.17 – Photography of the focusing part of the experiment and schematics of the two perpendicular imaging arms to position the focus at the center of the sphere.

we locate the focus with this plasma in the direction of the X axis, and we fix the CMOS camera above this plasma, providing a clean image of the plasma with a 4X magnification, represented by the block 2 in figure 5.17. Once the three coordinates have been identified, we position the center of the sphere at the coordinates of the plasma in air. With the two cameras, we can precisely align the sphere in every direction.

One additional difficulty of focusing inside a sphere remains in the geometry of the experiment. Indeed, using microscope objectives with high NA implies a short working distance (distance between the output of the objective and the focal plane), with high angles of incidence. For example, focusing the pump with $NA=0.85$ implies a distance of $200\ \mu\text{m}$ between the objective and the sphere, and a total angle of focusing almost equal to 120° . In order to release as much surface as possible on the sphere, we have designed and fabricated a new sample-holder shown in figure 5.18, with almost 180° free angle on the side where the pump is focusing.

5.3.2.2 Magnification of the imaging system

To detect the modification at the center of a sphere, we image the object through a spherical surface, and under 1 mm of Si. This configuration changes the magnification of the microscope system. With the small angle approximation, we can estimate the magnification induced by the sphere. If we consider a small object placed at the center of the sphere surrounded by air, we estimate that the magnification, with the presence of the sphere is increased by a factor equal to the index of the sphere, $n_{Si}=3.5$. This small angle approximation holds for objects smaller than the sphere, and for modest NA objectives. We expect that the size of the object will not exceed a few microns, so the condition on the size of the object is respected. Concerning the use of modest NA objectives, it remains questionable since the goal of the experiment is to investigate hyper NA ($NA \geq 1$).

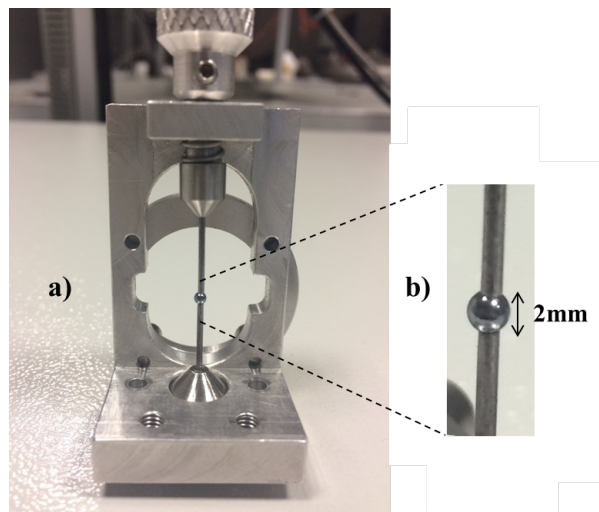


Figure 5.18 – a) Holder for our spherical sample of Si and b) zoom on the Si sphere.

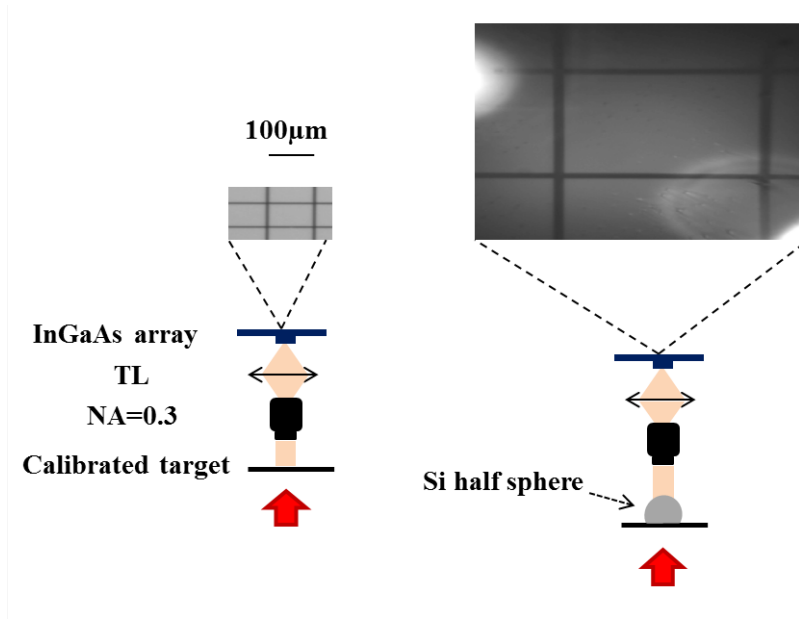


Figure 5.19 – Determination of the magnification induced by imaging through a silicon half-sphere. A calibrated target composed of squares with sides measuring $100\ \mu\text{m}$. By placing a half-sphere on the target, we measure the sides at $350\ \mu\text{m}$. The extra magnification given by the sphere is 3.5.

To verify our calculation, we measure this magnification by imaging a calibrated target through a half-sphere. We assume that imaging a plane in contact with a half-sphere is similar to image an object at the center of the sphere. This assumption is valid if the radius of the sphere and the half-sphere are equal, which is verified in this study. Figure 5.19 shows the images of the calibrated target taken with and without the Si half-sphere. The calibrated target is illuminated with white light and imaged with a microscope system allowing 20X magnification. The analysis of the images gives a 3.5X of magnification induced by imaging through the half-sphere of Si. This magnification is combined with the microscope magnification.

5.3.3 Demonstration of the first modification induced with a femtosecond pulse inside Si

5.3.3.1 Increase of the NA up to Si breakdown

In this section, we focus the pump at the center of the sphere of Si, and we progressively increase the NA to see if the energy delivery is improved before reaching the center of the sphere. First, we try to probe the interaction inside the sphere with the 60 fs probe beam. The focusing being so tight, we cannot perform a quantitative study on the transmission of the probe. However, we observe the confinement of the plasma when we increase the NA. Imaging the plasma inside the sphere is an important indication to know if the system is well aligned: the plasma is supposed to be generated at the center of the sphere. During the experiments, the symmetry of this plasma is taken as an indication of the quality of the alignment.

Figure 5.20 shows the evolution of the transient modifications located at the center of the sphere with the increase of the NA. The plasma is probed with 10 ps of delay between the pump and the probe. The energy has been increased up to $10 \mu\text{J}$ (a near maximum value considering the damage threshold for the objective lenses that are used). We clearly see with the images that the angle of focusing is increasing, allowing an extreme concentration of the light. We can compare the length of the plasma for $\text{NA}=0.3$, inside the cube of Si (section 3.1.2.) and inside the sphere. The size of the plasma is smaller inside the sphere than inside the cube for the same focusing objective, highlighting the improvement of the confinement of the interaction. There is no permanent modification induced from $\text{NA}=0.3$ to $\text{NA}=0.65$ (NA values in air), and we image the free-carrier density generated inside Si. Even at high energies, permanent modification of Si is not achieved. As predicted in the model, irradiating the sphere with NA up to 0.65 in air, corresponding to an apparent NA in the sphere of 2.27, does not induce any permanent modification inside silicon. Only one objective can provide a numerical aperture above 2.27: $\text{NA}_{\text{air}}=0.85$, giving an equivalent aperture in the sphere $\text{NA}_{\text{app}}=2.97$.

Irradiation of the sphere with $\text{NA}=2.97$ is performed with the microscope objective of 100X magnification. The working distance is 1.2 mm, meaning that the output of the objective is only $200 \mu\text{m}$ from the surface of the sphere. At the center of the sphere, the spot size can be estimated by:

$$w_0 = \frac{\lambda}{2n_{\text{Si}}\sin\theta} \quad (5.6)$$

According to table 5.2, $\theta=59.8^\circ$ for the 100X objective with $\text{NA}=0.85$, giving a theoretical waist at the focus $w_0=290 \text{ nm}$. Considering this sub-micrometer scale, we do not perform pump-probe measurements at the maximum NA. The sphere is illuminated continuously with white light to detect the potential modification *in situ*. We fix the incoming energy at 20 nJ, corresponding in this case to a theoretical fluence in vacuum of $F=7.5 \text{ J/cm}^2$, well above the fluence needed to reach the threshold for surface modification.

We first take one picture of the interior of the sphere before the laser irradiation. The sphere is irradiated by 1, 10, 100, 1000 and shots, on the same spatial coordinates. The number of shots is controlled with a mechanical shutter. Even after 1 shot, the modification appears at the center of the sphere [152], as it is illustrated

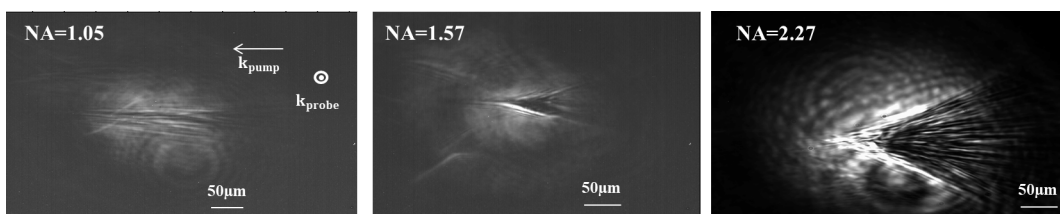


Figure 5.20 – Pump-probe images of the plasma at the center of the sphere for different NA (1.05 to 2.27). The pump is coming from the right. Energies are a few micro-joules, which is relatively high.

in figure 5.21. After 10 shots, the modification appears clearly and the size of the damage rapidly saturates. We have repeated the same experiment with the same energy, on 5 spheres. At $E=20$ nJ, the modification is highly reproducible.

It would have been interesting to estimate the free-carrier density generated by TPA, or the fluence delivered to the focus with this configuration. Imaging the beam through a Si sphere is unreasonable. One solution to transpose the beam imaging study (see Chapter 4) to this spherical arrangement is to image the beam at the rear face of a hemisphere. The main difficulty remains in the spot size, and in the resolution of the imaging beam set-up. Our beam imaging set-up relies on a long working distance objective with $NA=0.7$, and does not allow to image the propagation of the beam focused with $NA=0.85$.

We have, for the first time, induced a permanent modification inside a sample of intrinsic crystalline silicon with single ultra-short pulses. When we look at the images in figure 5.21, the damage area seems homogeneous compared to what can be observed in the nanosecond regime, where guiding structures and voids are mixed. To characterize the modified area inside a solid, several methods can be used, such as Raman spectroscopy [153], TEM (Transmission Electronic Microscopy) [154] or interferometry [155], like presented in Chapter 3. Raman spectroscopy and TEM are generally used to characterize the crystalline phase of the modified area but that requires complex sample preparation (precise cut through the modification). Interferometry allows to determine the change of the refractive index Δn . We have chosen to use our interferometry system presented before. However, in the framework of a new collaboration on the subject, spheres damaged at the center with our 60 fs laser have been sent to the *Laser Physics Centre* (Canberra, Australia). The method being implemented to analyze the spheres consists in removing matter around the modification by polishing, and then they will try to extract lamellas containing the modification, which could be analyzed with TEM and electron diffraction.

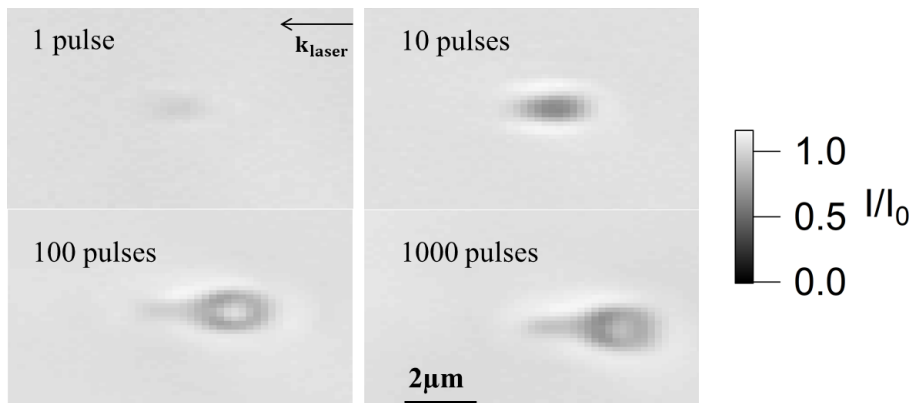


Figure 5.21 – White light images of the modification induced by 20 nJ pulses. The modification is visible since the first shot, and grows with the increase of the number of shots, until a saturation after 1000 shots.

5.3.4 Local change of the refractive index

5.3.4.1 Interferometry set-up

The interferometry set-up is the one described in section 3.2.2.1. We only adapt the final stage for imaging inside the sphere. The measurement is realized with the 60 fs probe. Because of the curvature of the sphere interface, the probe slightly focused at the center, inducing a restricted illuminated area. To have homogenous patterns between the object beam and the reference beam, a second sphere (without damage at the center) is placed at the object plane of the microscope objective on the reference beam (figure 5.22). The probe propagates through 2 mm of Si, inducing an change of the optical path compensated by the second sphere on the reference arm. We obtain two similar illuminations (phase and amplitude), allowing interferences and phase-shift measurements. The interference pattern is constituted of rings due to the residual difference of curvature between the reference and object beams. A typical image on the InGaAs camera is shown on the right side of figure 5.22.

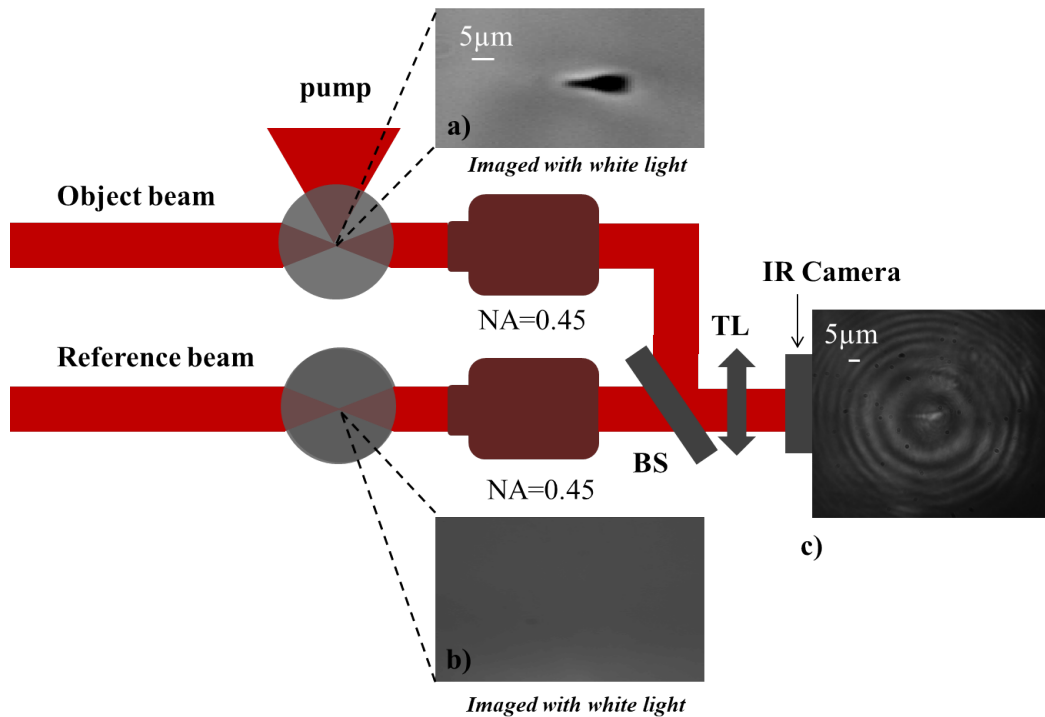


Figure 5.22 – Schematics of the last stage of the interferometer: the object beam propagates through the damaged sphere (image a is the modification illuminated with white light). The reference propagates through a blank sphere (image b is the reference illuminated with white light). The interference pattern obtained by recombining the two arms with a beam splitter (BS), a tube lens (TL) and a InGaAs camera is shown on image c), with the two femtosecond probe arms. The bright area at the center of the rings is the phase-shift induced by the damage.

5.3.4.2 Estimation of the refractive index change

We perform the same measurements as for the plasma inside Si: we apply the four-step procedure by moving the piezoelectric mirror. We have tried to induce several modifications inside the sphere. The modification has been induced at the center of the sphere with 1000 shots at 20 nJ pulses. The results are presented in figure 5.23. The modification corresponds to the blue area. We measure a negative phase-shift $\Delta\phi \approx -0.45$. We can deduce the refractive index change induced by the laser-induced modification with the formula:

$$\Delta n = \frac{\lambda \Delta\phi}{2\pi d} \quad (5.7)$$

where d is the modification size, Δn is the change of the refractive index, and $\Delta\phi$ is the corresponding phase-shift. Using equation 5.7 and taking a modification size of $1.3 \mu\text{m}$, the change of the refractive index induced by 1000 laser shots is: $\Delta n \approx -0.07$. Guiding structures demonstrated in the nanosecond regime present a positive change of the refractive index, meaning that the change of refractive index of our modified area in the sphere is apparently not similar to the one obtained in the nanosecond regime. Negative index changes have been reported previously in femtosecond dielectric modifications and are usually attributed to the formation of micro-voids [156].

To confirm this result, we apply another measurement illustrated in figure 5.24, still relying on interferometry, to retrieve the phase-shift induced by the modification. Instead of performing the 4-step procedure measurement, we move the piezo-electric mirror with 5 nm steps, on a total length of one λ . We report the intensity of the pixel located on two different sites. The first site is one pixel on the modified area (point A in figure 5.24). The second site is a pixel located on an area constituted of unmodified material (point B in figure 5.24). We chose two measurement sites close to each other that would provide the same phase measurement if there were no modification induced by the laser. Figure 5.24 shows the results obtained with this second method, consisting in plotting the phase of the unmodified material and the phase of the damaged material. This method provides directly the phase-shift between the unmodified material and the modified area, by reporting the space between two minima or maxima. We use the fitting curves represented by the blue and red lines in figure 5.24, and we find $|\Delta\phi| = 0.47$. The last crucial information is

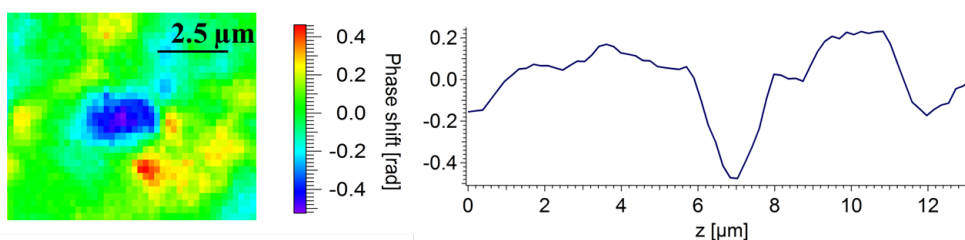


Figure 5.23 – Interferometry measurements performed on the modifications induced inside the sphere with 20 nJ pulses. We obtain a negative phase-shift of -0.45. The curve is the horizontal line profile at the center of the phase map.

the sign of this phase-shift, and for that we simply identify which curve is ahead, knowing the scanning direction for the piezo. We clearly see that the phase of the unmodified material is delayed compared to the damaged area. This indicates that the phase-shift is negative, which is consistent with the results deduced with figure 5.23. The four-step measurements and the reconstruction of the two sinusoid curves provide the same result: a maximum negative phase-shift of ≈ -0.45 . A negative phase-shift implies that the light propagates faster inside the modification than inside crystalline Si. We have then generated a rarefied area at the center of the sphere. We cannot definitively conclude that we have generated voids since the local change of refractive index for a void would be largely superior to -0.07 , but the presence of nanodisruptions or nanoporosity is a possible explanation.

Despite a change of the refractive index measured at a low value compared to voids, it remains a new result promising for future fundamental researches. In dielectrics, similar studies have been conducted in the bulk of transparent medium, and laser irradiation may induce extreme conditions of temperature and pressure (TPa and 100 eV) [17]. Under these conditions, new super dense phases of solids are possibly created. With these results, we can envision new micro-explosion experiments, combined to a time-resolved pump-probe diagnostic which could allow to study the dynamic of the phase change with femtosecond time resolution.

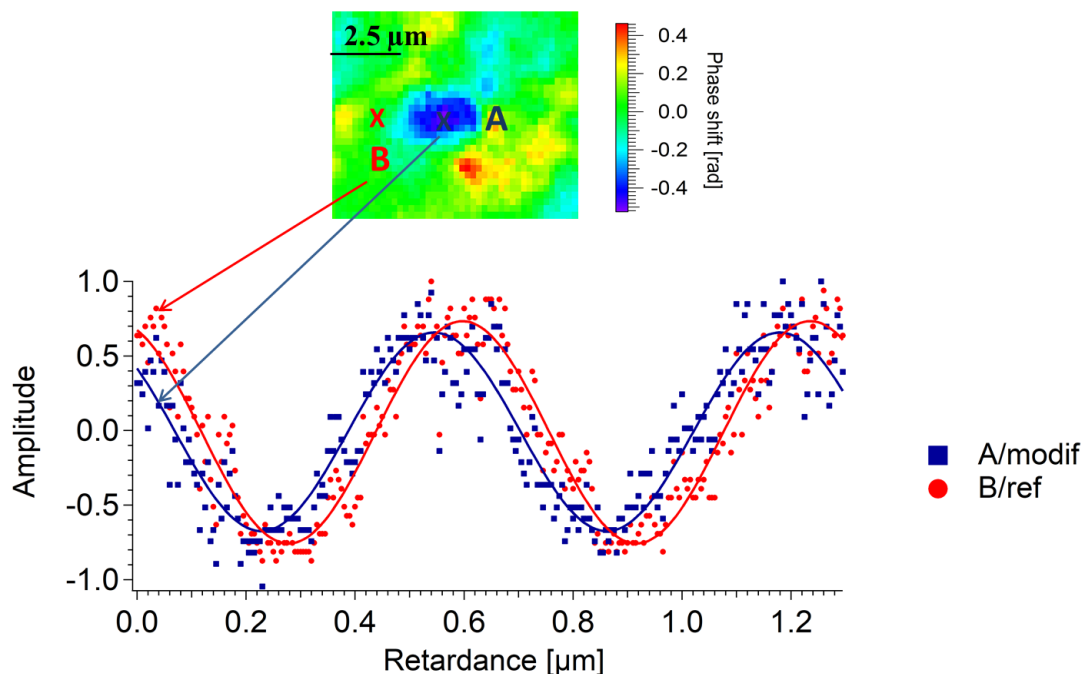


Figure 5.24 – Reconstruction of the phase evolution of the modified area A (blue square are experimental data and line is a fitting curve) and unmodified area B (in red) after 1000 shots at 20 nJ.

5.4 Conclusions

This Chapter was devoted to find experimental configurations to bypass the optical limitation to the energy delivery of femtosecond beams inside Si, preventing to modify the bulk of the material. We have taken advantage from a numerical model allowing to retrieve the nonlinear beam propagation 1 mm under the surface. With this numerical tool, new arrangements have been simulated, highlighting the ability of some possible configurations to provide Si modifications. The reliability of the solutions tested has been judged under two criteria: the delivered fluence has to reach the surface damage threshold $F=0.35$ J/cm², and/or the free-electron density has to increase up to the critical density at 1.3 μm inside Si, $N_c=6.6\times 10^{20}$ cm⁻³. Despite the difficulty to estimate the delivered fluence and/or the free-carrier density generated at the focus in the experiments presented in this Chapter, we assume that in the picosecond and nanosecond regime, the increase of the lattice temperature must lead to the bandgap closure playing a significant role in the damage mechanisms. The question of avalanche is still under debate since no signature of this process has been demonstrated. In the femtosecond regime, optical breakdown of bulk-Si has been achieved by delivering efficiently the energy with extreme focusing, allowing a rise of the excitation level above the damage threshold.

Femtosecond, picosecond and nanosecond regimes for modification in bulk-Si have been experimentally investigated. These three interaction domains present different characteristics, summarized in Table 5.3. The first results presented in this Chapter on the modifications induced by picosecond laser pulses do not allow to conclude completely on the performance for applications. This study needs to be continued to find the optimal and appropriate experimental conditions for controlled modification of Si. Concerning nanosecond laser irradiation, interesting results show a large capacity to write structures inside Si wafers but more efforts are needed to improve the level of control. Ultra-fast modification is an interesting regime to investigate after our feasibility demonstration with the sphere configuration. The challenge is now to adapt the solid-immersion technique allowing to bypass the optical limitation to the energy delivery inside Si, for 3-D micro-machining. The disadvantage of our set-up is the spherical sample, which is obviously not appropriate to address applications. Ideally, similar experiments need to be performed in Si-wafers. Micro-machining in 2-D is possible with the SIL technique, but controlled 3-D modification inside Si will require the conception of new experimental set-ups. This constitutes one of the perspectives of research resulting from this PhD research.

	Picosecond	Nanosecond	Femtosecond (in a sphere)
Conditions of bulk-modification	Multiple μJ pulses NA=0.45	Single μJ pulse NA=0.3	Single nJ pulse NA=3
Quality and precision	Non-reproducible Non-controllable	Highly reproducible Control of the modification depth inside the sample, no control on the homogenous change of refractive index	Highly reproducible Modifications can be written on a reasonable zone along the z-axis
Size of the modified area	Single shot damage not detected	Micrometer scale	Nanometer scale
Index change	Not measured	Positive index change [12]	Negative index change

Table 5.3 – Comparison of the focusing parameters (NA and half-angle of focusing) in a cube of Si (left part of the table) and in a sphere where there is no refraction at the air-Si interface (right part of the table). The NA equivalent in the sphere is the multiplication between the NA in air and n_{Si} .

Conclusion

Laser-induced modification of silicon is an active area of interest, both from a fundamental and a technological point of view. The mechanisms of ultra-short pulse laser ionization of Si have been discussed for decades, but there are still questions that researchers are facing: in particular, ultra-short pulses are inefficient to induce permanent changes in bulk-Si.

Different experimental techniques have been applied to increase our knowledge on the confined interactions inside the volume of Si. Ultra-fast imaging in the IR domain has revealed an under-dense micro-plasma [1]. The ultra-short pulse, focused tightly inside the material, is so intense that nonlinear ionization takes place and generates free-carriers in a localized volume. This cloud of free electrons has been imaged 10 ps after the propagation of the pump pulse. Even if the energy is increased, it reveals a saturation of the excitation at $N_e=3\times 10^{19}$ cm⁻³. In the literature, the critical density is generally considered as a criterion to reach the optical breakdown. In Si (at our working wavelength $\lambda=1.3$ μm) this density is $N_c=6.6\times 10^{20}$ cm⁻³, which is more than one order of magnitude above the maximal electron density reached in our experiment. The density of absorbed energy can be deduced from this result, assuming a two-photon absorption process. We obtain $\Delta E_{exp}=9$ J/cm³, being several orders of magnitude below the energy density needed to reach the melting point of Si ($\Delta E_{fus}=5$ kJ/cm³). These pump-probe experiments have highlighted a strong limitation of the interaction produced by an intense IR 60 fs-pulse in bulk-Si far below the excitation required to induce the optical breakdown.

A crucial question after these first results was: why the interaction undergoes a clamping despite a huge energy contained in the incoming pulse ? To bring new evidence of the clamping, the propagation of the beam has been fully reconstructed inside the material for different energies and different NAs. This study has provided the absolute fluence that was delivered along the propagation axis. In a similar way as the pump-probe study, a strict clamping of the interaction has been highlighted. The fluence which is delivered to the focus does not exceed $F=0.12$ J/cm² for the highest NA (0.65). We further compare this value to the fluence needed to reach the surface damage threshold. In dielectrics, it is generally assumed that the bulk modification threshold is above the surface damage threshold. We propose this surface damage threshold as a minimal fluence to reach in order to exceed the modification threshold in bulk-Si. Under the same conditions of irradiation (same laser and same sample), the surface damage threshold is experimentally determined at $F=0.35$ J/cm², which is higher than the maximal fluence delivered to the focus

inside Si. The 3-D reconstructions have also highlighted the increasing volume of the interaction when the incoming energy increases, mainly due to two-photon absorption (TPA) before the focus.

To go further, a numerical model has been developed to predict correctly the experimental results, and to identify the main physical mechanisms involved in the optical clamping [9]. This model has revealed the effect of several mechanisms which limit the excitation. Strong TPA in the prefocal region is responsible for large energy losses. The plasma absorption and plasma defocusing are the two main mechanisms that prevent the energy to be delivered to the focus. The model being in a good agreement with the experiment, it has been used to consider numerically new arrangements before undertaking experiments. Several possibilities which could lead to a better energy deposition at the focal volume have been investigated: an increase of the multiphoton order of the nonlinear ionization, an increase of the pulse duration, space and time focusing, beam shaping, or extreme focusing with a Gaussian beam.

Among the solutions numerically tested, the use of longer pulses is a relatively simple solution. Preliminary results on picosecond and nanosecond laser induced damage inside Si show that it is possible to damage the bulk with 100% of probability, but without the precision and the control offered by femtosecond lasers in dielectrics. To limit the strong absorption in the prefocal region and plasma effects at the focus with femtosecond pulses, we turned to solutions to increase the NA. With conventional focusing geometries, NA reaches 1.4 with the oil-immersion lens technique. Since our model predicted that it will not be sufficient to induce Si breakdown, we searched a new configuration to reach what we call "hyper-NA" values ($NA > 1.5$). The main limiting factor to high focusing angles inside Si is the material itself. Due to its high refractive index ($n_{Si}=3.5$), the interaction becomes indeed almost paraxial after crossing the Si surface. In our experiment, the incoming plane wave is transformed into a spherical wave by the focusing objective. By working inside a sphere instead of a cubic Si sample, the angular components of the incoming pulse are locally orthogonal to the surface. As the laser pulse matches perfectly the sphere interface, the refraction is suppressed at the interface of Si and the apparent NA is the NA multiplied by $n_{Si}=3.5$. We demonstrated that focusing an ultra-short laser pulse at the center of a Si sphere was one solution to achieve the optical breakdown of the material.

We obtained in particular two interesting results during this last development. First, we determined that the incident laser energy required to detect a modification with the IR microscope was 5 nJ. Secondly, the size of the modification is in the micro-metric scale, being extremely interesting to create new structures inside Si with a minimal size. Moreover, the preliminary analysis of the laser-induced modification realized in the sphere shows a negative change of the refractive index. This change is not sufficient to assume the creation of a micro-void inside Si, but it indicates that the structure generated tends to be nano-disruptions and/or laser-induced porosity in the material. This is an encouraging work concerning the field of micro-

explosion and new structural phases discovery, opening many perspectives to study matter under extreme confinement. To push this experiment to a higher level of confinement, irradiating the sphere with more beams (and thus more energy) would be interesting and new development. Each beam would induce extreme conditions (Mega bars pressures), meaning that only two beams coming from two opposite directions would induce temperature and pressure conditions that have probably never been reached so far in Si. A solid upon such strong thermodynamic conditions can present several crystalline arrangements and have very different properties (optical, electrical...). For example, diamond can be transformed into graphite, and these localized structural-phase transformations can be used in perspective of photonic crystals [157].

From an industrial point of view, working inside a Si sphere is not convenient. The most natural solution to benefit from our results and working in Si wafers (used in micro-electronics) is to place an half-sphere on a wafer, like the Solid Immersion Lens technique (SIL). The second geometrical focus, as it can be obtained with such a technique (see chapter 5) can be located inside a wafer, and the experiment can still benefit from the suppression of refraction at the interface air-Si if there is no air between the half-sphere and the wafer. The modification is then confined inside the wafer. This study has been initiated for a few months in the laboratory, and presents promising results. The main difficulty is that only 2-D writing is possible with this technique, since the depth coordinate cannot be displaced away from the geometrical focus. The other difficulty for 2-D writing process by moving only the wafer is the quality of the surfaces in contact (rear surface of the half-sphere and front surface of the wafer) that need to be perfect for adequate displacement of the wafer. This experiment still requires technical improvements before to develop a robust processing technique.

To conclude on this PhD research, the first demonstration of ultra-fast optical breakdown inside Si has been provided twenty years after the one inside dielectrics. The unconventional experimental configuration developed for this study remains strongly unadapted to industrial laser-Si processing, but brings a new powerful confinement technique with highly promising and exciting scientific perspectives like the discovery of new crystallographic phases of Si and other semiconductors.

List of Figures

1	Schéma du montage expérimental pour l'imagerie de plasma : un système laser titane saphir combiné à un OPA délivre des impulsions de 60 fs à $\lambda=1,3 \mu\text{m}$ avec une cadence égale à 100 Hz. Le faisceau polarisé linéairement est séparé en deux à l'aide d'une lame séparatrice (LS) : 10% de l'énergie est dédiée à la sonde, 90% constitue la pompe. La taille du faisceau est augmentée avec un système afocal composé d'une lentille divergente (L1) et une lentille convergente (L2) permettant un grandissement 1,5X. L'énergie de pompe est contrôlée grâce à une lame demi-onde et un polariseur ($\lambda/2 + P$) et focalisée avec un objectif de microscope (OF_1). Le délai entre la pompe et la sonde est ajusté avec une ligne à retard constituée de 4 miroirs or (M1 à M4). L'éclairement de la sonde est mis en forme à l'aide d'un diaphragme (D) et d'une lentille convergente (L3). Le plan focal de la pompe situé à 1 mm sous la surface du cube de Si est imagé à l'aide d'un microscope infrarouge constitué d'un objectif de microscope (OF_2), une lentille de tube (permettant un grandissement 20X ou 50X selon l'objectif) et une caméra infrarouge.	iv
2	Exemple d'image obtenue avec le montage pompe-sonde : le laser se propage de droite à gauche, un plasma d'électrons-trous est généré dans le volume. Les électrons libres absorbent les photons de la sonde par Bremsstrahlung inverse. Le délai entre la pompe et la sonde est de 10 ps, l'énergie de la pompe est de 10 nJ.	v
3	Exemple de la reconstruction du faisceau focalisé avec $NA=0,3$ pour différentes énergies : 15 nJ (haut), 83 nJ (milieu) et 345 nJ (bas). Le point focal de la pompe est à la coordonnée $z=1$ mm.	vi
4	Saturation de la fluence délivrée au plan focal en fonction de l'énergie incidente pour $NA=0,3$, $NA=0,45$ et $NA=0,65$. Le seuil d'endommagement de la surface est indiqué en pointillés.	vii
5	Simulations et mesures expérimentales de la propagation de l'impulsion pour $NA=0,3$ ($E=50$ nJ), $NA=0,45$ ($E=12$ nJ) et $NA=0,65$ ($E=11$ nJ). La colonne de gauche présente les résultats expérimentaux et la colonne de droite les simulations correspondantes.	viii
6	Images du dommage au centre de la sphère de Si éclairée en lumière blanche. $E=20$ nJ, $NA=3$	x

1.1	Energy-band structure of Si from [26]. E_g is the energy bandgap. Positive signs indicate holes in the VB, and negative signs indicate electrons in the CB.	3
1.2	Temperature-dependence of the bandgap energy of Si.	4
1.3	a) Band diagram of Si; b) Fermi-Dirac distribution and c) carrier concentration for intrinsic silicon at thermal equilibrium. From [26].	5
1.4	Schematic view of the photoionization processes involved in Si at $1.3 \mu\text{m}$. a) Two-photon ionization, and b) Tunnel ionization. PI processes inside Si are depicted in the case of a direct bandgap.	8
1.5	Schematics of the atom arrangement in the case of pure Si, N-doped Si with phosphorus and P-doped Si with Boron.	13
1.6	Simplified schematics of the type of recombination processes considered in this study: radiative, Shockley-Read-Hall (SRH) and Auger recombination.	15
1.7	Schematics of self-focusing process. The incoming laser beam with a Gaussian intensity profile propagates through a solid target whose refractive index becomes intensity-dependent. The refractive index increases and acts like a converging lens: the beam is focused.	19
1.8	Schematics of self-phase modulation and frequency shift in a medium irradiated with short optical pulse.	20
2.1	Design of ASUR platform.	26
2.2	Schematics of the stages of the laser system.	27
2.3	Spectrum of the incoming pulse after compression.	28
2.4	Evolution of the pulse duration when propagating through Si (red) or SiO_2 (blue) at $\lambda=1.3 \mu\text{m}$. The GVD for fused silica is equal to $-2.3 \text{ fs}^2/\text{mm}$, whereas for Si the GVD is $1462 \text{ fs}^2/\text{mm}$	30
2.5	a) Schematics of the amplification by frequency difference and b) Conservation of the energy.	31
2.6	Schematics of the different stages inside an OPA.	33
2.7	Experimental set-up for the beam imaging: the beam that we image is at the output of the OPA. We use a lens ($f'=200 \text{ mm}$) to image the beam onto a CMOS camera with a magnification of $\gamma=0.4$	34
2.8	Image of the beam taken with a CMOS camera. The fluence image is proportional to the square root of the camera image, due to nonlinear response of the camera at $1.3 \mu\text{m}$. The graphs are cross-sections (dots) of the beam profile, with a Gaussian fit (curves).	35
2.9	Schematics of measurement of the pulse duration with single-shot autocorrelation: the incoming beam is split with a beam splitter (BS) and propagates through a BBO crystal. The spatial and temporal overlap allows second harmonic (2ω) generation, and the autocorrelation trace is imaged on a CMOS camera. x_0 is the distance from the center of the crystal, and ϕ is the angle between the two arms inside the crystal.	37

2.10	Analysis of the signal $S(x)$: a) image captured by the single-shot autocorrelator and b) autocorrelation trace corresponding to a vertical profile. The profile is fitted by a Gaussian envelope corresponding to a pulse width of ≈ 60 fs (under the Gaussian pulse shape hypothesis).	37
2.11	Analysis of the spectrometer signal. The signal is centered at 1325 nm and the width at FWHM is $\Delta\lambda \approx 90$ nm.	38
2.12	Spatial profile taken with a CCD camera at the output of the fiber.	40
2.13	Pulse duration and spectrum measurement taken at the output of the fiber. The pulse duration is measured by collecting the temporal profile with an ultra-fast photodiode and a 33-GHz oscilloscope. The spectrum is measured with the spectrometer presented on section 1.2.2.2.	40
3.1	Description of the pump-and-probe experiment on ASUR. A Titanium:Sapphire laser source delivers 800 nm pulses at 30 fs, and an OPA converts the wavelength to 1300 nm to work in the transparency domain of Si. A 90:10 beam splitter (BS) separates the pump and the probe beams; an afocal system composed of a divergent lens (L1) and a convergent lens (L2) changes the size of the beam with a magnification 1.5; an half-wave plate (HWP) and a polarizing beam splitter (PBS) control the energy; the energy in excess is blocked on a beam dump (BD), and we use a microscope objective (MO) to focus the laser. For the probe, mirrors (M1 to M7) constitute the manual delay line; the homogeneity is controlled with a diaphragm (D) and a lens (LS).	46
3.2	Transverse illumination of the interaction by the probe. The probe propagates through 9 mm of Si before imaging the free-carrier generation, which leads to pulse broadening by dispersion. The detection of the excitation is shown on the image (right), the dark area is the pump excitation coming from the right. The energy of the pump is 6 nJ and the delay between the pump and the probe is fixed at 10 ps.	48
3.3	Evolution of the probe transmission as a function of the incoming pulse energy. The dash-line is an eye guide for the saturation.	50
3.4	Probe transmission as a function of the pump pulse energy and the depth inside Si. Pump-probe delay is fixed at 10 ps. Dashed arrow follows the shift of the absorption front. a)6 nJ, b)25 nJ and c)55 nJ.	51
3.5	Pump-probe observation of free-carrier diffusion inside Si. Images are taken with the InGaAs camera for different delays between pump and probe to observe the spatial spread of the plasma. Cross-sections are fitted by a Gaussian curve (bottom). The energy of the pump is 20 nJ focused with NA=0.3.	54
3.6	Evolution of the width of the plasma as a function of the delay in ns, for three different pump pulse energies. Markers are experimental data and lines are calculations.	55

3.7	Evolution of the probe transmission as a function of the delay in ns, for three different energies. Markers are experimental data and lines are calculations	56
3.8	Evolution of the probe transmission as a function of the delay in ns for 8-nJ pulses, taking a constant carrier lifetime (blue line) or recombination by Auger (red line). Experimental data are the blue circles.	57
3.9	Description of the ultra-fast-imaging microscope combined with Mach-Zehnder interferometer.	59
3.10	Phase map without (left) and with (right) the image processing procedure.	60
3.11	Description of the preparation of the calibrated sample. Step 1 is the ablation of the thin film of Si, and step 2 is the AFM scan to measure the optical path difference.	61
3.12	Interferometry measurement without the unwrapping and flattening procedure. The engraving line is in the red square.	61
3.13	Cleaning procedure for the phase-shift measurement. (a) Four-step procedure is applied with and without the pump beam, (b) the phase maps are reconstructed with equation 3.22 and (c) the subtraction of the maps with and without the plasma to get the phase shift.	62
3.14	Phase-shift measurement stability of the plasma for 96 acquisitions. The energy of the pump is constant and fixed at 15 nJ.	63
3.15	Amplitude stability of the minimal transmission of the plasma for 1000 acquisitions. The energy of the pump is constant and fixed at 15 nJ.	63
3.16	Amplitude (left) and phase (right) measurements for Si. The laser is coming from the right with 60 nJ energy pulses. $z=0$ is the geometrical focus.	64
4.1	Description of the beam imaging set-up. The pump (1300 nm-wavelength with a duration of 60 fs (FWHM)) is focused with a microscope objective (MO) in air, and is imaged by an IR microscope composed of a MO, an associated tube lens (TL) allowing 105X magnification on the IR camera.	70
4.2	Beam profiles acquired in air at low energy (26 pJ) for NA=0.3 (top). The reconstruction of the propagation (bottom) is all the cross-sections side by side.	72
4.3	Image of the beam taken at the focus of the propagation in air for NA=0.3. We extract from the image the sum of the pixels constituting the beam signal, the maximal value of the pixels, and the surface of the pixels.	72
4.4	Reconstruction of the beam propagation in air for NA=0.3 (top), NA=0.45 (middle) and NA=0.65 (bottom). At $z=0$, a line profile is taken to retrieve the beam diameter (right images).	73

4.5	Description of the beam imaging set-up. The pump is focused with a microscope objective (MO) at the rear face of a Si-wafer, and is imaged by an IR microscope composed of a MO, an associated tube lens (TL) allowing 105X magnification and an IR camera.	75
4.6	Reconstruction of the beam propagation in Si for NA=0.3 at 15 nJ (top), 83 nJ (middle) and 345 nJ (bottom). The geometrical focus is located at z=1 mm.	76
4.7	Gaussian pulse defined by its maximal intensity I_0 and FWHM.	77
4.8	Reconstruction of the beam propagation in air for NA=0.45 at a)12 nJ, b)35 nJ and c)260 nJ; NA=0.65 at d)11 nJ, e)80 nJ and f)240 nJ The geometrical focus is z=1 mm.	79
4.9	Saturation of the peak fluence as a function of the incoming energy for NA=0.3, NA=0.45 and NA=0.65.	80
4.10	Energy delivered on each plane which has been imaged along the z-axis for different incoming energies at NA=0.3. The geometrical focus is at z=1 mm.	81
4.11	Volume of energy absorbed from the surface for NA=0.3. The front face is at z=0, and the focus is at z=1 mm.	83
4.12	Experimental set-up for energy balance inside Si with NA=0.3. The incoming energy is measured with a photodiode (Pd ₁) combined with an integrating sphere (IS) and the transmitted beam is collected and refocused with L ₁ and L ₂ on a second photodiode (Pd ₂).	85
4.13	Transmitted signal collected after the wafer of Si.	85
4.14	Energy absorbed (in nJ) determined with two methods: the imaging set-up (green) and the energy balance with the photodiodes (blue).	86
4.15	Schematics of the transformation principle: the initial strong curved wavefront becomes flatter and the nonparaxial propagation becomes close to a paraxial by increasing the factor s . f is the focal distance, a is the radius of the focusing objective's aperture, and θ is the half-angle of the maximum cone of light. Figure from [9].	87
4.16	Simulations of the peak fluence distribution for two incoming energies with and without the term including Kerr effect for NA=0.45. The geometrical focus is z=1 mm.	90
4.17	Simulations of the peak electronic density for 10 nJ (left) and 500 nJ (right) with and without plasma effects for NA=0.45. IB is Inverse Bremsstrahlung and Plasma Def is plasma defocusing. The geometrical focus is z=1 mm.	91
4.18	Simulations of the beam propagation for NA=0.3 (E= 50nJ), NA=0.45 (E=12 nJ) and NA=0.65 (E=11 nJ). The left column is the experiments and the right column is the corresponding simulations.	92
4.19	Comparison between experiments (symbols) and calculations (lines) for NA=0.3, 0.45 and 0.65.	92
4.20	Determination of the fluence threshold for silicon surface modification with 60-fs laser pulses at 1300 nm. The threshold is defined as the fluence above which a modification of the surface is systematically detected with an optical microscope.	94

5.1	Numerical simulation of the delivered peak fluence (top), peak plasma density (middle) and pulse energy (bottom) along the propagation axis. Calculations for two-photon absorption with $\lambda=1.3 \mu\text{m}$ (green line) are compared to the numerical case where $\lambda=2.2 \mu\text{m}$, allowing 3 photon ionization, shown for two different values of the ionization rate (blue and red). The incoming energy is 500 nJ with NA=0.45.	101
5.2	Schematics of the temporal and spatial focusing from [128]. The wavelengths of the initial spectrum are separated and recombined at the geometrical focus.	102
5.3	Numerical simulation of the peak fluence delivered (top) and the energy delivered along the propagation axis (bottom). Calculations are performed for 3 pulse durations: 60 fs (orange), 120 fs (green) and 600 fs (blue). The incoming energy is 500 nJ with NA=0.45.	103
5.4	Numerical simulation of the fluence distribution for an Airy-ring beam focused inside Si, with a 10 nJ pulse.	105
5.5	Simulated focusing conditions for NA=0.65, 1.05 and 1.5 inside Si with 10 nJ pulses.	106
5.6	Maximum peak fluence as a function of NA, in comparison with the surface damage threshold at 0.35 J/cm^2 . The dashed line in blue is a guide for the eye.	107
5.7	Experimental set-up for bulk modifications in Si with transverse illumination and imaging with an infrared camera. The laser delivers $1.55 \mu\text{m}$ -wavelength pulses with pulse durations between 800 fs and 10 ps. A half wave-plate ($\lambda/2$) combined with a polarizer controls the energy; a telescope with one diverging and one converging lens provides the adapted size of the beam; a dichroic mirror reflects the pump and transmits the visible white light (DM); and microscope objectives are used to focus the pump (MO_1) and collect the light (Tungsten) for the imaging system composed of a microscope objective (MO_2) and a tube lens (L). The image is obtained on a camera working in the NIR.	109
5.8	Image of the bulk of Si: laser is coming from the top, and dark areas are permanent modifications induced by pulses at: a) $6.6 \mu\text{J}$ at 800 fs; b) $5.6 \mu\text{J}$ at 5 ps and c) $6.6 \mu\text{J}$ at 10 ps.	111
5.9	Evolution of the damage probability in bulk-Si as a function of the pulse duration. The energy is $E=6.6 \mu\text{J}$, and the number of shots is 15 000 (0.5 s of exposure at 30 kHz).	112
5.10	Experimental set-up for the study of nanosecond modifications in the volume of Si. The detection of damage is realized with an infrared microscope for imaging (a), and the energy balance measurement set-up is composed of (L1) diverging lens; (L2) converging lens; (HWP) half waveplate; (CP) polarizing beam splitter; (IS) integrating sphere; (PD) photodiode; (MO) microscope objective; (TL) tube lens; (W); white light (b).	114

5.11	Infrared image of the focal region after 500 laser shots in bulk-Si: laser is coming from the right, and the dark area is the permanent modification induced by 3.5 ns laser pulses at $E=13 \mu\text{J}$	115
5.12	Probability for bulk modifications in Si, in single-shot regime (black triangles) and multiple-shots regime (red circles). We deduce the energy threshold in our case: $E_{th} \approx 2.3 \mu\text{J}$ for single-shot measurement, and $E_{th} \approx 1.7 \mu\text{J}$ for 200 shots.	116
5.13	Integrated measurement of nanosecond laser pulses transmitted through the sample for different doping concentrations.	117
5.14	Comparison between classical focusing in glass with microscope objective (top) and oil-immersion lens focusing (bottom). With air, ($n_{air}=1$), focusing inside fused silica (SiO_2) with $\text{NA}=1.45$ at 800 nm, refraction at the interface lowers the half-angle. With an oil-immersion objective, there is no refraction at the interface of the sample since oil and glass have the same refractive index. θ is the half angle of the focusing cone. It provides a tighter focusing condition.	119
5.15	Refraction at air-Si interface in case of the cube of Si where k_i and k_r are incoming and refracted rays, respectively. We do not show the reflected one in the opposite direction. The right part shows the suppression of the refraction when the beam is focused at the center of a sphere of Si.	120
5.16	Schematics of the second aplanatic point inside a high-index sphere. R is the radius of the sphere.	121
5.17	Photography of the focusing part of the experiment and schematics of the two perpendicular imaging arms to position the focus at the center of the sphere.	122
5.18	a) Holder for our spherical sample of Si and b) zoom on the Si sphere.	123
5.19	Determination of the magnification induced by imaging through a silicon half-sphere. A calibrated target composed of squares with sides measuring $100 \mu\text{m}$. By placing a half-sphere on the target, we measure the sides at $350 \mu\text{m}$. The extra magnification given by the sphere is 3.5.	124
5.20	Pump-probe images of the plasma at the center of the sphere for different NA (1.05 to 2.27). The pump is coming from the right. Energies are a few micro-joules, which is relatively high.	125
5.21	White light images of the modification induced by 20 nJ pulses. The modification is visible since the first shot, and grows with the increase of the number of shots, until a saturation after 1000 shots.	126
5.22	Schematics of the last stage of the interferometer: the object beam propagates through the damaged sphere (image a is the modification illuminated with white light). The reference propagates through a blank sphere (image b is the reference illuminated with white light). The interference pattern obtained by recombining the two arms with a beam splitter (BS), a tube lens (TL) and a InGaAs camera is shown on image c), with the two femtosecond probe arms. The bright area at the center of the rings is the phase-shift induced by the damage.	127

5.23	Interferometry measurements performed on the modifications induced inside the sphere with 20 nJ pulses. We obtain a negative phase-shift of -0.45. The curve is the horizontal line profile at the center of the phase map.	128
5.24	Reconstruction of the phase evolution of the modified area A (blue square are experimental data and line is a fitting curve) and unmodified area B (in red) after 1000 shots at 20 nJ.	129

Bibliography

- [1] A. Mouskeftaras, A. V. Rode, R. Clady, M. Sentis, O. Utéza, and D. Grojo, “Self-limited underdense microplasmas in bulk silicon induced by ultrashort laser pulses,” *Applied Physics Letters*, vol. 105, no. 19, 2014.
- [2] D. Grojo, S. Leyder, P. Delaporte, W. Marine, M. Sentis, and O. Utéza, “Long-wavelength multiphoton ionization inside band-gap solids,” *Physical Review B*, vol. 88, no. 19, p. 195135, 2013.
- [3] E. Gamaly and a.V. Rode, “Physics of ultra-short laser interaction with matter: From phonon excitation to ultimate transformations,” *Progress in Quantum Electronics*, vol. 37, no. 5, pp. 215–323, 2013.
- [4] K. Yamaguchi and K. Itagaki, “Measurement of High Temperature Heat Content of Silicon By Drop Calorimetry,” *Journal of Thermal Analysis and Calorimetry*, vol. 69, pp. 1059–1066, 2002.
- [5] A. Mouskeftaras, M. Chanal, M. Chambonneau, R. Clady, O. Utéza, and D. Grojo, “Direct measurement of ambipolar diffusion in bulk silicon by ultrafast infrared imaging of laser-induced microplasmas,” *Applied Physics Letters*, vol. 108, no. 4, 2016.
- [6] V. V. Kononenko, V. V. Konov, and E. M. Dianov, “Delocalization of femtosecond radiation in silicon.,” *Optics letters*, vol. 37, no. 16, pp. 3369–71, 2012.
- [7] E. V. Zavedeev, V. V. Kononenko, V. M. Gololobov, and V. I. Konov, “Modeling the effect of fs light delocalization in Si bulk,” *Laser Physics Letters*, vol. 11, no. 3, pp. 2011–2014, 2014.
- [8] E. V. Zavedeev, V. V. Kononenko, and V. I. Konov, “Delocalization of femtosecond laser radiation in crystalline Si in the mid-IR range,” *Laser Physics*, vol. 26, no. 1, p. 016101, 2016.
- [9] V. Y. Fedorov, M. Chanal, D. Grojo, and S. Tzortzakis, “Accessing Extreme Spatiotemporal Localization of High-Power Laser Radiation through Transformation Optics and Scalar Wave Equations,” *Physical Review Letters*, vol. 117, no. 4, 2016.
- [10] E. Ohmura, F. Fukuyo, K. Fukumitsu, and H. Morita, “Internal modified-layer formation mechanism into silicon with nanosecond laser,” *Journal of*

- Achievements in Manufacturing Engineering*, vol. 17, no. 1-2, pp. 381–384, 2006.
- [11] P. C. Verburg, G. R. B. E. Römer, and J. Huis in't Veld, “Two-photon-induced internal modification of silicon by erbium-doped fiber laser,” *Optics Express*, vol. 22, no. 18, p. 21958, 2014.
- [12] M. Chambonneau, Q. Li, M. Chanal, N. Sanner, and D. Grojo, “Writing waveguides inside monolithic crystalline silicon with nanosecond laser pulses,” *Optics Letters*, vol. 41, no. 21, pp. 4875–4878, 2016.
- [13] X. Liu, D. Du, and G. Mourou, “Laser ablation and micromachining with ultrashort laser pulses,” *IEEE Journal of Quantum Electronics*, vol. 33, no. 10, pp. 1706–1716, 1997.
- [14] E. Bricchi, B. G. Klappauf, and P. G. Kazansky, “Form birefringence and negative index change created by femtosecond direct writing in transparent materials,” *Optics letters*, vol. 29, no. 1, pp. 119–121, 2004.
- [15] V. R. Bhardwaj, E. Simova, P. P. Rajeev, C. Hnatovsky, R. S. Taylor, D. M. Rayner, and P. B. Corkum, “Optically Produced Arrays of Planar Nanostructures inside Fused Silica,” *Physical Review Letters*, vol. 96, no. 057404, pp. 1–4, 2006.
- [16] K. M. Davis, K. Miura, N. Sugimoto, and K. Hirao, “Writing waveguides in glass with a femtosecond laser,” *Optics letters*, vol. 21, no. 21, pp. 1729–1731, 1996.
- [17] E. G. Gamaly, B. Luther-Davies, L. Hallo, P. Nicolai, and V. T. Tikhonchuk, “Laser-matter interaction in the bulk of a transparent solid: Confined microexplosion and void formation,” *Physical Review B*, vol. 73, no. 21, p. 214101, 2006.
- [18] E. Yablonovitch and E. Yablonovitch, “Breakdown Optical Dielectric Strength of Alkali-Halide Crystals Obtained by Laser-Induced Breakdown,” *Applied Physics Letters*, vol. 19, no. 11, pp. 495–497, 1971.
- [19] R. Soref, “The Past , Present , and Future of Silicon Photonics,” *IEEE journal of quantum electronics*, vol. 12, no. 6, pp. 1678–1687, 2006.
- [20] R. Soref, “Silicon photonics: A review of recent literature,” *Silicon*, vol. 2, no. 1, pp. 1–6, 2010.
- [21] A. H. Nejadmalayeri, P. R. Herman, J. Burghoff, M. Will, S. Nolte, and A. Tünnermann, “Inscription of optical waveguides in crystalline silicon by mid-infrared femtosecond laser pulses,” *Optics Letters*, vol. 30, no. 9, p. 964, 2005.
- [22] S. Leyder, *Ionisation nonlinéaire dans les matériaux diélectriques et semiconducteurs par laser femtoseconde accordable dans le proche infrarouge*. PhD thesis, Aix-Marseille Université, 2013.

- [23] M. Mori, Y. Shimotsuma, T. Sei, M. Sakakura, K. Miura, and H. Usono, "Tailoring thermoelectric properties of nanostructured crystal silicon fabricated by infrared femtosecond laser direct writing," *Physica Status Solidi (a)*, vol. 212, no. 4, pp. 715–721, 2015.
- [24] C. Kittel, "Introduction to solid state physics," p. 688, 1960.
- [25] J. Dabrowski and H.-J. Mussig, *Silicon surfaces and Formation of Interfaces: Basic Science in the Industrial World*. World Scientific Publishing Co. Pte. Ltd., 2000.
- [26] S. M. Sze and K. N. Kwok, *Physics of Semiconductor Devices*. John Wiley and Sons, Inc, 2007.
- [27] N. W. Ashcroft and N. D. Mermin, *Solid State Physics*. Harcourt, Inc, 1976.
- [28] V. Alex, S. Finkbeiner, and J. Weber, "Temperature dependence of the indirect energy gap in crystalline silicon," *Journal of Applied Physics*, vol. 79, no. 9, pp. 6943–6946, 1996.
- [29] C. D. Thurmond, "The Standard Thermodynamic Functions for the Formation of Electrons and Holes in Ge, Si, GaAs, and GaP," *Journal of The Electrochemical Society*, vol. 122, no. 8, p. 1133, 1975.
- [30] N. Bloembergen, "Laser Induced Electric Breakdown in Solids," *IEEE Journal of Quantum Electronics*, vol. 10, no. 3, pp. 375–386, 1974.
- [31] L. V. Keldysh, "Ionization in the field of a strong electromagnetic wave," *Soviet Physics JETP*, vol. 20, no. 5, pp. 1307–1314, 1965.
- [32] M. Dinu, F. Quochi, and H. Garcia, "Third-order nonlinearities in silicon at telecom wavelengths," *Applied Physics Letters*, vol. 82, no. 18, p. 2954, 2003.
- [33] A. D. Bristow, N. Rotenberg, and H. M. van Driel, "Two-photon absorption and Kerr coefficients of silicon for 850-2200 nm," *Applied Physics Letters*, vol. 90, no. 19, p. 191104, 2007.
- [34] V. S. Popov, "Tunnel and multiphoton ionization of atoms and ions in a strong laser field (Keldysh theory)," *Physics Uspekhi*, vol. 47, no. 9, pp. 855–8, 2004.
- [35] C. B. Schaffer, A. Brodeur, and E. Mazur, "Laser-induced breakdown and damage in bulk transparent materials induced by tightly focused femtosecond laser pulses," *Measurement Science and Technology*, vol. 12, no. 11, pp. 1784–1794, 2001.
- [36] B. Stuart, M. Feit, S. Herman, a. Rubenchik, B. Shore, and M. Perry, "Nanosecond-to-femtosecond laser-induced breakdown in dielectrics," *Physical Review B*, vol. 53, no. 4, pp. 1749–1761, 1996.
- [37] D. Du, X. Liu, G. Korn, J. Squier, and G. Mourou, "Laser-induced breakdown by impact ionization in SiO₂ with pulse widths from 7 ns to 150 fs," *Applied Physics Letters*, vol. 64, no. 23, p. 3071, 1994.

- [38] M. Lenzner, J. Krüger, S. Sartania, Z. Cheng, C. Spielmann, G. Mourou, W. Kautek, and F. Krausz, “Femtosecond Optical Breakdown in Dielectrics,” *Physical Review Letters*, vol. 80, pp. 4076–4079, 1998.
- [39] W. Maes, K. D. E. Meyer, and R. V. Overstraeten, “Impact ionization in silicon: a review and update,” *Solid-State Electronics*, vol. 33, no. 6, pp. 705–718, 1990.
- [40] P. Pronko, P. V. Rompay, C. Horvath, X. Liu, T. Juhasz, and G. Mourou, “Avalanche ionization and dielectric breakdown in silicon with ultrafast laser pulses,” *Physical Review B*, vol. 58, no. 5, pp. 2387–2390, 1998.
- [41] K. K. Thornber, “Applications of scaling to problems in high-field electronic transport,” *Journal of Applied Physics*, vol. 52, no. 1, pp. 279–290, 1981.
- [42] S. Leyder, D. Grojo, P. Delaporte, W. Marine, M. Sentis, and O. Utéza, “Non-linear absorption of focused femtosecond laser pulses at 1.3 μ m inside silicon: Independence on doping concentration,” *Applied Surface Science*, vol. 278, pp. 13–18, 2013.
- [43] H. M. Van Driel, “Kinetics of high-density plasmas generated in Si by 1.06- and 0.53- m picosecond laser pulses,” *Physical Review B*, vol. 35, no. 15, pp. 8166–8176, 1987.
- [44] K. Sokolowski-Tinten and D. von der Linde, “Generation of dense electron-hole plasmas in silicon,” *Physical Review B*, vol. 61, no. 4, pp. 2643–2650, 2000.
- [45] D. M. Riffe, “Temperature dependence of silicon carrier effective masses with application to femtosecond reflectivity measurements,” *J. Opt. Soc. Am. B*, vol. 19, pp. 1092–1100, May 2002.
- [46] M. D. Feit and J. A. Fleck, “Effect of refraction on spot-size dependence of laser-induced breakdown,” *Applied Physics Letters*, vol. 24, no. 4, pp. 169–172, 1974.
- [47] F. Berz, R. W. Cooper, and S. Fagg, “Recombination in the end regions of PIN diodes,” *Solid State Electronics*, vol. 22, pp. 293–301, 1979.
- [48] F. Wang, J. Shan, E. Knoesel, M. Bonn, T. F. Heinz, W. Street, N. York, and M. H. Road, “Electronic Charge Transport in Sapphire Studied by Optical-Pump / THz-Probe Spectroscopy,” *Proc. SPIE 5352, Ultrafast Phenomena in Semiconductors and Nanostructure Materials VIII*, 2004.
- [49] M. S. Tyagi and R. Van Overstraeten, “Minority carrier recombination in heavily-doped silicon,” *Solid State Electronics*, vol. 26, no. 6, pp. 577–597, 1983.
- [50] W. Van Roosbroeck and W. Shockley, “Photon-radiative recombination of electrons and holes in germanium,” *Physical Review*, vol. 94, no. 6, pp. 1558–1560, 1954.

- [51] J. Dziewior and W. Schimd, “Auger coefficients for highly doped and highly excited semiconductors,” *Applied Physics Letters*, vol. 31, no. 3, pp. 291–293, 1977.
- [52] C. H. Henry, B. F. Levine, R. A. Logan, and C. G. Bethea, “Minority Carrier Lifetime and Luminescence Efficiency of 1.3 microns InGaAsP-InP Double Heterostructures Layers,” *Journal of Quantum Electronics*, vol. 50, no. 6, pp. 5795–5799, 1983.
- [53] R. P. Mertens, J. L. V. Meerbergen, J. F. Nijs, and R. V. Overstraeten, “Measurement of the Minority-Carrier Transport Parameters in Heavily Doped Silicon,” *IEEE Transactions on Electron Devices*, no. 5, pp. 949–955, 1980.
- [54] A. Ohsawa, K. Honda, R. Takizawa, and N. Toyokura, “Instrument measuring temperature dependence of minority-carrier lifetime without contact,” *Review of Scientific Instruments*, vol. 54, no. 2, pp. 210–212, 1983.
- [55] C. A. Dimitriadis, D. E. Joannou, S. M. Davidson, N. Puhmann, G. Oelgart, T. Fuyuki, H. Matsunami, T. Tanaka, C. Donolato, M. L. Young, D. R. Wight, S. Srivastava, N. K. Swami, and G. P. Srivastava, “A SEM-EBIC minority-carrier lifetime-measurement technique,” *Journal of Physics D: Applied Physics*, vol. 13, no. 4, 1980.
- [56] W. Shockley and W. T. Read, “Statistics of the Recombination of Holes and Electrons,” *Physical Review*, vol. 87, no. 46, pp. 835–842, 1952.
- [57] T. Goudon, V. Miljanovic, and C. Schmeiser, “On the Shockley-Read-Hall Model: Generation-Recombination in Semiconductors,” *SIAM J. Applied Mathematics*, vol. 67, no. 4, pp. 1183–1201, 2007.
- [58] A. Alkauskas, C. E. Dreyer, J. L. Lyons, and C. G. Van De Walle, “Role of excited states in Shockley-Read-Hall recombination in wide-band-gap semiconductors,” *Physical Review B - Condensed Matter and Materials Physics*, vol. 93, no. 20, pp. 1–5, 2016.
- [59] A. R. Beattie and P. T. Landsberg, “Auger effect in semiconductors,” *Proceedings of the Royal Society of London. Series A. Mathematical and Physical Sciences*, vol. 249, no. 1256, pp. 16–29, 1959.
- [60] L. Huld, “Band-to-Band Auger Recombination,” *Energy*, vol. 173, pp. 173–187, 1971.
- [61] M. J. Kerr and A. Cuevas, “General parameterization of Auger recombination in crystalline silicon,” *Journal of Applied Physics*, vol. 91, no. 3, pp. 2473–2480, 2002.
- [62] G. E. Possin, M. S. Adler, and B. J. Baliga, “Measurement of heavy doping parameters in silicon by electron-beam-induced current,” *Transactions on electron devices*, vol. 27, no. 4, pp. 983–990, 1980.

- [63] A. Haug and W. Schmid, “Recombination mechanism in heavily doped silicon,” *Solid State Electronics*, vol. 25, no. 7, pp. 665–667, 1982.
- [64] A. Haug, “Band-to-band Auger recombination in semiconductors,” *Journal of Physics and Chemistry of Solids*, vol. 49, no. 6, pp. 599–605, 1988.
- [65] R. W. Boyd, *Nonlinear Optics*. Academic Press Inc., 1992.
- [66] R. L. Sutherland, *Handbook of nonlinear optics*. Marcel Dekker, Inc., 1996.
- [67] R. W. Boyd and S. G. Lukishova, *Self-focusing: Past and Present*. 2009.
- [68] P. L. Kelley, “Self-focusing of optical beams,” *Physical Review Letters*, vol. 15, no. 26, pp. 1005–1008, 1965.
- [69] W. Liu and S. L. Chin, “Direct measurement of the critical power of femtosecond Ti : sapphire laser pulse in air,” *Optics express*, vol. 13, no. 15, pp. 5750–5755, 2005.
- [70] A. Couairon and A. Mysyrowicz, “Femtosecond filamentation in transparent media,” *Physics Reports*, vol. 441, no. 2-4, pp. 47–189, 2007.
- [71] W. J. Tomlinson, R. H. Stolen, and C. V. Shank, “Compression of optical pulses chirped by self-phase modulation in fibers,” *Journal of Optical Society B*, vol. 1, no. 2, 1984.
- [72] V. V. Kononenko, E. V. Zavedeev, and V. M. Gololobov, “The effect of light-induced plasma on propagation of intense fs laser radiation in c-Si,” *Applied Physics A*, vol. 122, no. 4, pp. 1–7, 2016.
- [73] D. Grojo, A. Mouskeftaras, P. Delaporte, and S. Lei, “Limitations to laser machining of silicon using femtosecond micro-Bessel beams in the infrared,” *Journal of Applied Physics*, vol. 117, no. 15, 2015.
- [74] D. Strickland and G. Mourou, “No Title Compression of amplified chirped optical pulses,” *Optics Communications*, vol. 56, no. 3, pp. 219–221, 1985.
- [75] P. Maine, D. Strickland, P. Bado, M. Pessot, and G. Mourou, “Generation of Ultrahigh Peak Power Pulses by Chirped Pulse Amplification,” *IEEE Journal of Quantum Electronics*, vol. 24, no. 2, pp. 398–403, 1988.
- [76] G. Cheriaux, P. Rousseau, F. Salin, J. P. Chambaret, B. Walker, and L. F. Dimauro, “Aberration-free stretcher design for ultrashort-pulse amplification,” *Optics Letters*, vol. 21, no. 6, pp. 414–416, 1996.
- [77] E. B. Treacy, “Optical Pulse Compression With Diffraction Gratings,” *IEEE Journal of Quantum Electronics*, no. 9, pp. 454–458, 1969.
- [78] C. Rullière, *Femtosecond Laser Pulses Principles and Experiments Second Edition*. Springer-Verlag New York, 2003.

- [79] J.-C. Diels and W. Rudolph, *Ultrashort Laser Pulse Phenomenon: Fundamentals Techniques, and Applications on a Femtosecond Time Scale*. Academic Press, San Diego, CA, 2006.
- [80] C. C. Wang and G. W. Racette, “Measurement of parametric gain accompanying optical,” *Applied Physics Letters*, vol. 169, pp. 6–9, 1965.
- [81] C. Mauclair, K. Mishchik, A. Mermillod-Blondin, A. Rosenfeld, I. V. Hertel, E. Audouard, and R. Stoian, “Optimization of the energy deposition in glasses with temporally-shaped femtosecond laser pulses,” *Physics Procedia*, vol. 12, pp. 76–81, 2011.
- [82] W. Koechner, *Solid-state Laser Engineering*. Springer, 1976.
- [83] L. Sudrie, A. Couairon, M. Franco, B. Lamouroux, B. Prade, S. Tzortzakis, A. Mysyrowicz, T. Avance, and O. Applique, “Femtosecond Laser-Induced Damage and Filamentary Propagation in Fused Silica,” *Physical Review Letters*, vol. 89, no. 18, pp. 1–4, 2002.
- [84] R. R. Gattass and E. Mazur, “Femtosecond laser micromachining in transparent materials,” *Nature Photonics*, vol. 2, 2008.
- [85] M. F. Yanik, H. Cinar, H. N. Cinar, A. D. Chisholm, Y. Jin, and A. Ben-Yakar, “Functional regeneration after laser axotomy,” *Nature (London)*, vol. 432, no. December, p. 8057, 2004.
- [86] A. Vogel, N. Linz, and S. Freidank, “Femtosecond-Laser-Induced Nanocavitation in Water : Implications for Optical Breakdown Threshold and Cell Surgery,” *Physical Review Letters*, vol. 100, no. 038102, pp. 1–4, 2008.
- [87] M. Moshirfar, D. S. Churgin, and M. Hsu, “Femtosecond laser-assisted cataract surgery: a current review,” *Middle East African Journal of Ophthalmology*, vol. 18, no. 4, pp. 285–292, 2011.
- [88] X. Mao, S. S. Mao, and R. E. Russo, “Imaging femtosecond laser-induced electronic excitation in glass,” *Applied Physics Letters*, vol. 82, no. 5, pp. 697–699, 2003.
- [89] P. Martin, S. Guizard, P. Daguzan, and G. Petite, “Subpicosecond study of carrier trapping dynamics in wide-band-gap crystals,” *Physical Review B*, vol. 55, no. 9, pp. 5799–5810, 1997.
- [90] R. T. Williams, B. B. Craig, and W. L. Faust, “F-center formation in NaCl: picosecond spectroscopic evidence for halogen diffusion on the lowest excitonic potential surface,” *Physical Review Letters*, vol. 52, no. 19, pp. 1709–1712, 1984.
- [91] A. Couairon, S. Tzortzakis, L. Bergé, M. Franco, B. Prade, and A. Mysyrowicz, “Infrared femtosecond light filaments in air: simulations and experiments,” *Journal of the Optical Society of America B*, vol. 19, no. 5, pp. 1117–1131, 2002.

- [92] A. Ramer, O. Osmani, and B. Rethfeld, “Laser damage in silicon: Energy absorption, relaxation, and transport,” *Journal of Applied Physics*, vol. 116, no. 5, 2014.
- [93] A. Couairon, L. Sudrie, M. Franco, B. Prade, and A. Mysyrowicz, “Filamentation and damage in fused silica induced by tightly focused femtosecond laser pulses,” *Physical Review B - Condensed Matter and Materials Physics*, vol. 71, no. 12, pp. 1–11, 2005.
- [94] J. Linnros, “Carrier lifetime measurements using free carrier absorption transients . I . Principle and injection dependence Carrier lifetime measurements using free carrier absorption transients . I . Principle and injection dependence,” *Applied Physics Letters*, vol. 84, no. 275, 1998.
- [95] A. Richter, S. W. Glunz, F. Werner, J. Schmidt, and A. Cuevas, “Improved quantitative description of Auger recombination in crystalline silicon,” *Physical Review B*, vol. 86, no. 165202, pp. 1–14, 2012.
- [96] D. K. Schroder, *Semiconductor Material And Device Characterization*. John Wiley and sons, New Jersey, 1990.
- [97] S. K. Pang and A. Rohatgi, “Record high recombination lifetime in oxidized magnetic Czochralski silicon,” *Applied Physics Letters*, vol. 59, no. 2, pp. 195–197, 1991.
- [98] J. Linnros and V. Grivickas, “Carrier-diffusion measurements in silicon with a Fourier-transient-grating method,” *Physical Review B*, vol. 50, no. 23, pp. 16943–16955, 1994.
- [99] M. Rosling, H. Bleichner, P. Jonsson, and E. Nordlander, “The ambipolar diffusion coefficient in silicon: Dependence on excess carrier concentration and temperature,” *Applied Physics Letters*, vol. 75, no. 2855, 1994.
- [100] H. J. Eichler, F. Massmann, E. Biselli, K. Richter, M. Glotz, L. Konetzke, and X. Yang, “Laser-induced free-carrier and temperature gratings in silicon,” *Physical Review B*, vol. 36, no. 6, pp. 3247–3253, 1987.
- [101] Q. Sun, H. Jiang, Y. Liu, Z. Wu, H. Yang, and Q. Gong, “Measurement of the collision time of dense electronic plasma induced by a femtosecond laser in fused silica,” *Optics Letters*, vol. 30, no. 3, pp. 320–322, 2005.
- [102] V. V. Temnov, K. Sokolowski-Tinten, P. Zhou, A. El-Khamhawy, and D. Von Der Linde, “Multiphoton ionization in dielectrics: Comparison of circular and linear polarization,” *Physical Review Letters*, vol. 97, no. 23, pp. 1–4, 2006.
- [103] D. H. Auston, C. V. Shank, and P. Lefur, “Picosecond optical measurements of band-to-band auger recombination of high-density plasmas in germanium,” *Physical Review Letters*, vol. 35, no. 15, pp. 1022–1025, 1975.
- [104] B. E. Sernelius, “Optical free-carrier absorption of an electron-hole plasma in silicon,” *Physical Review Letters*, vol. 39, no. 15, 1989.

- [105] Q. Li, M. Chambonneau, M. Chanal, and D. Grojo, “Quantitative-phase microscopy of nanosecond laser-induced micro-modifications inside silicon,” *Applied Optics*, vol. 55, no. 33, pp. 2–8, 2016.
- [106] A. Safrani and I. Abdulhalim, “Real-time phase shift interference microscopy.,” *Optics Letters*, vol. 39, no. 17, pp. 5220–3, 2014.
- [107] J. H. Bruning, D. R. Herriott, J. E. Gallagher, D. P. Rosenfeld, A. D. White, and D. J. Brangaccio, “Digital Wavefront Measuring Interferometer for Testing Optical Surfaces and Lenses.,” *Applied Optics*, vol. 13, no. 11, pp. 2693–2703, 1974.
- [108] C. Xie, V. Jukna, C. Milián, R. Giust, I. Ouadghiri-Idrissi, T. Itina, J. M. Dudley, A. Couairon, and F. Courvoisier, “Tubular filamentation for laser material processing.,” *Scientific reports*, vol. 5, p. 8914, 2015.
- [109] I. B. Bogatyrev, D. Grojo, P. Delaporte, S. Leyder, M. Sentis, W. Marine, and T. E. Itina, “Non-linear absorption of 1.3- μm wavelength femtosecond laser pulses focused inside semiconductors: Finite difference time domain-two temperature model combined computational study,” *Journal of Applied Physics*, vol. 110, no. 10, 2011.
- [110] P. D. Desai, “Thermodynamic Properties of Iron and Silicon,” *Journal of Physics and Chemistry of Solids*, vol. 15, no. 3, 1986.
- [111] S. Chi and Q. Guo, “Vector theory of self-focusing of an optical beam in Kerr media.,” *Optics Letters*, vol. 20, no. 15, pp. 1598–600, 1995.
- [112] G. Fibich and B. Ilan, “Vectorial and random effects in self-focusing and in multiple filamentation,” *Physica D: Nonlinear Phenomena*, vol. 157, no. 1-2, pp. 112–146, 2001.
- [113] C. L. Arnold, A. Heisterkamp, W. Ertmer, and H. Lubatschowski, “Computational model for nonlinear plasma formation in high NA micromachining of transparent materials and biological cells,” *Optics Express*, vol. 15, no. 16, p. 10303, 2007.
- [114] P. Jakobsen and J. V. Moloney, “The effect of longitudinal electric field components on the propagation of intense ultrashort optical pulses,” *Physica D: Nonlinear Phenomena*, vol. 241, no. 19, pp. 1603–1611, 2012.
- [115] A. Couairon, O. G. Kosareva, N. A. Panov, D. E. Shipilo, V. A. Andreeva, V. Jukna, and F. Nesa, “Propagation equation for tight-focusing by a parabolic mirror,” *Optics Express*, vol. 23, no. 24, p. 31240, 2015.
- [116] N. M. Bulgakova, V. P. Zhukov, S. V. Sonina, and Y. P. Meshcheryakov, “Modification of transparent materials with ultrashort laser pulses : What is energetically and mechanically meaningful ?,” *Applied Physics Letters*, vol. 118, no. 233108, 2015.

- [117] M. Kolesik, J. V. Moloney, and M. Mlejnek, “Unidirectional optical pulse propagation equation.,” *Physical Review Letters*, vol. 89, no. 28, p. 283902, 2002.
- [118] H. H. Li, “Refractive index of silicon and germanium and its wavelength and temperature derivatives,” *Journal of Physical and Chemical Reference Data*, vol. 9, no. 3, pp. 561–658, 1980.
- [119] J. Zhang, Q. Lin, G. Piredda, R. W. Boyd, G. P. Agrawal, and P. M. Fauchet, “Anisotropic nonlinear response of silicon in the near-infrared region,” *Applied Physics Letters*, vol. 91, no. 7, p. 071113, 2007.
- [120] S. Pearl, N. Rotenberg, and H. M. van Driel, “Three photon absorption in silicon for 2300 - 3300 nm,” *Applied Physics Letters*, vol. 93, no. 131102, 2008.
- [121] D. Von Der Linde and H. Schuler, “Breakdown threshold and plasma formation in femtosecond laser-solid interaction,” *J. Opt. Soc. Am. B*, vol. 13, no. 1, pp. 216–222, 1996.
- [122] B. Chimier, O. Utéza, N. Sanner, M. Sentis, T. Itina, P. Lassonde, F. Légaré, F. Vidal, and J. C. Kieffer, “Damage and ablation thresholds of fused-silica in femtosecond regime,” *Physical Review B*, vol. 84, no. 094104, 2011.
- [123] D. Ashkenasi, a. Rosenfeld, H. Varel, M. Wähmer, and E. Campbell, “Laser processing of sapphire with picosecond and sub-picosecond pulses,” *Applied Surface Science*, vol. 120, no. 1-2, pp. 65–80, 1997.
- [124] Y. Zhang, L. Guilbert, and P. Bourson, “Characterization of Ti:LiNbO₃ waveguides by micro-raman and luminescence spectroscopy,” *Applied Physics B*, vol. 78, no. 3-4, pp. 355–361, 2004.
- [125] D. Von Der Linde and K. Sokolowski-Tinten, “Physical mechanisms of short-pulse laser ablation,” *Applied Surface Science*, vol. 109-110, pp. 1–10, 2000.
- [126] J. Bonse, S. Baudach, J. Krüger, W. Kautek, and M. Lenzner, “Femtosecond laser ablation of silicon - modification thresholds and morphology,” *Appl. Phys. A*, vol. 74, no. 1, pp. 19–25, 2002.
- [127] B. R. Tull, J. E. Carey, E. Mazur, J. P. McDonald, and S. M. Yalisove, “Silicon surface morphologies after femtosecond laser irradiation,” *MRS Bulletin*, vol. 31, pp. 626–633, 2006.
- [128] F. He, Z. Wang, B. Zeng, J. Ni, Y. Cheng, and K. Sugioka, “Extraordinary characteristics of spatiotemporally focused laser pulses and their roles in precision materials processing,” *2015 Conference on Lasers and Electro-Optics Pacific Rim*, 2015.
- [129] R. Kammel, R. Ackermann, J. Thomas, J. Götte, S. Skupin, A. Tunnermann, and S. Nolte, “Enhancing precision in fs-laser material processing by simultaneous spatial and temporal focusing,” *Light: Science & Applications*, vol. 3, no. 169, pp. 1–8, 2014.

- [130] T. E. Lanier and J. R. Gulley, “Nonlinear space-time focusing and filamentation of annular femtosecond pulses in dielectrics,” *J. Opt. Soc. Am. B*, vol. 33, no. 2, pp. 292–301, 2016.
- [131] P. C. Verburg, G. R. B. E. Römer, and A. J. Huis In’T Veld, “Two-temperature model for pulsed-laser-induced subsurface modifications in Si,” *Applied Physics A: Materials Science and Processing*, vol. 114, pp. 1135–1143, 2014.
- [132] X. Wang, Z. H. Shen, J. Lu, and X. W. Ni, “Laser-induced damage threshold of silicon in millisecond, nanosecond, and picosecond regimes,” *Journal of Applied Physics*, vol. 108, no. 033103, 2010.
- [133] Y. Izawa, Y. Tsurumi, N. Miyanaga, S. Tanaka, H. Kikuchi, M. Esashi, and M. Fujita, “Debris-free in-air laser dicing for multi-layer mems by perforated internal transformation and thermally-induced crack propagation,” *2008 IEEE 21st International Conference on Micro Electro Mechanical Systems*, pp. 822–827, Jan 2008.
- [134] M. K. Bhuyan, F. Courvoisier, P. A. Lacourt, M. Jacquot, R. Salut, L. Furfaro, and J. M. Dudley, “High aspect ratio nanochannel machining using single shot femtosecond Bessel beams,” *Applied Physics Letters*, vol. 97, no. 081102, 2010.
- [135] P. Panagiotopoulos, D. Papazoglou, A. Couairon, and S. Tzortzakis, “Sharply autofocused ring-Airy beams transforming into non-linear intense light bullets,” *Nature Communications*, vol. 4, pp. 1–6, 2013.
- [136] G. Siviloglou, J. Broky, A. Dogariu, and D. N. Christodoulides, “Observation of accelerating Airy beams,” *Physical Review Letters*, vol. 99, no. 213901, 2007.
- [137] G. A. Siviloglou and D. N. Christodoulides, “Accelerating finite energy Airy beams,” *Optics Letters*, vol. 32, no. 8, p. 979, 2007.
- [138] D. G. Papazoglou, N. K. Efremidis, D. N. Christodoulides, and S. Tzortzakis, “Observation of abruptly autofocusing waves,” *Optics Letters*, vol. 36, no. 10, p. 1842, 2011.
- [139] Y.-l. Zhang, Q.-d. Chen, H. Xia, and H.-b. Sun, “Designable 3D nanofabrication by femtosecond laser direct writing,” *Nano Today*, vol. 5, no. 5, p. 435, 2010.
- [140] R. Taylor, C. Hnatovsky, and E. Simova, “Applications of femtosecond laser induced self-organized planar nanocracks inside fused silica glass,” *Laser & Photonics Reviews*, vol. 2, p. 26, 2008.
- [141] S. Shapiro, *Ultrashort Light Pulses, Picosecond Techniques and Applications*. Springer-Verlag, 1977.
- [142] E. N. Glezer, Y. Siegal, L. Huang, and E. Mazur, “Laser-induced band-gap collapse in GaAs,” *Physical Review B*, vol. 51, no. 11, pp. 6959–6970, 1995.

- [143] X. Yu, X. Wang, M. Chanal, C. A. Trallero-Herrero, D. Grojo, and S. Lei, “Internal modification of intrinsic and doped silicon using infrared nanosecond laser,” *Applied Physics A: Materials Science and Processing*, vol. 122, no. 12, pp. 1–7, 2016.
- [144] S. M. Mansfield and G. S. Kino, “Solid immersion microscope,” *Applied Physics Letters*, vol. 57, no. 24, pp. 2615–2616, 1990.
- [145] A. N. Vamivakas, R. D. Younger, B. B. Goldberg, A. K. Swan, M. S. Ünlü, E. R. Behringer, and S. B. Ippolito, “A case study for optics: The solid immersion microscope,” *American Journal of Physics*, vol. 76, no. 8, pp. 758–768, 2008.
- [146] B. B. Goldberg, S. B. Ippolito, L. Novotny, Z. Liu, M. S. Ünlü, and S. Member, “Immersion Lens Microscopy of Photonic Nanostructures and Quantum Dots,” *IEEE Journal of Quantum Electronics*, vol. 8, no. 5, pp. 1051–1059, 2002.
- [147] E. Ramsay, N. Pleyne, D. Xiao, R. J. Warburton, and D. T. Reid, “Two-photon optical-beam-induced current solid-immersion imaging of a silicon flip chip with a resolution of 325 nm,” *Optics letters*, vol. 30, no. 1, pp. 26–28, 2005.
- [148] Z. Liu, B. B. Goldberg, S. B. Ippolito, A. N. Vamivakas, M. S. Ünlü, R. Mirin, Z. Liu, B. B. Goldberg, and R. Mirin, “High resolution , high collection efficiency in numerical aperture increasing lens microscopy of individual quantum dots High resolution , high collection efficiency in numerical aperture increasing,” *Applied Physics Letters*, vol. 87, no. 071905, 2005.
- [149] K. A. Serrels, E. Ramsay, P. A. Dalgarno, D. Brian, J. A. O. Connor, R. H. Hadfield, J. Richard, and D. T. Reid, “Solid immersion lens applications for nanophotonic devices,” *Journal of Nanophotonics*, vol. 2, no. 021854, 2008.
- [150] M. Born and E. Wolf, *Principles of Optics 7th edition*. Cambridge University Press, 2002.
- [151] S. B. Ippolito, B. B. Goldberg, and M. S. Ünlü, “High spatial resolution subsurface microscopy High spatial resolution subsurface microscopy,” *Applied Physics Letters*, vol. 78, no. 26, pp. 4071–4073, 2001.
- [152] M. Chanal, V. Y. Fedorov, M. Chambonneau, R. Clady, S. Tzortzakis, and D. Grojo, “Crossing the threshold of ultrafast laser writing in bulk silicon,” *Nature Communications*, vol. 8, no. 773, 2017.
- [153] J. W. Chan, T. Huser, S. Risbud, and D. M. Krol, “Structural changes in fused silica after exposure to focused femtosecond laser pulses,” *Optics Letters*, vol. 26, no. 21, p. 1726, 2001.
- [154] T. Gorelik, M. Will, S. Nolte, A. Tuennermann, and U. Glatzel, “Transmission electron microscopy studies of femtosecond laser induced modifications in quartz,” *Applied Physics A: Materials Science and Processing*, vol. 76, no. 3, pp. 309–311, 2003.

- [155] A. Barty, K. A. Nugent, D. Paganin, and A. Roberts, “Quantitative optical phase microscopy,” *Optics Letters*, vol. 23, no. 11, p. 817, 1998.
- [156] A. Martinez, M. Dubov, I. Khrushchev, and I. Bennion, “Photoinduced modifications in fiber gratings inscribed directly by infrared femtosecond irradiation,” *IEEE Photonics Technology Letters*, vol. 18, no. 21, pp. 2266–2268, 2006.
- [157] M. Shimizu, Y. Shimotsuma, M. Sakakura, T. Yuasa, H. Homma, Y. Minowa, K. Miura, and K. Hirao, “Periodic metallo-dielectric structure in diamond,” *Optics Express*, vol. 17, no. 1, pp. 46–54, 2009.

